SYNTHESIS AND CHARACTERIZATION OF SIZE-SELECTED PLATINUM CLUSTERS THROUGH SCANNING TRANSMISSION ELECTRON MICROSCOPY AND ELECTROCHEMICAL METHODS

Patrick James Harrison

A Thesis submitted to the University of Birmingham for the degree of Doctor of Philosophy

Nanoscale Physics Research Laboratory
School of Physics and Astronomy
University of Birmingham
Birmingham, UK

January 2020

Acknowledgements

I would like to thank my supervisor Dr Quanmin Guo for his help and support throughout my PhD.

Dr Andy Wain and Dr Jo Humphrey for their efforts to teach me, a physicist, electrochemistry and productive discussions throughout the project.

Dr Wolfgang Theis for interesting discussions and teaching me new code. Dr Ziyou Li for her insight and discussions on cluster fundamentals.

I would like to thank everyone I have met and worked with during my time at the University of Birmingham. Ross for his friendship, Scott for taking me under his wing initially, Alex for his patience with the microscope, and Daniel for his help in the chemical lab and electrochemical insights.

My family for being supportive and having understanding throughout the whole PhD. And for regularly reminding me of why I haven’t finished yet.

And, of course, I would like to thank Alê for pulling through the PhD with me during difficult times. There were many times when I needed support without realising it and you were patient, caring, and showed me the way.

Abstract

Platinum nanoparticles have a key role in today's society as catalysts for pharmaceutical applications and in the energy industry. As we strive to move away from fossil fuels, alternative energy sources suitable for mobile applications such as hydrogen fuel cells are becoming increasingly important. Platinum and its variants are currently the best-known catalysts for the electrocatalytic production of hydrogen and oxygen reduction reactions, which are important for energy storage applications and the operation of hydrogen fuel cells; this makes platinum the de facto catalyst for the hydrogen economy. One of the current setbacks on the road towards a carbon neutral society is the cost of alternative energies, where noble metal catalysts account for a significant proportion of the cost.

This thesis focuses on well-defined platinum nanoparticles, small enough that they are referred to as clusters of atoms. Platinum clusters were produced using physical methods and mass-selected before deposition to achieve high homogeneity. Electrochemical techniques and aberration-corrected scanning transmission electron microscopy have been utilised to characterise the clusters *en masse* and at the atomic scale. The hydrogen evolution performance of these clusters has been evaluated, which revealed a performance benefit with potential conditioning. Ex-situ imaging reveals that cluster migration and coalescence is affected by the anodic potential limit of the conditioning procedure. The results in this thesis have implications for the design and stability of future catalysts.

Table of Contents

List of figures

List of tables

Abbreviations

ADF	Annular dark field
AST	Accelerated stress test
BF	Bright field
CDF	Cumulative density function
CE	Counter electrode
CV	Cyclic voltammetry
DF	Dark field
Dh	Decahedral
DI	Deionised
DLA	Diffusion-limited aggregation
EDX	Energy dispersive x-ray
FC	Fuel cell
FCC	Face center cubic
FCEV	Fuel cell electric vehicle
FEG	Field emission gun
FFT	Fast Fourier transform
GC	Glassy carbon
HAADF	High angle annular dark field
HER	Hydrogen evolution reaction
HOPG	Highly oriented pyrolytic graphite
Ih	Icosahedral
IL	Identical location
LSV	Linear sweep voltammetry
MSE	Mercury sulphate electrode
NND	Nearest neighbour distribution
Oh	Octahedral
OHP	Outer Helmholtz plane
PDF	Probability density function
PEMFC	Polymer electrolyte membrane fuel cell
RE	Reference electrode
RHE	Reversible hydrogen electrode
SPM	Scanning probe microscopy
STEM	Scanning transmission electron microscopy
STM	Scanning tunneling microscopy
TEM	Transmission electron microscopy
WE	Working electrode

1 Introduction

1.1 Alternative energies

Our modern society has an ever-increasing demand for energy. World energy consumption increases year-on-year, and 2018 saw a 2.9 % increase in energy consumption compared to 2017[1]. As we are becoming increasingly aware of the effect greenhouses gases are having on the environment, there is a push towards finding fossil-fuel alternative energies. The increasing energy demand and reliance on clean energies puts more demand on the electricity grid[2]. In 2013 the California Independent System Operator published a chart which showed the potential for energy overgeneration from photovoltaics, which came to be known as the 'duck chart'[3]. Whilst generating excess clean energy may sound positive, in actuality overgeneration presents risks to generators in the grid network. More energy storage is needed in the grid network to provide redundancy for the extra energy produced by photovoltaics.

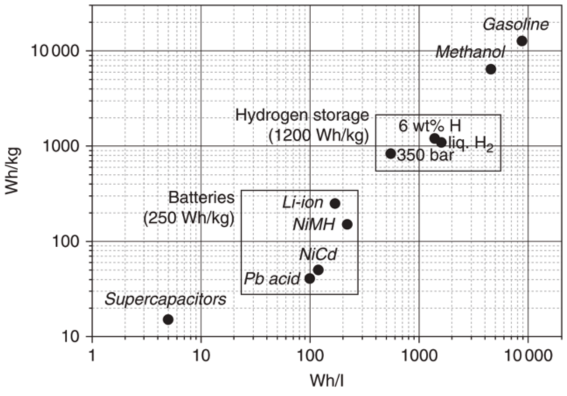

Figure 1.1.1: Energy densities for various energy storage systems. Figure reproduced from reference 4.

Batteries are possibly the most well-known energy storage medium. In most modern electronic devices energy is provided from a lithium-ion battery. In recent years batteries have found increasing use in transportation. The electric vehicle (EV) market grows year-on-year[5] as battery cost decreases[6]. A viable alternative to EVs are hydrogen fuel cell electric vehicles (FCEV)[7], however the global EV stock is orders of magnitude larger than the FCEV stock[5,8], which is in part due to an inferior hydrogen infrastructure, but also hydrogen production and storage costs[9]. The achievable energy densities for hydrogen surpass that of conventional batteries, so developing a more robust hydrogen economy has the potential to improve clean energy storage and transportation.

The conversion of energy from battery-powered devices happens at the atomic level and the study of atomistic processes is often called nanoscience. At sizes of just a few thousand atoms nanomaterials may exhibit dramatically different physical properties[10] and their large surface atom fraction makes them ideal heterogeneous catalysts. A classic example of nanoparticle catalysis are the gold nanoparticles of Haruta et al.[11]. Gold is known for being a noble metal and is not normally an active catalyst. Haruta et al. showed that nanoparticles of gold are in fact active for CO oxidation and outperform more common catalysts.

1.2 Clusters

Clusters are small (nano)particles normally defined as a collection of atoms, from a dimer up to many thousand atoms, which puts them in the size range between tenths of a nanometer to an upper limit of ~100 nm[12,13]. Clusters may be composed of metals[14], however they can be made from many different types of materials including noble gases[15], alloys[16], and semiconductors[17]. They are of high interest in the pharmaceutical community[18]. At this small scale the properties of clusters can be dramatically different to that of their respective bulk materials[19,20], for this reason they are an interesting class of materials to study and model. Despite their small size clusters have shown great promise as catalysts, often with activities well above bulk materials, and they have been used for many applications such as the removal of toxic gases from vehicle exhausts[21], water splitting[22], and in medicine for bacterial resistance[17].

The electronic properties of gold (Au) clusters have been shown to change drastically from the macroscopic yellow-tinted metal that is commonplace on necklines and ring fingers in society. Bulk gold is well known for being inert and a good electrical conductor, hence its use in jewellery and as a coating for wire contacts. However, gold clusters deposited on titania (TiO_2) and TiC have been shown to exhibit non-metallic properties[20,23], and in the study by Valden et al.[20] the size effects linked to the onset of non-metallic behaviour at small cluster sizes

(~3 nm diameter) is correlated with an increase in the activity of the gold clusters for the CO oxidation reaction.

1.2.1 Synthesis

Many different ways to synthesise clusters have been developed over the years[24], and by far the most common technique is wet chemical synthesis[25–27]. Wet synthesis methods are able to produce large amounts of nanomaterials, which is useful for catalytic applications, and these materials are often synthesised as colloidal liquids which can be easily transported and distributed. Wet chemical methods often use organic ligands as a capping agent during synthesis to limit growth along a specific crystallographic direction, and this proved to be a common technique to synthesise size or shaped controlled nanoparticles[28–30]. In the case of platinum, a common wet chemical route to synthesise nanoparticles is to precipitate platinum by reducing a platinum salt, often chloroplatinic acid, with a reducing agent such as sodium borohydride[28]. The synthesised nanoparticles are then drop cast onto a substrate, washed, and then dried before use. This process does not always produce clean nanoparticles however, and often the nanoparticles are cleaned further before use by heating or electrochemical conditioning[29,31].

An alternative to wet chemical synthesis is physical synthesis. Here a high purity bulk material, often a metal, is vaporised under high vacuum conditions, where it is condensed into larger clusters. The clusters are focussed into a beam are directed at a substrate for deposition. Cluster source development increased rapidly during the 1970’s[12]. A few different types of cluster source will be discussed here and the discussion will be limited to the production of metal clusters.

In a supersonic nozzle cluster source a bulk metal is vaporised in a hot oven. The vapour is directed towards a small nozzle by an inert carrier gas, producing a supersonic atomic beam. A vacuum is maintained on the other side of the nozzle which causes adiabatic cooling of the atomic beam. The cooled mixture becomes supersaturated and condenses into clusters. These types of cluster sources are limited to low boiling-point metals[32].

Laser ablation sources have been utilised to overcome this low-boiling point limitation[32], and in principle can be used to produce small clusters from many different metals. A metal is ablated by a high-power pulsed laser which produces a vapour. The vapour is then cooled in an inert gas, forming clusters, and ejected from a nozzle.

In the two cases described above clusters are formed by vapor cooling in an inert gas. By contrast a sputtering cluster source does not require cooling power to form clusters of a few atoms. Here, high-energy inert gas ions are bombarded at a metal to produce small metal clusters[12]. These metal clusters are initially hot and further cooling and condensation can lead to cluster growth. In this thesis a sputtering-type cluster source is used, and it will be discussed further in section 2.1.

1.2.2 Structures

All condensed matter consists of atoms. The arrangement of those atoms varies dramatically from the 'building block' constituent atoms up to the collective arrangement of many hundreds of thousands of atoms into macroscopic 'bulk' materials that are visible to the naked eye. Atoms consist of a collection of protons and neutrons in the nucleus and a number of electrons which surround the nucleus. The electron energy levels in a single atom are quantized. As multiple atoms interact their energy levels split. As more atoms interact their collective energy levels are better described by a band, and this behaviour continues until the collection of atoms resembles its bulk energy structure. A schematic depicting the change in electronic band structure with cluster size is shown in Figure 1.2.1.

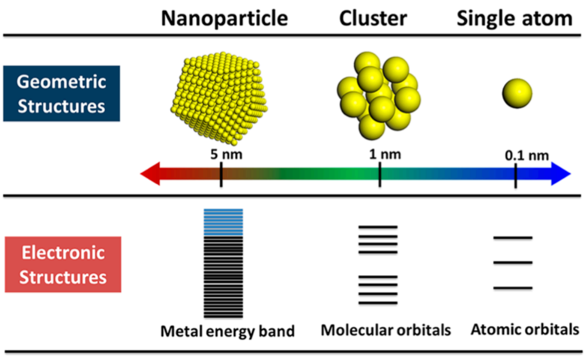

Figure 1.2.1: Geometric and electronic structures in single atoms, small clusters, and nanoparticles. Figure reproduced from reference 33.

As cluster science was taking off in the 1980's, Knight et al.[34] noticed relatively more intense peaks in the mass spectrum of small sodium clusters, see Figure 1.2.2. The relative intensity of these peaks did not change with the cluster formation conditions, which suggested that the mass spectrum peaks are from clusters sizes which are relatively more stable. The electronic energy of each sodium cluster was calculated by solving the Schrödinger equation with a spherically symmetric rounded potential well and yielded energy levels characterised by the quantum number l. The energy difference between neighbouring cluster sizes $E(N)-E(N-1)$ is defined as $\Delta(N)$ in Figure 1.2.2, and the peaks therefore correspond to closed electronic shells. The result of the calculation agrees well with the relative abundance in mass spectra for sodium clusters. Knight et al. therefore showed that electronic structure determines abundances in sodium clusters and that clusters at these sizes are relatively more stable or 'magic'.

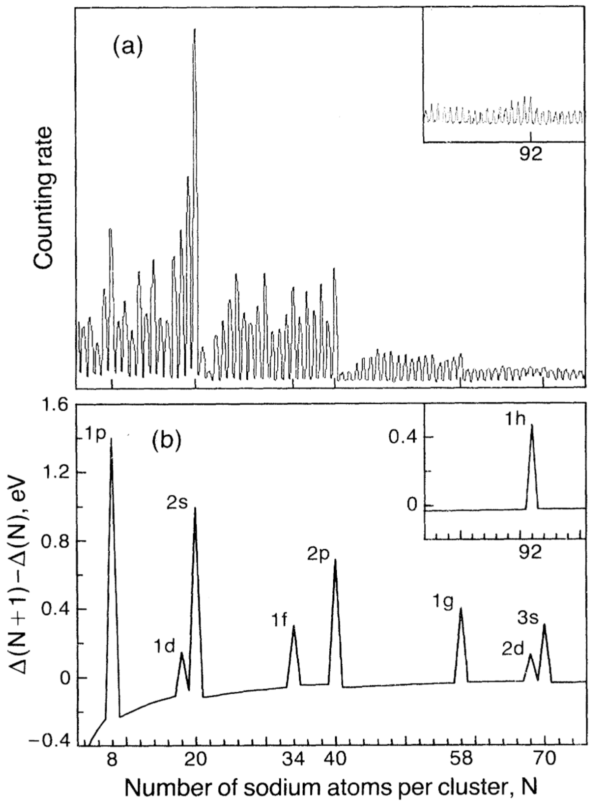

Figure 1.2.2: (a) mass spectrum of small (2<N<76) sodium clusters produced by a supersonic nozzle cluster source. (b) the calculated electronic energy difference for sodium cluster with N atoms. Figure reproduced from reference 34.

It can be seen in Figure 1.2.2 that the observable shell structure in the mass spectrum becomes less obvious as the cluster size increases. As the size of sodium clusters was increased above a hundred atoms a different type of shell structure was observed in the photoionization spectra, see Figure 1.2.3. The local maxima in the ionization energy spectra correspond to cluster sizes which are relatively more difficult to ionize, and therefore more stable. When plotted on the scale of $N^{1/3}$, the local maxima occur at approximately regular intervals, and their corresponding cluster sizes, 1415, 2057, 2869 etc., correspond to the size closed-shell icosahedra. It is believed that the presence of steps and under-coordinated sites on a surface can lower the ionization energy by creating electric dipole moments[13]. Cluster structures with incomplete shells are expected to have step sites, thus closed-shell structures should be relatively more stable.

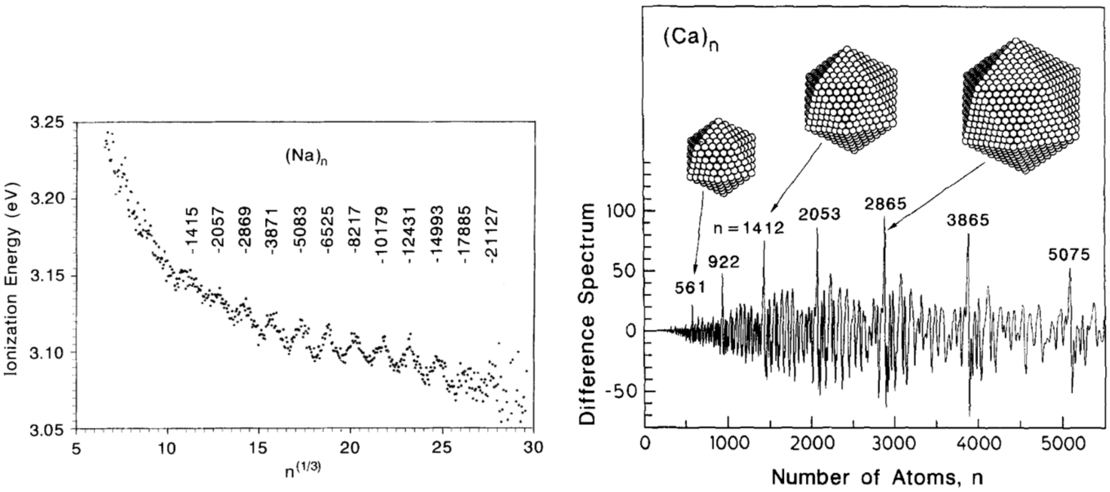

Figure 1.2.3: (left) photoionization energy spectra for sodium clusters. (right) difference spectra for calcium clusters. The peaks in the spectra correspond to closed-shell icosahedra. Figure reproduced from reference 13.

Mackay icosahedra[13,35] are formed by layering atoms around a central core atom. The total number of atoms N for K shells is:

$$N = \frac{10}{3}K^3 - 5K^2 + \frac{11}{3}K - 1, \quad 1.2.1$$

such that an icosahedron composed of seven, eight, and nine closed shells have 923, 1415, and 2057 atoms respectively. Figure 1.2.4 depicts how a partial layer is arranged on top of a 55-atom icosahedron. Calcium clusters have also been shown to have increased abundances at the sizes corresponding to closed-shell icosahedra[13], see Figure 1.2.3. These relative abundances of closed-shell structures are due to increased stabilities and as such they are referred to as geometric magic numbers. The number of atoms for each closed-shell structure is unique to the geometry of the clusters, for example sodium iodide clusters and indium clusters are cubic and octahedral[13], respectively, and the magic number sizes for these geometries are not the same as the icosahedral geometries discussed, see Figure 1.2.4.

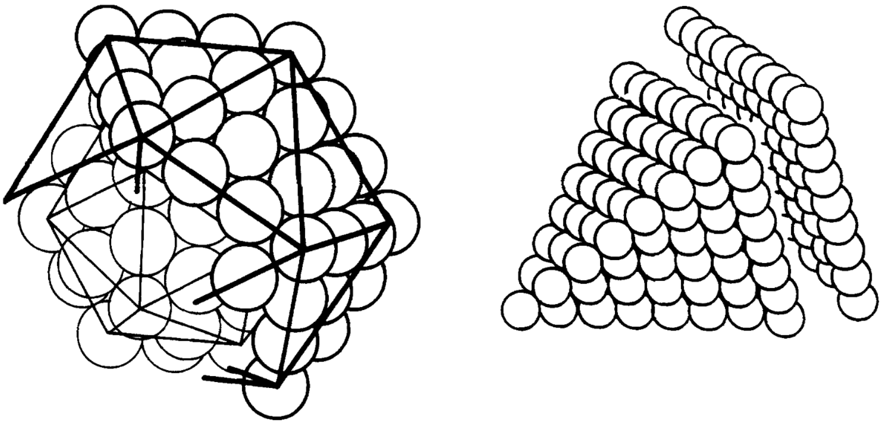

Figure 1.2.4: Shells of different geometric structures. (left) a 55-atom icosahedral structure and portion of the next shell. (right) the next shell layering of a tetrahedron is accomplished by adding a layer of atoms to just one face. Figure reproduced from reference 13.

The closed-shell sizes for octahedral and decahedral clusters are expected to be the same as icosahedra if they are truncated appropriately, which is to say their sizes can be calculated using equation 1.2.1. In the former case, an octahedron is truncated by a cube to expose {100} faces and this structure is called a cuboctahedron. In the latter case, a decahedron is truncated such that there are equal numbers of atoms along the edges of the {111} planes and the exposed {100} planes. These structures are depicted in Figure 1.2.5. Studies into the structures of small mass-selected gold clusters often focus on these structures as they are all predicted and observed for the same cluster size[36,37]. Figure 1.2.5 shows three possible closed-shell arrangements of 923 atoms, which is a geometric magic number. The {111} faces are close packed whereas the {100} faces are not and are expected to have a lower surface energy as a result. Octahedral structures can be cut directly from a face centered cubic (FCC) lattice.

Icosahedra, and more specifically the Mackay icosahedra[35], are a good example of geometric shell layering. The first 'shell' consists of a lone atom, and the second shell can be formed by layering twelve atoms around it as the vertices of an icosahedron. The third shell then consists of 42 atoms. These shells can be layered on top of the previous shell *ad infinitum*, however icosahedral structures are highly strained because the interatomic distances between shells are smaller than within each shell and so icosahedral structures are predicted to exist only for small clusters[13]. Icosahedra consist of 20 exposed close-packed {111} faces and twelve five-fold symmetry axes.

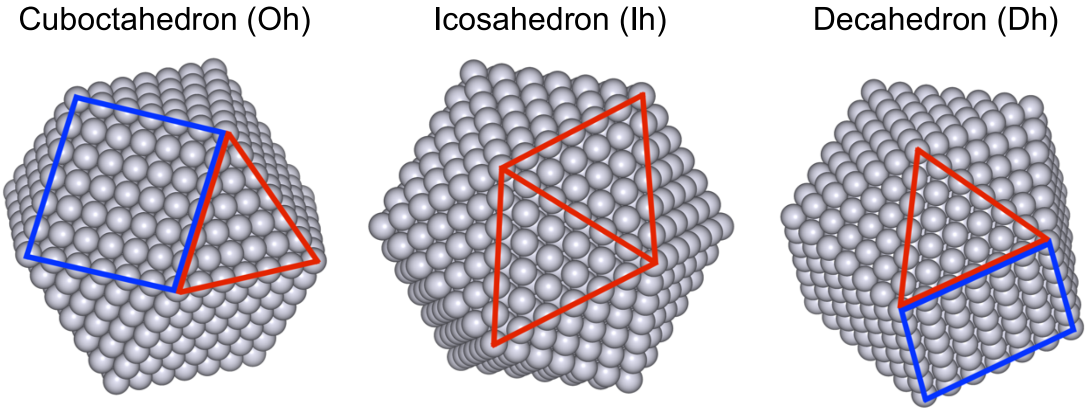

Figure 1.2.5: Possible closed-shell arrangements of 923 atoms which have low index surfaces. Exposed (100) and (111) surfaces are highlighted in blue and red respectively.

Another structure with five-fold symmetry is the decahedron, which only has exposed {111} faces. Decahedrons are not predicted to be a preferred structure at any cluster size as they are internally strained and possess a large surface area. The decahedron shown in Figure 1.2.5 has been truncated to expose {100} faces which make the cluster more spherical and reduce the total exposed surface area. The newly exposed {100} faces, however, are not close-packed. The decahedron can be further truncated at the twinning boundaries to expose re-entrant {111} faces, this structure came to be known as Marks decahedron[38].

Cluster structures can be difficult to measure through transmission electron microscopy as the image formed is a two-dimensional projection of a three-dimensional structure. Indirect structural measurements such as x-ray diffraction can be used to infer crystal structure on the sample scale, however these techniques are not as effective with small nanoparticles due to short-range fluctuations in structure[39]. Direct imaging techniques such as electron tomography have been employed to reconstruct three-dimensional structures from a series of two-dimensional projections, including chiral nanoparticles[40] and even defects within nanoparticles[25]. When nanoparticles are of the order of just a few tens or hundreds of atoms they can be structurally unstable and interact with the electron beam[14] which limits the time and beam exposure of the experiment[41]. Electron tomography experiments can take hours to cover the range of angles required for successful reconstruction of a single nanoparticle and this limits the technique to study only small populations of a sample.

A common technique employed to identify cluster structures is to compare the images recorded in STEM with simulated images of clusters[36,37,42–44]. Clusters can adopt many configurations on surfaces and the same structure may look different during imaging due to its rotation with respect to the electron beam. An experimental STEM image can be compared to simulated images of different cluster structures in different arrangements to accurately identify its structure. Cluster modelling and simulations will be discussed further in section 3.

1.2.3 Nanostructured surfaces

Physical cluster synthesis is most commonly performed in the gas phase, and while there are techniques used to study unsupported clusters[45], it is often most useful to deposit these particles onto a support such that they can easily be transported to other systems for characterisation. The interaction between a cluster and surface at the time of deposition can be damaging to both parties involved depending on the energy scale of the interaction. These energy scales can be categorized into low- and high-energy processes, often referred to as 'soft-' and 'hard-' landing respectively. The deposition process is an important step towards creating nanostructured surfaces as the cluster-surface interaction can lead to different physical characteristics, despite being constituted from the same building blocks. Both deposition regimes can be well described by experiments performed with mass-selected clusters and graphite surfaces.

Bromann et al.[46] initially studied the controlled deposition of mass-selected silver clusters onto the platinum (111) surface under UHV conditions at low temperatures (80-90 K) with STM. They found that Ag_{19} clusters were initially located on the Pt(111) basal plane at 80 K, however the clusters became mobile and relocated to step-edge sites when the temperature was gradually increased to 300 K. This was a similar finding from the same group that saw thermally evaporated silver atoms form branched island structures at 80 K but were unstable at 300 K, again migrating to step-edge sites. Ag_7 clusters were then deposited with higher kinetic energies, 2.9 and 13.6 eV per atom, and clusters were found on the Pt(111) basal plane after annealing to 300 K, where the number density increased with deposition energy. The authors then posit that these hard-landing conditions create defect sites in the Pt(111) surface which then act as pinning centres, inhibiting cluster diffusion. In a final experiment the authors pre-adsorb 10 monolayers of argon onto the Pt(111) surface before depositing Ag_7 at 2.9 eV per atom. In contrast to the same experiment on the bare substrate, clusters were not observed on the Pt(111) basal plane after annealing to 300 K, showing that the buffer layer acts to reduce the impact energy and prevent cluster pinning.

Similar experiments were performed by Carroll et al.[47] and then Di Vece et al.[48] with mass-selected silver, gold, and nickel clusters onto graphite surfaces. The interaction between adsorbed molecules or clusters in this case and graphite surfaces are quite weak due owing to sp_z carbon bonds. The interaction of clusters with carbon is however of high interest in catalysis applications as carbon is commonly used as an electrode. In the study performed by Carroll at al. small silver clusters, between 50 and 200 atoms, were deposited onto graphite with a range of impact energies. By studying the fraction of clusters observed on the basal plane, the pinning threshold energy was determined to be 10.4 eV per atom. A similar study was performed by Di Vece at al. who found the pinning energy for gold and nickel clusters on graphite to be 15.6 and 5.7 eV per atom, respectively. In general, the pinning threshold energy is inversely proportional to the cluster mass.

The surface mobility of hard-landed clusters may be reduced by the creation of surface defects on impact which prevent diffusion and therefore sintering. However, high impact energies can lead to cluster restructuring on impact[46]. Soft-landed clusters are thought to mostly retain their gas phase structure on impact but are weakly bound to the surface and may diffuse to defect sites, such as step-edges, or collide with other clusters and sinter over time. A third deposition regime has been studied which involves soft-landing clusters on supports with prefabricated defects. Palmer et al.[49] and Claeyssense et al.[50] have studied the effect of soft-landing silver clusters on graphite surfaces which had previously been irradiated with 500 eV argon ions. The clusters studied retained a well-defined size distribution, due to soft-landing, and were pinned at the pre-fabricated defect sites; thus demonstrating a method to produce well-defined, well-ordered nanostructured surfaces.

1.3 Platinum

Platinum is one of the most important materials for catalysis to this day, and arguably the first catalyst material discovered. An experiment performed by Humphry Davy in 1817 discovered that oxygen and coal gas would combine at a reduced temperature over platinum and palladium wires, but not in the presence of other metals[51]. After the experiment the platinum wires remained chemically unchanged, simultaneously demonstrating the reusability and performance benefit of heterogeneous catalysis. Today platinum is commonly used as an electrocatalyst for reduction[52], oxidation[53], hydrogenation[54], in the petroleum industry[55], and beyond.

Platinum clusters as small as a four atoms have been shown to have three dimensional geometries[56], and more specifically tetrahedral structures, which represent a bulk growth mode as bulk platinum is FCC. Baletto et al.[57] studied the lowest energy structures small platinum clusters. The authors found that platinum clusters transition from icosahedral to FCC motifs at a size less than 100 atoms. Blackmore[58] studied the structure of platinum clusters up to 600 atoms in size. The clusters were soft landed onto amorphous carbon supports and imaged with aberration-corrected scanning transmission electron microscopy. The images were compared to a series of simulated atlases for platinum in octahedral, decahedral, and icosahedral motifs. The results of this study are shown in Figure 1.3.1. The study showed a clear trend towards octahedral structures as the cluster size increased. As octahedral structures can be cut from an FCC lattice[13] this finding shows that platinum prefers bulk structures from as few as a few hundred atoms. Throughout the size range studied a small fraction of decahedral structures were found, however no icosahedral structures were identified. By comparison Foster et al.[14,42] studied the structures of small gold clusters and identified a large proportion of decahedral structures, which differs from its bulk FCC structure.

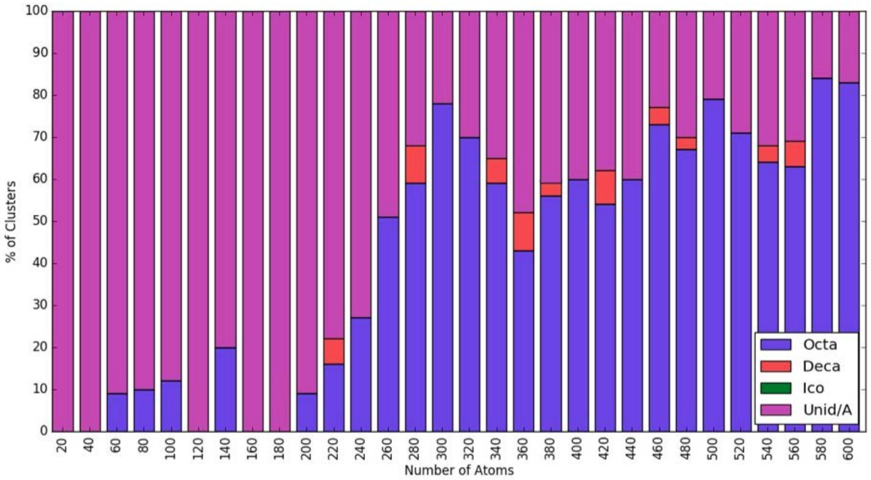

Figure 1.3.1: Structure of mass-selected platinum clusters up to 600 atoms in size. Figure taken from reference 58.

1.4 Electrochemistry

Electrochemistry is the study of the relationship between electricity and chemical changes. In many electrochemical studies an applied potential is used to drive chemical change, and this is useful in catalysis. Platinum is a commonly studied electrocatalyst for hydrogen[59] and oxygen[60] evolution, and methane[61] and carbon[62] oxidation due to its performance. Research efforts are being made to reduce platinum usage[16,63–65] due to its high cost inhibiting its use at scale. At the same time, fundamental studies on pure platinum[53,59,66,67] are able to shed light on the design of future catalysts. The following introduction to electrochemistry is based on the book Electrode Dynamics by Fisher[68].

1.4.1 Electrode-electrolyte interaction

The electrode-electrolyte interface represents a discontinuity within the electrolyte that leads to different behaviour at the interface than in the bulk solution. A voltage is typically applied to the electrode during experimentation which leads to accumulation of charge at the electrode surface which attracts oppositely charged ions within the electrolyte. In the Helmholtz model the electrode charge is completely neutralised by a layer of solvated ions, see Figure 1.4.1, termed the electrical double-layer. The plane through the center line of the solvated ions is called the Outer Helmholtz Plane (OHP) and it represents the distance from the electrode where the potential ϕ is dropped to that of the bulk solution ϕ_s. In this model the electrode-electrolyte interaction is effectively represented by a capacitor where the potential drop across OHP is linear.

Gouy and Chapman found that the electrode potential is not fully dropped across OHP due to Brownian motion of the ionic species which tends to scatter the excess ions at the electrode surface. In their model ionic species are represented as a charge density and the potential is dropped across a single 'diffuse layer'. The potential drop in this model is concentrated at the electrode surface however some excess charge is found at a distance further than OHP from the electrode surface.

Stern suggested that the ions have a minimum displacement from the electrode surface and that a diffuse layer exists further from the electrode surface, see Figure 1.4.2. The Stern model effectively combines both the Helmholtz and Guoy-Chapman models. Grahame later suggested that some neutral, or even charged, species may adsorb to the electrode surface depending on the specific electrode-ion interaction. These ions were termed to be 'specifically adsorbed'.

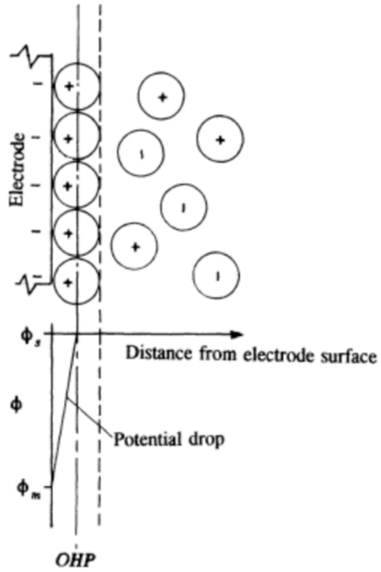

Figure 1.4.1: Helmholtz model for the interaction between the electrode and electrolyte termed the electrical double layer. (a) a layer of electrolyte ions neutralises the charge accumulated at the electrode surface. (b) the potential drops to the solution potential ϕ_s within the Outer Helmholtz Plane (OHP). Figure reproduced from reference 68.

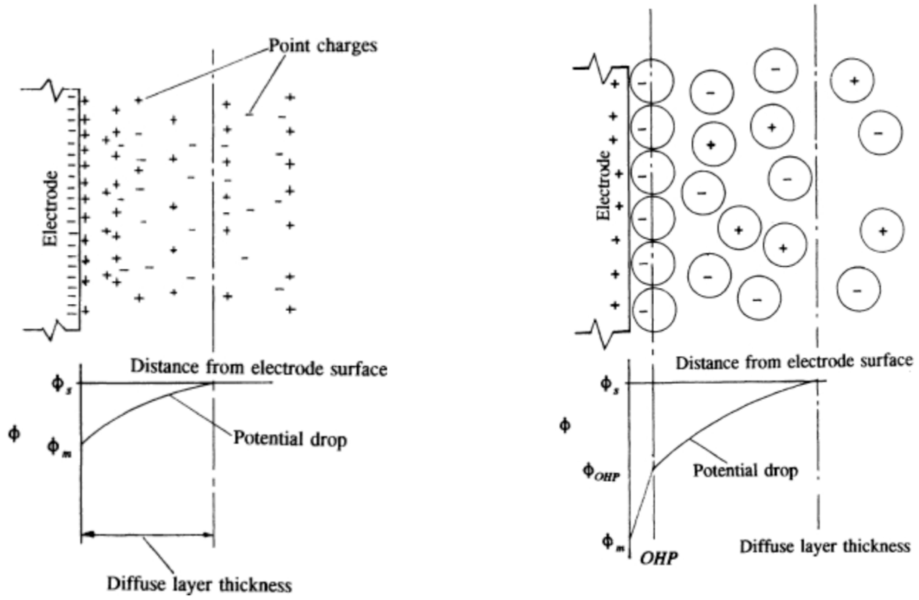

Figure 1.4.2: (left) Guoy-Chapman and (right) Stern models of the electrical double layer. Figure reproduced from reference 68.

An ion in solution may exchange an electron with an electrode, if the ion accepts an electron it is reduced:

$$Fe_{aq}^{3+} + e \rightarrow \; Fe_{aq}^{2+} \qquad 1.4.1$$

or oxidised if the ion donates an electron:

$$Fe_{aq}^{2+} \rightarrow Fe_{aq}^{3+} + e. \qquad 1.4.2$$

In an electrochemical cell both reduction and oxidation processes happen simultaneously. The current borne from the movement of charge in a redox process is given by:

$$i = nAFj, \qquad 1.4.3$$

where i is the current, n is the number of electrons involved in the reaction (assumed to be one herein), A is the electrode area, and j is the ionic flux at the electrode surface. The ionic flux can be written as $j = k_0[Fe^{3+}]$ for the reaction shown in equation 1.4.1 where k_o is the reaction specific rate constant for heterogeneous electron transfer and the last term denotes the concentration of Fe^{3+} ions at the electrode surface.

Focussing on the reduction reaction above, after the reaction has occurred the concentration of Fe^{3+} at the electrode surface has been reduced and the local concentration of Fe^{2+} has increased. For further reduction reactions to take place more Fe^{3+} ions must make their way to the electrode surface. Depending on the relative rates at which the reactant is replenished at the electrode surface and the rate constant of the reaction, the current may be said to be mass-transport limited or rate-limited. The reaction is mass-transport limited when the reaction proceeds faster than new reactants can get to the electrode surface or rate-limited when sluggish reaction kinetics determine the overall current.

Electrode kinetics are in many ways analogous to chemical kinetics and the rate constants are modelled by an Arrhenius type equation in transition state theory:

$$k_{red} = Z \cdot \exp\left(\frac{-\Delta G^{\ddagger}_{red}}{RT}\right). \tag{1.4.4}$$

In the above equation the exponential prefactor Z represents the attempt frequency for the reaction, $\Delta G^{\ddagger}_{red}$ is the Gibbs energy of activation, ie. the energy barrier for the reaction as shown in Figure 1.4.3, R is the universal gas constant, and T is temperature.

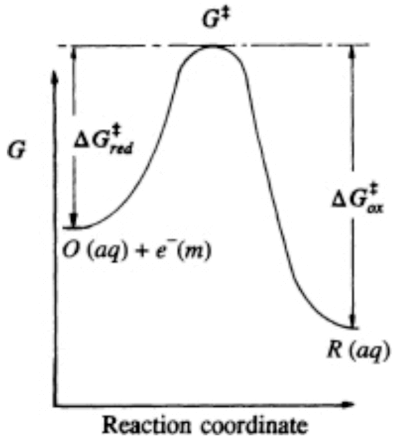

Figure 1.4.3: Gibbs energy plot for the reduction reaction of an oxidised species O. $G^{\ddagger}$ is the Gibbs energy of the intermediate transition state. Figure reproduced from reference 68.

The Gibbs energy of the reactants (Fe^{3+} and one electron) is:

$$G_{Fe^{3+}} = c + 3F\phi_s - F\phi_m = c + 2F\phi_s - F(\phi_m - \phi_s), \tag{1.4.5}$$

and the product Fe^{2+}:

$$G_{Fe^{2+}} = c' + 2F\phi_s, \tag{1.4.6}$$

where c is a constant and ϕ_s and ϕ_m are the potentials of the solution and metal electrode, respectively. The Gibbs energy of the transition state is assumed to take an intermediate value such that:

$$G^{\ddagger} = c'' + 2F\phi_s - (1-\alpha)F(\phi_m - \phi_s), \tag{1.4.7}$$

where α is the transfer coefficient which takes a value between 0 and 1. The value of the transfer coefficient provides information about the sensitivity of the reaction to the potential drop between the electrode and the solution. For example, if $\alpha \sim 1$ then the potential dependence of the transition state more closely resembles the products. Typically, $\alpha \sim 1/2$ which suggests that the transition state has an intermediate dependence on potential.

The Butler-Volmer equation defines the current flowing through the cell to be the sum of the reductive and oxidative currents such that:

$$i = i_0 \left(\exp \frac{(1-\alpha)F\eta}{RT} - \exp \frac{-\alpha F\eta}{RT} \right) \tag{1.4.8}$$

where i_0 is the exchange current for the reaction and η is the difference between the applied potential and the cell's equilibrium potential and is more commonly known as the overpotential.

When the exchange current is large both anodic and cathodic currents are driven from small overpotentials, this is referred to as a reversible reaction. However, when the exchange current is small large overpotentials are required to drive currents, this is known as an irreversible reaction. These behaviours are shown in Figure 1.4.4. In the case where the overpotential is large and positive the anodic process is driven and cathodic currents will be small, the Butler-Volmer equation then simplifies to:

$$\ln i = \ln i_0 + \frac{(1-\alpha)F\eta}{RT}, \tag{1.4.9}$$

and in the case where the overpotential is large and negative such that the cathodic process is driven:

$$\ln -i = \ln i_0 - \frac{\alpha F\eta}{RT}. \tag{1.4.10}$$

By plotting the logarithm of the measured current against overpotential the exchange current and transfer coefficient can be determined by the axis intercept and gradients, respectively. This is known as Tafel analysis and is demonstrated in Figure 1.4.4. The value of the Tafel slope provides information about the rate determining step of the reaction. For the case of hydrogen evolution in acidic media, which will be discussed in more detail in the next section, each possible reaction step possesses different kinetics. A Tafel slope value of ~120 mV/dec indicates that hydrogen adsorption (Volmer reaction) is the rate limiting step, whereas values of ~30 mV/dec and ~40 mV/dec indicate the Tafel and Heyrovsky reactions, respectively[69].

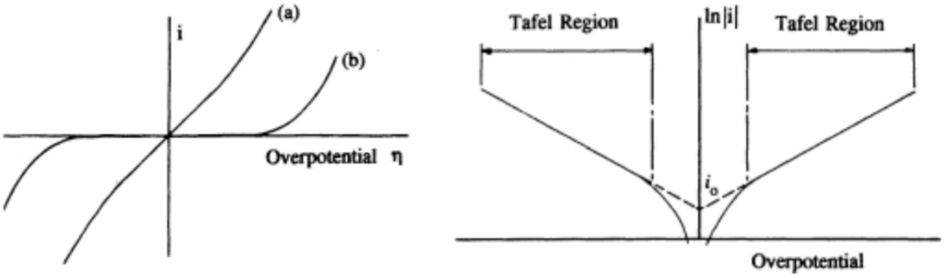

Figure 1.4.4: (left) the effect of overpotential on net current from a (a) reversible and (b) irreversible reaction. (right) Tafel analysis. Figure reproduced from reference 68.

1.4.2 The Hydrogen Evolution Reaction

Hydrogen must be produced efficiently at scale in order to drive the hydrogen economy[30]. Molecular hydrogen, however, is not readily available and hydrogen is often found bonded to other elements, most commonly in the form of hydrocarbons or water. Hydrogen must be refined into molecular form for use as a fuel. This process occurs industrially via steam reforming, which simultaneously produces greenhouse gases and is energy intensive[70,71]. Alternative techniques exist which include the electrocatalytic splitting of water which has the overall reaction:

$$2H_2O \rightarrow 2H_2 + O_2, \qquad 1.4.11$$

where the half reaction:

$$4H^+ + 4e^- \rightarrow 2H_2 \qquad 1.4.12$$

is known as the hydrogen evolution reaction (HER). HER in acidic media starts with the adsorption of a hydrogen ion onto a catalyst surface which involves the exchange of an electron:

$$H_{aq}^+ + e^- \rightarrow H_{ads}, \qquad 1.4.13$$

and is known as the Volmer reaction. The adsorbed hydrogen then reacts through one of two mechanisms to form molecular hydrogen. In the first case the adsorbed hydrogen reacts with another hydrogen ion from the electrolyte:

$$H_{ads} + H_{aq}^+ + e^- \rightarrow H_{2(g)}, \qquad 1.4.14$$

which is known as the Heyrovsky reaction. Alternatively, the adsorbed hydrogen reacts on the surface with another adsorbed hydrogen:

$$H_{ads} + H_{ads} \rightarrow H_{2(g)}, \qquad 1.4.15$$

and this is known as the Tafel reaction. For platinum in acidic media it has been shown that recombination is the rate limiting step at low overpotentials[70]. As the overpotential is increased hydrogen coverage on platinum approaches saturation, and at this point hydrogen adsorption becomes the rate limiting step. In all cases the reaction initially proceeds by hydrogen adsorption onto a surface and so the surface-hydrogen interaction is of fundamental importance. If this interaction is too weak then hydrogen may desorb from the surface before forming molecular hydrogen. At the same time, it follows that if the interaction is too strong the adsorbed hydrogen may react to form molecular hydrogen, but the product may not be released from the surface. In both of these cases the surface interaction is antagonistic to HER.

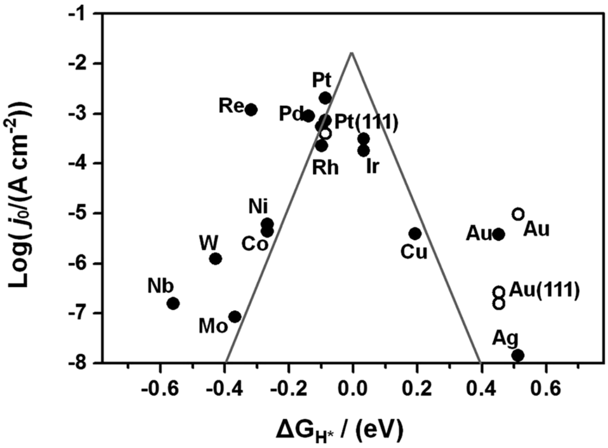

Figure 1.4.5: Volcano plot of exchange current density versus the theoretical Gibbs energy (ΔG_H) of adsorbed atomic hydrogen on metal surfaces. Figure reproduced from reference 70.

The Gibbs energy of the interaction between atomic hydrogen and many different surfaces is shown in Figure 1.4.5. When plotted against the exchange current density the graph forms an inverted 'V' shape which explains why these types of plots are commonly called volcano plots. The maximum exchange current is centered around a Gibbs energy of ~0 eV. Materials with a negative Gibbs energy adsorb hydrogen more strongly. Platinum lies around the apex of the volcano plot, as the energy of adsorption of hydrogen onto platinum surfaces is approximately thermodynamic equilibrium and as a result it is one of the most active HER electrocatalysts. HER performance may also be improved by alloying platinum with other materials, such as titanium[16] and cobalt[72].

1.4.3 Degradation

The goal of the use of catalysts is improved performance, which is more yield (product) for less input (energy). Arguably just as important as performance is durability. IUPAC describes that a catalyst is not consumed by a reaction[73], such that a catalyst is able to be repeatedly reused. Catalyst durability is arguably most important in real-world use cases. The US Department of Energy has set fuel cell durability targets in their 2016 report[74]. In the drive for alternative energies it is important that fuel cells or batteries are able to perform as well as their internal combustion engine counterparts, along with reliability and convenience in equality.

As prepared nanoparticle catalysts may change under many different conditions such as when they are subjected to elevated temperatures[75], electrochemical cycling[75], or, in some cases, exposure to atmosphere[42]. One of the most common aging routes is nanoparticle growth, which is driven by an overall reduction in surface energy. The chemical potential of a nanoparticle μ is related to its curvature through its radius r according to the Gibbs-Thomson relation[76]:

$$\mu = \mu_0 + 2\gamma\Omega/r, \qquad 1.4.16$$

where μ_O is the chemical potential of an infinitely sized particle, γ is the surface energy of the nanoparticle, and Ω is the atomic volume. The system may do work to minimise its Gibbs energy[77] $G = \sum_i \mu_i N_i$ which results in the growth of larger particles with smaller chemical potential at the expense of smaller particles. This process may occur through different routes[78] such as nanoparticle migration and coalescence, known as Smoluchowski ripening[37,79], or atomic processes such as Ostwald ripening[37,80].

In the case of Smoluchowski ripening supported nanoparticles have enough energy to undergo diffusion on the surface, which may be mediated by self-diffusion[79] due to Brownian motion of the adatoms, leading to collision with another nanoparticle and subsequent coalescence. Coalescence is normally preceded by neck growth between neighbouring nanoparticles and subsequent neck elimination[79,81]. In the case of Ostwald ripening, atomic species migrate by surface diffusion or through an external medium resulting in nanoparticle growth[37,80]; this may proceed by the formation of volatile species in the vapour phase[79] or ionic species in electrolyte[75]. The factors determining whether Smoluchowski or Ostwald ripening are dominant include nanoparticle size[37], ease of adatom detachment[80], and the interaction between the nanoparticle and support[82].

Diffusion-limited aggregation (DLA)[83,84] is a model that describes nanoparticle aggregation and growth under the assumption that growth is limited by mass transport. The resulting aggregates tend to form fractal branched geometries, which have been observed for colloidal systems[83] and also nanoparticle aggregation[85]. Celardo et al.[85] studied the aggregation of titania nanoparticles produced by pulsed laser deposition onto different surfaces. On a graphite surface the nanoparticles remained isolated and spherical, whereas on silicon and quartz surfaces the nanoparticles formed both branched, or dendritic, and chain-like structures indicative of DLA on the surface after deposition. The authors modelled DLA using a Monte Carlo method with good reproducibility of the observed structures.

In the field of PEMFC there have been many studies into the stability of carbon-supported platinum catalysts. Maillard et al.[86] have laid out the various known platinum degradation mechanisms, which include nanoparticle migration and coalescence on the substrate, substrate corrosion, and dissolution-redeposition or 3D Ostwald ripening, as outlined in Figure 1.4.6.

In their study, carbon-supported platinum was subjected to accelerated stress testing (AST), common in the field of fuel cell research, in electrolytes purged with three different atmospheres: Ar, CO, and O_2. They found that the catalyst degraded even with the modest potentials, 0 to 0.50 V vs RHE, applied during the AST. Nanoparticle migration and subsequent coalescence were common in all atmospheres, as was nanoparticle detachment. Only in the oxygen atmosphere was carbon corrosion clearly observed. The authors of this study also found an increase in 3D Ostwald ripening as the anodic potential limit was increased to 1.23 V vs RHE.

Whilst ex-situ imaging provides an overview, in-situ measurements are able to provide more granular insights into surface processes. Wantanabe et al.[87] investigated the Pt(111) surface during potential cycling with in-situ STM. The adsorption of oxygen species was observed at potentials above 0.90 V vs RHE, with the Pt(111) surface becoming increasingly rough as the potential was increased to 1.30 V vs RHE. This was put down to platinum place-exchange during oxidation. The most significant surface morphology change, however, was observed in the cathodic sweep. After full platinum reduction, platinum islands and pits had formed on the (111) terraces, and this was coupled with an increase in step-site defects.

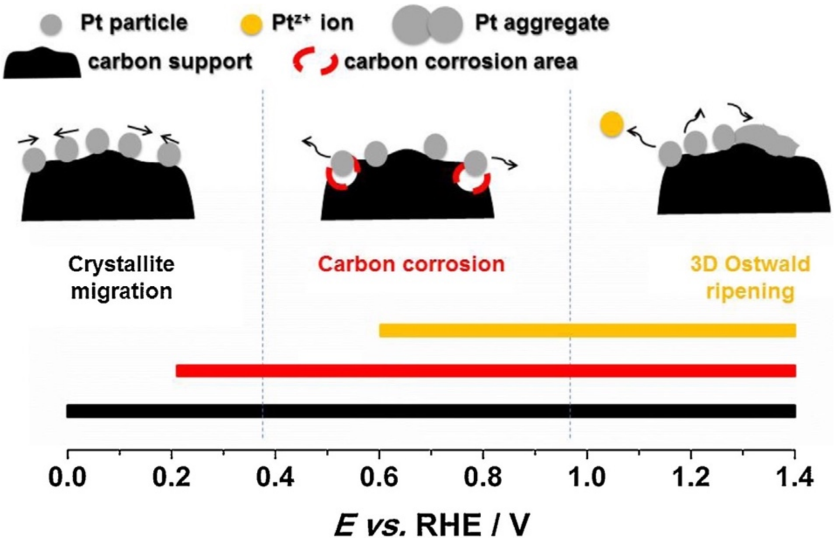

Figure 1.4.6: Schematic showing how the applied electrochemical potential affects various carbon-supported platinum degradation mechanisms. Figure reproduced from reference 86.

Imai et al.[88] performed a real-time study into the electrochemical oxidation of platinum in acidic media. They found that the surface of 2 nm platinum nanoparticles was covered with hydroxyl species at 1.08 V vs RHE, which was oxidised to Pt-O_{ads} as the potential was increased to 1.35 V vs RHE. In potential step experiments at 1.40 V vs RHE they showed that the platinum surfaces were covered with hydroxyl species within 10 seconds, and these were further oxidised into adsorbed oxide species within 20 s. At times longer than 30 s up to two minutes platinum oxide species were formed within the first two platinum surface layers, and the oxide penetration depth increased with time.

Platinum is also a known carbon oxidation catalyst. Studies have shown that adding platinum to a particulate filter for diesel motors aids the production of CO and CO_2 from carbon particulates[89]. More recently it has been shown that the electrocatalytic production of carbonate species by platinum nanoparticles promotes nanoparticle detachment and therefore catalyst degradation[90]. The authors of this study showed that the better carbon oxidation catalysts produced more carbonate species, destabilising the nanoparticle catalysts, thus leading to increased rates of detachment in what can be thought of as a negative feedback loop[90].

Alloyed materials may have different modes of degradation. The effect of anodic potentials on PtZn binary clusters in acidic conditions was explored by Bizzotto et al.[91]. PtZn nanoparticles were synthesised with a Zn-rich core, however after polarization at potentials larger than 1.0 V vs RHE the Zn surface atom fraction increased by a factor of 4. This surface segregation effect was not observed at smaller applied potentials, and at potentials larger than 1.25 V vs RHE the Zn surface atom fraction was severely reduced due to leaching.

1.4.4 Electrochemical methods

Commonly, electrochemical experiments utilise a three-electrode electrochemical cell, as depicted in Figure 1.4.7, and a potentiostat. As the name suggests, in a three-electrode cell there are three electrodes: the working electrode (WE), counter electrode (CE), and reference electrode (RE). The electrochemical processes on the WE will be studied and as such it contains the materials of interest in the experiment. The RE is used to provide a stable potential reference for WE and the CE provides the current to complete the circuit. All three electrodes are connected to a potentiostat which controls the applied potentials and records the current generated.

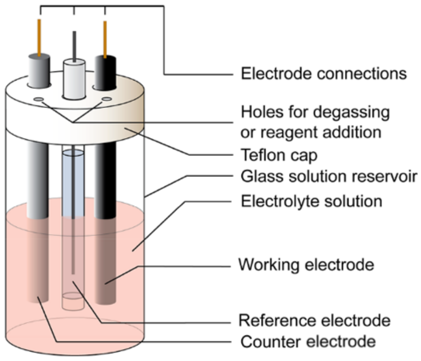

Figure 1.4.7: A three-electrode electrochemical cell. Figure reproduced from reference 92.

Common electrochemical techniques include Linear Sweep Voltammetry (LSV) and Cyclic Voltammetry (CV). In an LSV experiment the potential E applied to the WE is changed between an initial E_1 and final E_2 value at a constant rate, as shown in Figure 1.4.8. The potentiostat records the generated current i and the data is typically plotted as i-E.

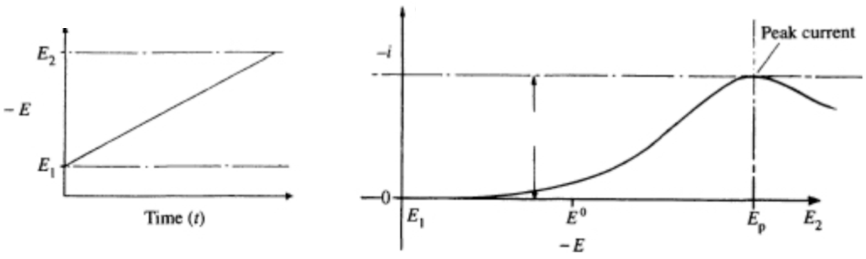

Figure 1.4.8: Signals in an LSV experiment. (left) E-t graph showing how the potential applied to the WE is changed from E1 to E2 at a constant rate. (right) currents recorded during the potential sweep are commonly plotted against the applied potential in an i-E graph. Figure reproduced from reference 68.

CV is an extension of LSV. In CV the potential is repeatedly swept between E_1 and E_2 at a constant rate, the resulting E-t graph resembles a sawtooth wave as shown in Figure 1.4.9. CV drives both oxidative processes in the anodic sweep and reductive processes in the cathodic sweep. The number of cycles performed is dependent on the information required from the experiment and can range from one to tens in the case of potential conditioning[93] up to thousands in the case of stress testing[94]. LSV and CV in many ways represent a kind of spectroscopic analysis of electrochemical processes occurring at the WE. An example of this is the electrochemical response of different single-crystal platinum surfaces in sulphuric acid solution[95], as shown in Figure 1.4.10. The data shown in this figure was recorded using CV, however only currents from the anodic sweep are shown for clarity. The large peak around 0.1 V vs RHE is due to hydrogen desorption on Pt(110) facets and as such the peak intensity is reduced as the (110) step density decreases. The peak around 0.27 V vs RHE in the Pt(111) CV is due to hydrogen desorption from a small amount of Pt(100) sites, whereas the sharp peak around 0.45 V vs RHE can be attributed to the order-disorder transition of adsorbed bisulphate ions on (111) terraces. The data shown in this figure demonstrates the use of CV as a spectroscopic tool that can provide information about both electrochemical processes and the structure of the working electrode at the atomic level.

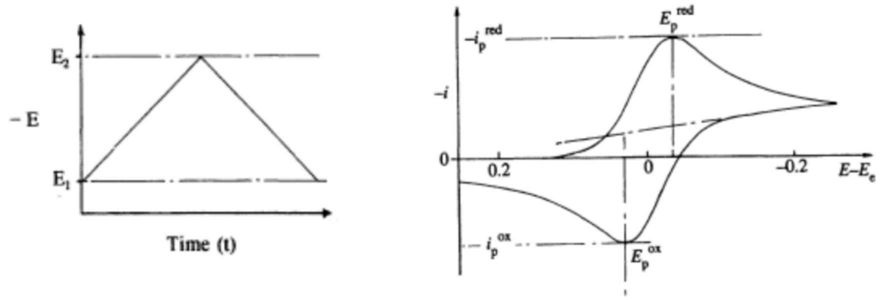

Figure 1.4.9: Signals in a CV experiment. (left) E-t graph showing how the potential is changed during one cycle. (right) i-E graph shows both oxidative and reductive currents depending on the sweep direction for a reversible reaction. Figure reproduced from reference 68.

The Butler-Volmer equation predicts that current should increase with overpotential, however in both of the examples provided in Figure 1.4.8 Figure 1.4.9 the current peaks at a value denoted i_p. As described earlier, this is due to depletion of reactants at the electrode and the peak current therefore reflects the balance between reaction kinetics and mass-transport. Reactants may be replenished at the electrode surface through diffusion as described by Fick’s law. The reaction at the electrode may also produce small amounts of heat or products with different densities, this leads to natural convection through thermal and density gradients in the electrolyte.

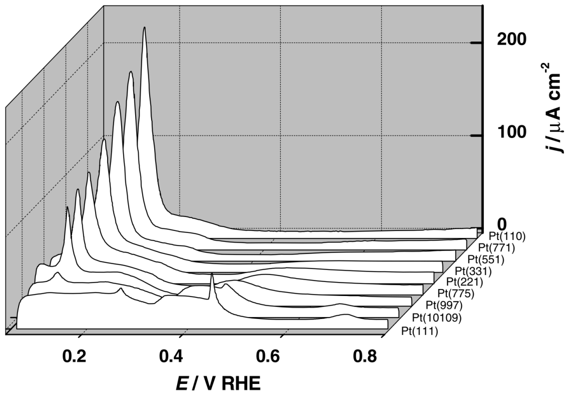

Figure 1.4.10: Voltammetric profiles of single crystal Pt(hkl) surfaces in 0.5 M H_2SO_4. Figure reproduced from reference 95.

One may introduce forced convection into the electrolyte to provide more consistent mass-transport to the electrode. This is commonly acheieved by rotating the working electrode at a fixed speed as shown in Figure 1.4.11. The rotation speed should be chosen to provide stable laminar flow of the electrolyte to the electrode. In contrast is the rotation speed is too high the fluid flow becomes turbulent which is chaotic and inconsistent. The Reynolds number for a cylindrical system is given by $\mathrm{Re} = \omega r^2/v$, where ω is the rotation frequency, r is the radius of the electrode setup, and v is the viscosity of the electrolyte. The magnitude of Re should be kept below ~10^5 to create laminar flow.

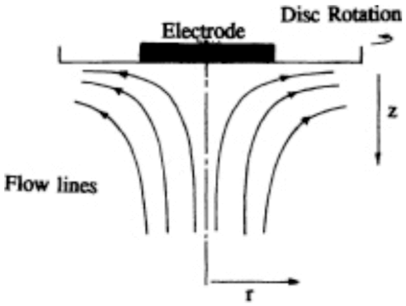

Figure 1.4.11: A rotating working electrode setup is used to provide forced convection and stable mass-transport. Figure reproduced from reference 68.

1.5 Nanoparticle growth

In many degradation mechanisms the movement of material can lead to nanoparticle growth. Granqvist and Buhrman[96] discussed the relationship between the growth mechanism and size distribution of nanoparticles. In the case of growth driven by coalescence the size distribution is expected follow a log-normal distribution with a tail towards larger particle sizes. In contrast, for growth driven by Ostwald ripening, the size distribution is expected to exhibit a tail towards smaller particle sizes and so the two growth mechanisms are qualitatively different.

Yu et al.[75] studied the effect of electrochemical conditioning on different sizes of platinum nanoparticles in-situ using small angle X-ray scattering. They found that platinum nanoparticles larger than 3-5 nm had improved stability and that the growth mechanism was driven by dissolution-redeposition. In this study the nanoparticles grew progressively when subjected to potential cycling between 0.56 and 1.16 V vs RHE. However, growth was not observed when the anodic potential limit was reduced to 0.96 V vs RHE indicating that dissolved ionic platinum species are involved in the growth mechanism.

Virkar and Zhou[97] studied the effect of platinum nanoparticle growth in the presence of dissolved platinum ions at elevated temperatures. Significant particle growth occurs over the period of hours to weeks when particles are supported on a conductive carbon substrate. The same system exhibits no growth when the particles are supported on an insulting alumina substrate, despite the presence of platinum ions in the solution. The implication from these experiments is that Ostwald ripening in ionic media occurs through the coupled transport of dissolved ions in solution and electrons through the substrate.

1.6 Electron Microscopy

The advent of scanning probe microscopy (SPM), more specifically scanning tunnelling microscopy (STM), is often credited as the birth of nanotechnology[98]. In all forms of SPM, a probe is scanned or rastered across a specimen and the data acquired is used to create a map. In the case of STM a bias is applied between a conductive, atomically sharp tip and a surface and the gap between them is reduced until a tunnelling current is recorded. The tip is then rastered across the surface and variations in either the current or z-position of the tip are recorded and mapped to create an electro-topographical image.

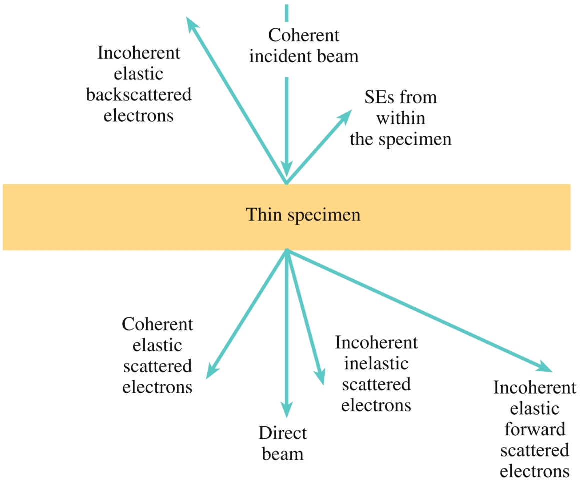

Figure 1.6.1: The different types of interaction between electrons and matter. Figure reproduced from reference 99.

In the case of electron microscopy, a beam of high energy electrons can be used as a probe. The electrons interact with the specimen and can be collected by a detector to form an image. There are many different types of electron microscopy, but this thesis will focus on transmission electron microscopy (TEM) and more specifically scanning transmission electron microscopy (STEM).

The electron beam originates from an electron source, also known as an electron ‘gun’. Common electron sources used in electron microscopes are thermionic source, field emission guns (FEG), and Schottky sources. Thermionic sources operate on the principle of thermionic emission where a material is heated to a temperature high enough such that the energy of the electrons within the material is great enough to overcome the materials work function and are subsequently emitted. Originally, thermionic sources used tungsten filaments as tungsten has a high melting temperature. More recently thermionic guns use a LaB_6 crystal as the gun due to the low work function of the material. FEGs consist of a high voltage applied to a sharp tungsten tip. At the tip apex the electric field density is high enough to lower the material work function potential barrier for electron emission. The electron gun used in the JEOL 2100F TEM used in this thesis is a Schottky-type source. In a Schottky source a tungsten filament is coated with a thin layer of ZrO which acts to reduce the work function of the tip. To aid electron emission the tip is heated, albeit to a lower temperature than used for thermionic emission, and a large electric field is applied to the tip. Schottky sources have the advantage of producing stable emission currents.

Emitted electrons are accelerated to operating voltage which may be between 80 kV and 1 MV depending on the microscope. Magnetic lenses are used in TEM to focus and form the electron beam. They consist of current-carrying copper coils surrounding a magnetically soft pole piece, typically made of iron, see Figure 1.6.2. The current in the surrounding coil induces a magnetic field in the pole piece which is used to focus the electrons passing through the bore. The focussing ability of magnetic lenses is not perfect, however. The electrons passing through a lens further from its optical axis are deflected more than those at the center with the result that not all electron paths are focussed in the same plane, see Figure 1.6.2, and this effect is known as spherical aberration, denoted C_S. The result of these aberrations is that a point object will be imaged as a disk due to the finite width of the probe, and this reduces the effective resolution of the microscope. The JEOL 2100F used in this thesis is equipped with a spherical aberration correction system (CEOS, GmbH) which utilises hexapole lenses to create an effective negative C_S value to compensate for the spherical aberrations induced by previous lenses in the illumination system. The result of this correction is that microscope resolution is increased to the angstrom level such that atomic resolution can by readily achieved.

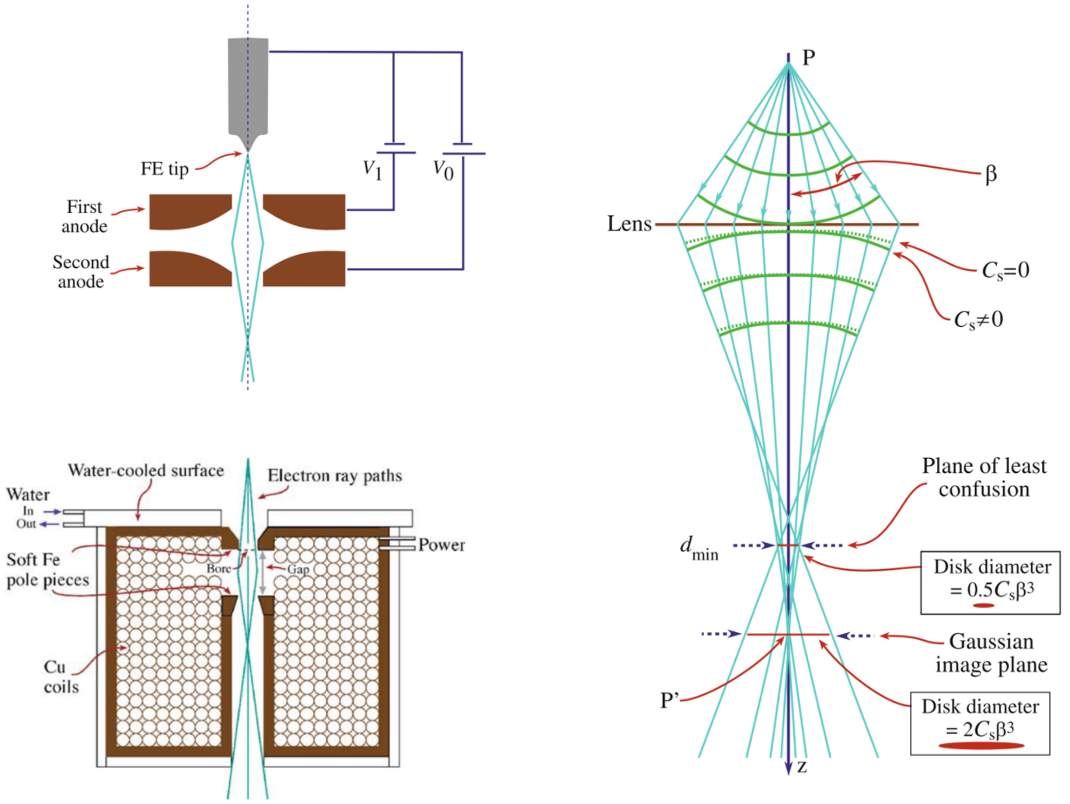

Figure 1.6.2: Parts of a typical TEM. (upper left) arrangement of an FEG for electron extraction (V_1) and acceleration (V_0). (lower left) cross section of a magnetic lens. (right) ray diagram showing spherical aberrations created by a magnetic lens. Figures reproduced from reference 99.

Electrons interact with matter in many different ways, a schematic outlining different types of interaction is shown in Figure 1.6.1. The electrons which are forward scattered or transmitted, shown below the specimen in the figure, are used as signals in TEM. The specimen must be thin enough such that it is mostly transparent to electrons to be suitable for use in transmission mode, this depends on the mean free path of the electrons in the material. As an example, at electron energies greater than 100 keV the mean free path of electrons through carbon is a few hundred nanometers, this compares with just tens of nanometers for metals such as gold and copper and defines an upper limit to specimen thickness. Electron microscopes are operated under high vacuum to minimize scattering of the electron beam by gaseous species. The vacuum is maintained by an array of pumps and cold traps and common operating pressure are on the order of 10^{-7} mbar which is classified as high vacuum.

Transmitted electrons either remain on their original path, known as the 'direct beam', or they are scattered through an angle. Electron scattering from the specimen's electron cloud results in small scattering angles, whereas larger scattering angles are observed by scattering from the nuclear potential, such as in Rutherford scattering.

Rutherford scattering represents a type of incoherent elastic scattering. The Rutherford scattering cross section σ_R is defined as[99]*:*

$$\sigma_R(\theta) = \frac{e^4 Z^2}{16(4\pi\varepsilon_0 E_0)^2} \cdot \frac{d\Omega}{sin^4 \frac{\theta}{2}}, \qquad 1.6.1$$

where e is the elementary charge, Z is the atomic number, ε_o is the permittivity of free space, E_o is the energy of the electrons, θ is the scattering angle, and Ω is the solid angle of collection. It is clear to see that the scattering cross section, and therefore the scattering probability, is inversely proportional to the fourth power of the scattering angle for small angles. The scattering cross section can decrease by orders of magnitude as the scattering angle is increased from 0 to 180 degrees, which means that electrons are predominantly scattered at lower angles. Each scattering event can be considered as a single interaction so there is no phase relationship between the scattered electrons and the incident electron beam, thus Rutherford scattering is considered incoherent.

From equation 1.6.1 it is clear that the scattering cross section has a squared dependence on the atomic number, such that heavy elements like gold or platinum scatter more than lighter elements such as carbon or oxygen. While it is the case that heavier elements scatter more than lighter elements, the dependence on Z is reduced due to electronic screening around the nucleus. Similar results have been found in practice and an imaging technique known as Z contrast imaging[100] can be used to exploit the strong Z dependence of scattered electrons. Here the signal from high angle (greater than ~5 degrees) scattered electrons is collected on an annular detector and used to form an image; this technique is often called high angle annular dark field (HAADF)-STEM.

There have been many studies to verify the screening effect of the electron cloud. In a study by Palmer et al.[101] HAADF-STEM was used to image mass selected gold and palladium clusters. They found that the HAADF intensity, which is proportional to the number of electron collection events by the detector, was larger for gold clusters (Z = 79) than for the same size of palladium clusters (Z =

47). In the same experiment they found that the dependence Z^{α} increased from $\alpha = 1.2$ at low collection angles (14 mrad) to 1.8 at larger collection angles (70 mrad), consistent with reduced electronic screening.

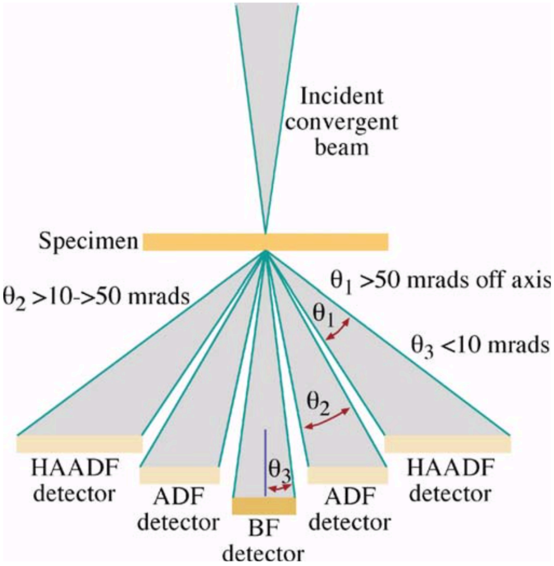

Figure 1.6.3: Detector layout for Z-contrast imaging in STEM. Figure reproduced from reference 99.

There are different STEM modes that collect electrons which have interacted differently with the specimen. Three different collection modes are highlighted in Figure 1.6.3. As mentioned above HAADF-STEM collects electrons scattered at high angles and leads to *Z* contrast. ADF-STEM has a smaller collection angle and is therefore less sensitive to atomic number than HAADF whilst producing more strain contrast[102]. Bright field (BF) collects the electrons in the direct beam and at very low scattering angles and is most similar to TEM. The inner collection angle of the ADF detector can be set by changing the camera length of the microscope.

Example STEM images of platinum nanoparticles on an amorphous carbon support acquired with different signals are shown in Figure 1.6.4. The ADF- and HAADF-STEM images were acquired using a camera length of 200 and 100 mm, respectively. The intensity histograms show that the signal due to platinum is more intense in the ADF image than the HAADF image due to increased scattering cross section at lower collection angles. Apart from the clear contrast inversion between BF and ADF imaging, atomic imaging is clearer in the ADF signals whilst BF shows increased phase contrast in the carbon support.

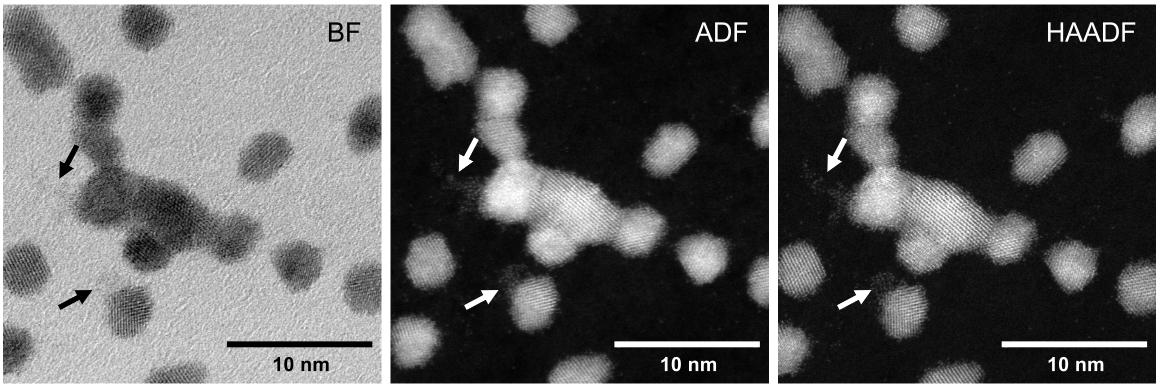

Figure 1.6.4: Comparison of different signals in STEM. The same area of a platinum nanoparticle sample is imaged in all cases. (left) bright field image acquired with maximum collection angle of 10 mrad, (center and right) dark field images acquired with an annular detector with an inner collection radius of 31 and 62 mrad, respectively. Arrows indicate individual platinum atoms.

Electron microscopy has been employed to image many different materials, including clusters[14] and nanoparticles[103], surfaces[104], and biological samples[105]. More recently a technique called identical location (IL) TEM has been employed to study catalyst degradation[31,86,94,106]. IL-TEM involves reimaging the exact location after some process to observe any changes, in the case of platinum nanoparticles this may be electrochemical potential cycling[86]. This technique has many benefits which includes studying particle migration or structural changes, and it does not have to be governed by statistical differences. Improving on IL-TEM are in-situ techniques, where the same processes occur in real-time during imaging. Whilst IL-TEM can be compared to before and after photography, in-situ electron microscopy is the video camera. In-situ microscopy has been used to study particle growth[107], degradation[108], and coalescence[109]. The field of in-situ liquid or electrochemical TEM still has its problems however, the electron beam is known to induce gas formation within the liquid or change the local chemistry of the electrolyte[110].

This thesis focuses on the production, characterisation, and electrochemical processing of well-defined mass-selected platinum clusters. Clusters were produced by physical methods, without the use of ligands, and characterised by both electrochemical techniques and STEM. In the first experimental chapter the structures of platinum clusters are characterised with STEM and examples of the invasive effect of the electron beam are presented. In the second experimental chapter the same platinum clusters are characterised through electrochemical potential cycling in acidic media and from the data it becomes clear that electrochemical conditioning changes the overall sample morphology. In the third experimental chapter an in-depth study into the effect of electrochemical potential conditioning is presented. And in the final chapter the effect of plasma treatment on well-defined clusters is presented. The effect of plasma treatment on the cluster samples bears resemblance in some cases to the electrochemical processing and comparisons between the two are drawn.

2 Experimental and Methods

In this chapter the techniques used in this thesis to produce, characterise, and analyse cluster samples will be presented. This chapter is laid out in the rough order that the order of work follows. Firstly, the magnetron sputtering gas condensation cluster source used for cluster production will be presented, then the scanning transmission electron microscope which was used to image and characterise the samples. The electrochemical techniques used to characterise the clusters *en masse* will be described before an overview of the analysis techniques used in this thesis.

2.1 Magnetron sputtering gas condensation cluster source

The clusters studied in this thesis were produced solely in a magnetron sputtering gas condensation cluster source and is described in detail in reference [111]. Within the group there have been many studies into clusters produced by this source, including gold[14], platinum[58], palladium[112], silver[42], nickel[48], and molybdenum disulphide[113]. The cluster source can be separated into three regions: cluster formation, cluster beam focussing, and mass-selection. The schematic shown in Figure 2.1.1 outlines these regions and other important features within the source. The cluster source itself is kept under high vacuum conditions during operation with five turbomolecular pumps and achieves a base pressure ~10^{-6} mbar.

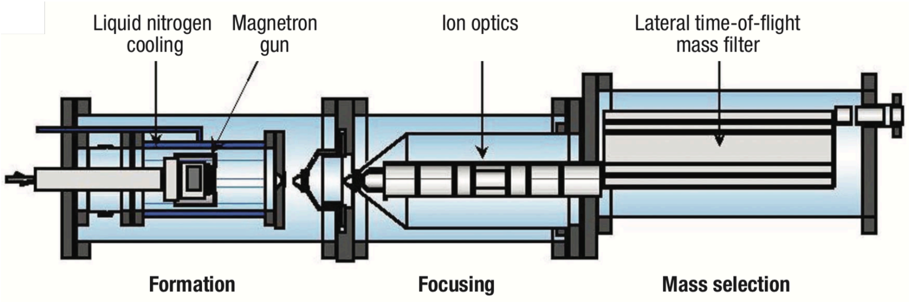

Figure 2.1.1: Schematic of the magnetron sputtering gas condensation cluster source used in this thesis. The source is split into three regions (from left to right): sputtering and cluster formation, beam focussing, and mass selection. Figure from reference 49.

Cluster formation initially begins in the condensation chamber, which is kept cold (~100 K) under the flow of liquid nitrogen. In this chamber a target material is vaporised by plasma sputtering. In this thesis a 2-inch diameter high purity platinum target (99.99%, PI-KEM) is predominantly used. Argon gas is bled into the condensation chamber around the sputtering target and the flow rate is controlled by a mass flow controller. A large negative DC potential, of the order of a few hundred volts, is applied to the target to ignite a plasma. A magnetron is used to confine the plasma around the target. Magnetrons have been utilized effectively in sputtering and coating techniques and can produce high sputtering yields and high purity deposits[114]. The high energy ions within the plasma bombard the target surface to produce a high density of atomic species and small clusters just in front of the target. These small cluster species are further condensed in cold helium gas which is bled into the back of the chamber. The total condensation time can be controlled by varying the total distance travelled before leaving the chamber, also called the 'condensation length', and this parameter has been shown to have an effect on cluster structural isomerization[44]. The formed clusters exit this chamber by an adjustable nozzle which can be used to increase the chamber pressure and tune cluster size. The operating pressure of the condensation chamber is typically in the range of 0.1-1 mbar.

Upon leaving the condensation chamber the pressure drops rapidly to ~10^{-5} mbar due to differential pumping and the cluster beam undergoes supersonic expansion. A pair of skimmers are used to filter out all but the center of the beam. A high proportion (~30 %) of the formed cluster beam is ionized due to the plasma and these species are focussed by electric lenses into a well-defined cluster beam. A pair of deflection plates allow for fine adjustment of the beam trajectory. The beam energy is defined by a common potential, typically 500 V, throughout the focussing optics.

By the time the clusters have entered the third chamber they are part of a well-defined, focussed beam. Some cluster sizes are preferentially focussed by the electric lenses, however there is still a broad range of masses of clusters in the beam. A lateral time-of-flight (LToF) mass selector is used to accurately filter clusters by mass before deposition[115] and a schematic is shown in Figure 2.1.2. LToF works by accelerating the clusters in a direction perpendicular to their velocity, letting them drift along a known length, and then decelerating them to their original velocity.

In Figure 2.1.2 the clusters enter LToF at the bottom left of the figure. A positive voltage pulse of plate 1 accelerates all clusters within L vertically, however only clusters located within l are transmitted into the field-free region between plates 2 and 3. In this field-free region the clusters are allowed to drift. The vertical velocity imparted to each cluster depends on its mass. As the clusters enter the region between plates 3 and 4 a positive voltage pulse decelerates the cluster to their original velocity. As all clusters receive the same impulse the timing between pulses is key to mass selection.

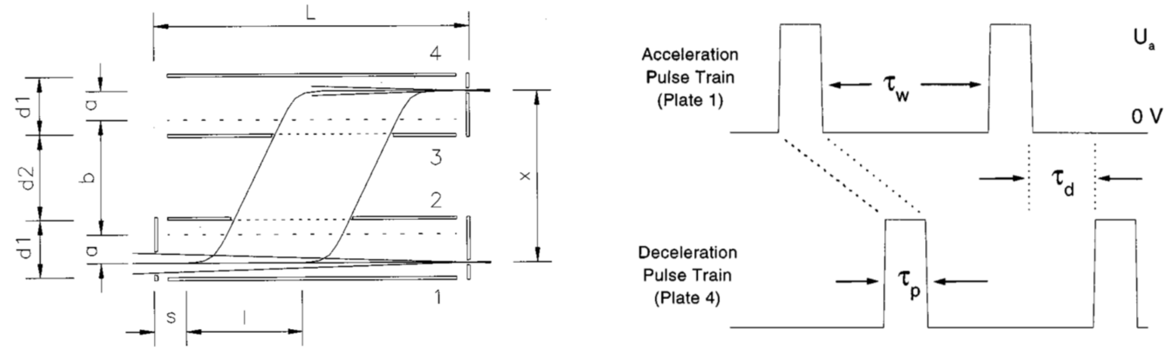

Figure 2.1.2: Schematics showing the operating principle of the lateral time-of-flight mass selector. (left) geometry of the equipment, and (right) voltage pulse timing sequence. Figures reproduced from reference 115.

Following arguments laid out by Palmer et al.[115], the duration of each voltage pulse T_P is calculated such that the selected clusters of mass m traverse a distance a:

$$T_P = \frac{2a}{v_m} = \frac{2a}{\sqrt{2eU_P/m}}, \qquad 2.1.1$$

where v_m is the final velocity of the cluster. The delay time T_d between accelerating and decelerating pulses is such that the cluster is allowed to drift a distance b before receiving another impulse, opposite in voltage but otherwise identical to the first, and during this time the cluster has then travelled a distance x. It then follows that if a cluster of mass M receives the same impulse it will drift a distance $x_M = x \cdot m/M$. The spread of displacements around the selected mass is therefore:

$$\left.\frac{dx_M}{dM}\right|_{M=m} = -\frac{x}{m}. \qquad 2.1.2$$

The convolution of the cluster beam profile with the exit aperture size Δx, determines the mass resolution of the source:

$$R = \frac{M}{\Delta M} = \frac{dM}{dx_M} \cdot \Delta \mathrm{x} = \frac{\Delta \mathrm{x}}{x}. \qquad 2.1.3$$

The exit aperture can be set at different widths and was set at 8 mm in this thesis. The displacement length b in LToF in this source is 150 mm, which gives a mass resolution of 5 %.

After transmission through the LToF the clusters can be focussed again with an einzel lens before deposition. A substrate can be inserted into the cluster source without breaking vacuum through a fast entry lock. The impact energy is defined by the bias applied to the substrate, and as discussed in section 1.2.3, can lead to many different types of cluster-surface interaction. In this thesis in general clusters were soft-landed at a kinetic energy of 1 eV per atom. An example of a loaded sample plate and the sample reception area is shown in Figure 2.1.3.

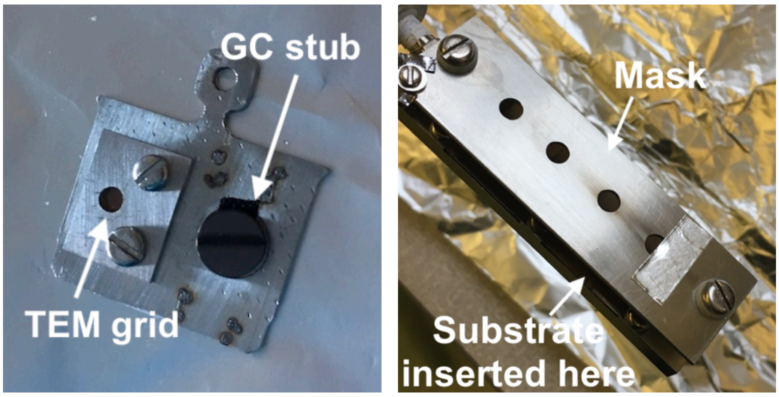

Figure 2.1.3: (left) sample plate loaded with a TEM grid, which is kept in place by a cover and screws, and a mirror-polished glassy carbon stub. (right) the sample reception area. The substrates are electrically connected to the back plate but not the mask, which is at beam potential. The metallic tape covering half of a hole in the mask was successfully used to deposit onto only half of a TEM grid, demonstrating the versatility of the cluster source.

Daily operation of the cluster source involves maintaining the vacuum and cooling the condensation chamber under a flow of liquid nitrogen for at least one hour prior to making clusters. Samples can be loaded through a fast entry lock, which takes typically 20 minutes to pump down to base pressure. Synthesising large clusters from scratch is an iterative process. Typically, the condensation length is reduced to its minimum (150 mm) and the nozzle is opened fully to achieve the lowest pressure possible. A plasma is then ignited and LToF is set to transmit a single atom, eg. 108 amu for silver. The ion optics are then tuned to maximise this current, and the sample reception positions are defined. At this point any changes to the LToF apertures are made. To make a dimer the condensation length is increased to about the middle of its range (200 mm) and the argon flow rate is increased. This process is repeated until clusters tens of atoms in size are being produced by the source. Small changes to the nozzle, gas flow mixtures, or plasma power can have a large effect on the cluster population being produced by the source.

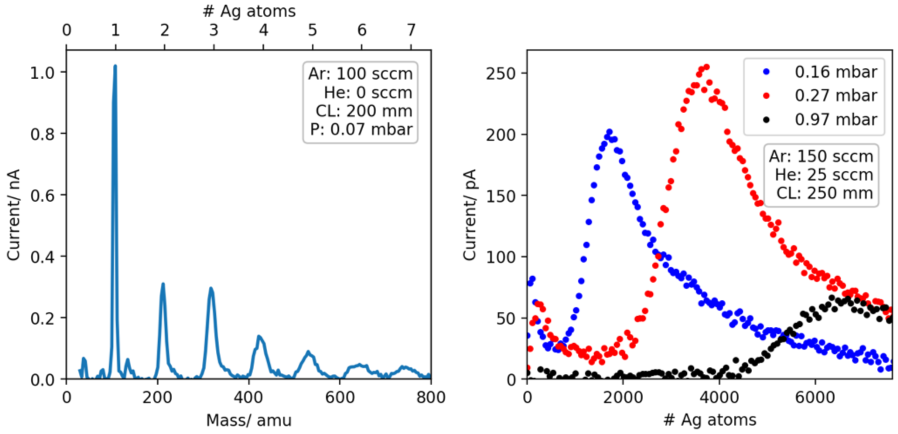

Figure 2.1.4: Silver cluster production with the cluster source. (left) example of the resolution of the cluster source, and (right) how the cluster population can be tuned be changing source parameters, in this case the nozzle was gradually closed which increased the condensation chamber pressure.

An example of operation of the cluster source is shown in Figure 2.1.4. In this case the target material was silver and was chosen for a structural study into silver clusters. The well-defined peaks in the mass spectrum are due to small Ag_N clusters. The mass resolution in this case was determined by fitting gaussians to the current peaks in the mass spectrum and on average $M/\Delta M \approx 34$, which compares well to the theoretical mass resolution of 36 for the 5 mm exit aperture used in this case. The second graph shows how the chamber pressure affects the cluster population in the source. In this case the nozzle was closed to increase the pressure from 0.16 mbar up to ~1 mbar, and as a result the peak cluster mass produced by the source was increased from ~1700 to ~6300 atoms.

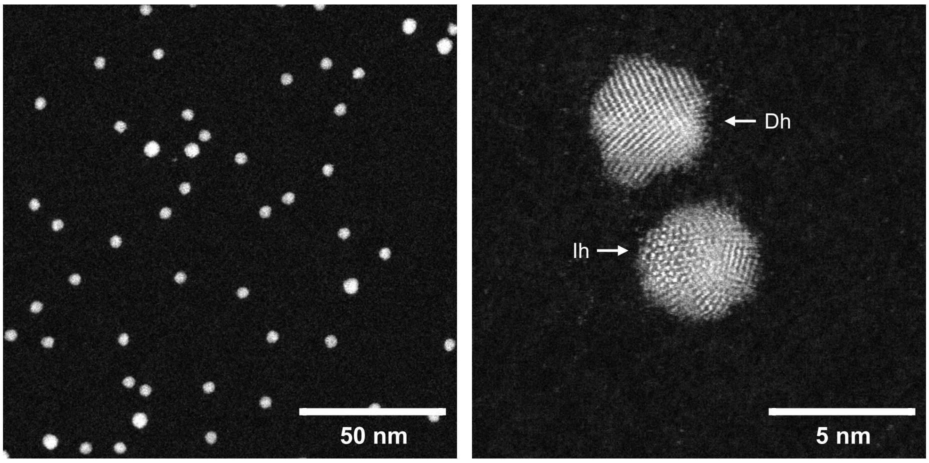

Figure 2.1.5: ADF-STEM images of Ag_{2255} *clusters produced using the cluster source. (left) low magnification sample showing well-defined clusters distributed homogeneously on the amorphous carbon support, and (right) high magnification image showing cluster structures.*

2.2 Scanning transmission electron microscope

TEM was discussed in detail in section 1.6. In this work a JEOL 2100F with spherical aberration correction (CEOS, GmbH) was used for imaging. The microscope was used in STEM mode with an accelerating voltage of 200 kV. The gun emission current was typically 150 ± 10 μA and the current density impingent on the sample was typically 3 pAcm^{-2}. Electrons were collected by a photomultiplier tube type annular detector with an inner and outer collection angle of 62 and 164 mrad, respectively[101,116]. The beam convergence angle used for imaging was typically 19 mrad. Images were typically recorded at a resolution of 512 x 512 pixels with 38 μs pixel dwell time.

2.3 Electrochemical techniques

Electrochemical testing was performed in 0.5 M sulphuric acid, which was prepared daily from concentrated sulphuric acid (96 % Ultrapur, Sigma Aldrich) and deionized water (18.2 MΩcm, Merck Millipore). The electrolyte was deaerated by bubbling nitrogen gas for 30 minutes prior to experimentation and the cell atmosphere was kept under nitrogen gas throughout. This procedure produced negligible oxygen reduction current graphite samples which were sputter-coated with platinum. A mercury-mercurous sulphate (MSE) reference electrode (RE) (RE-2CP, ALS Co., E_0 = 0.687 V vs RHE) was used to avoid potential chloride contamination. All potentials have been converted to reversible hydrogen electrode potential (RHE) herein. A platinum wire was cleaned daily with water and flame-annealed under a propanol flame until orange-hot before being used as a counter electrode (CE). Electrochemical cell apparatus was cleaned in either hot (60 °C) piranha solution or with green acid[113] prepared adding KMnO4 (ACS ≥ 99%, Sigma-Aldrich) to concentrated H_2SO_4 (96%, Alfa Aesar). All apparatus was washed thoroughly in deionized water and swilled with electrolyte before use.

2.3.1 Mass-selected platinum clusters on graphite

Electrochemical studies on graphite were undertaken at the National Physical Laboratory, Teddington, UK. Graphite (ZYH, NT-MDT) was prepared using a scotch tape cleave method. Platinum cluster samples were prepared using the magnetron sputtering gas condensation cluster source at the University of Birmingham, Birmingham, UK, transported under nitrogen atmosphere and kept in a vacuum desiccator until use. Despite the attention taken to limit contamination and oxidation of the samples it should be noted that the samples would have been exposed to ambient conditions for prolonged periods before use. Cluster samples were soft-landed at 1 eV per atom onto graphite at a constant number density of 20000 clusters per square micron.

The graphite used in these experiments was cut as approximately 7 mm x 7 mm squares and this represented a challenge to use in an electrochemical cell, as available apparatus was suited to circular electrodes. It was decided that the electrochemical cell used in these experiments should be free of any unwanted solvents, such as silver paint or conductive glue, which can be used to create a temporary electrical contact, in order to avoid potential contamination. A custom electrochemical cell was manufactured to house the square graphite pieces and expose only the platinum decorated surface, the cell is shown in Figure 2.3.2. A 2.5 mm radius hole cut in a silicone gasket placed directly on top of the graphite defined the electrolyte exposed area. The steel back contact was sputter coated with gold to an attempt to improve conductivity, however no discernible difference was observed in testing.

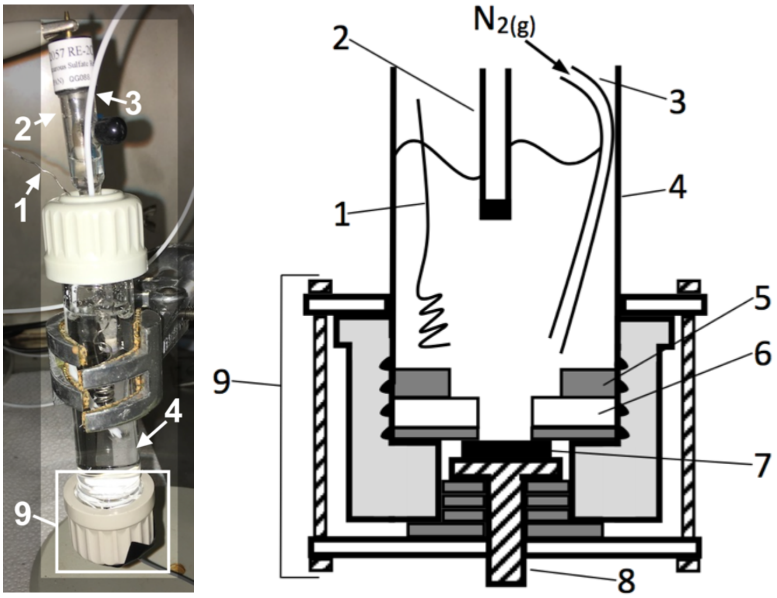

Figure 2.3.1: (left) photograph and (right) schematic of the custom built electrochemical cell with a solvent-free electrical graphite 'back contact'. (1) Pt wire counter electrode, (2) MSE reference electrode, (3) gas inlet tube, (4) Pyrex cell, (5) silicone gasket, (6) teflon gasket, (7) graphite working electrode, (8) steel screw 'back contact', and (9) scaffolding used for stability and to apply pressure to the ensemble.

A CH Instruments 760c was used as the potentiostat for these experiments. No electrochemical preconditioning was performed. Sample characterisation was performed using cyclic voltammetry (CV). The cathodic limit for the CVs was at the onset of hydrogen evolution at 0.05 V vs RHE, whilst the anodic limit was gradually increased. CVs were performed at different sweep rates until the response was stable.

CO stripping experiments were performed with analytical grade CO. The working electrode (WE) was held at a potential of 0.1 V vs RHE during CO dosing such that CO would displace any adsorbed hydrogen. The electrolyte was dosed with gaseous CO for three minutes to ensure surface saturation, before being purged with nitrogen for 30 minutes to purge any dissolved CO. The stripping sweep was initiated in the cathodic direction to check for any hydrogen adsorption current before the anodic sweep to a maximum potential of 1.45 V vs RHE to ensure full CO oxidation.

2.3.2 Mass-selected platinum clusters on TEM grids

Potential conditioning experiments were performed on a TEM grid such that the change in sample morphology could be imaged with TEM. Platinum clusters were soft-landed at 1 eV per atom onto amorphous carbon TEM grids (EM Resolutions). The amorphous carbon layer was supported by a gold mesh to avoid any potential contamination from other common mesh materials, such as copper.

Multiple methods were tested to create a solvent-free electrical contact to the TEM grid. A 1 mm diameter gold wire was cut at one end and then crimped onto the TEM grid. This method yielded good results however the TEM grid was often damaged or ripped on removing the crimp, making it unsuitable for imaging. A second technique involved passing a thin gold wire through the TEM grid key to create an electrical contact. This method however was extremely difficult to perform reliably and required a very steady hand. Ultimately it was not explored much further due to its difficulty and doubts about the quality of the connection and conductivity.

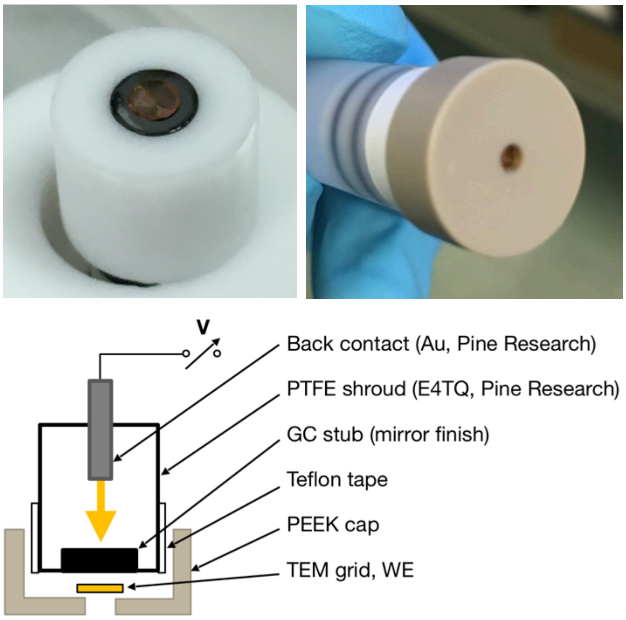

Figure 2.3.2: Configuration for electrochemical studies on a TEM grid. (top row) photographs of TEM grid and GC stub configuration without (left) and with (right) the PEEK cap. (bottom) schematic showing the internal arrangement and materials used.

A cap-type electrode setup was ultimately found to be the easiest to setup, least invasive, and most reliable. A polyether ether ketone (PEEK) cap with 1 mm wall width was manufactured to fit a Pine Research E4TQ ChangeDisk RDE Tip, which is an apparatus commonly used to insert different electrode materials into a Pine Research rotator. 5 mm glassy carbon (GC) stubs (Type II, Alfa Aesar) were cut and polished with successively finer diamond and alumina paste (Bruker) to a mirror finish for use as the base electrode. The base glassy carbon stub was polished daily to the 1 micron level and its quality assessed through CVs. The TEM grid was placed on top of the glassy carbon electrode and kept in place using the PEEK cap, as shown in Figure 2.3.2. The TEM grid was exposed to the electrolyte by a 2 mm diameter hole cut into the cap. The cap provides stability to the setup by ensuring that the TEM grid does not move on and remains in firm contact with the base electrode. The cap setup was tested up to 1500 rpm rotation speed.

The rotation speed during potential cycling was maintained at 500 rpm to alleviate any mass transport effects. Care was taken to remove any air bubbles from the exposed WE surface.

2.4 Image analysis

The majority of analysis performed in this thesis is from data obtained through STEM imaging, and more specifically HAADF-STEM. In the case of platinum clusters on amorphous carbon substrates, the platinum clusters appear bright on a dark background by HAADF-STEM imaging.

In TEM the images produced are a measure of the count of electrons on the detector over a period of time. In the simple cases of noble metals, for example platinum, on carbon surfaces the high atomic number of the material produces large amounts of high-angle scattering which we integrate over an annular detector to avoid the direct beam and low-angle scattering contributions. In this case the images produced have two well defined classes, foreground and background, which represent the nanoparticles of interest and the substrate respectively.

Most of the analysis performed in this thesis is as a result of image processing. Python was used predominantly for analysis, and more specifically the NumPy, scikit-image[117], and SciPy[118] packages. Figures were typically produced using the Matplotlib[119] package. Images were analysed using the Gwyddion SPM analysis suite[120] and its underlying API. Nearest neighbour analyses were performed using custom scripts built upon functions in the NumPy and SciPy packages.

2.4.1 Image segmentation methods

Common methods of image segmentation include thresholding, clustering, edge-detection, and histogram-based methods. One of the most common automated segmentation techniques is Otsu's method[121] which is histogram-based clustering technique. The only input to Otsu's method is the image itself, and the algorithm determines an optimal threshold by maximising the intra-class variance of the classes of pixels above and below the threshold level.

An example histogram calculated from an image containing two features is shown in Figure 2.4.1. Two common threshold levels are located at the intersection of the functions describing the two features and at the valley minimum of the overall histogram[122]. Otsu's method calculates a threshold level that is skewed towards the foreground feature and is inadequate in this case.

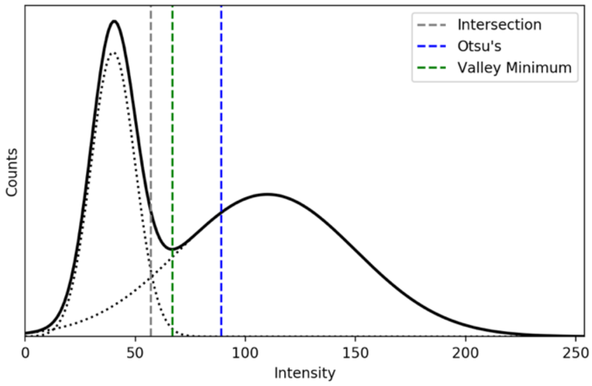

Figure 2.4.1: Common threshold levels on a bimodal histogram.

Otsu's method is defined as the following[121]: consider a greyscale image which is made up of N pixels with grey levels [1, 2, ... L]. The number of pixels at each grey level n_i, where $N = \sum_i^L n_i$, can be described by a probability $p_i = n_i/N$, given that $\sum_i^L p_i = 1$. In order to segment the image into two classes, ie. foreground and background, a threshold level t is defined where $1 \leq t \leq L$ such that the background pixels belong to class C_0 containing grey levels [1, 2, ... t] and the foreground pixels belong to class C_1 containing grey levels [t+1, ... L]. The class means are calculated by the weighted probabilities $\mu(t) = \sum_i^t i p_i$ and the probability of class occurrence at threshold level t is $\omega_0 = \sum_i^t p_i = \omega(t)$ and $\omega_1 =$

$1 - \omega(t)$. The optimal threshold level is chosen to maximise the intraclass variance, which is defined as:

$$\sigma_B^2 = \omega_0(\mu_0 - \mu_T)^2 + \omega_1(\mu_1 - \mu_T)^2, \qquad 2.4.1$$

where μ_T is the mean of the total image.

Otsu's algorithm provides good results in many cases. In practice it calculates a threshold close to the intersection point between two classes, however it has been shown that the calculated threshold is skewed towards the class with the largest variance[123] and this is inadequate in some cases. Yang et al.[124] modified Otsu's threshold by using the class medians to calculate the intraclass variance rather than the class means. In the case of skewed or long-tailed distributions the median is a more robust descriptor than the mean.

The samples studied predominantly in this thesis are noble metal nanoparticles on carbon supports which are imaged with HAADF-STEM, a comparison of different image thresholding techniques is shown in Figure 2.4.2. For these types of samples the image histogram is composed of two main peaks: the background peak and nanoparticle peak. The background peak is typically narrower than the nanoparticle peak as background is homogeneous and the nanoparticles have variable thickness and therefore intensity due to their spherical shape. Otsu's threshold is therefore biased towards the nanoparticle peak and the calculated threshold is typically too high which results in classification errors at the nanoparticle edges. By comparison when the median descriptor is used in Otsu's method (as described by Yang et al.[124]) the calculated threshold is lower in intensity than Otsu's method, and closer to the intersection point of the two histogram peaks whilst still being located within the histogram valley basin. As a result, the edges of the nanoparticles are classified as expected with the nanoparticle bulk and the overall result is more accurate.

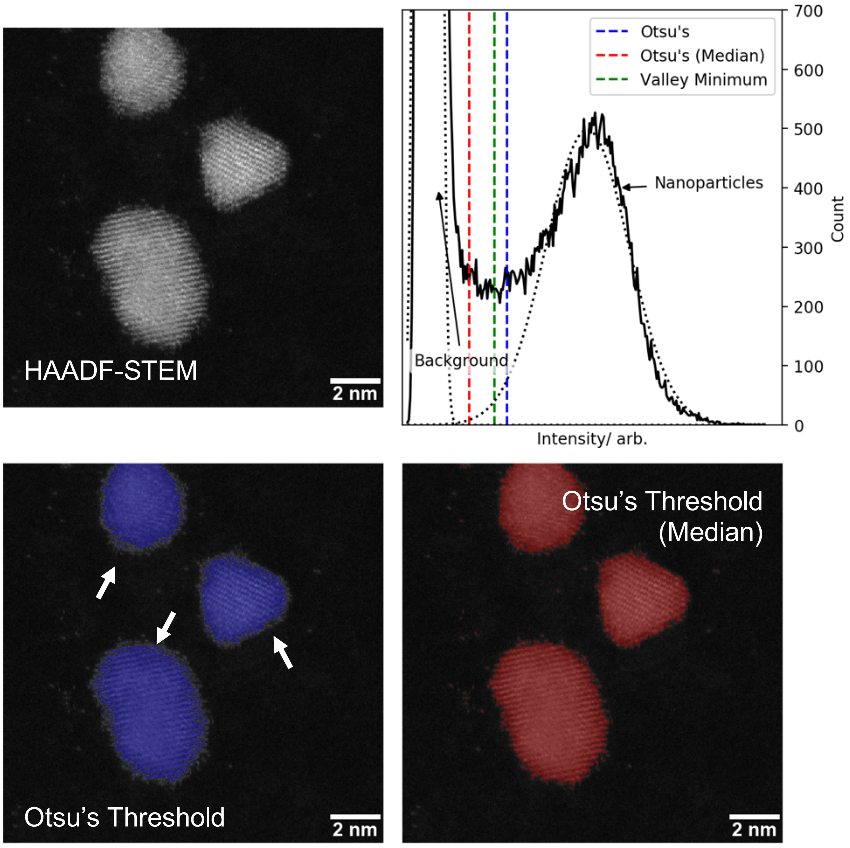

Figure 2.4.2: Image thresholding analysis of platinum nanoparticles. (top left) HAADF-STEM image. (top right) the image intensity histogram is composed of two main peaks from the background (amorphous carbon in this case) and the nanoparticles which have higher intensities. Different thresholding algorithms calculate different optimal threshold levels. (bottom row) the thresholding results from Otsu's method[121] (left) and Yang's adaptation[124] (right) are overlaid on the original image. Arrows depict missing features due to the calculated threshold.

In some cases image histograms do not exhibit bimodality which obfuscates the correct threshold value and cause problems for methods such as Otsu's algorithm[125,126] which rely on histogram bimodality. An example of data exhibiting unimodality is shown in Figure 2.4.3. Here, the HAADF-STEM image shows Pt_{55} clusters which are bright against an amorphous carbon support. The image histogram however is unimodal and the contribution from the platinum clusters is a small foot in the histogram at high intensity, as shown in the inset. The optimal threshold level is not clear as there is no valley minimum in the histogram. Rosin[127] explored thresholding unimodal histograms using a geometric triangle method with good results. In the triangle algorithm a line is drawn between the histogram maximum and the end of the histogram tail, representing the hypotenuse of the triangle. The threshold level is defined as the level with maximum perpendicular distance to this line. Coudray et al.[125] developed a thresholding technique they called the T-Point method which is less sensitive to histogram noise than the triangle method. In this case the threshold level segments two sides of the histogram: a steep descending slope from the histogram maximum and a shallow tail. The two sides of the histogram segmented by a threshold level are fit using linear regression and the total cost of the threshold is calculated as the sum of piecewise least squares residuals between the histogram data and the fitted line. The threshold level is increased iteratively, and the optimal threshold is defined as the minimum of the cost function. An example application of the T-Point algorithm to HAADF-STEM data is shown in Figure 2.4.3.

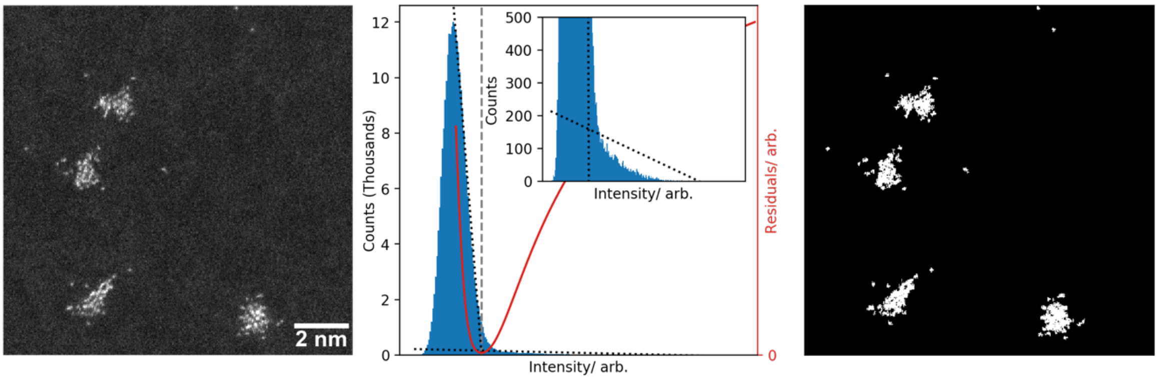

Figure 2.4.3: T-Point algorithm applied to HAADF-STEM images of Pt_{55} on amorphous carbon (left). (center) image histogram and the evaluation of the T-Point threshold. The histogram is unimodal with a small foot (see inset). The optimal threshold level (dashed grey line) is at the minmum of the total cost function (red curve) which is evaluated for many different threshold levels. Each side of the threshold level a line is fitted to the histogram in a piecewise fashion. The first line is fit to the histogram peak slope between the histogram maximum and the threshold level. The second line is fit between the threshold level and the end of the histogram. The two fitted lines corresponding to the optimal threshold are shown as black dotted lines. (right) the image thresholding result.

Edge-detection algorithms are also commonly employed. The Canny edge detector[128] uses hysteresis thresholding alongside the Sobel operator to detect edges, or high frequency changes in the image.

Figure 2.4.4 demonstrates the accuracy and validity of common image analysis techniques at different magnifications. Image thresholding was performed in two cases, using Otsu's method, and a derivative of Otsu's method which uses the class medians[124], rather than the class means in the former, as the descriptor for threshold calculation. This calculation been shown to perform well with skewed histogram distributions and more accurately detects the edges of the nanoparticles. The Canny edge detection algorithm by comparison can have issues with incomplete boundaries leading to false-positive background detection and missing areas, highlighted by the red and white arrows in Figure 2.4.4, respectively.

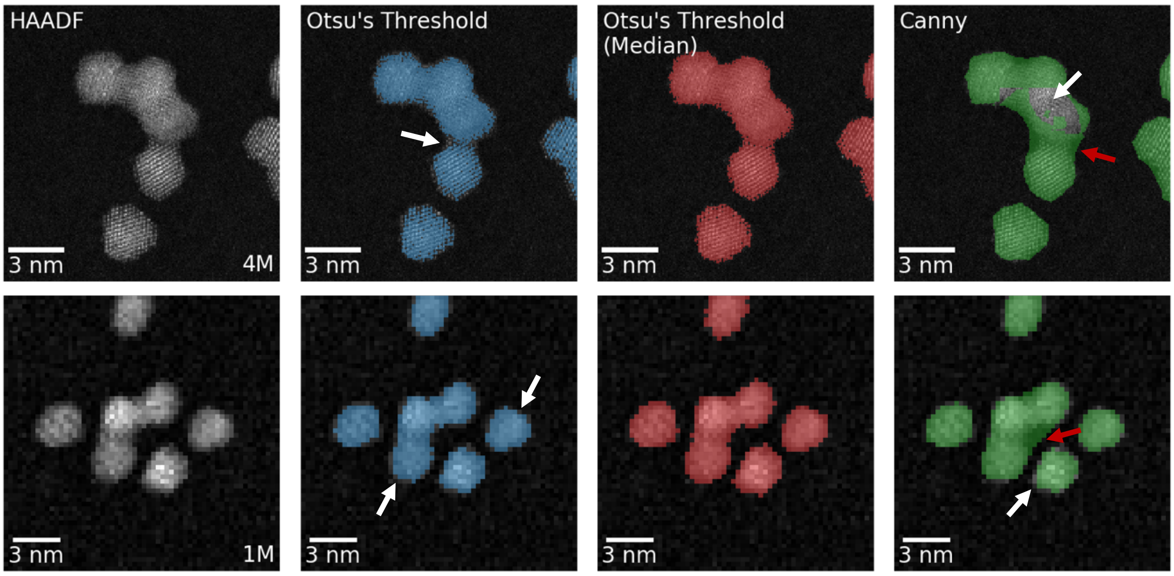

Figure 2.4.4: Comparison of different image detection techniques at 4 million (top row) and 1 million (bottom row) magnifications. The detected areas are overlaid on the original HAADF image in each case. Arrows point to regions of interest. The white arrows show missed pixels and red arrows show incorrectly detected pixels.

To compare the aforementioned analysis techniques a mass-selected Pt_{923} sample was created and imaged with HAADF-STEM. The clusters in produced here are well-defined to a mass resolution of less than 5 % and are therefore ideal model particles suitable for comparing these algorithms. The images were analysed with the and the projected area size distributions are summarised Figure 2.4.5. The peaks in each histogram are attributed to Pt_{923} clusters (Pt_{923} singlets) and two sintered Pt_{923} clusters (doublets) and were fit with gaussians to determine the average projected area and standard deviation in each case. The results are summarised in Table 2.4.1.

The average singlet size deviates by as much as 20 % between the three techniques. Figure 2.4.4 shows that Otsu's median-adapted threshold most precisely describes the nanoparticle projected area in the case of both low and high magnification. One disadvantage, however, is that it this technique may overestimate the projected area at the edges of the nanoparticles, as evident by some single pixel discontinuities at the nanoparticle boundaries. By comparison, Otsu's threshold appears to underestimate the nanoparticle projected area due to under-detection at the nanoparticle boundaries. In the high magnification case this actually manifests as the missed detection of atomic columns in many cases. Image detection can be subjective, but in the cases described here it appears as though Otsu's median-adapted threshold is more accurate for nanoparticle detection and so it is used consistently throughout this thesis.

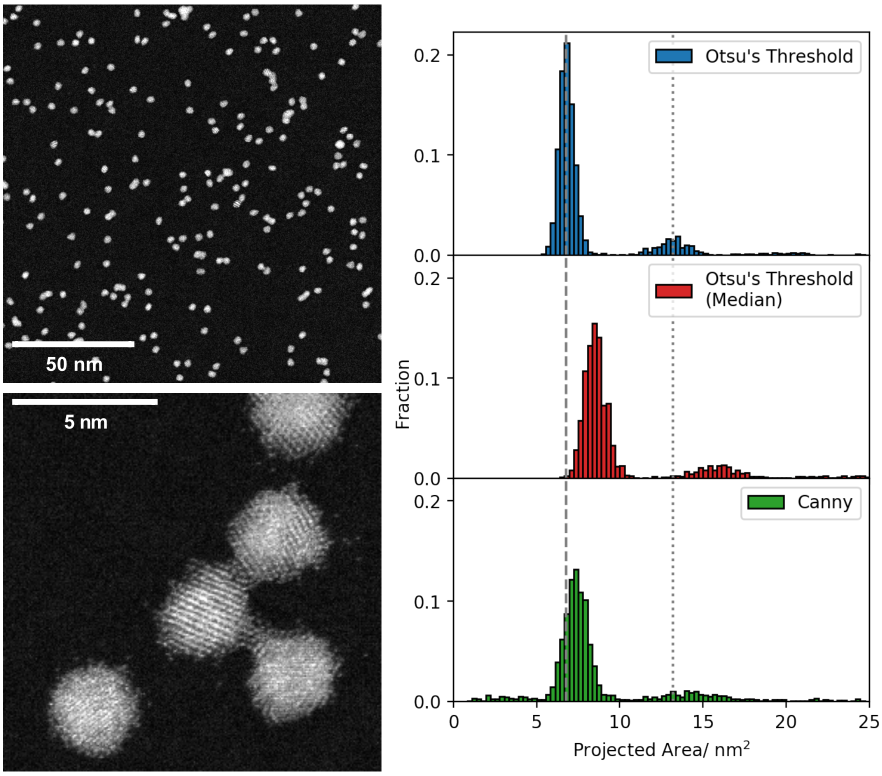

Figure 2.4.5: Comparison of nanoparticle size distributions calculated by different image analysis techniques. (upper left) representative HAADF-STEM image of Pt_{923} clusters on amorphous carbon at 1 million magnification used to compare analysis techniques. (lower left) Pt_{923} clusters at 4 million magnification with atomic resolution showing cluster shape, atomic planes, and necking between clusters. (right) projected area size distributions of approximately 2000 nanoparticles detected using Otsu's algorithm (blue), Otsu's median-adapted algorithm (red), and the Canny edge detector (green). The dashed and dotted grey lines show the peak position for Pt_{923} singlets and doublets as determined by Otsu's algorithm.

In any case it is useful to know the limitations of the techniques used. Despite the drawbacks mentioned here both algorithms are calculated automatically and are therefore not subject to the same degree of human error and inconsistency reserved for manual thresholding.

	Singlet area (nm^2)	Radius (nm)	Doublet area (nm^2)	Doublet: singlet area ratio	Count
Otsu's	6.77 ± 0.44	1.46 ± 0.05	13.19 ± 0.93	1.95	2003
Otsu's (median)	8.46 ± 0.61	1.64 ± 0.06	15.82 ± 1.27	1.87	1954
Canny	7.34 ± 0.69	1.52 ± 0.07	14.25 ± 1.99	1.94	2093

Table 2.4.1: Fit parameters for the image analysis techniques discussed in Figure 2.4.4. Values are quoted with one standard deviation.

Neighbouring nanoparticles in close proximity are known to sinter [109,129], and this is often preceded by the formation of a narrow material 'bridge' between the nanoparticles, also known as 'necking'[81]. An example of necking between Pt_{923} clusters is shown in Figure 2.4.6, these nanoparticles are in the early stages of sintering and should therefore be treated as one nanoparticle.

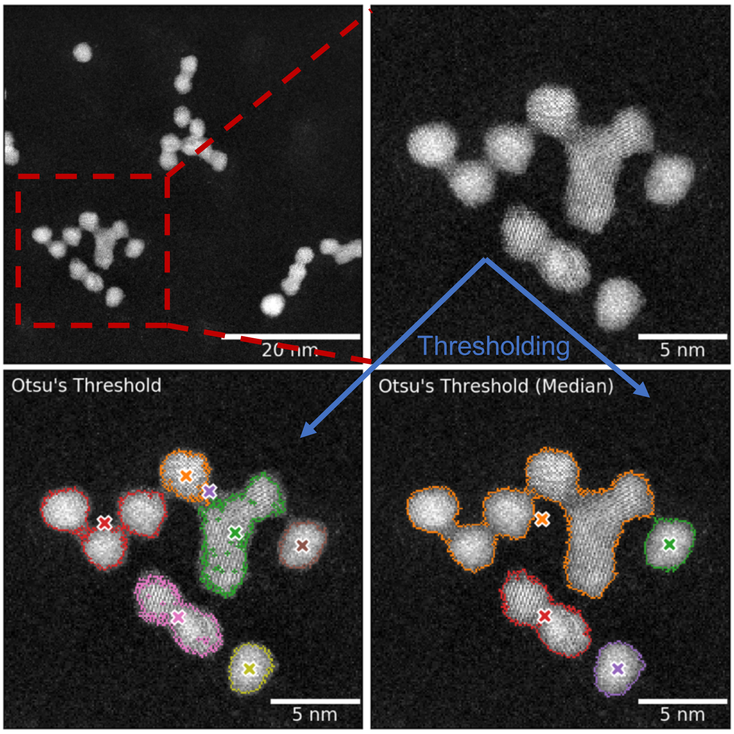

Figure 2.4.6: Segmentation of sintered platinum nanoparticles by different thresholding algorithms. HAADF-STEM image taken at 4 million magnification after oxygen plasma treatment showing particle grouping, sintering, and necking. (top row) original image (left) and inset (right). (bottom row) the boundaries of the detected nanoparticles after thresholding with Otsu's algorithm (left) and its median adaptation (right). Each nanoparticle boundary is represented by a different colour and its center of mass is shown as a cross.

Otsu's algorithm and its median adaptation were used to threshold the images in Figure 2.4.6. Each detected nanoparticle has been assigned a colour and the nanoparticle boundaries have been plotted. Otsu's algorithm has incorrectly assigned the large nanoparticle as three smaller nanoparticles (red, orange, and green). This is because the platinum bridges between nanoparticles have not been detected by the algorithm and so the main bodies of the platinum clusters remain unbridged. By comparison Otsu's median-adapted threshold does detect the platinum bridges and therefore the whole agglomerated mass is detected as one nanoparticle. Also of note is that Otsu's threshold leaves undetected holes within the nanoparticles, evident by the coloured boundaries within the main body of the nanoparticles, due to the internal fine structure of the nanoparticle from atomic columns and lattice planes. This is a drawback of Otsu's threshold for accurate nanoparticle detection at these intermediate magnifications.

In order to more accurately determine the detection limit, line profiles were taken traversing the platinum bridges, labelled as lines 1-3 as shown in Figure 2.4.7. For comparison line profile 4 is taken across one Pt_{923} cluster. Li et al. have shown that the integrated HAADF intensity can be used to weigh metal clusters[130], and that HAADF intensity is proportional to the number of atoms in an atomic column[41]. All line profiles were fit with a parabolic step in Gwyddion and the intensity contribution from the platinum atoms were recorded. Assuming that 923 atoms in a Mackay's icosahedron structure are equivalent to a width of 13 atoms, the bridge size can be deduced from the intensity ratios. Line profiles 1 and 2 are equivalent to ~7 and ~6 bridging atoms respectively, whilst line profile 3 is equivalent to ~2 bridging atoms. The quoted ratios differed from integer values by less than 0.2 in each case. The threshold values calculated by Otsu's algorithm and its median adaptation are plotted as broken grey lines in Figure 2.4.7. In the case of Otsu's threshold, the larger threshold intensity means that only the bridge described by line profile 1 is classified as connecting two neighbouring nanoparticles, the intensity from bridges 2 and 3 are too low to meet the threshold. In the case of Otsu's median adapted threshold, which is used throughout this thesis, bridges 1 and 2 clearly meet the threshold whilst bridge 3 does not. The lower bound on nanoparticle sintering is therefore by this algorithm is therefore defined as more than 2 bridging atoms.

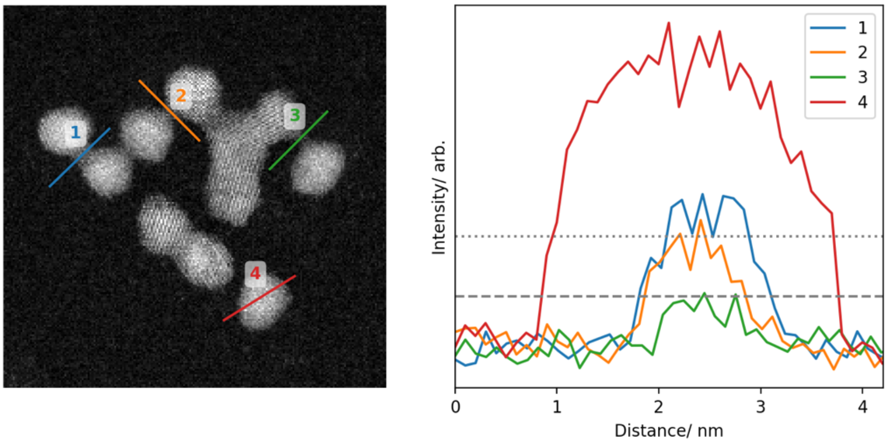

Figure 2.4.7: Analysis of neck sizes between sintering nanoparticles. (left) HAADF-STEM image of Pt_{923} sintered nanoparticles and associated line profiles across (right). Line profiles 1-3 are taken across platinum bridges between two neighbouring clusters. Line profile 4 shows the intensity across one Pt_{923} cluster for reference. Line profiles are averaged across 3 pixels. The threshold values calculated by Otsu's algorithm and its median adaptation are shown as grey dotted and dashed lines respectively.

2.4.2 Nearest neighbour algorithms

In many cases the arrangement of material on a substrate is of high interest, especially when considering nanoparticle migration[93] or diffusion fields[131,132]. Real space imaging can characterise the morphology and displacements between regions of interest and these can be quantified through image analysis.

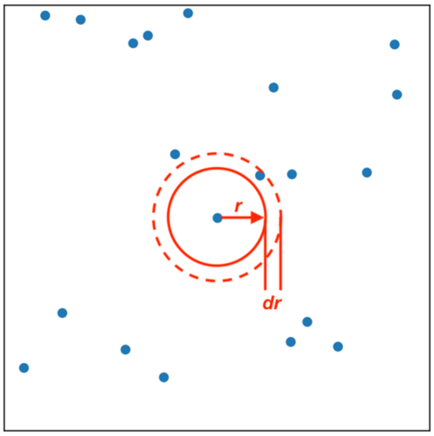

Figure 2.4.8: Nearest neighbour model in two dimensions. In two dimensions each point is expanded by a concentric circle of radius r. The nearest neighbour distribution can be calculated by the product of probabilities that there are no points within radius r but there is a point within radius r+dr.

A descriptor commonly used to quantify particle arrangements is the nearest neighbour distribution (NND). In the case of discrete data NND is the minimum distance between any particle and its closest neighbour, and this can be extended to any k nearest neighbours. In two dimensions, which is the case for nanoparticles bound to a surface, each particle has a radius r in which no other particle is found, but a second particle can be found within the expanded radius $r+dr$, as depicted in Figure 2.4.8.

The nearest neighbour distribution *D(r)* is therefore the product of probabilities that no particle exists within radius r, but one is contained within the radius $r+dr$, denoted P_1 and P_2 respectively. Given that the particles are randomly distributed with an as yet unknown NND *w(r)* and number density ρ, the probability of not finding a particle in radius r is:

$$P_1 = 1 - \int_0^r D(r')dr', \qquad 2.4.2$$

and the probability of finding a particle within an infinitesimal radius dr is:

$$P_2 = \rho \cdot 2\pi r dr, \qquad 2.4.3$$

The nearest neighbour distribution is therefore

$$D(r)dr = \rho \cdot 2\pi r dr \left(1 - \int_0^r D(r')dr'\right). \qquad 2.4.4$$

Differentiating equation 2.4.4 gives

$$\frac{dD(r)}{dr} = \rho \cdot 2\pi \left(\left(1 - \int_0^r D(r')dr'\right) - r\frac{d}{dr}\left(\int_0^r D(r')dr'\right)\right). \qquad 2.4.5$$

Leibniz's rule for differentiating under the integral sign is applied to the second term in equation 2.4.5

$$\frac{d}{dr}\left(\int_0^r D(r')dr'\right) = D(r) \cdot 1 - D(0) \cdot 0, \qquad 2.4.6$$

and substituting equations 2.4.4 and 2.4.6 into equation 2.4.5 gives

$$\frac{dD(r)}{dr} = D(r)\left(\frac{1}{r} - \rho \cdot 2\pi r\right). \qquad 2.4.7$$

Equation 2.4.7 can be solved by integration

$$\int \frac{1}{D(r)} dD(r) = \int \left(\frac{1}{r} - \rho \cdot 2\pi r\right) dr \qquad 2.4.8$$

$$\ln\big(D(r)\big) = \ln(r) - \rho \cdot \pi r^2 + C, \qquad 2.4.9$$

and rearranging gives

$$D(r) = kre^{-\rho \cdot \pi r^2} \qquad 2.4.10$$

where the constant $k = 2\pi\rho$ is determined by the boundary condition $\int_0^\infty D(r)dr = 1$.

Figure 2.4.9 compares the analytical nearest neighbour distribution described by equation 2.4.10 and simulated random data. In this example 15000 uniformly distributed random data points are arranged on a 1024 x 1024 grid. The measured nearest neighbour histogram is described well by equation 2.4.10. However, in the case of impenetrable 'hard' particles, shown in the lower half of Figure 2.4.9, equation 2.4.10 does not describe the nearest neighbour histogram. Non-overlapping hard particles with a radius of 10 pixels were simulated onto a 1024 x 1024 grid using a random sequential adsorption (RSA) algorithm and the Gwyddion software[120]. 50 monolayers were 'deposited' in the simulation, however only the particles that did not impinge on a previously deposited particle were 'adsorbed' onto the surface. The coverage simulated by RSA was 53 % for all simulations which is well below the close packing fraction for disks. Considering the center points of the particles as data points, the minimum nearest neighbour distance is one particle diameter, equivalent to 20 pixels in this simulation. The minimum nearest neighbour histogram shows that the measured minimal nearest neighbour distance is 19 pixels, which is within error of the simulation.

Torquato et al.[133,134] have previously considered the nearest neighbour distribution of interacting particles in multiple dimensions. For hard disks in two dimensions the nearest neighbour distribution is given by

$$D(x) = \frac{4\eta \cdot (2x - \eta)}{\sigma \cdot (1 - \eta)^2} \cdot \exp\left(- \frac{4\eta}{(1 - \eta)^2} \cdot \left(x^2 - 1 + \eta \cdot (x - 1) \right) \right), \qquad 2.4.11$$

where σ is the particle diameter, $x = r/\sigma$ is a scaled distance, and $\eta = \rho \cdot v_2(\sigma/2) = \rho \cdot \pi(\sigma/2)^2$ is the reduced density, which is valid for distances larger than the particle diameter $r > \sigma$. The expected NND for this distribution is shown as a dashed red line in Figure 2.4.9 for σ=10 pixels and ρ=0.017 per pixel, which is in good agreement with the measured distribution. On the same graph the NND point model, calculated from equation 2.4.10 with the same density, is also shown as a black dashed curve to illustrate the models' discrepancy with the data.

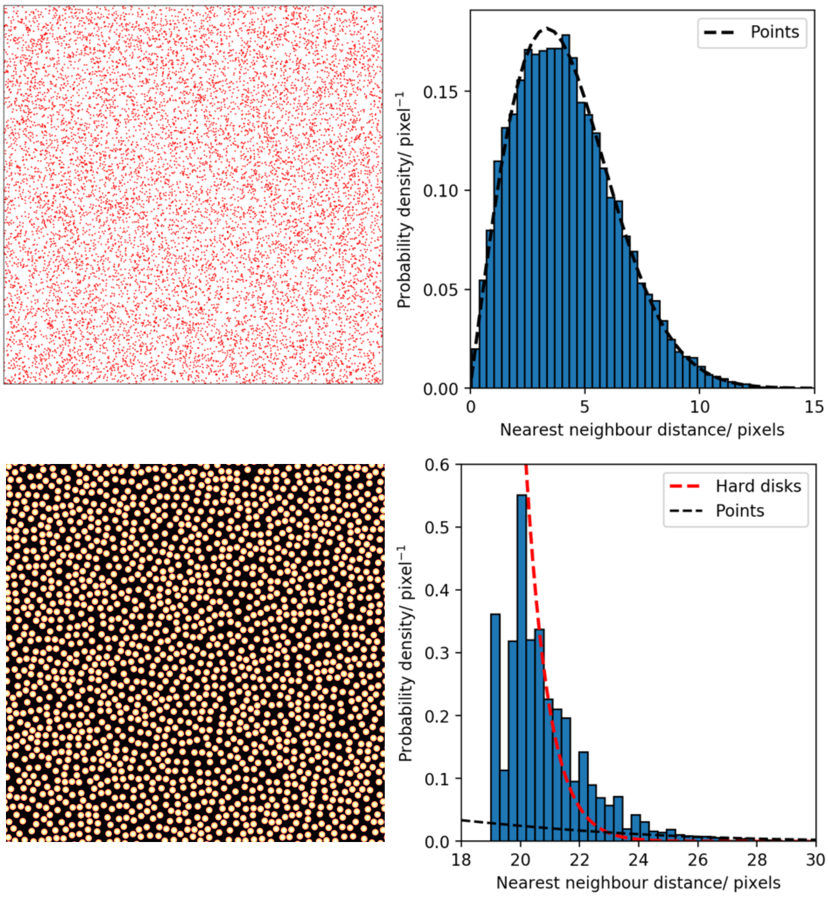

Figure 2.4.9: Simulated data and associated nearest neighbour distributions for point data (top row) and hard disks (bottom row). (top row) 15000 randomly distributed points in a 1024 x 1024 grid. (left) arrangement of points in the grid and (right) first nearest neighbour histogram and expected distribution (black dashed curve) calculated with equation 2.4.10 where ρ=15000/1024^2=0.014 per pixel. (bottom row) simulated hard particles with radius 10 pixels in a 1024 x 1024 grid and a maximum coverage of 74 %. (left) arrangement of particles in the grid and (right) first nearest neighbour histogram calculated from three different particle arrangements. The black dashed curve is the expected nearest neighbour distribution for randomly arranged points calculated from 2.4.10, and the red dashed curve is the expected distribution for randomly arranged hard disks. In both cases ρ=0.017 per pixel as measured from the images.

An example of nearest neighbour analysis is shown in Figure 2.4.10. Here, the nanoparticles are detected by thresholding as described previously. The regions, often called grains, determined to be nanoparticles form a binary image, and the individual grains are then grouped by first-degree connectivity, where pixels are determined to be connected if they have a shared face. Each of these grains is then labelled and its center of mass is calculated. The nearest neighbour distribution can be calculated from the grains' centers of mass.

For regular grain shapes the center of mass is a useful descriptor. However, in the case of agglomerated platinum nanoparticles as discussed in this thesis the agglomerated nanoparticles are often branched or chain-like, many examples of these structures can be seen in Figure 2.4.10. A more accurate, albeit slower, analysis is to determine the edge-edge nearest neighbour distance. The center of mass and edge nearest neighbour analysis are compared in Figure 2.4.10. The two distributions share a common shape except that the edge nearest neighbour distribution is shifted to smaller distances by approximately one Pt_{923} diameter (~3nm).

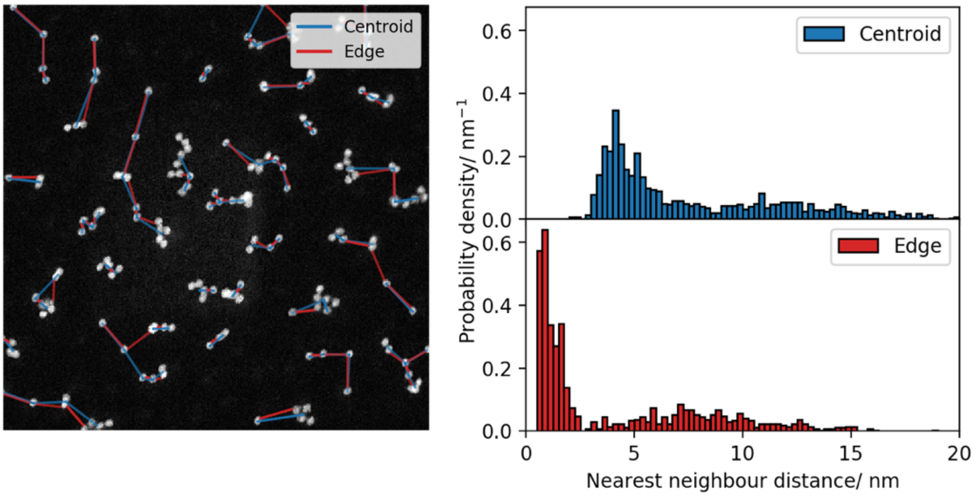

Figure 2.4.10: Comparison of nearest neighbour distributions obtained from the centers of mass (blue) and the edges (red) of nanoparticles. (left) HAADF-STEM image overlaid with the nearest neighbour vectors, and (right) first nearest neighbour distributions.

2.4.3 Background subtraction

It is well known that beam exposure in electron microscopy can lead to surface contamination from carbonaceous species which in turn reduces the image quality. Ennos[135] has reported that the contamination seen in the electron microscope is predominantly due to residual organic vapours within the microscope which is subsequently pinned on the substrate by the electron beam. Takahara et al.[136] have retrospectively fit an oxygen plasma device around the sample stage in their electron microscope in efforts to reduce carbon contamination to good effect. In Figure 2.4.11 the relatively higher background intensity seen in the center of the image is due to a previous high magnification scan which is used for focussing.

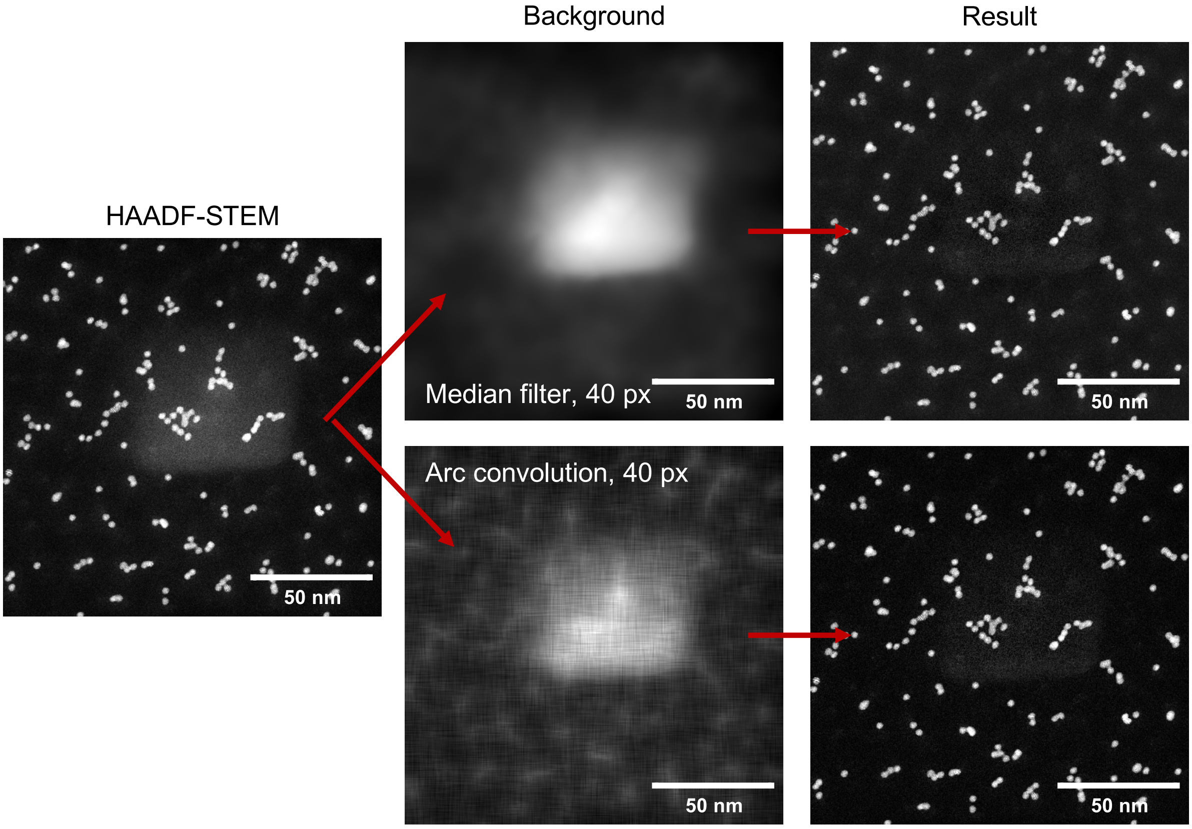

Figure 2.4.11: Background subtraction techniques. (left) 512 x 512 pixel HAADF-STEM image of Pt923 after oxygen plasma treatment showing higher background intensity in the center of the image as a result of contamination from a previous high magnification image. This image is then background subtracted using either a median filter (top row, 40 pixel square kernel) or arc convolution (bottom row, 40 pixel radius). 40 pixels in this case is equivalent to 12.3 nm which is much larger than the features in question. The calculated backgrounds (center) and resultant image (right) are shown in each case. Note that the intensity scales are not equivalent in each case.

Background contamination can lead to errors in image analysis and thresholding techniques are particularly affected. Two effective background subtraction techniques, median filtering and arc convolution, are presented in Figure 2.4.11. The result in both cases is a significant improvement in image quality in the center of the image which produces more accurate thresholding results. For reference calculation times for the median filter and arc convolution take 4.83 s and 16.3 ms respectively, making arc convolution more appropriate for batch processing and real-time applications.

The effect of background subtraction on thresholding and therefore the calculation of nanoparticle size is laid out in Figure 2.4.12. The difference map shows that the nanoparticle edges are more accurately reproduced by thresholding after background subtraction. A more thorough analysis reveals that the calculated threshold value is closer to the mean background intensity due to the removal of the contaminated areas.

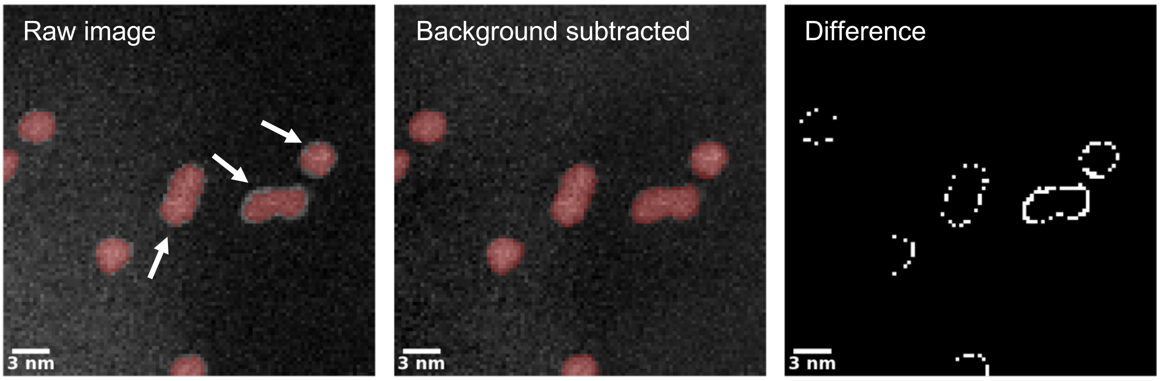

Figure 2.4.12: The effect of background subtraction on nanoparticle detection. Detected areas are overlaid in red. Thresholding was calculated with Otsu's median-adapted algorithm. (left) grains were calculated from the raw image (which had contamination as in Figure 2.4.11, visible on the left side of the image) and no image processing or background subtraction had been performed. White arrows indicate show the edges of the nanoparticles which have been incorrectly detected due to image contamination. (center) grains were calculated after background subtraction (arc convolution, 12.3 nm radius). (right) The difference map between the two methods of grain detection.

2.4.4 Feature segmentation

It is clear that thresholding is a useful technique to separate foreground and background data in these types of images. In the case of Pt_{923} cluster agglomeration, as shown in Figure 2.4.13, the nanoparticles can be seen to form chain-like structures by sintering at one common edge. In this case it is clear by eye to see that the chain-like structure is formed from three individual Pt_{923} singlets. Thresholding algorithms are able to resolve the chain-like structure in entirety, but in certain types of analyses, such as nearest neighbour distributions, it is useful to segment these larger structures into its constituents.

A watershed algorithm can be used for greyscale image segmentation; its implementation is such that 'water' is poured into 'basins' at pre-defined points, as the water level increases the basins fill up until the water effectively pours out of the basin. As the water level rises, the segmentation boundary is defined at the point where two separate water sources meet. An example of the result of this algorithm applied to Pt_{923} agglomerates is shown in Figure 2.4.13. In this case a Laplacian of Gaussian filter is used for 'blob' detection which works to detect foreground peaks in the image. The result is shown as red circles in Figure 2.4.13. This technique can find blob-like features in larger structures and is therefore well suited to the type of chain-like sintered structures exhibited by Pt_{923}. The blob centers are then used as basins (initial drop sites) for the watershed algorithm which produces a segmented result shown on the right in Figure 2.4.13. This example shows that image segmentation can accurately separate agglomerated branch-like nanoparticles into their constituents.

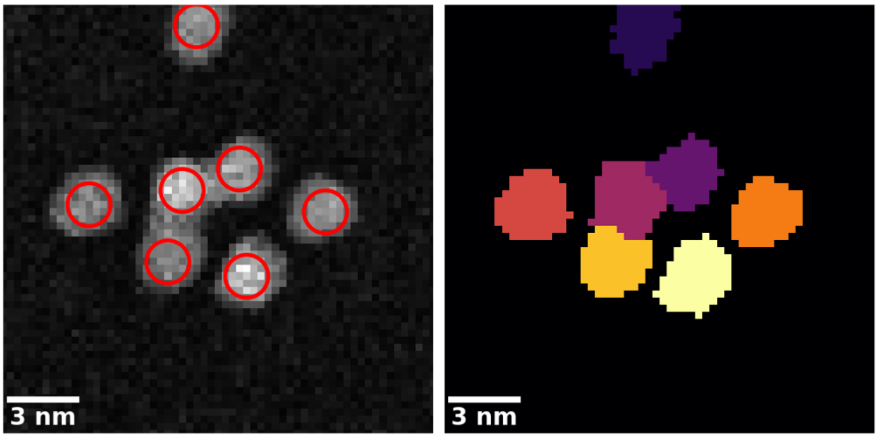

Figure 2.4.13: Segmentation of sintered Pt_{923}. (left) techniques such as blob detection can be used to detect nanoparticle locations in images even within agglomerated features. In this case a Laplacian of Gaussian detection algorithm was used, and the detected features are shown as red circles where the radius corresponds to σ of the detection, in this case $\sigma \approx 3$ pixels ≈ 1 nm. (left) boundaries within sintered nanoparticles can be estimated using segmentation. The original grain mask (see Figure 2.4.4) can be segmented using a watershed-type algorithm, with initial basin locations determined by blob detection, to calculate the approximate grain boundaries. Regions segmented to different nanoparticles are shown coloured here.

The segmentation analysis accuracy was benchmarked on many Pt_{923} sample images. Due to the predominantly 2D sintering observed between Pt_{923} clusters and the well-defined size of individual clusters, the number of clusters in an image is approximately equal to the ratio between the total projected area in the image and the projected area due to one cluster. This is equivalent to the expected number of clusters in an image. Figure 2.4.14 compares real raw data of Pt_{923} clusters (without segmentation) to the same segmented data. In the case shown here, which is analysed in detail in section 6.2.1, the as-deposited sample is over 80 % Pt_{923} singlets and so image segmentation does not have much of an effect on the number of individual detected nanoparticles. The number of Pt_{923} singlets decreases after oxygen plasma treatment at the expense of larger nanoparticles. Segmentation analysis shows that there is an increase in the number of detected nanoparticles in these cases, and the data after segmentation is clustered around the expected unity ratio. In almost all cases the number of measured nanoparticles is less than expected from the projected area analysis, and in the other cases the number measured is not significantly larger than expected and certainly within the accuracy of the analysis.

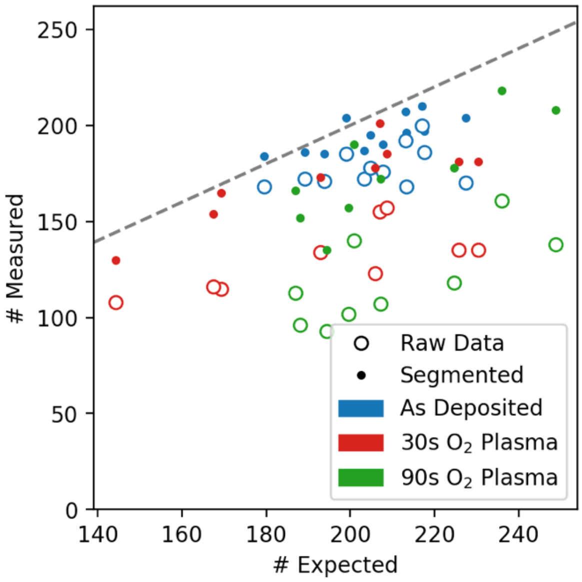

Figure 2.4.14: Segmentation analysis of real data. A comparison of the number of individual clusters measured without processing (open circles) and after segmentation (closed circles). Figure constructed from data shown in section 6.2.1. Grey dashed line represents the unity ratio for clarity.

2.4.5 Integrated Intensity

Images are inherently two-dimensional data. A TEM image is a measurement of the electron flux on the camera after the incident electrons have interacted with the specimen. In ADF-STEM the signal measured by the detector is proportional to the electron flux and therefore is proportional to the scattering cross-section of the specimen at every probe position. The pixel intensity is therefore dependent on the material and its thickness. In the case of elemental materials, such as pure platinum clusters, the pixel intensity is only dependent on the thickness of the material. The integrated HAADF intensity has been shown to scale linearly with cluster size for elemental clusters such as gold[101,137] and palladium[101]. This linear relationship has been tested up to an cluster size of approximately 6500 atoms[137] where dynamical electron scattering effects come into play.

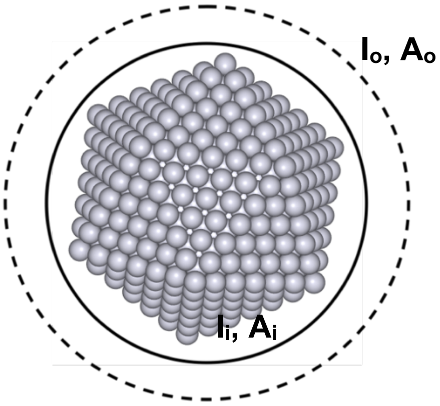

Figure 2.4.15: Schematic of integrated intensity analysis. The integrated intensity (I) is calculated within the ellipse aresa (A) of the inner (i, solid line) and outer (o, dashed line) ellipses.

An algorithm was developed in Python to analyse the integrated intensity of clusters. The integrated intensity contribution from a cluster can be calculated after subtracting the contribution from the local background. The schematic shown in Figure 2.4.15 demonstrates the principles of the algorithm which is outlined in Table 2.4.2. The integration boundaries for the cluster and local background are defined by the solid and dashed lines, denoted inner and outer respectively. The background contribution to the inner ellipse can be calculated as:

$$I_{BG} = A_i \cdot \frac{I_o - I_i}{A_o - A_i}, \qquad 2.4.12$$

such that the intensity contribution from the cluster is: $I_{CL} = I_i - I_{BG}$. The integrated intensity of materials containing N atoms with different atomic numbers Z are related by:

$$\frac{I_1}{I_0} = \frac{N_1}{N_0} \cdot \frac{Z_1}{Z_0}^{\alpha}, \qquad 2.4.13$$

where α is the Rutherford scattering exponent which should be calibrated at the required magnification[138].

An example of the working algorithm is shown in Figure 2.4.16. The features in a HAADF-STEM image are segmented into a mask, typically using a thresholding algorithm, and are then tidied by filling in any holes in the features and by removing small features such as noise. The mask is then labelled to separate distinct features. A watershed algorithm is performed to define the basin of each feature which is used to prevent overlapping of the ellipse boundaries. The algorithm prevents overlapping of the inner ellipses which would lead to erroneous results in the cases where features are in close proximity.

	Integrated Intensity Algorithm Inputs: image, labelled mask Outputs: integrated intensity values
1.	Perform watershed on labelled image to define feature basins
2.	Fit an ellipse to each feature and scale until the features are completely contained within their respective ellipse- inner ellipse
3.	Fit a second larger ellipse to each feature- outer ellipse
4.	Ensure the inner ellipse is located wholly within its watershed basin by removing pixels that do not satisfy this condition
5.	Allow overlap between outer ellipses but remove outer ellipse pixels that overlap with any inner ellipses
6.	Sum intensities within inner and outer ellipses in the image
7.	Calculate local background intensities by equation 2.4.12
8.	Subtract local background from inner ellipse intensity
9.	Scale intensities by real pixel size
10.	Return intensities

Table 2.4.2: Integrated intensity algorithm.

The integrated intensity is more robust to the accuracy of the mask than other descriptors such as projected area and mean radius. The integrated intensity is also a measure of the total nanoparticle volume compared to the projected area which is not able to discern a spherical from a hemispherical or plate-like structure.

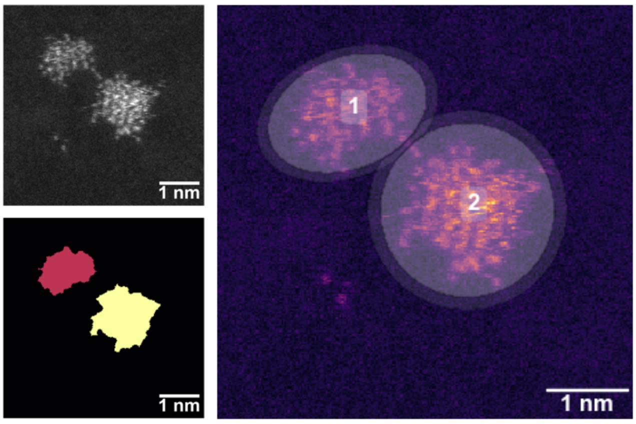

Figure 2.4.16: Integrated intensity analysis workflow. A HAADF-STEM image of two platinum clusters (top left) is segmented using the T-Point algorithm to give the feature mask (bottom left). (right) two ellipses are then fit to the edge pixels of each feature to give the inner and outer integration areas which are shown.

3 Magic-number mass-selected platinum clusters investigated by HAADF-STEM

Scanning transmission electron microscopy is a powerful tool for imaging of nanomaterials and is the primary technique used to study clusters in this thesis. In this chapter aberration-corrected HAADF-STEM is utilised to investigate mass-selected clusters at atomic resolution to study their structure. The effect of the electron beam, which is not benign, is also investigated, and techniques to measure cluster sizes are discussed.

3.1 Structures of mass-selected platinum clusters

The structures of platinum clusters can affect their catalytic performance. Platinum tetrahedra and octahedra are predicted to have superior oxygen reduction performance[139], clusters with (100) surfaces have been shown to have improved ammonia oxidation activities[140], and Pt(110) surfaces have been shown to be the most active for HER performance[141]. Mass-selected platinum clusters were synthesised for an investigation into the structure of well-defined catalytically relevant nanomaterials. Clusters were produced using a magnetron-sputtering gas-condensation cluster source, as described in section 2.1, and soft-landed onto amorphous carbon TEM grids at 1 eV per atom in an attempt to preserve cluster structure. The cluster densities were kept low at 2000 per square micron to limit sintering. An example low-magnification (1 million magnification) HAADF-STEM image which shows the sample morphology is shown in Figure 3.1.1.

The assignment of cluster structures was performed by comparing experimental images to simulated structures. Cluster structures can be simulated geometrically using the ASE software[142], and STEM images can be simulated using software such as QSTEM[143]. For these simulations, kinematic scattering[144,145] is a good approximation for electron scattering from thin materials less than ~50 atoms thick. In a kinematic model every electron is scattered once and the total scattering intensity is proportional to the number of atoms projected parallel to the beam direction, which is defined as *z* herein. The image of a structure may be simulated by considering a fine grid of coordinates (x, y) onto which the atomic positions are projected. Every atom in the model contributes to the intensity at point (x_j, y_j) such that:

$$I(x_j, y_j) = \sum_i I_{atom}(i), \qquad 3.1.1$$

and the intensity contribution from each atom I_{atom} is:

$$I_{atom}(i) = Z^n \cdot \exp(-\alpha d_i^2), \qquad 3.1.2$$

where Z is the atomic mass of each atom, n is the Rutherford scattering coefficient, and α is a Gaussian constant. n has a value of 2 for pure Rutherford scattering, although values of n between 1.2 and 1.8 have been measured[101,130] depending on the ADF collection angle. α has a value 0.55 which takes into account the width of the electron beam, as well as aberrations and defocus[145].

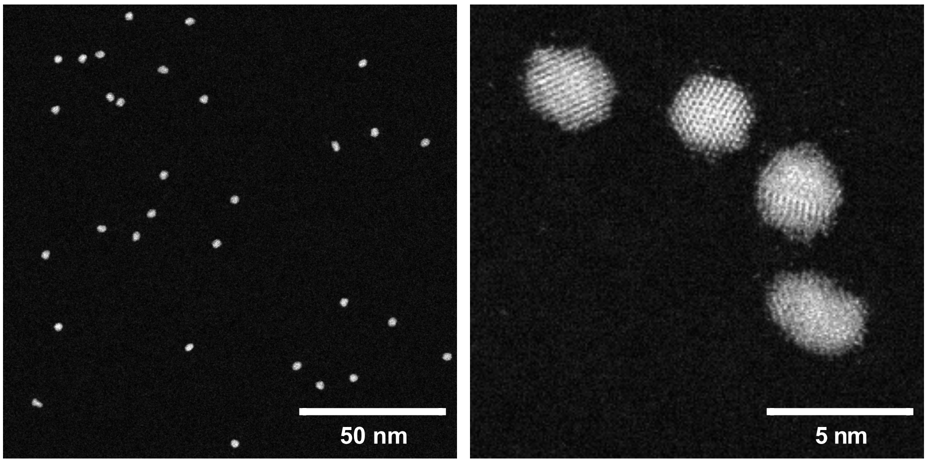

Figure 3.1.1: Pt_{923} mass-selected clusters soft-landed onto amorphous carbon TEM grids. (left) low-magnification sample morphology, and (right) high-magnification image detailing cluster structure.

The main advantage of kinematic simulation is that it is orders of magnitude less computationally intensive than multislice simulation techniques. In multislice the structure is sliced into cross sections and the electron beam interacts with the atomic potentials in the incident slice before propagating to the next slice. He et al.[144] have shown that the kinematic model is in good agreement with multislice simulations when applied to nanoparticles and metal oxides.

Multiple projections of the same structure relative to the electron beam are simulated to create a structure atlas which is used for identification. Structure atlases have been used previously to identify the structures of gold[42,146], platinum[58], and palladium[36] clusters. An example atlas for cuboctahedral Pt$_{923}$ is shown in Figure 3.1.2. Each simulation was produced using a grid 256 x 256 pixels with α=0.55 and the colour scaling is constant throughout the atlas. The simulated atomic model under no rotation is on the {100} zone-axis, and the resulting simulation is of a square lattice consistent with FCC {100}. As the lattice is rotated around θ or ϕ, which are both <100>, a hexagonal projection is exposed at the orientation where two {100} and two {111} faces meet on the cluster surface.

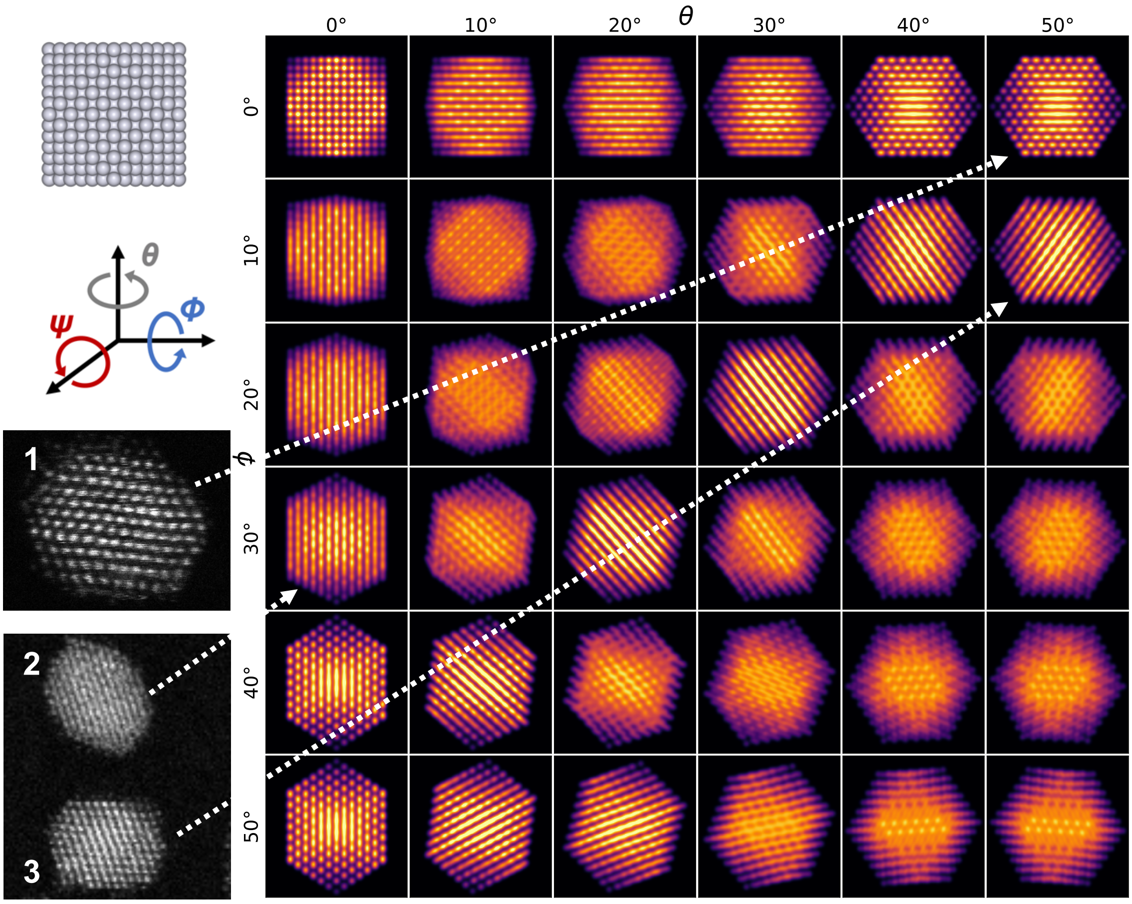

Figure 3.1.2: Simulated structure atlas for a Pt$_{923}$ cuboctahedron. ADF-STEM images are simulated using a kinematic model, as discussed in the text. A ball model of a 923-atom cuboctahedron is shown for clarity. Experimental HAADF-STEM images of Pt$_{923}$ clusters which can be identified using this atlas are shown.

Three examples of structural identification using the atlas are shown in Figure 3.1.2. Identification using an atlas is inherently subjective[42,58], however key features such as the arrangement of atoms and atomic planes can be identified in the HAADF-STEM images and identified in the atlas. Clusters 1 and 3 have a hexagonal motif which can be clearly identified. Cluster 2 has atomic plane spacings perpendicular to its long axis but does not exhibit atomic columns which suggests its orientation is off-axis. Structure atlases for cuboctahedral, truncated decahedral, and icosahedral structures were simulated and used to identify the imaged clusters. These geometric structures are commonly considered for small clusters[13,43,57,147]. In many cases a perfect match between a simulated and imaged structure could not be made, however there are discernible features between simulated structures that aid in identification. As an example, cuboctahedral structures commonly exhibit parallel lattice planes, as shown in Figure 3.1.2, which are not present in icosahedral or truncated decahedral structures. Likewise, icosahedral structures have unique ring-like features when imaged near their five-fold axis, an example of which is shown in Figure 3.1.3.

A range of mass-selected platinum cluster samples, Pt_N with N=55, 147, 309, 561, 923, 1415, were prepared to study the effect of cluster size on structure. These cluster sizes were chosen as they are geometric magic number sizes for shell-layered truncated decahedral, cuboctahedral, and icosahedral motifs[13]. All clusters were soft-landed onto amorphous carbon TEM grids and transferred through air to the electron microscope. High magnification HAADF-STEM imaging was performed to study the structure of these clusters and a selection of images are shown in Figure 3.1.3. High magnification imaging was performed using a 'one-shot' technique which has been used previously[42,58] to avoid beam-induced structural transformations which are more common at high magnifications due to possible heating effects[42], see Figure 3.1.4.

The overall trend in structure is increased crystallinity with increasing cluster size. At small cluster sizes the observed structures appear mostly amorphous. Pt_{55} clusters do not appear to have any consistent identifiable structure or geometry. A large fraction of the clusters are non-spherical and many individual atoms are visible on the surface suggesting that the atoms are only loosely bound to the clusters and frequently dissociate. Pt_{147} have more spherical geometries and exhibit 'ring-dot'[58] features which are indicative of icosahedral-like structures. A simulated icosahedral Pt_{147} cluster tilted 10° off its five-fold axis is shown Figure 3.1.3 for comparison. Whilst Pt_{147} exhibit icosahedral-like geometries the overall structure is not totally icosahedral. Blackmore[58] found similar ring-dot features in Pt_{147} clusters and suggested that the structures are better matched with twinned structures calculated by a genetic algorithm than purely geometrical structures.

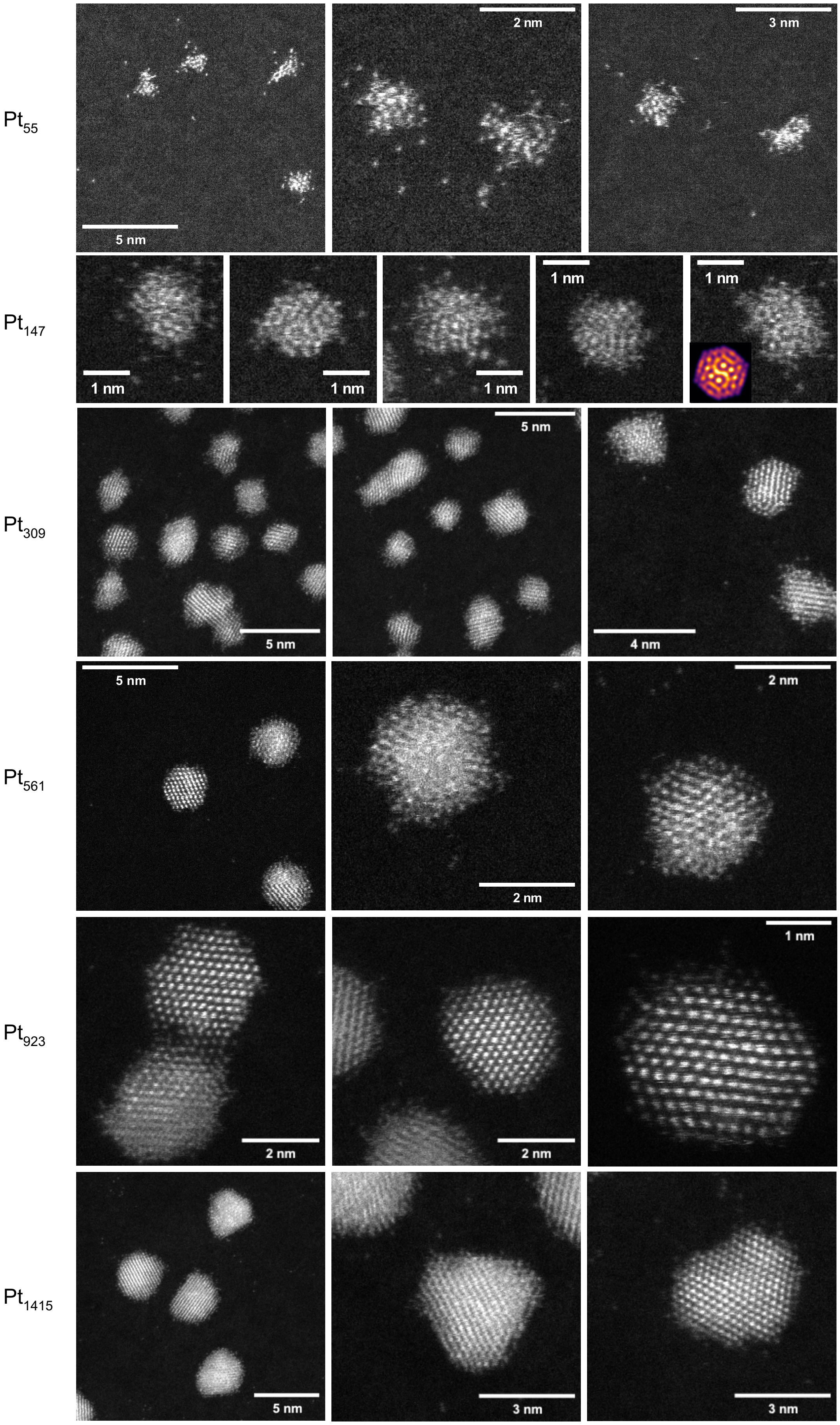

Figure 3.1.3: HAADF-STEM images of mass-selected platinum clusters soft-landed onto amorphous carbon films.

Pt_{309} clusters have predominantly cuboctahedral or FCC geometries, which can be identified with the atlas shown in Figure 3.1.2. Lattice plane features are clearly visible with 0.22 nm spacings which is consistent with Pt(111). Pt_{561} are also increasingly cuboctahedral in structure, which is consistent with the transition from higher energy structures to bulk structure as the cluster size increases. These results are in agreement with Blackmore[58] who also found increasing proportions of FCC structures with cluster size.

Pt_{923} and Pt_{1415} are almost completely crystalline with FCC structures. Pt_{923} structures are closely related to cuboctahedral structures whereas Pt_{1415} geometries have trigonal projections in many cases indicating a possibly tetrahedral structure. As both octahedrons and tetrahedrons can be cut from an FCC lattice these results show that platinum clusters have bulk-like structures at sizes greater than ~900 atoms under these synthesis conditions.

Baletto et al.[57] have considered the energetics of platinum clusters at different sizes through molecular dynamics simulations. They found that icosahedral geometries are only favoured at small sizes less than ~100 atoms. At larger sizes decahedral or FCC geometries are favoured, which is in agreement with the observed structures. Plant et al.[44] showed that Au_{923} clusters have increasing fractions of bulk-like structures at the expense of icosahedral structures when synthesised with longer relaxation times. The same cluster formation conditions were used in this study which may explain the bulk-like platinum structures observed.

Imaging clusters at high magnification under the electron beam is an invasive technique. The electron beam has been shown to induce structural transformations in clusters[42], aids the build-up of organic contamination[135], induce sintering in neighbouring nanoparticles[148], and has been used to manipulate and drag small clusters[149]. To test the effect of the electron beam the same area of a Pt_{55} sample was imaged continuously over multiple frames, shown in Figure 3.1.4. The cluster in the upper half of each image can be seen to restructure and lone surface atoms move between the frames. The two clusters in close proximity in the lower half of each image undergo sintering as a result of beam exposure. Over the course of one image the electron beam probe is rastered from the top left to the bottom corner where the fast and slow scan axes are horizontal and vertical, respectively. In Figure 3.1.5 atomic movement is visible as streaks in the image within one frame between lines in the slow scan direction.

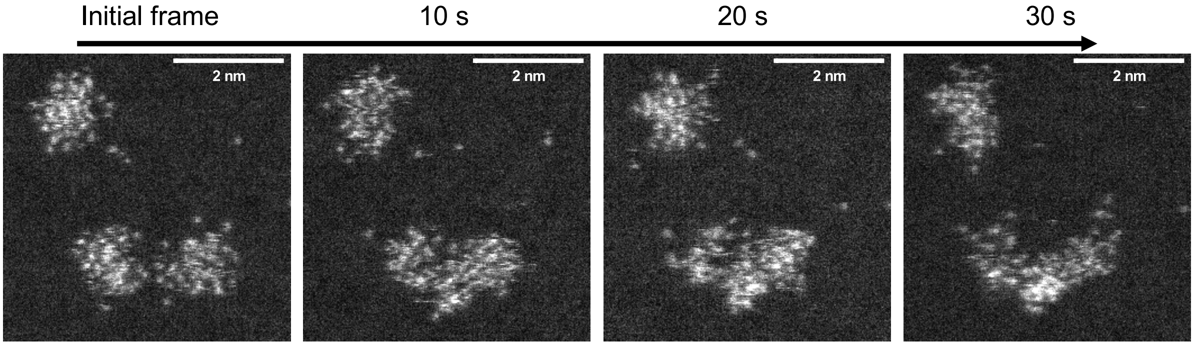

Figure 3.1.4: Stills from a video series of Pt$_{55}$ under the electron beam showing restructuring and agglomeration. Dose rate was 190000 electrons per square Angstrom per frame.

When clusters are in close proximity it is common to observe sintering under prolonged electron beam irradiation. Figure 3.1.6 shows images from a video series of Pt$_{923}$ clusters sintering under the electron beam. Initially the two clusters to the right of the frame are isolated, however a neck[79] begins to form between the clusters which grows under increasing beam exposure. During the initial stages of sintering the neck between two nanoparticles grows to reduce the chemical potential at the boundary[150], where mass transport to the neck can proceed by surface diffusion.

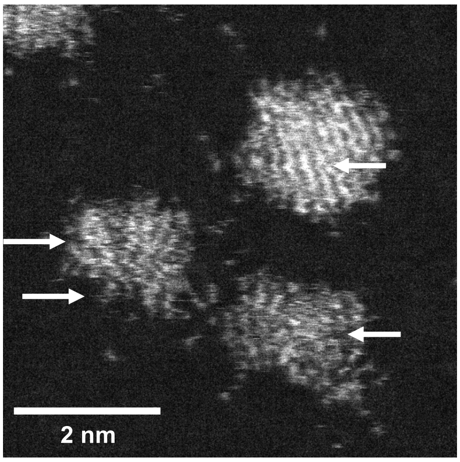

Figure 3.1.5: HAADF-STEM image of Pt$_{147}$ and agglomerate showing atomic movement and restructuring during scanning under the electron beam. Image taken at 25 million magnification. Dose rate was 520000 electrons per square Angstrom per frame.

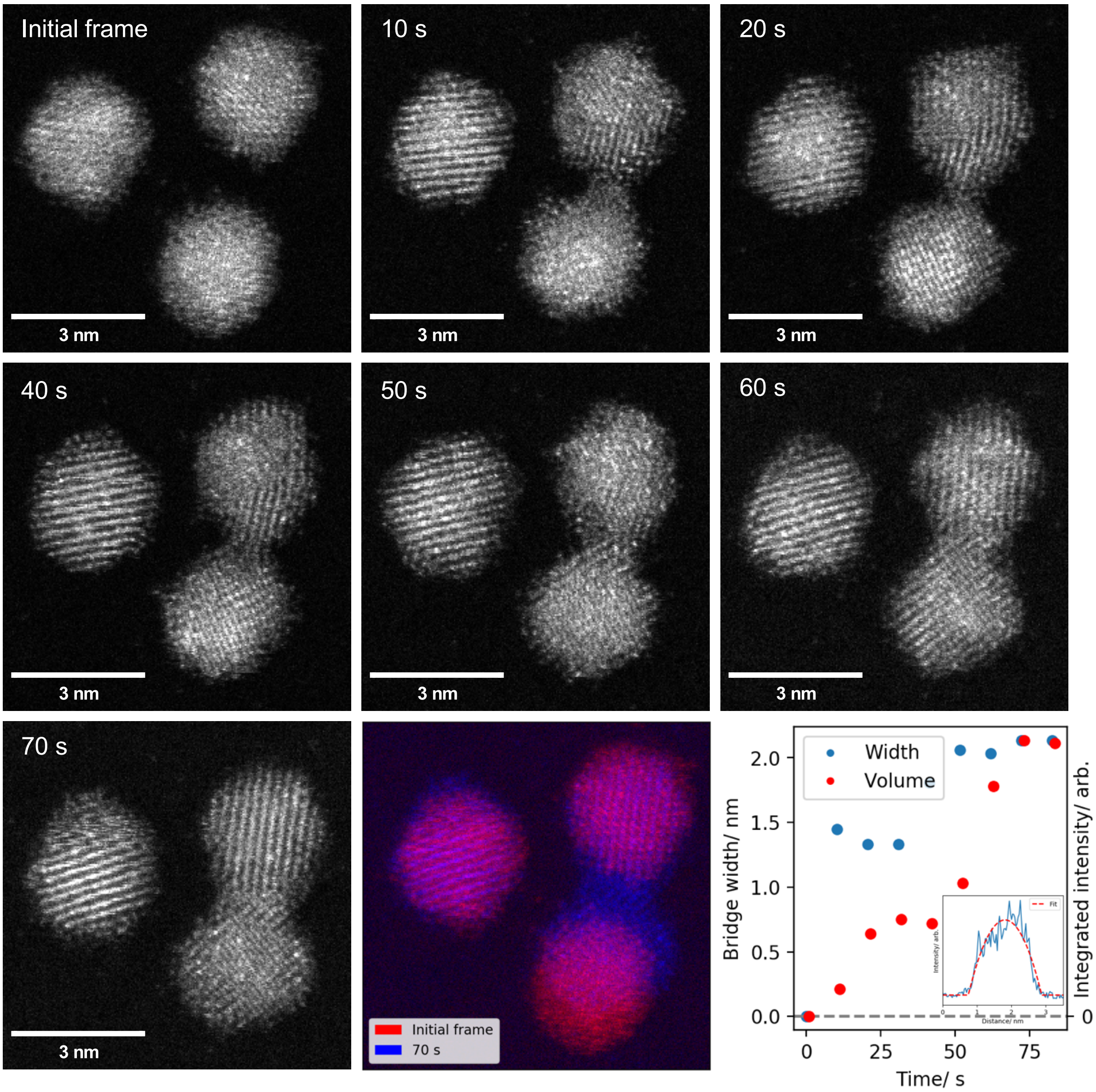

Figure 3.1.6: HAADF-STEM images from an image series of Pt$_{923}$ clusters showing sintering under the electron beam. Dose rate was 330000 electrons per square Angstrom per frame.

The neck width was estimated by fitting a parabolic step to the intensity line profile across the neck. The parabolic step is defined as a piecewise function:

$$f(x) = y_0 + \begin{cases} h \cdot \left(1 - \left(\frac{x - x_0}{w/2}\right)^2\right), & x_0 - {}^{w}\!/_{2} < x < x_0 + {}^{w}\!/_{2}, \\ 0, & otherwise \end{cases} \qquad 3.1.3$$

where y_o is the offset and h, x_o, and w are the step height, center, and width, respectively. The neck width and volume were measured as the total width of the parabolic step and the integrated HAADF intensity under the curve, respectively. The integrated HAADF intensity has been shown to be linear with the number of atoms under the assumption of kinematic scattering[137]. Figure 3.1.6 shows that whilst the neck width increases by only ~0.5 nm over the duration of the experiment, the neck volume increases more significantly. The rate of neck growth does not appear to be linear with time as expected sintering mediated by surface diffusion[150]. By overlaying the initial and final frame, shown in Figure 3.1.6, it is clear that sintering is initiated by the migration of the lower cluster in the frame towards the upper cluster and subsequent neck formation.

As two nanoparticles undergo sintering the neck region typically broadens due to mass transport from the nanoparticles. The dihedral angle ψ between the grain boundary at the neck and the cluster surface is related to system energies by[81,150]:

$$\gamma_g = 2\gamma_s cos\frac{\psi}{2}, \qquad 3.1.4$$

where γ_g is the grain boundary energy and γ_s is the surface energy. For bulk platinum $\gamma_g / \gamma_s = 0.29$[150], which is equivalent to an equilibrium dihedral angle of ψ = 163°.

To estimate the dihedral angle the sintered clusters were segmented using the method shown in Figure 2.4.13. The edges of each cluster were used as data points and fit to a circle by minimizing the sum of residuals J where:

$$J = \sum_i \left(\sqrt{(x_i - x_c)^2 + (y_i - y_c)^2} - r\right)^2. \qquad 3.1.5$$

In the above equation the fitted circle is described by its center (x_c, y_c) and its radius r, and each data point has coordinates (x_i, y_i).

The dihedral points used to define the dihedral angles ψ_1 and ψ_2 are calculated by one of two methods. In the first case the convex hull defining the edge points of each region are fit to a circle. The intersection points of these two circles defines the dihedral points. In the event where these circles do not intersect a second method is used. In this case the center line between the two fitted circles is used to define a perpendicular bisector. A line profile across this bisector is taken and fit to a parabolic step which defines the dihedral points. The dihedral angles are then calculated as angle between the dihedral points and the outward-facing tangents between each circle. A schematic depicting the geometric layout of the algorithm is shown in Figure 3.1.7. The maximal dihedral angle measured after 70 s beam exposure is ~130°, which is less than the expected equilibrium value, and is approximately constant after 40-50 s exposure. Previous studies[151] have found that the equilibrium dihedral angle may not be reached due to surface tension imbalances at the grain boundary or misaligned lattice planes.

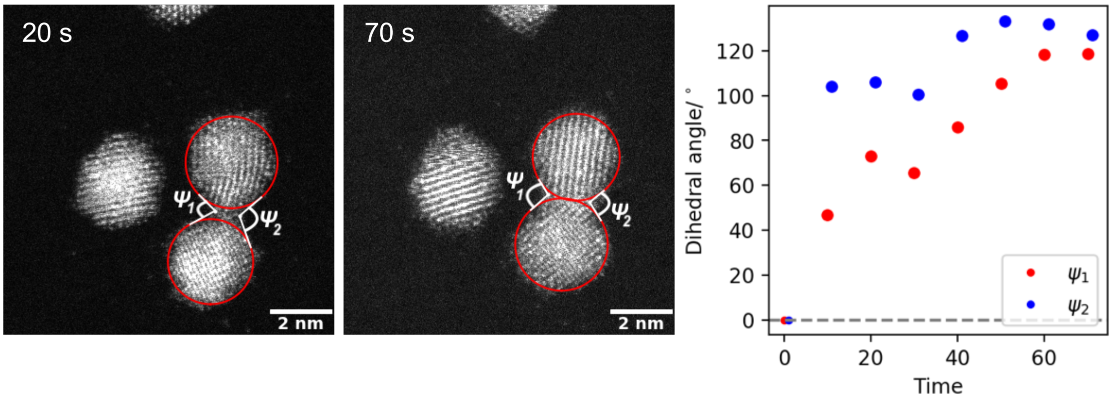

Figure 3.1.7: Estimation of the dihedral angle ψ during sintering of two Pt_{923} clusters. Two frames are shown from Figure 3.1.6: (left) 20 s and (center) 70 s of beam exposure. The cluster boundaries were fit to circles using least squares minimization (red circles). (right) analysis of all frames shows how the dihedral angle changes over time.

3.2 Measuring cluster sizes

As previously discussed, the size of a cluster can affect its electronic properties and catalytic performance. As such it is essential to accurately measure the size of nanoparticles and this is commonly achieved through image processing. In section 2.4 it was discussed how different size distributions may be produced from the same sample depending on the analysis performed. Automatic thresholding may be used to reduce human errors from manual analysis or discrepancies between users. Large atomic number clusters on thin amorphous carbon films appear bright against a dark background when imaged with ADF-STEM and are therefore easily thresholded. The thresholding result of three different algorithms is shown in Figure 3.2.1 where it can be seen that all algorithms produce different results. In all cases the center of each cluster, which contains the most intense pixels, is correctly segmented; the difference between each algorithm's threshold level manifests in the detection of lower intensity pixels around the cluster edges. From visual inspection it appears as though the threshold level calculated by Otsu's algorithm is set too high resulting in missing edges and also interior pixels. The T-Point threshold segments the clusters well and is less affected by the internal cluster structure such as atomic columns and lattice planes than the other methods. Otsu's median-adapted[124] algorithm performs well, however the segmented regions are still partially broken by internal cluster structure.

The effect of thresholding on Pt_{561} analysed at different imaging magnifications is shown in Figure 3.2.2. At each magnification HAADF-STEM images were analysed by each algorithm and a histogram was produced. The primary peak in each histogram is attributable to the as-deposited cluster size and the secondary peaks are due to agglomerated clusters. The peaks were fit with multiple gaussian distributions and the fit of the primary peak is plotted in Figure 3.2.2 where the error bars represent one standard deviation of the fit. The average cluster size calculated by the three different thresholding algorithms tested increases as Otsu's < Otsu's with median adaptation < T-Point in agreement with the arguments described previously. This trend arises from the thresholding result at the cluster boundary which is somewhat subjective. Analysis of the images shows that Otsu's algorithm tends to under-segment the clusters, whereas the T-Point algorithm potentially over-segments but is unaffected by fine internal structure.

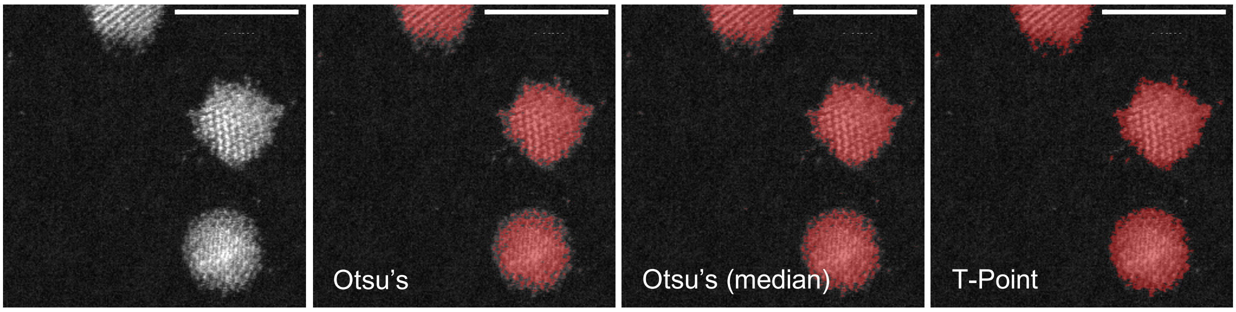

Figure 3.2.1: HAADF-STEM images of Pt_{561} clusters soft-landed onto amorphous carbon films taken at 8 million magnification. The regions thresholded by various algorithms are overlaid on each image in red. (from left) initial image, Otsu's threshold, Otsu's median-adapted threshold[124], and T-Point threshold. Scale bars are 4 nm.

At magnifications below 1 million it can be seen that the measured Pt_{561} size is larger than average for both Otsu's and the T-Point algorithms. At 800 thousand magnification each Pt_{561} cluster is described by ~40 pixels with a perimeter of ~20 pixels which is equivalent to a boundary to area fraction of ~0.5. At 3 million magnification the same clusters have a boundary to area fraction of ~0.15 due to the reduced pixel size. As shown in Figure 3.2.1 the discrepancy between thresholding algorithms is mostly localised to the cluster edges, and as such the thresholding result on any individual pixel has a larger effect on the overall size at lower magnifications. If the thresholding result on every pixel on the cluster boundary is to be considered subjective then it is better to minimize the boundary to area fraction to alleviate this uncertainty. Assuming clusters are perfect disks then the boundary to area fraction scales as $2/r$ where r is the disk radius and so the magnification should be increased to minimise perimeter errors. Above 2 million magnification the measured cluster areas remain mostly unchanged, at this magnification boundary to area fraction of Pt_{561} clusters is ~0.23.

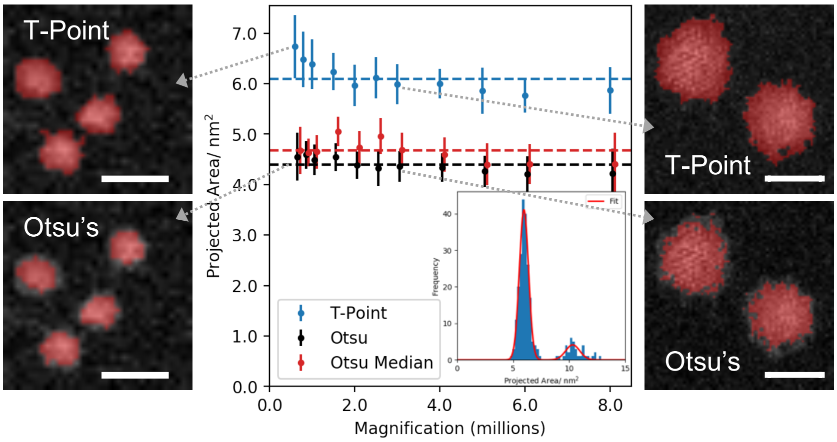

Figure 3.2.2: Projected area of Pt_{561} clusters at different imaging magnifications determined by different thresholding algorithms. Dashed lines are the mean projected area weighted by the inverse of each distribution's standard deviation. (inset) example size distribution and fit for size distribution at 2 million magnification. HAADF-STEM images and thresholded segments by Otsu's and T-Point methods are shown for the same clusters at 800 thousand (left) and 3 million magnification (right).

The sizes of mass-selected platinum clusters described in section 3.1 were measured using Otsu's median-adapted threshold. Figure 3.2.3 shows that the measured cluster sizes are in agreement with the projected areas expected by perfect spheres at bulk platinum density[152] of 21.45 g/cm^2. This finding is in agreement with previous studies[137] of soft-landed gas phase clusters which show that they retain spherical geometries on amorphous carbon films.

The projected area as a descriptor is commonly used in microscopy, however a nanoparticle's measured size is shown to be dependent on the algorithm and imaging magnification used. At low imaging magnifications increased statistics can be accrued, however there is a trade off with the uncertainty of the thresholding result at the cluster boundary. At higher magnifications the measured size is more accurate, however more images must be acquired at the expense of time for better statistics and beam induced transformation effects must be considered. The same thresholding algorithm should be used throughout analysis for consistency and automatic rather than manual thresholding aids in reducing human errors. A particular algorithm may produce unacceptable results depending on the morphology of the image, for example Otsu's algorithm will under-segment features when there are small amounts of brighter features[123] commonly observed in ADF-STEM when nanoparticles sinter. In any case the results obtained by automatic techniques are considered to be more consistent than manual techniques.

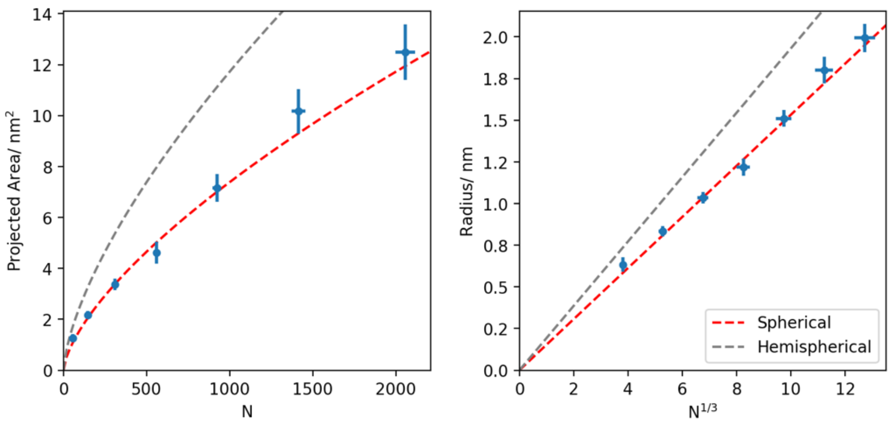

Figure 3.2.3: Comparison of sizes of mass-selected platinum clusters soft-landed onto amorphous carbon films. (left) projected areas as a function of number of atoms N and (right) equivalent radius. Red and grey dashed lines are the expected sizes for spherical and hemispherical clusters calculated at bulk density, respectively.

3.3 Clusters as mass calibration standards

Li et al.[101,137,138] have previously shown that gold and palladium clusters can be weighed using their integrated HAADF intensity, however a relationship has not been established for platinum clusters. The integrated intensity of different sizes of mass-selected platinum clusters was analysed at different imaging magnifications. For this study various microscope parameters were set and remained unchanged between samples and magnifications. The HAADF detector inner and outer collection angles were 62 and 164 mrad respectively and the detector brightness and gain were set at 2750 such that no clipping was observed in the image intensity histogram. Images were acquired at a resolution of 512 x 512 pixels with a pixel time of 38 µs. Imaging was performed over one continuous session to reduce any errors related to gun emission fluctuations or probe misalignment. The transmitted beam current measured on the phosphorous screen under imaging conditions was 3.3 pA/cm^2.

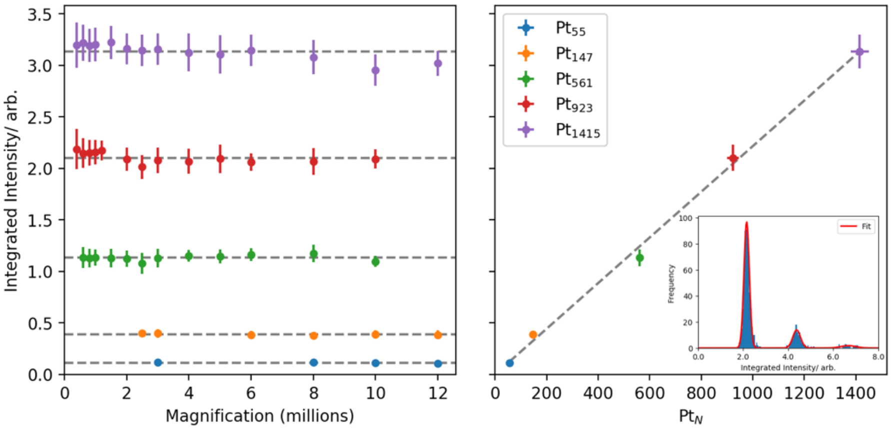

Figure 3.3.1: Integrated intensity analysis of mass-selected platinum clusters. (left) measured integrated intensity as a function magnification. Error bars represent one standard deviation. Grey dashed lines are the mean value for each cluster size weighted by the inverse of each distributions' standard deviation. (right) the relationship between cluster size and integrated intensity. Vertical and horizontal error bars are the standard error of the mean and derived from the mass resolution of the cluster source N/ΔN = 20, respectively. The grey dashed line is a linear regression of the data with an R^2 value of 0.998. Inset is an integrated intensity histogram of Pt_{923} at 1 million magnification with a multiple gaussian fit.

A histogram of all integrated intensities was produced for each cluster size at each magnification, an example of which is shown in Figure 3.3.1. The primary peak in each histogram is attributable to the as-deposited cluster size and secondary peaks are due to sintered clusters. The histogram is fit with multiple gaussians and the mean and standard deviation of the primary peak are used to describe the sample in each case.

The results in Figure 3.3.1 show that the integrated intensity for each cluster size is independent of imaging magnification, confirming that the integrated intensity is a robust descriptor for metal nanoparticles[153] which is unaffected by common changes in imaging conditions. The observed linear relationship between cluster size and integrated HAADF intensity confirms that mass-selected platinum clusters can be used as mass standards over the tested size range.

4 Electrochemical characterisation of mass-selected platinum clusters

One of the main research directions aiming to reduce platinum group metal usage is the principle that 'every atom counts'. As with heterogeneous catalysis only the surface atoms are able to act as binding sites, and so the subsurface atoms do not directly contribute to catalytic performance. Availability of all catalyst atoms can be achieved through both monolayer and dispersed monatomic catalysts. Nanoparticles containing subsurface atoms have a surface area to volume ratio that is less than unity, and this ratio decreases with increasing number of shells.

Typically, transmission electron microscopy is used to characterise nanoparticles at high resolution and from the images it is often possible to determine the nanoparticle structure and surface facets. However, such analysis is laborious and the number of nanoparticles imaged, let alone analysed, is typically in the hundreds compared the number of nanoparticles actually deposited, which is ~10^{12} for 10 percent coverage on a 3.05 mm TEM grid. This type of analysis therefore leads to a large extrapolation from the few nanoparticles studied to all of those deposited on the sample. By contrast electrochemical studies are macroscopic in scale, in that the whole sample is studied simultaneously, but the energetics are defined by interactions at the nanoscale.

Mass-selected clusters represent a class of well-defined materials which can be used to gain insights into more fundamental processes[18]. Small clusters can exhibit vastly different catalytic properties with the addition of just one atom[62,154,155]. Previous work has shown that platinum clusters with more than ~300 atoms are predominantly octahedral when investigated with TEM[58]. Here, mass-selected clusters supported on graphite are characterised electrochemically to compare the structures of individual clusters with their bulk electrochemical response.

4.1 Electrochemical characterisation of mass-selected platinum clusters deposited onto HOPG

The interaction between platinum and carbon is of particular interest in the field of fuel cells, particularly PEM fuel cells. Current research in this field involved increasing catalytic performance and stability, and there have been many research efforts into both of these feats[53,156–158]. Graphite is a common support material in nanotechnology as it is stable in air, conductive, can be prepared easily, and, importantly, is cheap. Carbon sp^2 materials such as graphite have attracted significant research interest since graphene became the subject of the Nobel Prize in Physics in 2010[159], and carbon nanotube based materials have since found uses in medicine[160].

Mass-selected platinum clusters were produced with the cluster source described in section 2.1. The clusters were soft landed with kinetic energy of 1 eV per atom onto HOPG which had been pre-sputtered with 500 eV argon ions to create pinning centers on the graphite basal plane. Platinum clusters were deposited with a number density of 25000 per square micron, which is equivalent to 20% surface coverage for Pt_{923}. The argon defect to cluster ratio was 10:1 ensuring many more defects than clusters in an attempt to prevent cluster migration and sintering. In this case the substrate may be more comparable to activated carbon than pristine graphite. The electrochemical experimental setup and apparatus is discussed in section 2.3.1.

4.1.1 CVs of Pt_{561} and Pt_{923}

CVs of Pt_{561} and Pt_{923} clusters are shown in Figure 4.1.1. Each sample was first cycled between the onset of hydrogen evolution, 0 V vs RHE, at the cathodic end, and the onset of platinum oxidation, 0.95 V vs RHE, at the anodic end of the cycle and the CV responses are shown in blue in Figure 4.1.1. The CVs show predominantly capacitive response, due to the electrochemical double-layer, in all regions greater than 0.2 V vs RHE. In the region 0–0.2 V vs RHE there is an increase in current, which can be attributed to hydrogen ion adsorption and desorption, the so-called hydrogen under potential deposition (HUPD) region.

The HUPD region for both cluster samples is undefined indicating that the platinum clusters are mostly amorphous at this stage.

The anodic limit was then increased to 1.20 V vs RHE, an intermediate oxidative potential, and CVs were recorded until the response was stable (red curves). The HUPD area of Pt$_{561}$ increases and defined peaks at 0.08 and 0.17 V vs RHE are now visible in the anodic sweep; these peaks are consistent with desorption of hydrogen Pt(110) and Pt(100) planes respectively[161]. Equivalent hydrogen adsorption peaks are visible in the cathodic sweep at the same potentials, as this reaction is reversible. At higher anodic potentials, above 0.8 V vs RHE, there is an increase in current due to oxygen adsorption and subsequent platinum oxidation. As the sweep is reversed a broad peak at 0.71 V vs RHE is measured in the cathodic sweep due to platinum reduction, or oxide stripping.

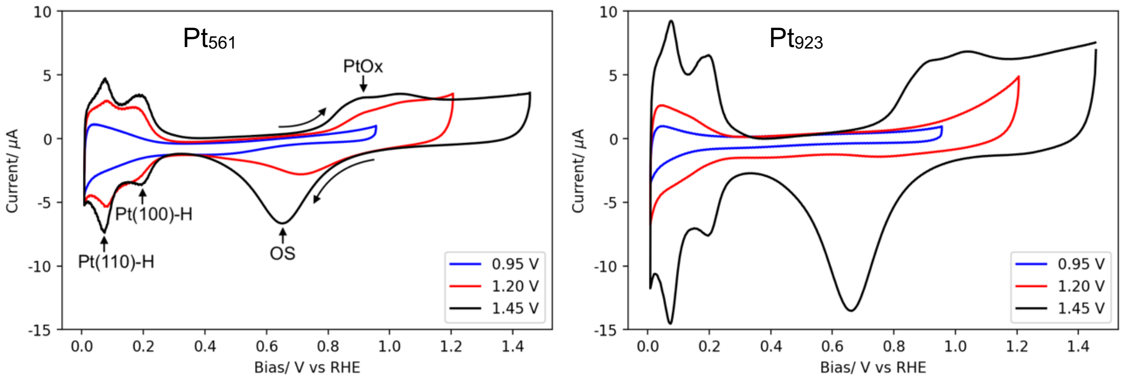

Figure 4.1.1: CVs of Pt$_{561}$ (left) and Pt$_{923}$ (right) on argon-sputtered HOPG in 0.5 M H_2SO_4 with different anodic potential limits. Each sample was subjected to potential conditioning in turn to anodic limits of 0.95, 1.20, and finally 1.45 V vs RHE, in increasing order. The labelled peaks are attributed to platinum oxidation (PtO$_x$), platinum reduction (or oxide stripping, OS), and the adsorption of hydrogen ions onto different platinum surface sites (Pt(100)-H and Pt(110)-H), which have corresponding desorption peaks at the same potentials in the anodic sweep. Black arrows indicate the sweep direction. Sweep rate was 0.5 Vs^{-1} in all cases.

Equivalent CVs on the Pt$_{923}$ sample also show an increase in HUPD surface area, however the HUPD region does not show signs of specific faceting like the Pt$_{561}$ sample, suggesting that the Pt$_{923}$ samples remain somewhat amorphous. The oxidation region, at potentials greater than 0.8 V vs RHE, is also not well formed as there is only a small current attributable to oxide formation and stripping. It is known that oxide formation on platinum leads to surface restructuring[162,163], and so the lack of well-defined surfaces in the HUPD region could be due to the lack of oxide formation and subsequent restructuring. It is more likely however that the Pt_{923} sample is relatively more contaminated, or that any trace contaminants are more strongly bound, such that less platinum surface atoms are exposed to the electrolyte. This would explain the lack of HUPD definition and the small increase in currents from oxygen and hydrogen adsorption.

As the anodic limit was further increased to 1.45 V vs RHE the HUPD area of both Pt_{561} and Pt_{923} samples increases and the peaks become more defined, suggesting that more platinum surface area is available for adsorption and these surfaces exhibit larger (100) and (110) fractions. The total charge transfer was calculated by integrating the charge under the HUPD region whilst subtracting the capacitive contribution from the double-layer region as discussed in section 1.4.1:

$$Q = \frac{1}{\frac{dV}{dt}} \cdot \int_{V_{min}}^{V_{max}} IdV, \qquad 4.1.1$$

where Q is the charge, dV/dt is the sweep rate, I is the measured current, and V is the potential. The HUPD region was evaluated between V_{min} = 0 V, and V_{max} = 0.30 V vs RHE, and the double-layer capacitive contribution was evaluated between V_{min} = 0.325 V, and V_{max} = 0.375 V vs RHE and assumed constant over the potential range of the experiment. The charge transferred by a monolayer deposition of hydrogen ions onto a platinum surface can be calculated geometrically, and is equivalent to 210 $\mu C/cm^2$ [164]. The calculated surface area and capacitive contributions for both Pt_{561} and Pt_{923} are shown in Figure 4.1.2. For both Pt_{561} and Pt_{923} the electrocatalytic surface area increases with anodic limit, however the largest surface area increase for Pt_{561} is seen as the anodic limit is raised to 1.20 V vs RHE, compared with 1.45 V vs RHE for Pt_{923}, which may be indicative of different amounts of trace contamination within the cells or that the contaminants are more strongly bound to Pt_{923}. Given that the radius of Pt_{561} is 1.22 nm as measured by STEM imaging, and the sample coverage is 20% on an exposed area of 1.5 mm radius, the total platinum surface area is expected to be 1.0 mm^2. Equivalent arguments for Pt_{923}, with a measured radius of 1.51 nm, the total platinum surface area is 1.5 mm^2. These calculated surface areas agree with the measured surface areas within 25%, but only after potential conditioning to 1.45 V vs RHE. The anodic potential limit was not increased further due to the onset of the oxygen evolution reaction at potentials larger than 1.45 V vs RHE.

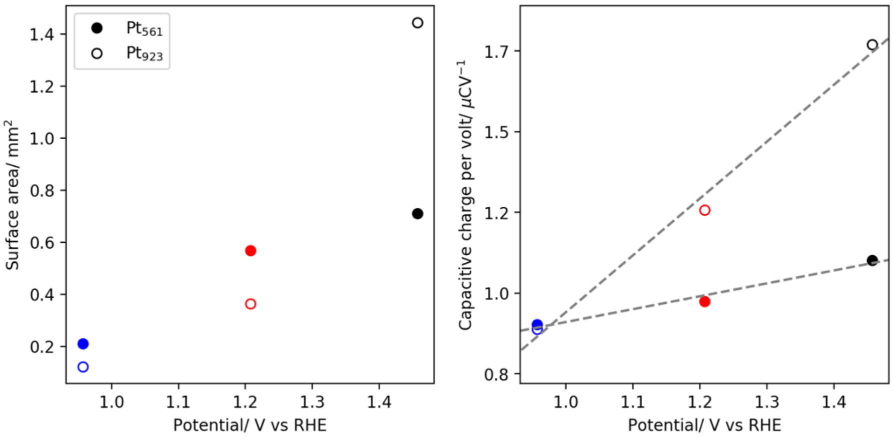

Figure 4.1.2: Measured surface area from HUPD measurements (left) and capacitance (right) values for Pt_{561} (closed points) and Pt_{923} (open points) after potential conditioning to different anodic limits. Grey dashed lines are linear trends to guide the eye.

4.1.2 CV evolution

From Figure 4.1.1 it is clear that potential conditioning is changing the sample morphology from the measured electrochemical response. As the anodic limit is increased the sample is being perturbed from its previously stable state, so the question remains as to at which point the sample reaches its equilibrium state.

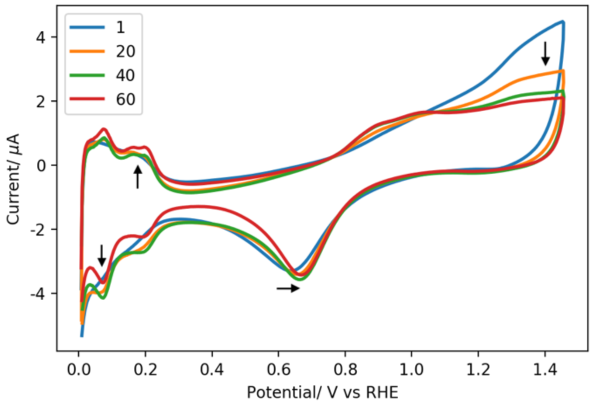

Figure 4.1.3: CV evolution of Pt_{923} sample as anodic limit was increased to 1.45 V vs RHE. Selected CVs are shown: 1st (blue), 20th (orange), 40th (green), and 60th (red). The first CV represents the first time the sample had seen potentials higher than 1.20 V vs RHE. Black arrows show the evolution trends as the cycle number was increased. Sweep rate was 0.1 Vs^{-1}.

An example of the dynamic evolution of Pt_{923} is shown in Figure 4.1.3 as the anodic limit was increased from 1.20 to 1.45 V vs RHE, where the blue curve represents the first time the sample had been exposed to potentials greater than 1.20 V vs RHE. The sample shows significant change, especially in the HUPD region, between the first and 60th CV. The HUPD region becomes significantly more defined after 40 CVs.

To quantify the sample evolution shown in Figure 4.1.3 the electrochemical surface area, as measured from the HUPD region, capacitive charge, and oxide stripping potential were measured as a function of sweep number, as shown in Figure 4.1.4. Over the course of 60 CVs to 1.45 V vs RHE the electrochemical surface area increases by approximately 20%, whilst the double-layer capacitive contribution decreases by almost 50%. The increase in HUPD surface area is indicative of a cleaning mechanism which creates more platinum availability for hydrogen adsorption. The reduction of double-layer capacitance has been observed in other size-dependent studies[165] and is consistent with increasing particle size and therefore reduction in overall surface area. The oxide stripping potential shifts 30 mV towards smaller overpotentials indicating that the oxide species formed by the potential conditioning have become easier to remove.

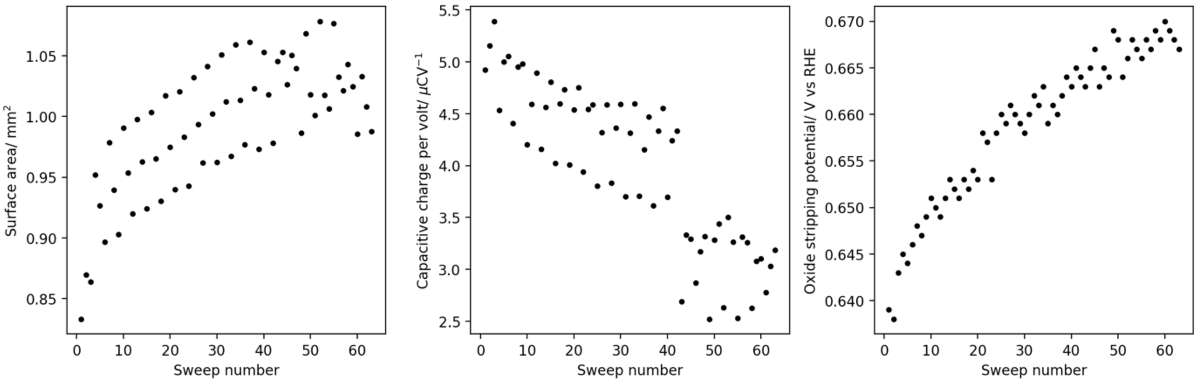

Figure 4.1.4: Changes in Pt$_{923}$ CV response with sweep rate as the anodic limit is increased to 1.45 V vs RHE. (left) electrochemical surface area as calculated using the HUPD region, (center) change in double-layer capacitive contribution, and (right) oxide stripping potential.

4.1.3 CO stripping analysis

CO stripping analysis on platinum surfaces is a useful technique which allows for the characterisation of platinum electrochemical surface area surface structure, on both extended surfaces and nanoparticles. It has been proposed that CO oxidation on platinum surfaces follows the Langmuir-Hinshelwood mechanism[166]:

$$Pt + H_2O \rightarrow Pt - OH_{ads} + H^+_{aq} + e^- \qquad 4.1.2$$

$$Pt - CO_{chem} + Pt - OH_{ads} \rightarrow Pt + CO_2 + H^+_{aq} + e^- \qquad 4.1.3$$

which follows a two-electron transfer process.

After electrochemical conditioning to 1.20 V vs RHE and 1.45 V vs RHE, the electrolyte was saturated with CO gas for 20 minutes whilst holding the WE potential at 0.05 V vs RHE. CO adsorbs strongly to platinum and can often displace surface contaminants[167], so will displace the weakly adsorbed hydrogen covering the platinum surface at the applied potential. After saturating with CO gas the electrolyte was then purged with nitrogen gas to displace any dissolved CO. CVs were then performed between 0.1 V vs RHE, initially sweeping in the cathodic direction, to 1.45 V vs RHE. The resulting CO stripping CVs of the Pt_{923} sample, after potential conditioning to 1.25 and 1.45 V vs RHE, are shown in Figure 4.1.5. In both cases this sweep shows no platinum HUPD region, which is consistent with all platinum surface sites being occupied with CO. The double-layer capacitive contribution is also significantly reduced. As the sample potential is increased above 0.7 V vs RHE there is a large increase in current which is consistent with CO stripping, or CO oxidation.

After potential conditioning to 1.20 V vs RHE the CO stripping potential was measured to be 0.89 V vs RHE. The same experiment performed after potential conditioning to 1.45 V vs RHE shows a peak shift of 60 mV to lower overpotentials, and also the development of a 'pre-peak' at 0.70 V vs RHE. In studies performed on size-controlled nanoparticles, albeit with less size-control compared to this study, the pre-peak has been attributed to defects in well-ordered domains in CO stripping studies on shaped platinum nanoparticles[166]. In another study[165] comparing the nanoparticle size-effect with CO oxidation it has been suggested that the rate of CO oxidation is limited by hydroxyl anion adsorption onto platinum surfaces. In this study the cluster density is much less than a monolayer, however the effect of potential conditioning is yet unknown on these samples, and it is certainly possible that larger domains are formed through nanoparticle ripening that could lead to the formation of defects from more well-defined cuboctahedrons.

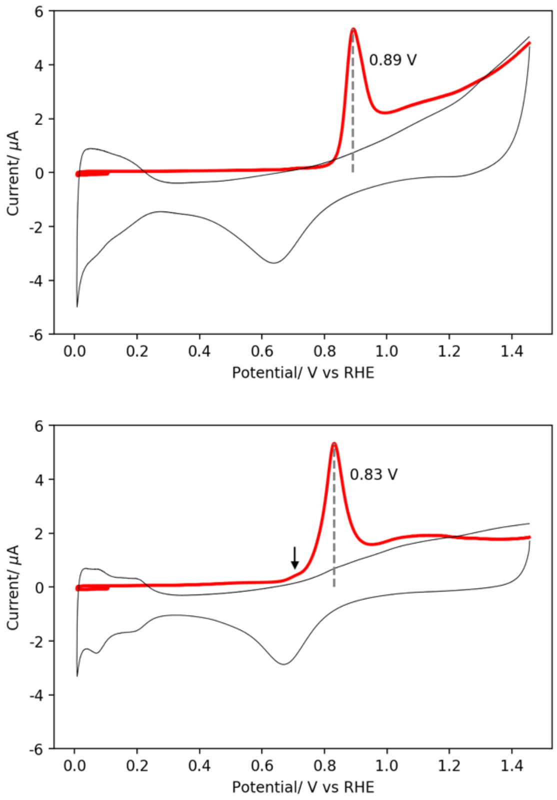

Figure 4.1.5: CO stripping voltammetries of Pt_{923} after potential conditioning up to an anodic limit of 1.20 V vs RHE (left) and 1.45 V vs RHE (right). CO strip is plotted in red and subsequent CV is plotted in black. The vertical dashed lines indicate the CO stripping peak potential, and the black arrow indicates the CO stripping pre-peak.

The platinum surface area can be calculated from the integrated charge transferred by CO oxidation. As CO oxidation is a two electron process the charge transferred per surface atom on Pt(111) is 420 μC/cm^2 [168]. The charge attributed to CO oxidation was integrated between 0.6 and 1.0 V vs RHE, and the background charge, calculated between the same potential limits, from the subsequent baseline CV was subtracted. A summary of the measured surface areas from both CO stripping and HUPD techniques is presented in Table 4.1.1. In all cases the measured surface area is less than the theoretically deposited 1.57 mm^2. For the CO stripping experiments the measured surface area is less dependent on the samples previous potential conditioning than the HUPD measurement. As CO can displace contaminants on platinum surfaces which would block hydrogen adsorption[164], this result also indicates a contamination effect. In fact previous studies have suggested that maximum achievable CO coverage on platinum surfaces is around 0.7 monolayers[164]; in this case the charge transferred during CO oxidation is equivalent to 70% of the total platinum surface area and the adjusted electrochemical surface areas as determined by CO stripping are more similar to the theoretical values, and also to the HUPD value in the case of post-potential conditioning to 1.45 V vs RHE.

	Surface Area (mm^2)		
	HUPD	CO stripping (0.7 L)	Spherical
1.20 V vs RHE	0.36	0.87 (1.24)	1.57
1.45 V vs RHE	1.44	1.07 (1.53)	1.57

Table 4.1.1: Calculated surface areas of Pt_{923} *clusters from the HUPD region and CO stripping peak. The spherical surface area presented theoretically calculated from the number of deposited clusters as described in 4.1.1. For CO stripping measurements the adjusted calculated platinum surface areas for 0.7 L of CO coverage are given in brackets.*

4.1.4 Reversibility of potential conditioning

In 4.1.1 it was shown how the anodic limit affected the CV response, and therefore nanoparticle structure, of Pt_{923}, and in 4.1.2 the time scale of the restructuring was laid out. The question still remains as to the reversibility of potential cycling.

After performing successive potential conditioning experiments laid out in 4.1.1, CVs were recorded as the anodic limit was reduced, and the steady-state CVs are shown in Figure 4.1.6. By comparison to Figure 4.1.1 it can be seen that CVs with lower anodic limits retain resolved HUPD peaks at 0.07 and 0.20 V vs RHE attributed to hydrogen adsorption and desorption from Pt(110) and Pt(100) sites respectively. The total surface area, as measured by the charge transferred during HUPD, gradually decreased with sweep number and the rate was more pronounced as the anodic limit was decreased, as shown in Figure 4.1.7. The reduction of platinum surface area is indicative of a recontamination effect, however the surface areas measured are still larger for lower anodic limits than measured before potential conditioning (see Figure 4.1.2). The oxide stripping peak overpotential was decreased from 0.67 to 0.73 V vs RHE as the anodic limit was reduced from 1.45 to 1.20 V vs RHE, and the peak potential was unchanged with the total number of sweeps to both anodic limits indicating that platinum oxide formation and reduction had reached an equilibrium by this time.

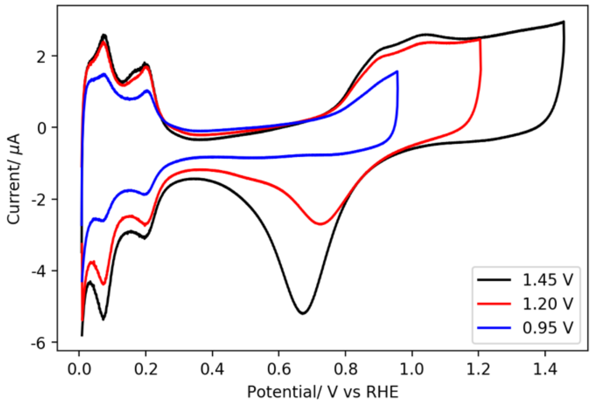

Figure 4.1.6: CVs of Pt_{923} sample after potential conditioning to 1.45 V vs RHE. CVs were recorded as the anodic limit was reduced from 1.45 to 1.20 to 0.95 V vs RHE to see test the reversibility of the performed potential conditioning. Scan rate was 0.2 Vs^{-1} in all cases.

The discussed contamination is likely in the form of trace organics introduced from the experimental procedure. The cluster samples were prepared under vacuum but were transported through atmosphere before testing. It is possible that contaminants were introduced through glassware or the prepared solution despite large efforts to minimise this possibility. The electrochemical characterisation of mass-selected platinum clusters has raised more questions than it has answered. The peaks in HUPD peaks observed for both Pt_{561} and Pt_{923} are consistent with (100) and (110) facets, both of which are found on truncated octahedral structures which have been observed previously for these clusters[58] and discussed in the previous chapter. The potential cycling and CO stripping experiments have indicated a dynamic system that is perturbed by the anodic limit, but the actual form of this change can only be inferred without direct observation. It is also noted that the recorded CVs exhibit an ohmic drop consistent with a significant resistance across WE. This possibly originates from the unconventional electrochemical cell setup to avoid the use of soluble pastes, or that graphite has low electrical conductance in the direction normal to the basal plane[169].

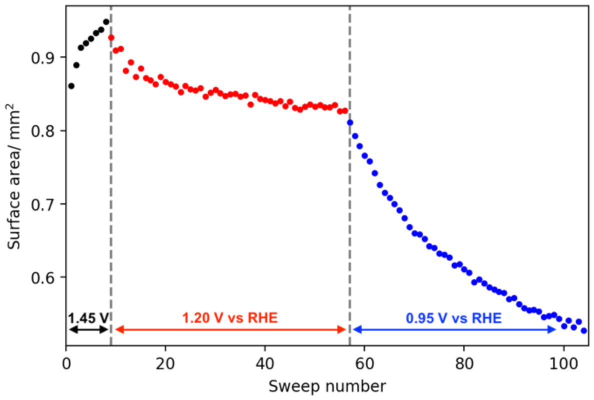

Figure 4.1.7: HUPD surface area of Pt_{923} sample as the anodic limit was decreased.

4.2 HER performance of mass-selected Pt clusters on glassy carbon supports

To build on the information provided by the electrochemical characterisation of platinum clusters on graphite, and to alleviate any problems associated with poor conductivity across the working electrode, mass-selected platinum clusters were deposited onto glassy carbon substrates for electrochemical characterisation. GC is an amorphous carbon material and is a well-used support material for electrochemical applications due to its good electrical conductivity and corrosion resistance[170]. The GC working surface is typically conditioned before use by polishing to a mirror-finish.

Pt_N clusters were synthesised with N=147, 309, 561, 923, 1415, and 2057 atoms to explore the size-effect on hydrogen evolution reaction performance. Pt_N clusters were soft-landed with 1 eV per atom or less onto polished GC stubs. The samples were characterised in argon saturated 0.5 M H_2SO_4. The HER performance of each sample was tested as a function of the anodic limit of previously performed potential conditioning and the experimental protocol is outlined in Figure 4.2.1. The samples were subjected to potential cycling between the onset of hydrogen evolution at 0.05 V vs RHE and a set anodic potential. The HER performance and electrochemical characterisation of each sample are therefore a function of the samples' history of potential conditioning.

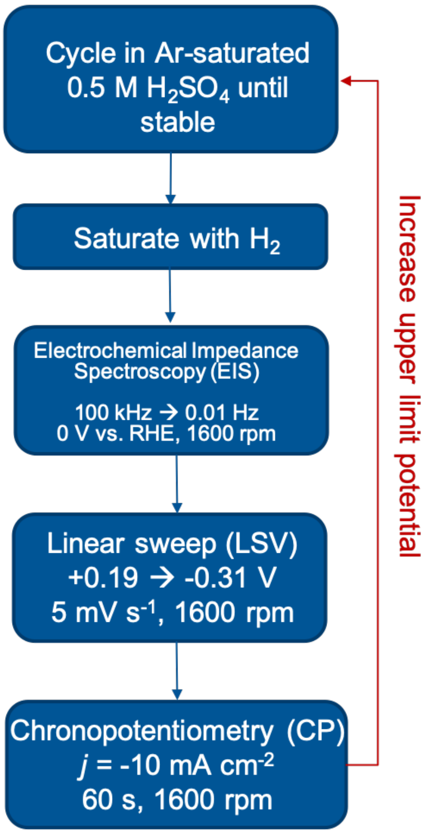

Figure 4.2.1: Experimental protocol to test the short-term HER performance of catalysts. Figure reproduced from work by J Humphrey and A J Wain at NPL.

Figure 4.2.2 shows the how the CV response and HER performance develops with maximum anodic limit for Pt_{1415} clusters, and similar responses were measured for all platinum clusters studied. Initially the sample is characterised with CVs between 0.05 and 0.50 V vs RHE (red curve). The CV response is dominated by double-layer which is the same behaviour found in the study on HOPG. HER performance at this point in the sample's development generates 10 mAcm^{-2} at 200 mV overpotential based on an equilibrium standard potential of 0 V vs RHE. The sample is conditioned up to 1.1 V vs RHE without significant change in CV response or HER performance.

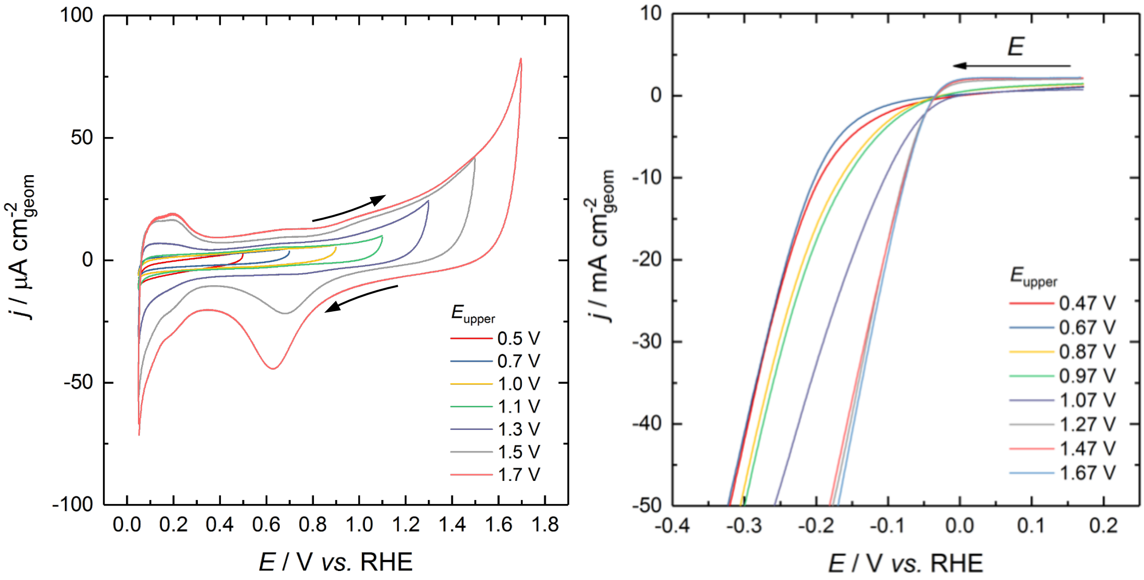

Figure 4.2.2: CV response and HER LSV of Pt_{1415} clusters in 0.5 M H_2SO_4. (left) CV response in argon saturated electrolyte, black arrows represent the sweep direction. HUPD region is clearly visible between 0.05 and 0.30 V vs RHE in the CVs performed with anodic limits greater than 1.3 V vs RHE (purple, grey, and orange curves). Oxide stripping peak is observed in the cathodic sweep around 0.7 V vs RHE for CVs performed with anodic limit greater than 1.5 V vs RHE. The onset of oxygen evolution is seen around 1.7 V vs RHE. (right) HER LSV sweeps after sample CV response had been stabilised at different maximum anodic limits. The black arrow represents the sweep direction. Experiments performed and figures produced by J Humphrey and A J Wain at NPL.

As the anodic limit is further increased to 1.3 V vs RHE, a small shoulder becomes visible around 1.1 V vs RHE which is consistent with oxygen adsorption and the adsorption of hydroxyl species. This is accompanied by increased HUPD response and larger electrochemical capacitance, both of which can be attributed to a larger electrochemical surface area, either consistent with removal of contamination or possibly surface roughening through platinum oxidation[162]. The lack of HUPD response prior to this point in the sample's development suggests that the removal of organic contamination is a likely factor, as even monatomic hydrogen will have HUPD response[171] and its absence prior to this point is evidence that the exposed platinum surface sites are unavailable for adsorption or 'poisoned'.

The HER performance plateaus as the anodic limit is increased beyond 1.3 V vs RHE, however the CV response continues to develop. As the anodic limit is increased to 1.5 V vs RHE and beyond there is an increase in HUPD current density which is accompanied by resolved HUPD, which are most easily visible in the anodic sweep. The position of these peaks, around 0.1 and 0.2 V vs RHE, is consistent with desorption of hydrogen ions onto Pt(110) and Pt(100) planes respectively[161]. At this stage in the sample's development there is also an increase in electrochemical capacitance. The cathodic sweep exhibits a peak around 0.7 V vs RHE which is attributed to platinum reduction, or oxide stripping. The position of this peak shifts from around 0.7 to 0.6 V vs RHE as the anodic limit is increased from 1.5 to 1.7 V vs RHE, respectively, indicating that a larger overpotential is required to reduce the platinum. It has previously been observed that the oxide stripping peak is shifted to higher overpotentials for smaller platinum nanoparticles subjected to the same conditioning[165]. It is possible that the platinum clusters are degrading into smaller clusters by a dissolution-redeposition mechanism, however in this case it is more likely that the increased anodic limit has formed more strongly bound oxide species which require a larger overpotential to remove.

Figure 4.2.3 demonstrates how the CV response of Pt_{923} clusters varied with sweep rate. The peak positions of all features do not shift in potential, which would be expected for significant cell ohmic resistance, however the HUPD peaks are more clearly resolved for faster sweep rates. This could be due to a contamination removal and recontamination or platinum restructuring effect which are both time dependent. At faster sweep rates there is less time between oxide stripping and hydrogen adsorption. From the performed experiments, high anodic potentials are required to remove contamination so there is a smaller recontamination time window at faster scan rates which would lead to the observed, improved HUPD response. At the same time, it is known that platinum reduction leads to surface roughening through the oxygen place exchange effect[162]. As these oxide layers are reduced the surface platinum will restructure and roughen into unstable structures which will relax over time. The roughening effect may act to increase the exposed platinum surface area, and the relaxation time explains why this effect is only observed at fast sweep rates. As the total time between oxide stripping and hydrogen adsorption at 1 Vs^{-1} is on the order of tenths of a second, the observed behaviour is consistent with the time scales of diffusion and recontamination rather than atomic restructuring.

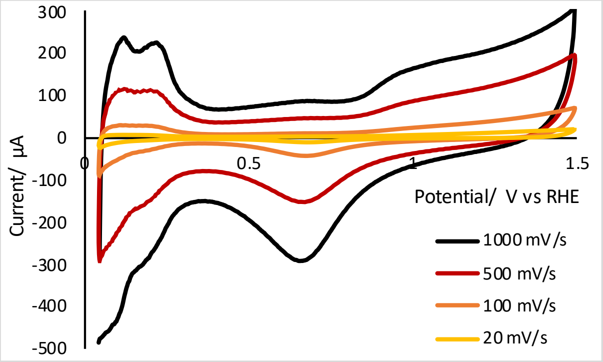

Figure 4.2.3: CV response of Pt_{923} at different scan rates. Experiments performed by J Humphrey and A J Wain at NPL.

The HER performance for all tested cluster sizes is shown in Figure 4.2.4 and it can be seen that the HER performance trend is similar for all cluster sizes. The HER performance of the prepared cluster samples improves as the anodic limit of the potential conditioning is increased above 1.1 V vs RHE, which is consistent with adsorption of oxygen on platinum and the formation of oxide species. The HER performance plateaus above 1.4 V vs RHE where higher anodic limits do not improve HER performance. The range of anodic limits between 1.1 and 1.4 V vs RHE broadly represent an intermediate regime between initial and optimal HER performance.

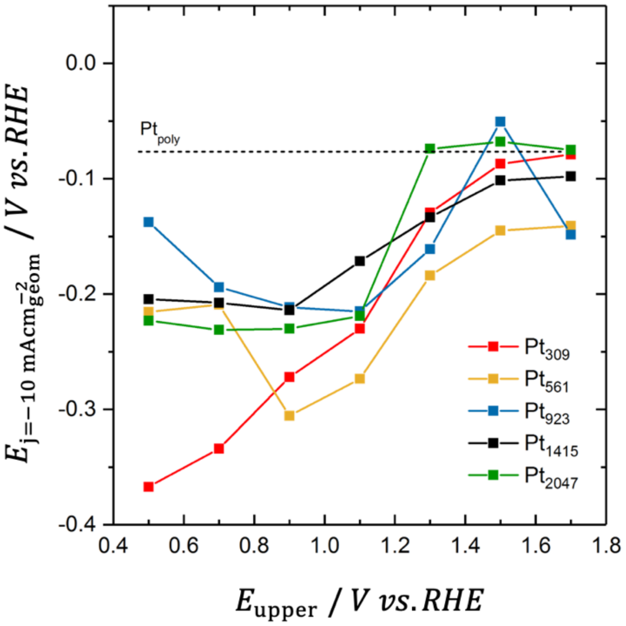

Figure 4.2.4: HER performance data for Pt_N clusters as a function of the anodic limit of potential conditioning. The HER performance was classified using the overpotential required to generate 10 $mAcm^{-2}$ geometric current density. Experiments performed by J Humphrey and A J Wain at NPL.

In summary mass-selected platinum clusters have been characterised electrochemically in sulphuric acid electrolyte. The cluster samples were subjected to potential conditioning with an increasing anodic limit which resulted in improved HER performance. The onset of improved HER performance is at approximately the same potential as oxygen adsorption onto platinum and subsequent oxidation which suggests some particle restructuring. CO stripping experiments also suggest that some form of restructuring is occurring due to the potential conditioning. Experiments at different sweep rates and at reducing anodic limits suggest that contamination removal may play a role in the improved HER performance and CV response. The origin of any contamination is not known, however it is most likely trace amounts or organic compounds from the electrolyte or atmosphere. Ex-situ STEM experiments performed in the next chapter directly visualise the sample at different stages in its development to gain further insight.

5 The effect of electrochemical potential conditioning on Pt_{923} clusters as studied by HAADF-STEM

As discussed in the previous chapter, electrochemical potential conditioning can improve the HER performance and CV response of mass-selected platinum clusters. The electrochemical experiments provide information of the sample *en masse* but does not give direct insight into the behaviour and change of the individual nanoparticles. In this chapter TEM is used to study the effect of electrochemical potential conditioning of well-defined mass-selected platinum clusters on carbon supports. TEM has been used extensively to characterise nanoparticles before and after performance testing[86,94,172] at both the population level and atomic scale. In TEM the substrate needs to be thin, often less than a few hundred nanometers, to be transparent to electrons and as such millimeter-thick glassy carbon stubs are not suitable. TEM grids are commonly used as supports for drop-cast or physically deposited nanomaterials. In this case amorphous carbon film TEM grids were used as substrates in place of glassy carbon as both materials are composed of types of amorphous carbon. It is noted however that glassy carbon does contain some two-dimensional crystalline ordering which is not present in amorphous carbon[173].

All experiments performed in this chapter were performed in a three-electrode electrochemical cell. The WE was an amorphous carbon film Au mesh TEM grid (200 mesh, EM Resolutions) placed on top of a GC stub support which was polished to a mirror finish using alumina paste (Bruker), see section 2.3.2. The RE was MSE (ALS Co., Japan, E0 = 0.687 V vs RHE in 0.5 M H_2SO_4) and the CE was a flame annealed platinum wire. 0.5 M H_2SO_4 electrolyte was prepared daily with DI water (18.2 MΩ, Merck Millipore) and concentrated sulphuric acid (Ultrapur, Alfa Aesar), and was purged of oxygen by bubbling nitrogen gas for 30 minutes prior to any experimentation. The cleanliness of the GC stub was checked by performing CVs over the breakdown region of the electrolyte, the potential region between hydrogen and oxygen evolution, commonly referred to as the solvent window. Once the quality of the GC stub had been confirmed it was washed with DI water and dried under a stream of nitrogen gas. The TEM grid was then placed on top of the GC stub mesh side down. A single layer of Teflon tape was typically used to surround the GC stub housing to ensure a good seal and this was followed by a PEEK cap placed over the top of the whole WE shaft. The PEEK cap has a dual purpose, firstly it exposes only the TEM grid to the electrolyte, and secondly it acts as a clamp to ensure the electrical connection between the GC stub and the grid. All experiments were performed with 500 rpm WE rotation speed and under a constant nitrogen atmosphere.

5.1 Electrochemical response of amorphous carbon film Au mesh TEM grids

CVs were performed to test the electrochemical response of the support materials. The electrochemical response of the bare GC stub support after polishing is shown in Figure 5.1.1. The electrochemical response of GC in sulphuric acid is well known[174] so this test was used to confirm the GC stub quality and the cleanliness of the preparation procedure. The CV exhibits mostly double-layer electrochemical capacitance. The redox pair around 0.55 V vs RHE can be attributed to the formation of oxidised carbon species such as quinones[175]. At the turning points of the CV the current increases due to onset of hydrogen evolution and oxygen evolution at the cathodic and anodic ends, respectively.

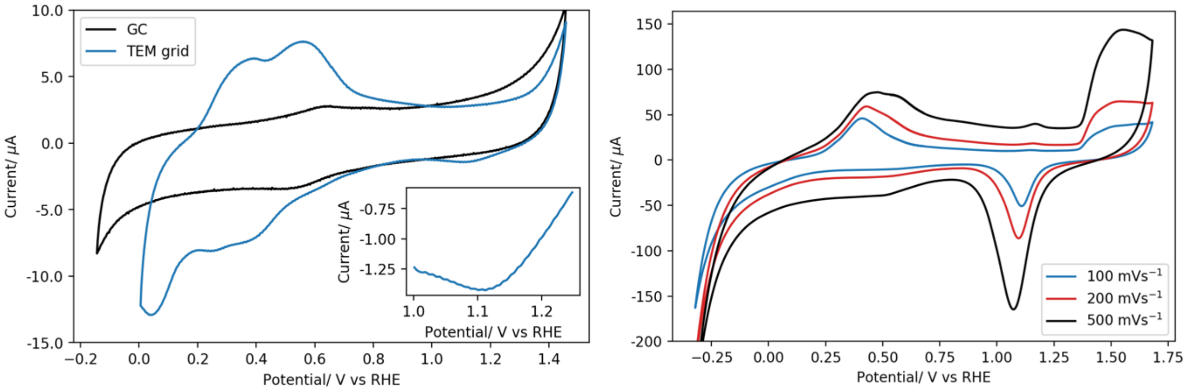

Figure 5.1.1: CVs of amorphous carbon film on Au mesh TEM grid from different companies: (left) EM Resolutions and (right) Agar Scientific. (left) CVs of the base glassy carbon support (black) and the EM Resolutions TEM grid (blue) as used in this thesis. The inset shows a magnification of the Au reduction peak in the cathodic sweep. (right) CVs of an Agar Scientific TEM grid at different scan rates clearly show Au oxidation and subsequent reduction at anodic potentials. CVs were recorded in 0.5 M H_2SO_4 *after purging with nitrogen gas and under 500 rpm WE rotation and the sweep rate was 0.1* Vs^{-1} *unless otherwise stated.*

CVs of blank TEM grids supported on GC from two different companies were then recorded s supported on a GC stub in the cap arrangement described previously, as shown in Figure 5.1.1. The CVs of both grids contain unidentified redox pairs in the range 0.2-0.7 V vs RHE which are likely due to organic residues from the fabrication of the TEM grids. Currents at the above ~1.30 V vs RHE in the anodic sweep are due to gold oxidation[176]. The peak in the cathodic sweep observed at ~1.1 V vs RHE is consistent with gold oxide reduction[176,177] and this confirms no significant potential drop across the electrode setup. Jiang et al.[177] have studied the electrochemical response of carbon film Au mesh TEM grids in acidic and alkaline media and found them to have good stability over many hours across the applied potential range of 1.0-1.8 V vs RHE in their experiment. The authors did not comment on the potential range containing the redox pairs observed in Figure 5.1.1, so the origin of these peaks is only speculation. They did find, however, that up to 10% of grid squares may break over the course of one experiment, and experience suggests that this may be due as much to handling the fragile grids as the experimental conditions.

Pt_{923} was chosen as the particle size to explore as it is approximately the mean cluster size in terms of number of atoms and diameter from the HER performance testing in the previous chapter. The cluster samples were initially prepared with a coverage of less than 10% to limit the amount of agglomeration and sintering to study the effect of potential conditioning on individual clusters. Clusters were imaged with STEM in HAADF mode in at least three different non-neighbouring grid squares before potential cycling and the location of these grid squares was recorded. The same grid squares were imaged after potential conditioning in a pseudo identical-location TEM[31,86,106] study. Due to the homogeneous nature of the cluster samples it was not possible to reimage exactly the same location without the use of fiducial markers, however the location could be estimated within the order of a micron using this technique. This methodology reduces the effect of any sample cluster density fluctuations which may have originated during the deposition process.

5.2 Potential cycling up to 1.05 V vs RHE

5.2.1 Intermediate density: 7000 clusters per square micron

Pt_{923} clusters were deposited with 1 eV per atom kinetic energy onto amorphous carbon TEM grids with a measured density of 7000 ± 500 clusters per square

micron, equivalent to 6.4 ± 0.6 % area coverage. The as-deposited sample morphology and size distribution can be seen in Figure 5.2.1. The majority of clusters are normally distributed with projected area of 8.2 ± 0.6 nm^2, which is in agreement with the expected size from bulk calculations, see Figure 3.2.3. A second smaller peak in the size distribution is due to clusters with approximately twice the projected area of the dominant peak. The origin of this peak is due to two sintered Pt_{923} clusters either at landing or after diffusion on the surface. The morphology of the sintered Pt_{923} clusters is chain-like suggesting that the clusters had undergone diffusion on the surface followed by collision and sintering with another cluster, also known as Smoluchowski ripening, as opposed to head-on collision at the time of deposition from the cluster beam which would produce more non-spherical clusters[178,179]. Closer inspection of the sintered clusters reveals that sintering is preceded by neck formation, growth, and subsequent elimination[79] which may produce grain boundaries within the agglomerates, as observed in
Figure 5.2.4.

Integrated intensity analysis of the HAADF-STEM images was performed to 'weigh'[137] the nanoparticles and the resulting distributions are shown in Figure 5.2.2. The integrated intensity is a more robust descriptor than projected area for atomic clusters[153] as discussed in chapter 3, and is less affected by non-uniform cluster shapes as it is a measure of cluster volume. The integrated intensity analysis reveals a clear third peak that is obfuscated in the projected area analysis due to a large spread in the geometries of agglomerated nanoparticles. The integrated intensity ratios between the secondary peaks and dominant peak are linear with peak number confirming that the secondary peaks are in fact due to multiple sintered Pt_{923} clusters. The sintered nanoparticles are referred to as Pt_{923} singlets, doublets, and triplets herein.

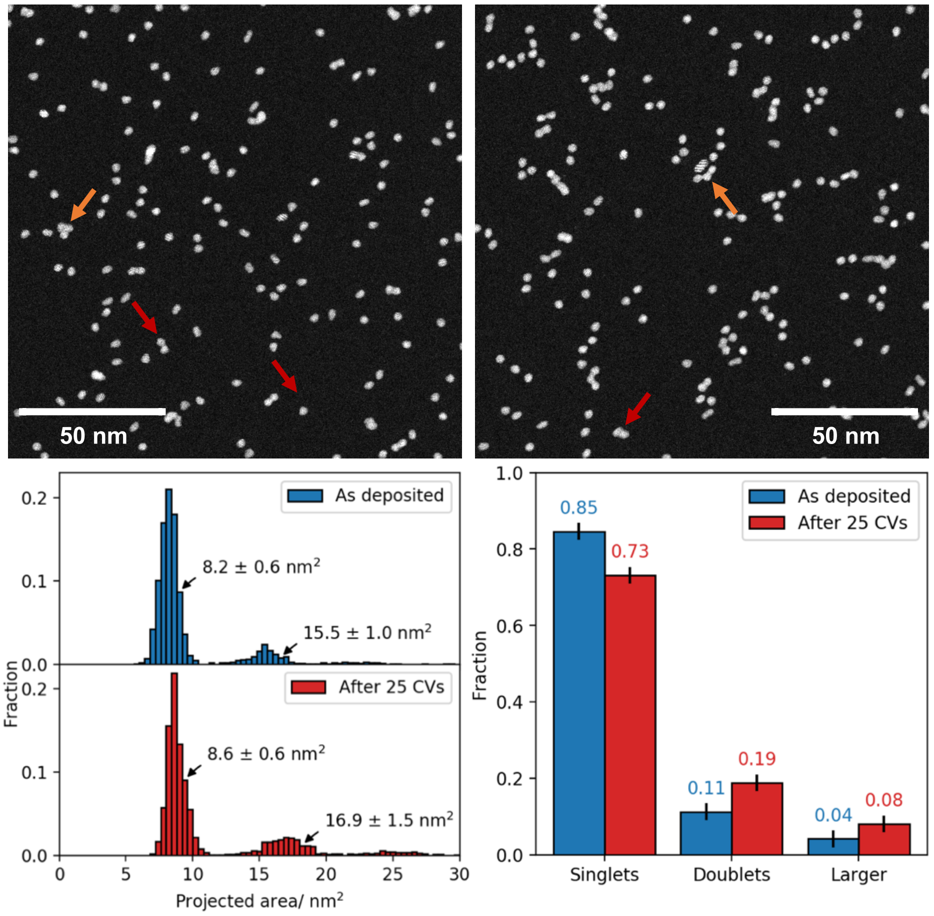

Figure 5.2.1: Pt_{923} after 25 CVs between 0 and 1.05 V vs RHE at 0.1 Vs^{-1}. (top row) HAADF-STEM images of Pt_{923} deposited with a number density of 7000 ± 500 per square micron on amorphous carbon. (left) as deposited, and (right). The red and orange arrows show selected doublets and triplets respectively. (bottom row) (left) size distribution of Pt_{923} as deposited (blue) and after potential conditioning (red). (right) the population distribution of the sample shows a reduction in Pt_{923} singlets and increased Pt_{923} doublets after the potential cycling. Error bars are $1/N^{1/2}$.

The nearest neighbour distribution of the as-deposited sample is shown in Figure 5.2.3. The cumulative density function (CDF, red line) is obtained by integrating the probability density function (PDF, histogram) over all observed nanoparticles. The CDF is compared to the expected distribution from a randomly deposited sample of impenetrable disks of diameter d_{923} = 3.2 nm (black dashed line) and is in good agreement. During the deposition process the sample was rastered across the cluster beam which possesses a gaussian beam profile[111] and distribution of cluster impacts is expected to be random. This result confirms that the clusters have not undergone any significant amount of diffusion from their impact site as they are likely pinned on defects in the amorphous carbon[49].

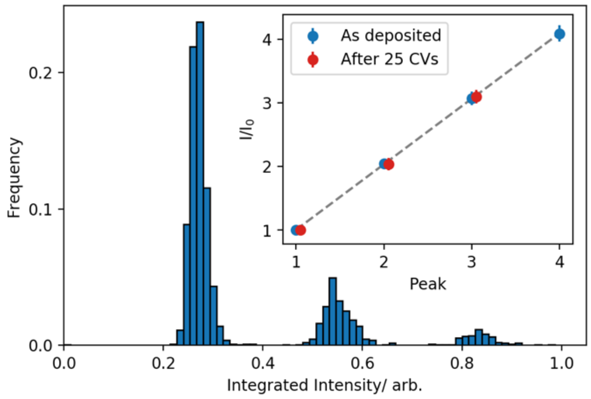

Figure 5.2.2: Integrated intensity histogram of Pt_{923} *clusters as-deposited. (inset) the integrated intensity ratios between the secondary peaks and the primary peak. The grey dashed line is a fit with slope 1.03 and an* R^2 *value of 0.9999.*

The sample was then subjected to 25 CVs between 0 and 1.05 V vs RHE in deaerated 0.5 M H_2SO_4 at a scan rate of 0.1 Vs^{-1}. As discussed in chapter 4 this anodic potential limit is less than required to improve the HER performance of the mass-selected platinum clusters. The sample morphology after potential conditioning is shown in Figure 5.2.1. Initial inspection appears to show that the arrangement of clusters on the surface is now more ordered and that the Pt_{923} singlets have grouped together into chains or small islands.

The size distribution of the sample post-conditioning shows that the singlet and doublet sizes remain unchanged within error. This is, however, accompanied by some nanoparticle sintering. The proportion of observed singlets has fallen from 85 to 73 %, and the fraction of doublets has increased from 11 to 19 %. The potential conditioning appears to have induced nanoparticle migration which has subsequently led to small amounts of sintering. The nearest neighbour distribution post-conditioning shows a slight deviation from the as-deposited distribution, however it does not elucidate the observed nanoparticle grouping.

Post-conditioning the number density is reduced by 17 % to 5800 ± 600 nanoparticles per square micron, however the total surface coverage remains unchanged at 6.4 ± 0.6 %. These observations are consistent with nanoparticle sintering and rules out any significant amounts of nanoparticle detachment from the surface. The potential conditioning appears to have induced cluster mobility which has led to sintering in many cases. The observed behaviour is consistent with Smoluchowski ripening rather than more atomistic processes.

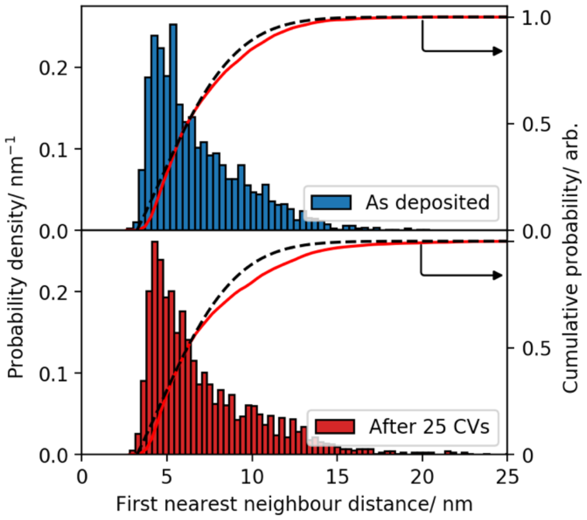

Figure 5.2.3: First nearest neighbour distribution of Pt_{923} *(upper, blue) as-deposited and after 25 CVs between 0 and 1.05 V vs RHE at 0.1* Vs^{-1} *(lower, red). The cumulative distributions are plotted as the red curve in each case. The black dashed curve is the cumulative distribution expected for a random distribution of impenetrable particles with number density 7000 per square micron.*

High magnification HAADF-STEM imaging, shown in
Figure 5.2.4, was performed to see if potential cycling had induced any structural transformations in the clusters. The clusters observed after potential cycling are predominantly FCC structures, such as the cuboctahedrons shown, with no obvious signs of oxidation. Surface oxide species would normally appear as a dim halo[42] compared to a metal cluster core as imaged with HAADF-STEM, as oxygen has a low atomic number and therefore a low Rutherford scattering cross-section. The as-deposited Pt_{923} clusters have predominantly FCC structures so it is difficult to conclude whether the potential conditioning induced any structural transformations from the performed experiment.

Further observation of the sintered nanoparticles reveals that they often contain grain boundaries where the crystalline phase may be discontinuous across the boundary. This is consistent with nanoparticle growth due to Smoluchowski ripening and subsequent neck growth[151]. The grouping behaviour may affect the catalytic performance of the sample as the mass transport to nanoparticles at the center of these groups will be reduced due to an inhibited diffusion field[131,132].

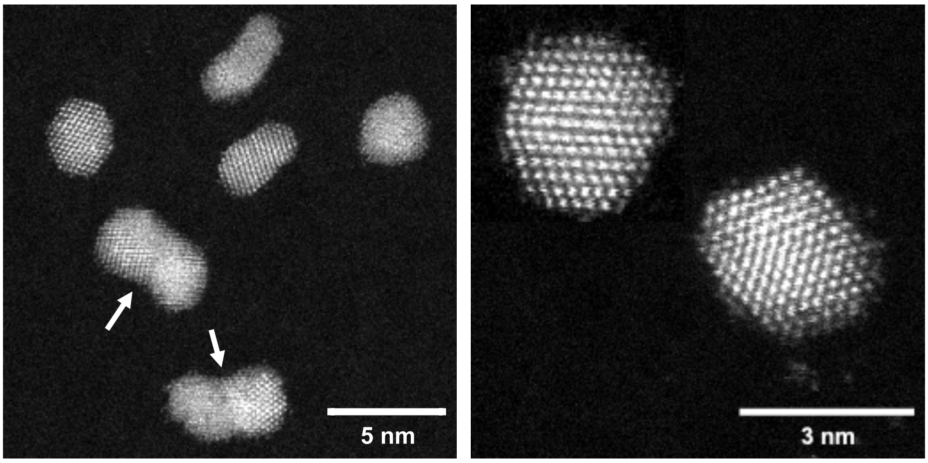

Figure 5.2.4: High magnification HAADF-STEM images of selected Pt_{923} (left) as-deposited, and (right) after 25 CVs between 0 and 1.05 V vs RHE at 0.1 Vs^{-1}. In both cases atomic columns and facets are clearly resolved and singlet clusters have cuboctahedral structures. Larger clusters resemble sintered singlet clusters, where the sintering boundary is identified with a white arrow.

5.2.2 Low density: 3000 clusters per square micron

To further test whether the observed sintering is due to a hit-and-stick type mechanism, the same experiment was performed with a reduced number density of 3000 ± 300 clusters per square micron. The experiment described in section 5.2.1 suggests that the cluster-surface interaction is weakened during potential cycling; as a result the clusters become mobile and undergo Brownian motion on the surface where they may collide or interact with another cluster forming a group. By reducing the cluster number density the chance of finding another cluster during a random walk is reduced and the collision rate is expected to decrease[180].

HAADF-STEM images of the sample as-deposited and after 25 potential cycles between 0 and 1.05 V vs RHE at 0.1 Vs^{-1} are shown in Figure 5.2.5. The as-deposited cluster arrangement is random, as expected and shown in Figure 5.2.6, and groups of clusters are clearly observed after potential cycling, consistent with the experiment performed in section 5.2.1. The cluster size distribution demonstrates that the majority of nanoparticles are Pt_{923} singlets in both cases and that there is no significant sintering due to the potential conditioning due to the reduced nanoparticle density.

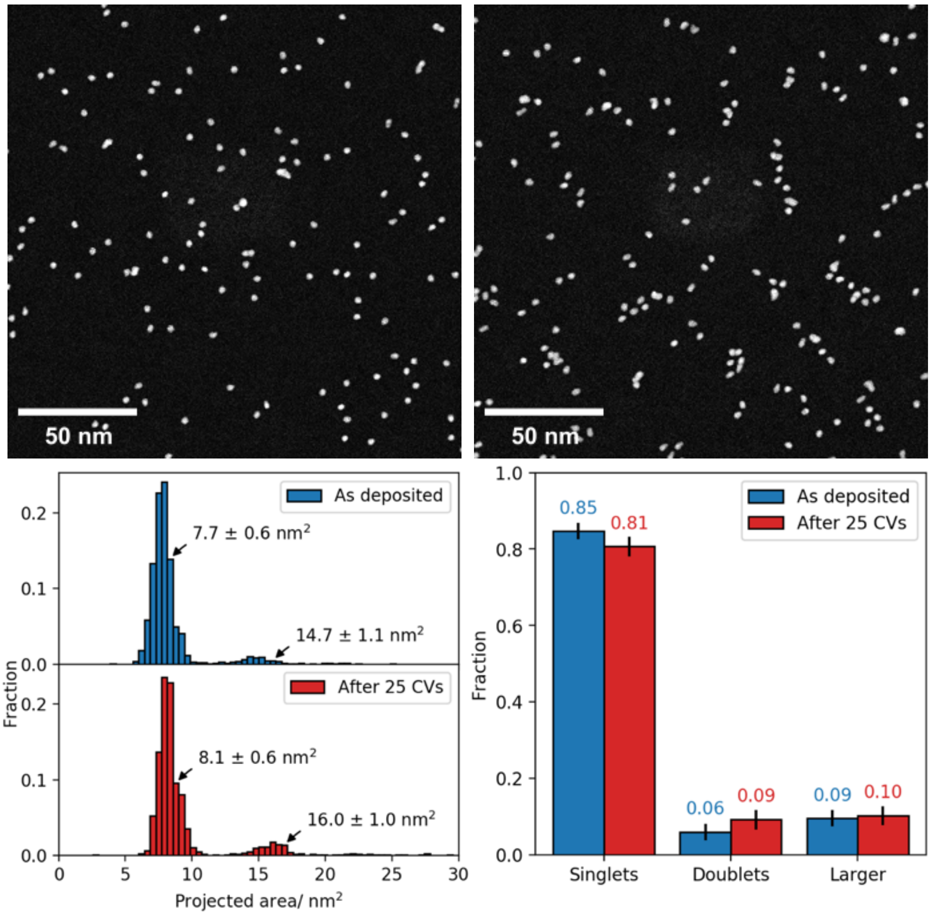

Figure 5.2.5: Pt$_{923}$ after 25 CVs between 0 and 1.05 V vs RHE at 0.1 Vs^{-1}. (top row) HAADF-STEM images of Pt$_{923}$ deposited with a number density of 3000 ± 300 per square micron on amorphous carbon. (left) as-deposited, and (right) after 25 CVs. (bottom row) (left) size distribution of Pt$_{923}$ as-deposited (blue) and after 25 CVs (red). (right) the population distribution of the sample shows no significant change due to the potential cycling. Error bars are 1/N$^{1/2}$.

The reduced nanoparticle density does elucidate the grouping mechanism, however. The nearest neighbour distributions shown in Figure 5.3.2 show that the clusters are initially deposited in the expected random arrangement, however post-conditioning the nearest neighbour distribution is strongly peaked around 5 nm and deviates significantly from the expected random distribution. In fact, just 27 % of clusters had a nearest neighbour less than 7 nm apart as-deposited compared to 58 % post-conditioning. The modal core-core distance of 5 nm is equivalent to ~2 nm edge-edge distance for Pt$_{923}$ with a diameter of ~3 nm.

In both the as-deposited and post-conditioning data there are no observed nearest neighbour distances less than 3.4 nm. Given that the Pt$_{923}$ clusters are have a radius of ~1.5 nm, the smallest equivalent edge-edge is less than 0.4 nm which is on the order of one atom. It has been previously observed that sintering of gold clusters may be mediated by atomic species bridging the gap between two adjacent clusters[129] and that gold clusters ‘jump-to-contact’ at edge-edge spacings of 0.5 nm. Given the distances measured in this experiment it is possible that platinum clusters also have a jump-to-contact sintering threshold which is on the order of 0.4 nm.

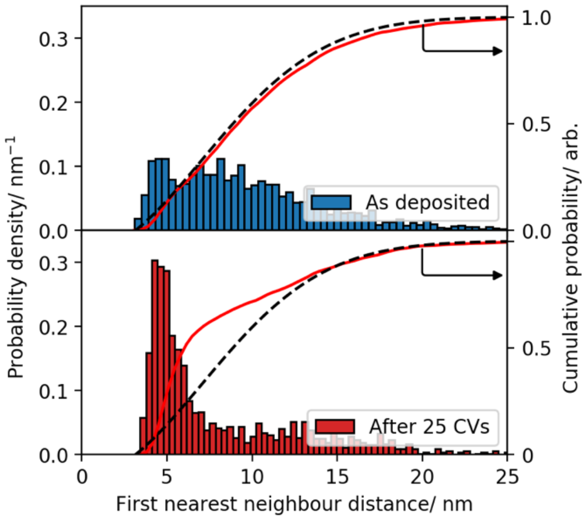

Figure 5.2.6: First nearest neighbour distribution of Pt$_{923}$ (upper, blue) as-deposited and after 25 CVs between 0 and 1.05 V vs RHE at 0.1 Vs^{-1} (lower, red). The cumulative distributions are plotted as the red curve in each case. The black dashed curve is the cumulative distribution expected for a random distribution of impenetrable particles with number density 3000 per square micron.

The nearest neighbour distribution post-conditioning was fit by two gaussian distributions to approximate its bimodal nature and their intersection point was chosen as a threshold for cluster classification. A visual representation of this analysis is presented in Figure 5.2.7. Distances shorter and longer than the threshold are represented by red and blue lines respectively. It can be seen in the STEM image that the dominant peak in the nearest neighbour distribution (red) is due to clusters that have grouped together but not sintered. The higher number density in section 5.2.1 likely obfuscated the grouping effect in the nearest neighbour distribution, despite the presence of groups by visual inspection of the HAADF STEM images.

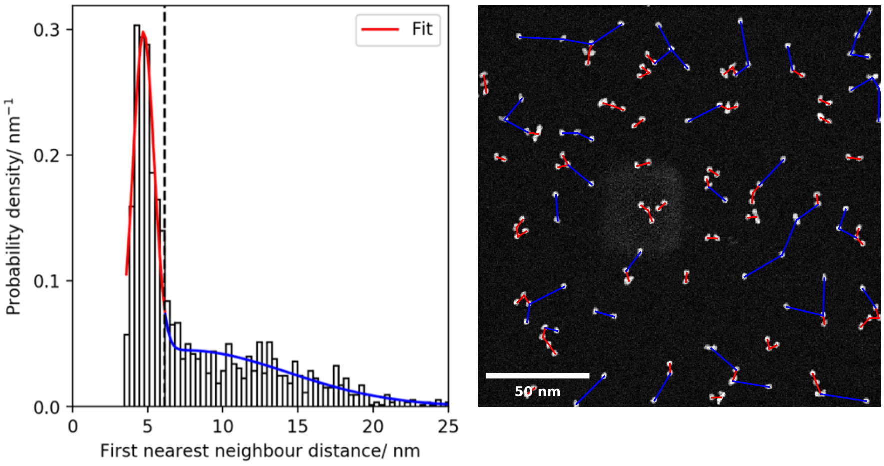

Figure 5.2.7: Visual representation of the first nearest neighbour distances. The low-density Pt_{923} sample had been subjected 25 CVs between 0 and 1.05 V vs RHE at 0.1 Vs^{-1}. (left) first nearest neighbour distribution created from multiple images. The distribution was fit with two gaussian distributions, and their intersection point between them is shown as a black dashed line. The total fit is shown as the red-blue solid line. (right) HAADF-STEM image of the sample after potential conditioning. Each nanoparticle has its first nearest neighbour shown as a coloured solid line. Distances shorter and larger than the threshold value are plotted as red and blue respectively.

The nearest neighbour distribution was then analysed up to each nanoparticles' sixth nearest neighbour. The resulting distribution and comparison of each distribution's statistics is shown in Figure 5.2.8, where the median and mode of each distribution are compared. It should be noted that the trend of the distribution means were similar to the distribution medians. For all n nearest neighbours it can be seen that the distribution mode is smaller than the median and this is consistent for distributions with positive skew. The expected n'th nearest neighbour distance for a random distribution[181] is shown as a grey line and is in good agreement with the as-deposited data. Post-conditioning all nearest neighbour distances are reduced overall and the first and second nearest neighbour distances are reduced significantly. The trend in nearest neighbour distances after the third nearest neighbour is approximately as expected for a random distribution. The mode appears to be a more representative statistic for first and second nearest neighbour distributions post-conditioning. The grouping effect observed and discussed only appears to be correlated to each nanoparticle's second nearest neighbour on average, equivalent to an average group size of three nanoparticles.

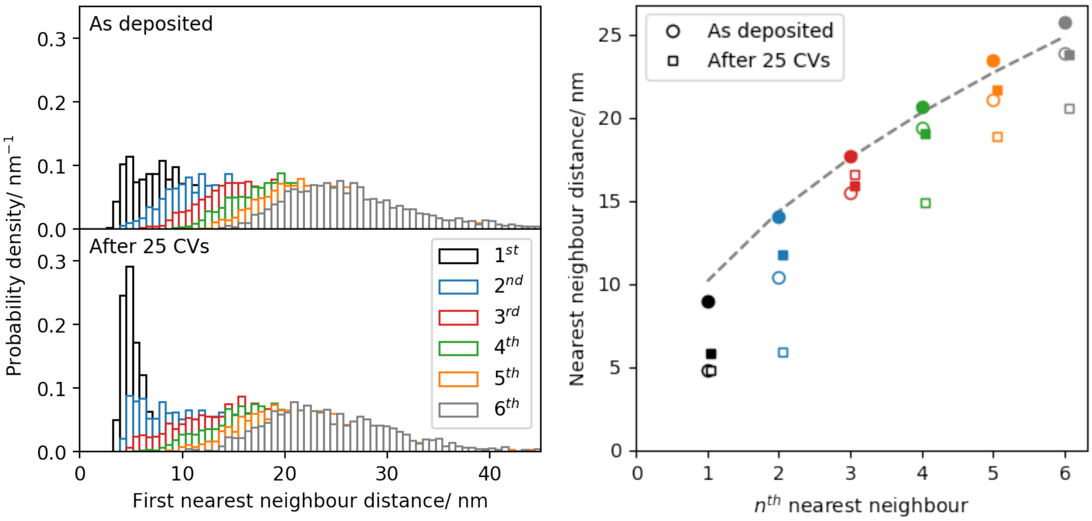

Figure 5.2.8: n'th nearest neighbour distribution. (left) nearest neighbour distribution of Pt_{923} as-deposited (upper) and after 25 CVs between 0 and 1.05 V vs RHE at 0.1 Vs^{-1} (lower). The first six nearest neighbours for each nanoparticle were analysed in each case. (right) comparison of the median (filled) and mode (open) of the nearest neighbour distribution for the sample as-deposited (circles) and post-conditioning (squares). The grey dashed line is the expected nearest neighbour distance for a random point distribution[181]. The squares are offset for clarity. The colours represent the same distributions in both plots.

5.2.3 High density: 15000 per square micron

A high-density sample was prepared to further explore how the amount of sintering is affected by the density. The as-deposited sample morphology and size-distribution are shown in Figure 5.2.9. A significant proportion of the sample is now agglomerated due to the high cluster density, but the clusters are deposited randomly on the surface, as shown in Figure 5.2.10. The nearest neighbour CDF has the same shape as the expected from a random distribution and the deviation is likely due to the fact that a significant portion of the clusters are larger than the singlet size.

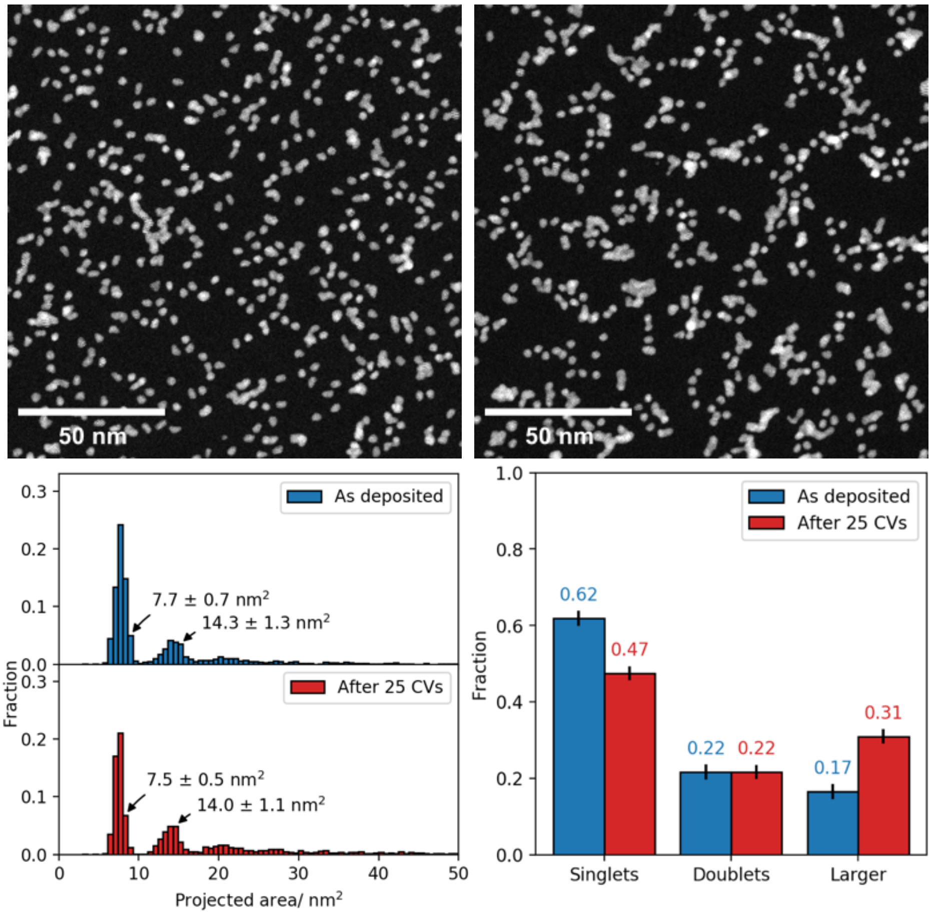

Figure 5.2.9: Pt$_{923}$ after 25 CVs between 0 and 1.05 V vs RHE at 0.1 Vs^{-1}. (top row) HAADF-STEM images of Pt$_{923}$ deposited with a number density of 15000 ± 400 per square micron on amorphous carbon. (left) as-deposited, and (right) after 25 CVs. (bottom row) (left) size distribution of Pt$_{923}$ as-deposited (blue) and after 25 CVs (red). (right) the population distribution in each case.

The sample was subjected to 25 CVs between 0 and 1.05 V vs RHE at 0.1 Vs^{-1}. STEM imaging shows that ~15 % of the clusters have sintered as a result. Interestingly the proportion of doublets remains unchanged, although this is likely because they too have sintered to form larger nanoparticles. The increased cluster density has resulted in more sintering events when compared to lower densities, this is likely due to an increased amount of collisions. The cluster density has fallen by 24 % as a result of sintering, whereas the total coverage remains unchanged. Post-conditioning the nearest neighbour distribution represents a random distribution and is almost identical to the as-deposited distribution. Any cluster grouping is hard to correlate by eye at this high density and if it is present, as was the case in sections 5.2.1 and 5.2.2, it does not manifest in the nearest neighbour statistics.

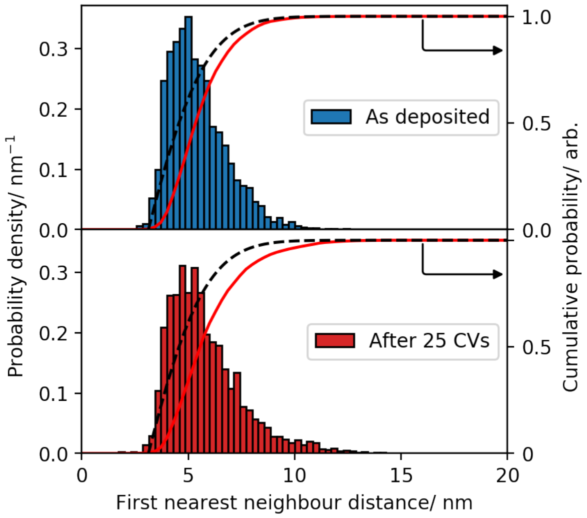

Figure 5.2.10: First nearest neighbour distribution of Pt_{923} *(upper, blue) as deposited and after 25 CVs between 0 and 1.05 V vs RHE at 0.1 Vs*$^{-1}$ *(lower, red). The cumulative distributions are plotted as the red curve in each case. The black dashed curve is the cumulative distribution expected for a random distribution of particles with number density 15000 per square micron, as measured in STEM.*

5.3 Potential cycling up to 1.20 V vs RHE

The anodic potential limit was then increased to 1.20 V vs RHE, which is in the transitional region before the HER performance plateau observed in chapter 4. The CV response of platinum clusters conditioned to this anodic limit showed increased HUPD response and improved HUPD resolution overall. The CV response of platinum clusters at potentials above 1.0 V vs RHE showed currents due to platinum oxidation on the anodic sweep and subsequent platinum oxide reduction on the cathodic sweep.

5.3.1 Intermediate density: 6000 clusters per square micron

A sample identical to that in section 5.2.1 was prepared and subjected to 25 CVs between 0 and 1.20 V vs RHE. The sample morphology as-deposited and post-conditioning is shown in Figure 5.3.1. The size distribution shows that the as-deposited sample is predominantly Pt_{923}, and the nearest neighbour distribution is characteristic of a randomly arranged sample, see Figure 5.3.2.

Post-conditioning the sample morphology has changed such that larger chain- or branch-like nanoparticles are present. The This size-distribution reflects this observation as an increased proportion of larger nanoparticles and agglomerates of three of more Pt_{923} singlets can be seen in Figure 5.3.1. The number density as-deposited was 6000 ± 600 and this was reduced by 40 % due to sintering whilst the coverage remained unchanged at 5.1 ± 0.6 %. The size distribution remains quantised post-conditioning and there is no obvious change in singlet or doublet size compared to the as-deposited distribution. These observations are consistent with Smoluchowski ripening rather than more atomistic degradation mechanisms and rules out significant nanoparticle detachment from the surface.

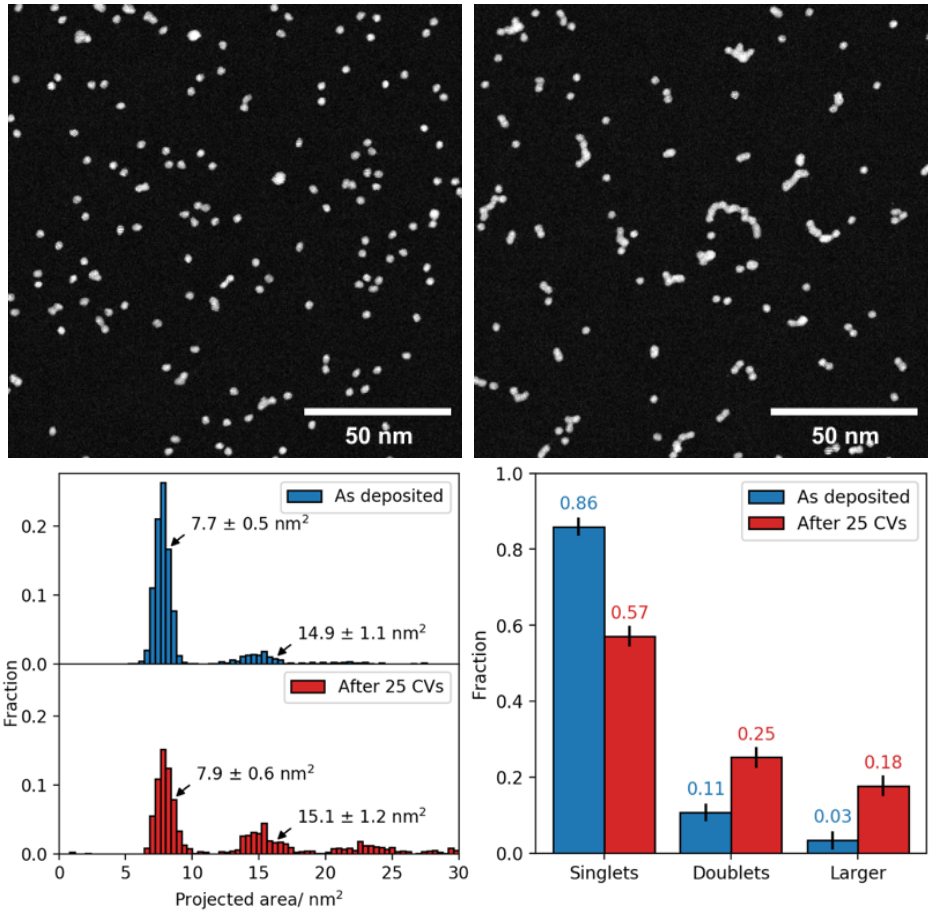

Figure 5.3.1: Pt_{923} after 25 CVs between 0 and 1.20 V vs RHE at 0.1 Vs^{-1}. (top row) HAADF-STEM images of Pt_{923} sample deposited at a number density of 6000 per square micron. (left) the sample morphology as-deposited, and (right) post-conditioning after 25 CVs. (bottom row) (left) size distribution of Pt_{923} as-deposited (blue) and post-conditioning (red), and (right) the population distribution in each case.

These branch-like structures may be created by a hit-and-stick type sintering mechanism[93]. In agreement with the results seen during potential conditioning at lower anodic potential limits in section 5.2, the clusters appear to have increased mobility during potential cycling and undergo diffusion on the surface until they interact with another cluster or defect on the surface. At potentials larger than 1.0 V vs RHE platinum oxidises which may cause surface restructuring[162], and the high anodic potentials may oxidatively remove organic. These combined effects may lead to increased amounts of sintering at higher anodic potentials.

The nearest neighbour distribution post-conditioning shown in Figure 5.3.2 deviates significantly from the as-deposited distribution, which is in excellent agreement with a randomly arranged distribution of nanoparticles. The CDF post-conditioning is consistent with a random distribution with a number density of 3500 per square micron, which is the measured number density post-conditioning, and is represented in Figure 5.3.2 as a black dotted line. This information suggests that despite the cluster migration and sintering the modified cluster arrangement post-conditioning is still random.

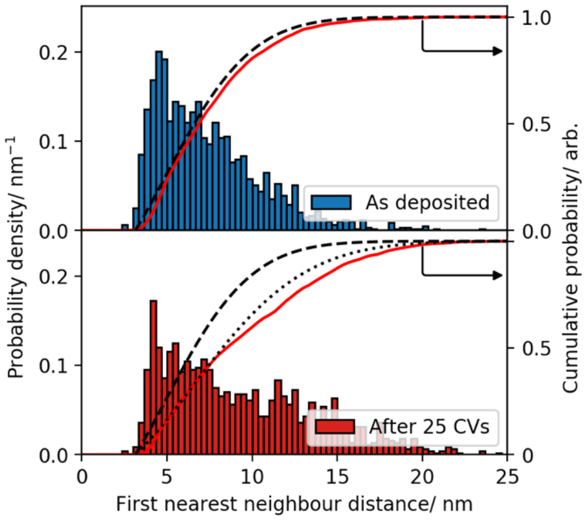

Figure 5.3.2: First nearest neighbour distribution of Pt_{923} (upper, blue) as deposited and after 25 CVs between 0 and 1.20 V vs RHE at 0.1 Vs^{-1} (lower, red). The cumulative distributions are plotted as the red curve in each case. The black dashed curve is the cumulative distribution expected for a random distribution of particles with number density 6000 per square micron, as measured in STEM. The black dotted line is expected distribution for a number density of 3500 per square micron.

5.3.2 Low density: 1300 clusters per square micron

A low-density experiment was performed to test how potential conditioning with an increased anodic limit affects the nanoparticle displacement. Pt_{923} was deposited with a density of 1350 ± 250 clusters per square micron and then subjected to 25 CVs between 0 and 1.20 V vs RHE at 0.1 Vs^{-1}. The sample morphologies as-deposited and post-conditioning are shown in Figure 5.3.3. At low sample density the population distribution shows that no significant sintering occurs, and the mean number density post-conditioning does not change within one standard deviation. However the nearest neighbour distribution, see Figure 5.3.4, as well as the STEM images, show that the clusters were initially randomly deposited and have formed groups, similar to that observed in section 5.2.2.

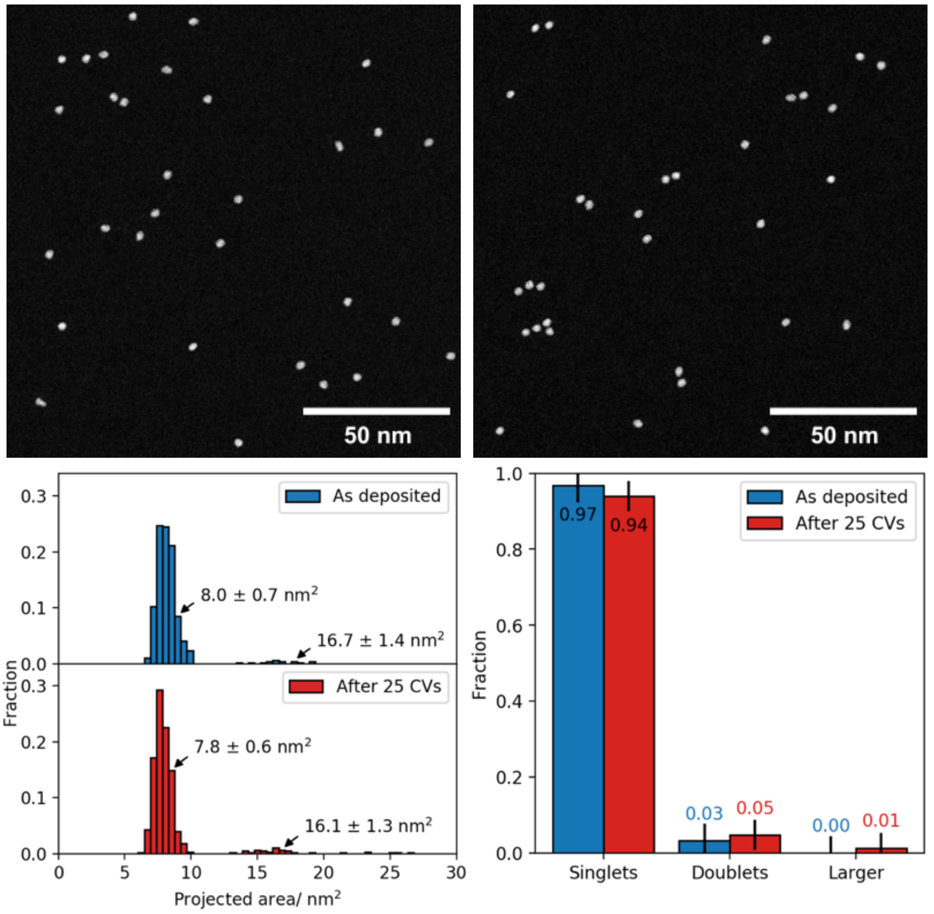

Figure 5.3.3: Pt_{923} after 25 CVs between 0 and 1.20 V vs RHE at 0.1 Vs^{-1}. (top row) HAADF-STEM images of Pt_{923} sample deposited at a number density of 1350 per square micron. (left) the sample morphology as-deposited, and (right) post-conditioning after 25 CVs. (bottom row) (left) size distribution of Pt_{923} as-deposited (blue) and after 25 CVs (red), and (right) the population distribution in each case.

In section 5.3.1 potential conditioning Pt_{923} clusters with a higher density lead to significant amounts of sintering, however despite the clear migration effect this result was not replicated in this experiment. The nearest neighbour distributions in Figure 5.3.4 show that 32 % of clusters have a nearest neighbour less than 6 nm away post-conditioning, compared to just 11 % as-deposited and the modal nearest neighbour distance is just 4 nm center-center which is equivalent to a 1 nm edge-edge gap.

The reduced amount of sintering is the same as observed in the low-density experiment in section 5.2.2 and can be explained by a reduced cluster collision probability. Comparison of experiments at higher cluster densities in sections 5.2.1 and 5.3.1 showed that an increased anodic potential limit led to increased amounts of sintering. This was not observed at low densities, despite the formation of groups. It is possible that there is some barrier to sintering unique to this sample, such as the presence of organic contaminants[182]. Given the low cluster density in this experiment it is likely that the clusters have been in close proximity for a shorter amount of time as they are less likely to collide. It has been observed previously that small gold clusters may exist in close proximity (around ~1 nm) and will not coalesce unless mediated by a bridging atom[129] or until their orientations are aligned in a manner that is energetically favourable[183]. This latter process, called oriented attachment, has also been observed for platinum[184,185] and iron[109] nanoparticles and is believed to play a role in nanocrystal growth. Li et al.[109] studied the coalescence of large iron nanoparticles in-situ and found that two nanoparticles may come into close contact for a prolonged period of time before oriented attachment takes place.

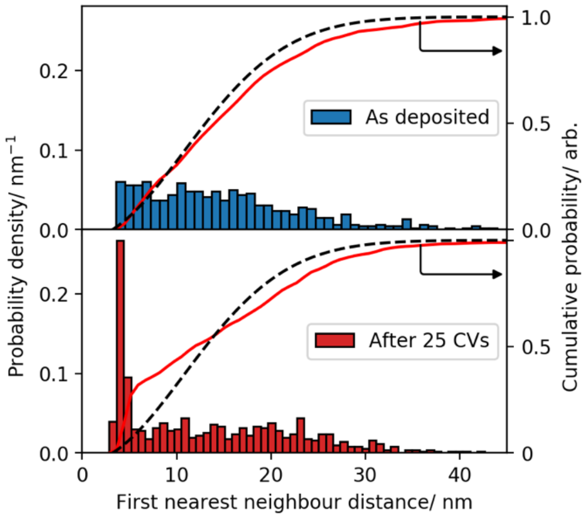

Figure 5.3.4: First nearest neighbour distribution of Pt_{923} *(upper, blue) as-deposited at a density of 1300 clusters per square micron and after 25 CVs between 0 and 1.20 V vs RHE at 0.1* Vs^{-1} *(lower, red). The cumulative distributions are plotted as the red curve in each case. The black dashed curve is the cumulative distribution expected for a random distribution of particles with number density 1300 per square micron, as measured in STEM.*

5.3.3 High density: 11500 clusters per square micron

Given that the degree of sintering has been shown to be a function of initial density, a high-density experiment was also performed. The as-deposited number density was 11500 ± 400, equating to a coverage of 12.5 ± 0.3 %. The sample morphology as-deposited and post-conditioning is shown in Figure 5.3.5. The Pt_{923} clusters have again formed branch-like structures post-conditioning and the overall mean nanoparticle radius has increased 41 % post-conditioning from 1.83 ± 0.44 nm as-deposited. The measured number density has dropped by approximately 50 % whilst the overall coverage remains unchanged within one standard deviation.

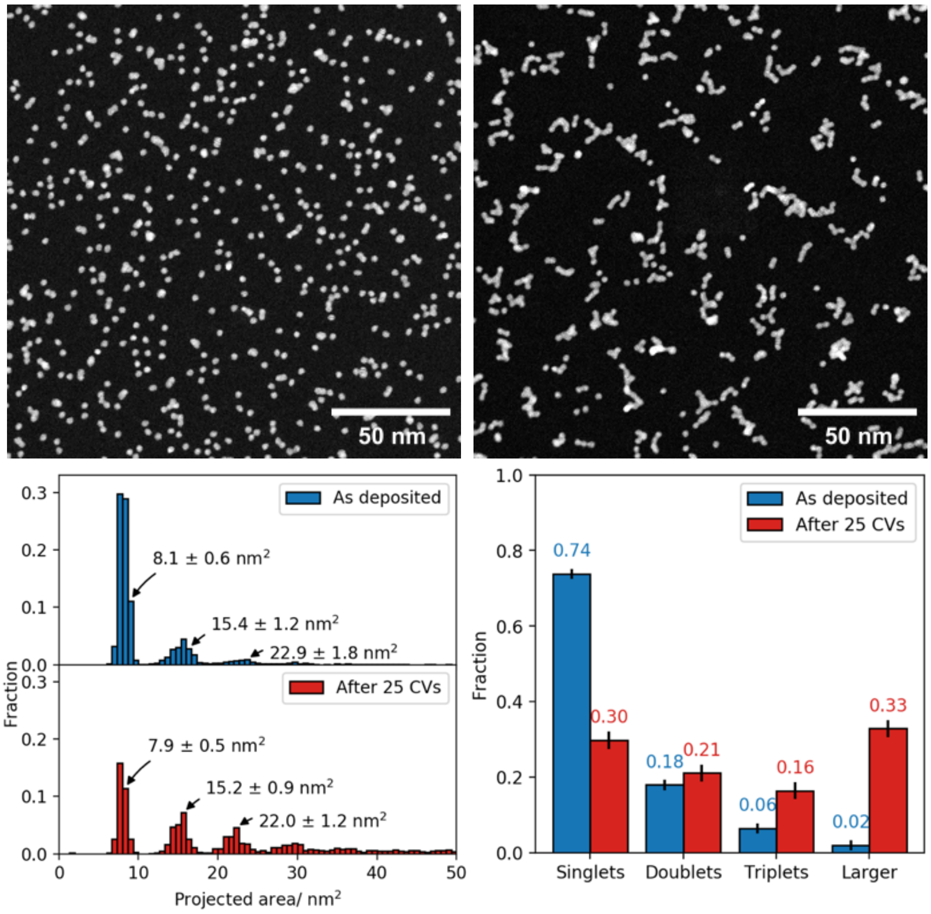

Figure 5.3.5: Pt_{923} after 25 CVs between 0 and 1.20 V vs RHE at 0.1 Vs^{-1}. (top row) HAADF-STEM images of Pt_{923} sample deposited at a number density of 11500 per square micron. (left) the sample morphology as-deposited, and (right) after 25 CVs. (bottom row) (left) size distribution of Pt_{923} as-deposited (blue) and post-conditioning (red), and (right) the population distribution in each case.

The Pt_{923} singlet and doublet sizes remain unchanged post-conditioning, consistent with Smoluchowski ripening, and the cluster sizes remain quantised.

At this density approximately three quarters of the as-deposited nanoparticles were Pt_{923} clusters, whereas after potential conditioning approximately 70 % of nanoparticles are larger than the as-deposited size. The remaining 30 % of nanoparticles that have not sintered account for only 10 % of the total deposited platinum by projected area confirming that the sample morphology at this stage in its evolution cannot be accurately described as well-defined mass-selected Pt_{923}.

Integrated intensity analysis was performed to compliment the projected area analysis. The cluster post-conditioning projected area in Figure 5.3.5 shows the presence of three clear peaks, and possibly a fourth peak, however fitting algorithms were not able to reliably fit the latter. The integrated intensity analysis of the same dataset is shown in Figure 5.3.6. The peaks in the integrated intensity data are sharper and more clearly resolved than in the projected area analysis. The integrated intensity descriptor is more robust to nanoparticle geometry than projected area[153] which can be affected by nanoparticle orientation with respect to the beam, especially in the case of non-spherical geometries. As a result, there are six discernible peaks in the integrated intensity analysis post-conditioning compared to only four in the projected area analysis.

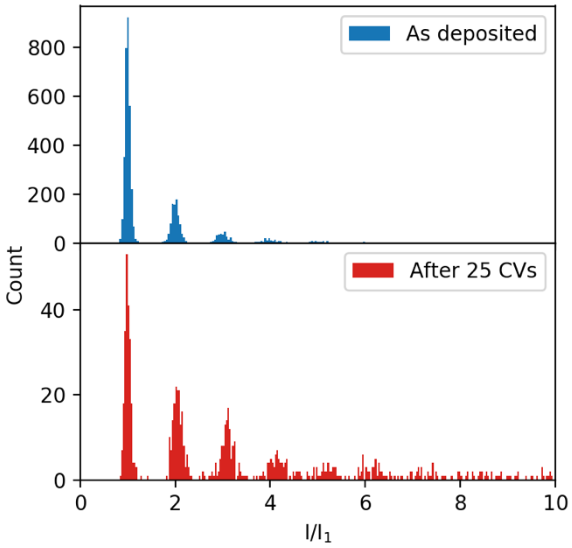

Figure 5.3.6: Integrated intensities of the Pt_{923} cluster sample as-deposited (top) and after 25 CVs between 0 and 1.20 V vs RHE at 0.1 Vs^{-1} (bottom). The integrated intensity values (arbitrary units) are shown as a ratio of the Pt_{923} singlet value in both cases.

The peaks in the integrated intensity data were then fit by gaussian distributions and their magnitudes are expressed as a ratio of the first peak in each case. The result is shown in Figure 5.3.7 where it is compared to the same analysis for the projected areas. In Figure 5.3.7 the grey dashed lines have a unity gradient and represent the expected peak magnitudes if the measured nanoparticles were made of exactly n Pt_{923} clusters. The projected area and integrated intensity analysis are both clustered around this line, however the projected area values are consistently smaller than expected which may lead to the interpretation of some loss of material during coalescence. The integrated intensity analysis, however, shows that this is not the case as all of the peaks are located on the expected line within one standard deviation. The deviation in the projected area analysis is likely due to the morphology argument made previously. Only considering the projected area analysis, it would appear as the Pt_{923} clusters undergo Smoluchowski ripening during potential conditioning forming nanoparticles up to Pt_{923} quartets, and whilst there are clearly larger nanoparticles in Figure 5.3.5, they are not necessarily made from integer numbers of Pt_{923} clusters. The integrated intensity analysis extends this up to Pt_{923} sextets and larger particles may be discernible over more statistics. Whilst the absolute integrated intensity magnitude between the as-deposited sample and sample post-conditioning cannot be easily compared due to differing microscope parameters between imaging sessions[102,137,186], it does allow for relative comparisons within the same sample with the same imaging conditions. This analysis shows that no significant amounts of material are lost during coalescence. It may be expected that smaller nanoparticles would undergo any dissolution during potential cycling at an increased rate due to their increased surface area, which would effectively increase the integrated intensity ratio of larger particles, however this analysis shows that significant amounts of dissolution are unlikely.

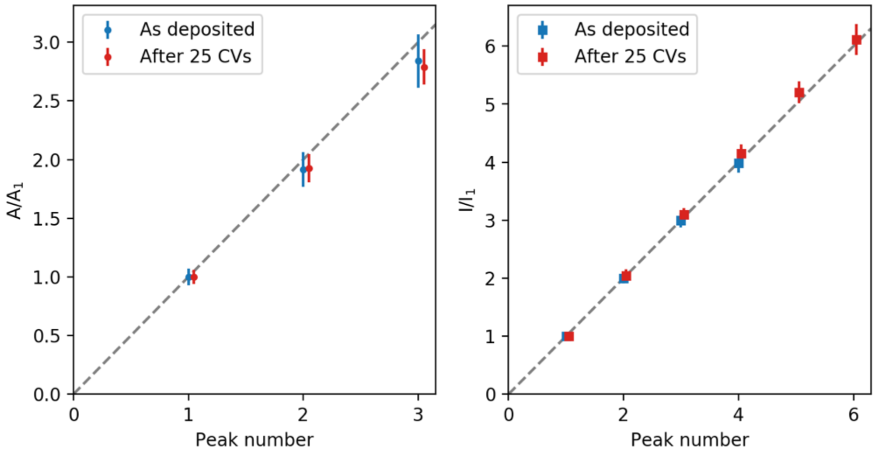

Figure 5.3.7: Projected area (left, points) and integrated intensity (right, squares) analysis of the fitted Pt_{923} cluster sample as-deposited (blue) and after 25 CVs between 0 and 1.20 V vs RHE at 0.1 Vs^{-1} (red). The peak values are represented as a ratio of the singlet peak value in each case. The grey dashed lines have a unity gradient and are used to guide the eye. Red data points have been offset for clarity.

The nearest neighbour distribution as-deposited agrees well with that predicted by a random distribution of impenetrable disks at the measured cluster density of 11500 per square micron, see Figure 5.3.8. Post-conditioning the nearest neighbour distribution has changed but it still agrees well with a random distribution albeit at the measured density of 5600 per square micron. Despite the formation of chain-like nanoparticles, the collective nanoparticle nearest neighbour distribution is still random which implies that the motion of the Pt_{923} clusters under potential conditioning is random or Brownian-like.

High magnification HAADF-STEM images of the coalesced platinum nanoparticles formed during potential conditioning are shown in Figure 5.3.9. The agglomerated nanoparticles have undergone significant sintering, including neck elimination[79], but the structures still resemble their constituent Pt_{923} clusters in many cases and the degree of coalescence appears to be confined to two dimensions. The nanoparticle edges are well defined and do not show any signs of platinum-oxide species which would appear as a dull halo[42] around the nanoparticle edge due to the presence of oxygen which has a low atomic number. In a number of cases spherical clusters are observed and these are depicted with white arrows in Figure 5.3.9. These clusters have projected areas in agreement with Pt_{923} singlets. Despite the fact that these clusters are in close proximity with multiple other clusters they have not sintered, possibly due to lattice misorientation[109]. The observed lattice fringes are 0.22 nm in almost all cases, which is consistent with Pt{111}. In some cases Fourier transform analysis reveals higher frequency lattice spacings such as 0.138 nm which is attributable to Pt{220}.

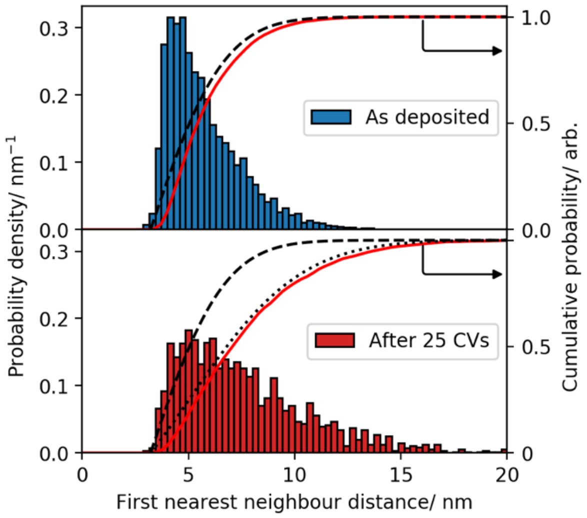

Figure 5.3.8: First nearest neighbour distribution of Pt_{923} (upper, blue) as-deposited at a density of 11500 per square micron and after 25 CVs between 0 and 1.20 V vs RHE at 0.1 Vs^{-1} (lower, red). The cumulative distributions are plotted as the red curve in each case. The black dashed curve is the cumulative distribution expected for a random distribution of particles with number density 11500 per square micron, as measured in STEM. The black dotted curve is the expected distribution for randomly arranged particles with a number density 5600 per square micron.

It has been shown that nanoparticle coalescence may proceed by neck formation, growth, and subsequent elimination[81,150] which is driven by a reduction in chemical potential in a classical sintering model[151]. The observed sintered nanoparticles have wide necks and large crystal domains through their length with is consistent with late stage sintering[187]. Many factors may influence the sintering mechanism, such as original crystal orientations, temperature, and original separation distance[188], and in some cases crystallisation of originally amorphous clusters may initiate at the sintering boundary[188]. Computational studies of cluster sintering mechanisms have found that relative crystal orientation preceding sintering has a large effect on the final coalesced product[188]; the degree of sintering for two Ta clusters facing each other with <100> facets was less than when the same clusters were oriented with adjacent <100> and <110> facets and this is due to the fact that the clusters had no opportunity to rotate and maximise their interfacial area owing to the high symmetry of the initial configuration in the former case[188].

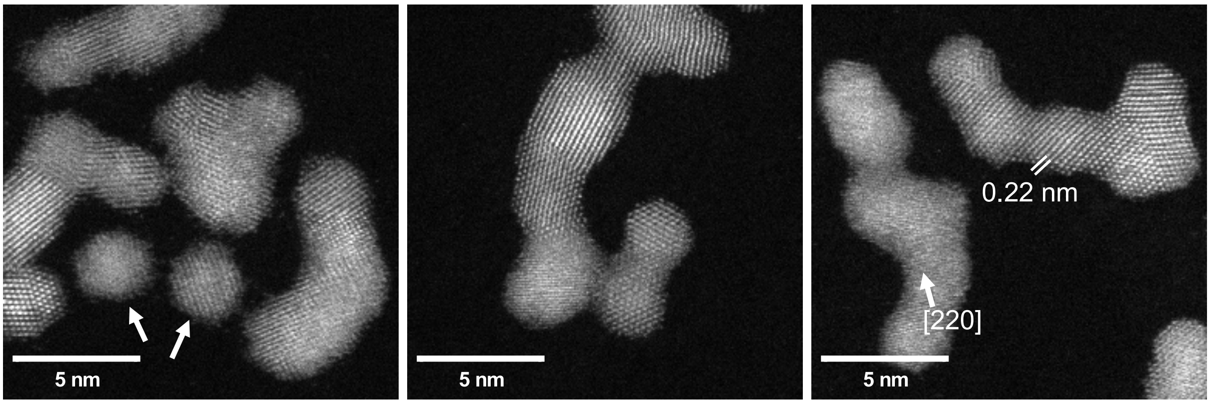

Figure 5.3.9: High magnification HAADF-STEM images of platinum agglomerates formed after potential cycling Pt_{923} sample between 0 and 1.20 V vs RHE at 0.1 Vs^{-1}. The white arrows show Pt_{923} clusters.

The HAADF-STEM image in Figure 5.3.10 shows an inhomogeneous cluster arrangement in one area of this sample compared to its surroundings. This feature is likely due to a trapped microscopic air bubble on the TEM grid surface during electrochemical cycling. The nanoparticle morphologies in areas external to this feature are chain-like consistent with Figure 5.3.5. Inside the feature, however, the nanoparticle morphologies are predominantly isolated spherical clusters. These clusters would have been isolated from the potential conditioning due to the lack of any conduction path through the air bubble and so the observed morphology is consistent with the as-deposited morphology as expected and confirm that the effects seen in this chapter are due to the potential conditioning.

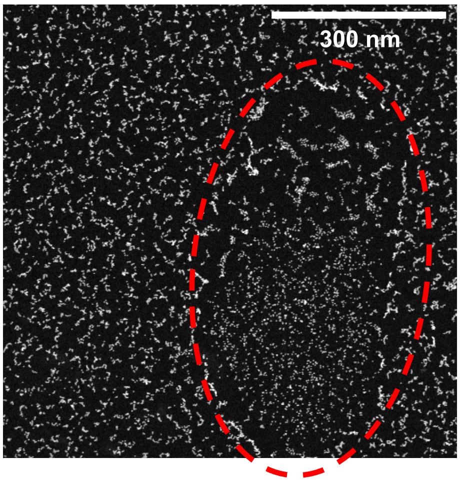

Figure 5.3.10: Low magnification HAADF-STEM image of the high density Pt_{923} sample after 25 potential cycles between 0 and 1.20 V vs RHE at 0.1 Vs^{-1}. The area approximately enclosed by the red dashed ellipse represents an artefact due to an air bubble on the sample.

5.4 Potential cycling up to 1.45 V vs RHE

Pt_{923} samples were then subjected to potential conditioning with an anodic limit of 1.45 V vs RHE which represents the plateau region of maximum HER performance. At potentials above 1.30 V vs RHE it has been shown that platinum may oxidise to Pt^{4+} which represents bulk oxidation[189].

5.4.1 Intermediate density: 6000 per square micron

The sample morphology as-deposited and after 10 CVs between 0 and 1.45 V vs RHE at 0.1 Vs^{-1} is shown in Figure 5.4.1. As was the case in sections 5.2 and 5.3, the Pt_{923} clusters have migrated to form groups and in many cases they have sintered to form chain-like structures.

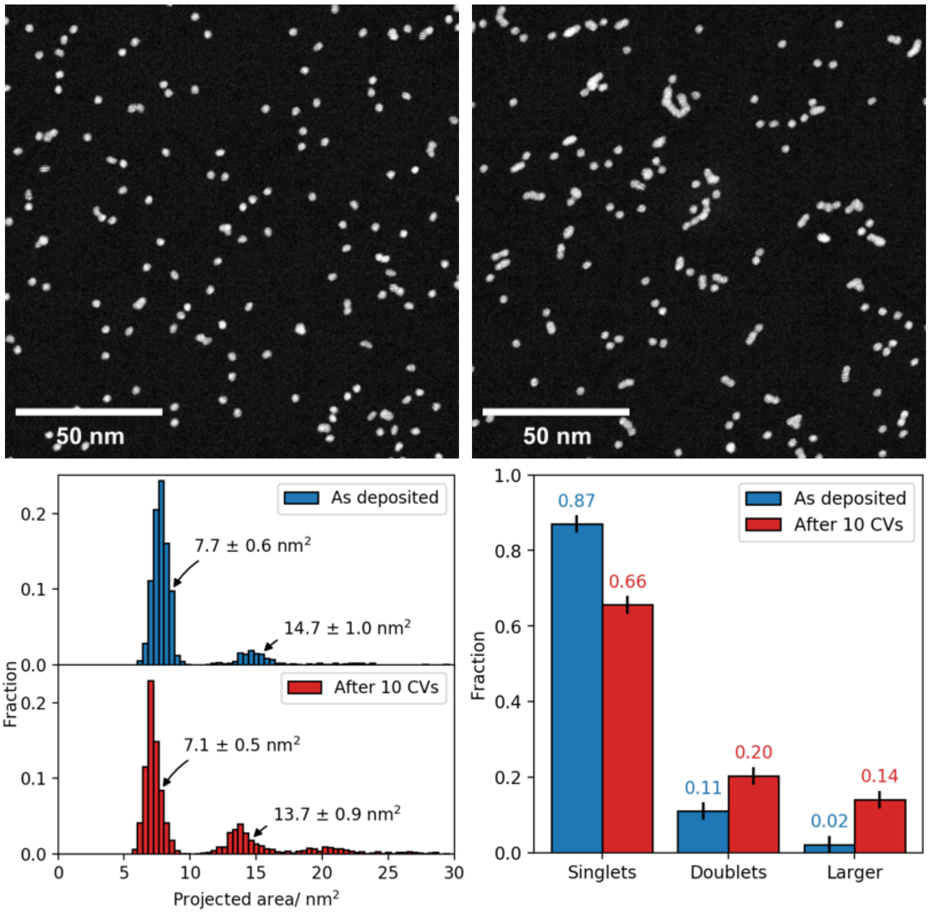

Figure 5.4.1: Pt_{923} after 10 CVs between 0 and 1.45 V vs RHE at 0.1 Vs^{-1}. (top row) HAADF-STEM images of Pt_{923} sample deposited at a number density of 6000 per square micron. (left) the sample morphology as-deposited, and (right) after 10 CVs. (bottom row) (left) size distribution of Pt_{923} as-deposited (blue) and post-conditioning (red), and (right) the population distribution in each case.

The size distribution confirms that the as-deposited sizes are quantised into Pt_{923} singlets and doublets etc., and the fraction of larger nanoparticles observed post-conditioning has increased. The singlet size has actually decreased from 7.7 ± 0.6 nm^2 to 7.1 ± 0.5 nm^2 projected area, which is substantial as the two distributions only overlap now within their standard deviations. Such a significant size decrease was not observed when potential conditioning to lower anodic potential limits. It is possible that the increased anodic limit has induced increased platinum dissolution[190] reducing the overall singlet size.

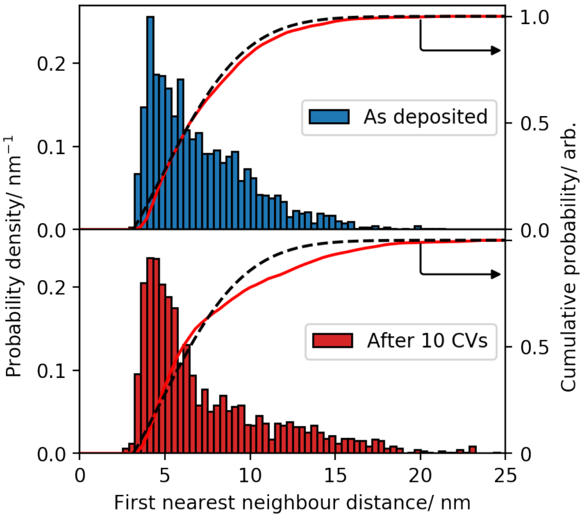

Figure 5.4.2: First nearest neighbour distribution of Pt_{923} (upper, blue) as-deposited at a density of 6000 per square micron and after 10 CVs between 0 and 1.45 V vs RHE at 0.1 Vs^{-1} (lower, red). The cumulative distributions are plotted as the red curve in each case. The black dashed curve is the cumulative distribution expected for a random distribution of particles with number density 6000 per square micron, as measured in STEM.

The population distribution shows that significant amounts of sintering have occurred. The fractional decrease in singlets is more than measured after 25 CVs with an upper anodic limit of 1.05 V vs RHE in section 5.2.1, but less than observed after 25 CVs with an upper anodic limit of 1.20 V vs RHE in section 5.3.1. Cluster grouping are sintering are evident in the STEM images, and the nearest neighbour distribution post-conditioning is positively skewed and deviates from the expected random distribution. The positive nearest neighbour distribution bimodality and skew is characteristic of the cluster grouping effect observed.

5.4.2 High density: 14500 per square micron

A high-density Pt_{923} sample was prepared to test whether sintering would occur with only a small number of potential cycles. The as-deposited in this case cluster density was 14500 ± 1000 per square micron. The sample morphology as-deposited can be seen in Figure 5.4.3. The size distribution shows that the nanoparticle sizes are quantised and that only 50 % of the deposited nanoparticles are Pt_{923} singlets due to surface agglomeration. This cluster density, equivalent to a surface coverage of 23.5 ± 2.1 %, effectively defines the cluster threshold where the majority of the sample remains the size in the cluster beam after surface diffusion. This coverage threshold is likely to increase with cluster-support interaction and cluster size, both of which would act to limit surface diffusion[79]. Using the projected area as an effective estimate of volume, Pt_{923} singlets account for only 23 % of the deposited material at this density.

The nearest neighbour distribution, shown in Figure 5.4.4, trends in agreement with that expected from a random distribution, however the actual values deviate by approximately 10 %. This is likely due to the fact that the model is based on uniform hard disks and not only are these clusters not hard, but half of the disks are larger than the modelled size d_{923} = 3.2 nm.

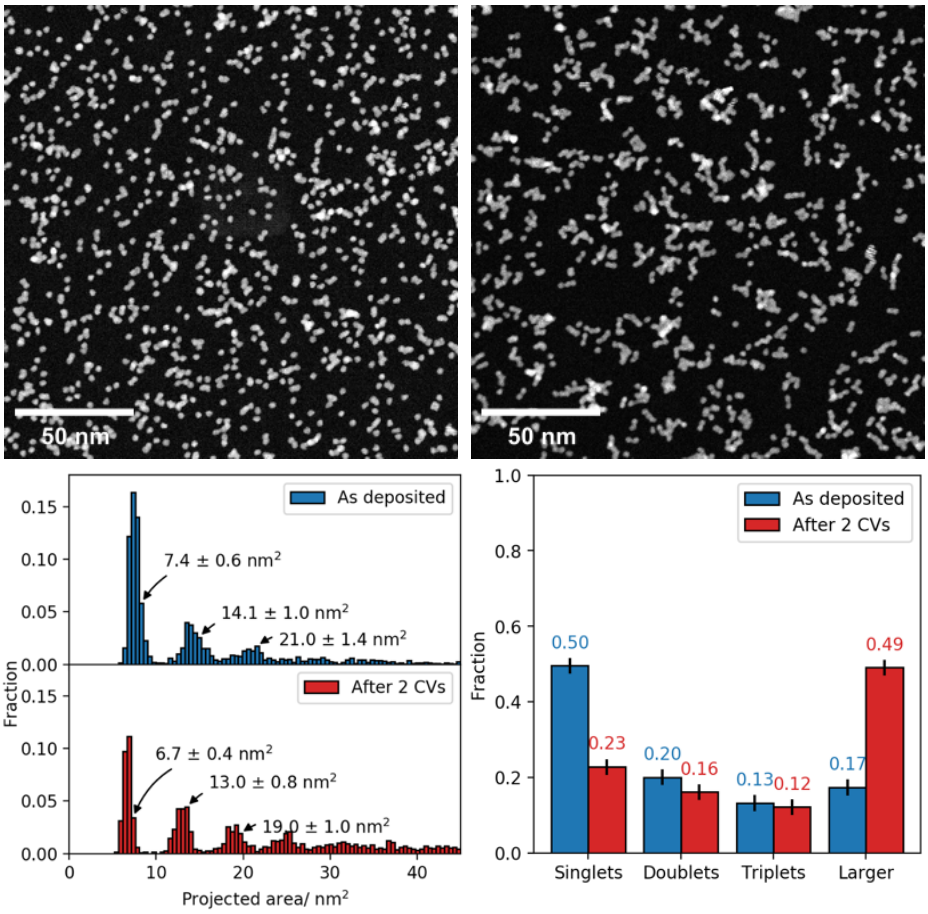

Figure 5.4.3: Pt_{923} after 2 CVs between 0 and 1.45 V vs RHE at 0.1 Vs^{-1}. (top row) HAADF-STEM images of Pt_{923} sample deposited at a number density of 14500 per square micron. (left) the sample morphology as-deposited, and (right) after 2 CVs. (bottom row) (left) size distribution of Pt_{923} as-deposited (blue) and post-conditioning (red), and (right) the population distribution in each case.

The sample was subjected to 2 CVs between 0 and 1.45 V vs RHE at a sweep rate of 0.1 Vs^{-1}. The sample morphology post-conditioning shows that over three quarters of the observed nanoparticles are now larger than Pt_{923} singlets. In this case the fraction of doublets and triplets also decreased at the expense of larger nanoparticles. The singlet size has decreased by approximately 10 %, which was observed in section 5.4.1. The number density post-conditioning decreased by approximately 50 % to 7500 ± 1500 per square micron, whereas the coverage remained the same within error at 22.0 ± 1.2 %. The trend in the nearest neighbour distribution post-conditioning is in agreement with a random distribution at the measure number density of 7500 per square micron, again showing a deviation due to arguments described previously.

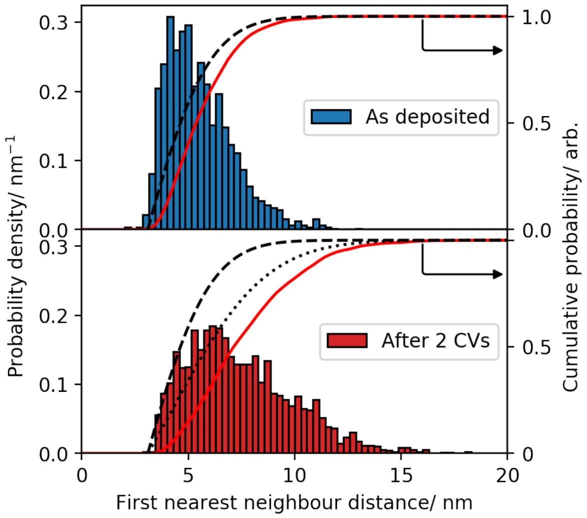

Figure 5.4.4: First nearest neighbour distribution of Pt_{923} (upper, blue) as-deposited at a density of 14500 per square micron and after 2 CVs between 0 and 1.45 V vs RHE at 0.1 Vs^{-1} (lower, red). The cumulative distributions are plotted as the red curve in each case. The black dashed curve is the cumulative distribution expected for a random distribution of particles with number density 14500 per square micron, as measured in STEM. The black dotted curve is the expected distribution for randomly arranged particles with a number density 7500 per square micron.

Integrated intensity analysis, shown in Figure 5.4.5, confirms that the cluster volumes are quantised and that the significant amounts of platinum dissolution due to potential cycling is unlikely, which is expected due to the small number of potential cycles.

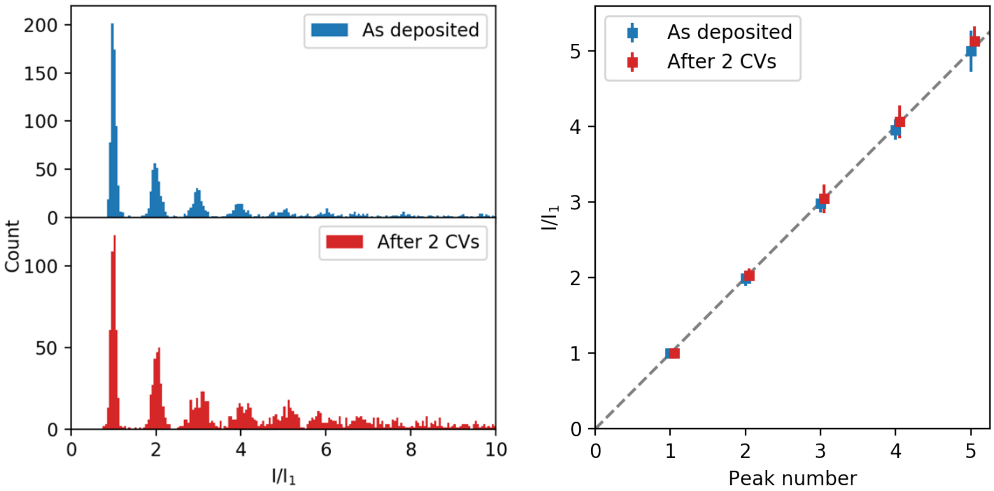

Figure 5.4.5: Integrated intensity analysis of Pt_{923} sample as-deposited and post-conditioning. (left) integrated intensity distribution of the Pt_{923} cluster sample as-deposited (top, blue) and after 2 CVs between 0 and 1.45 V vs RHE at 0.1 Vs^{-1} (bottom, red). The integrated intensity values (arbitrary units) are shown as a ratio of the Pt_{923} singlet value in both cases. (right) the integrated intensity peak values as a ratio of the singlet peak value in each case. The grey dashed lines have a unity gradient and are used to guide the eye. Red data points have been offset for clarity.

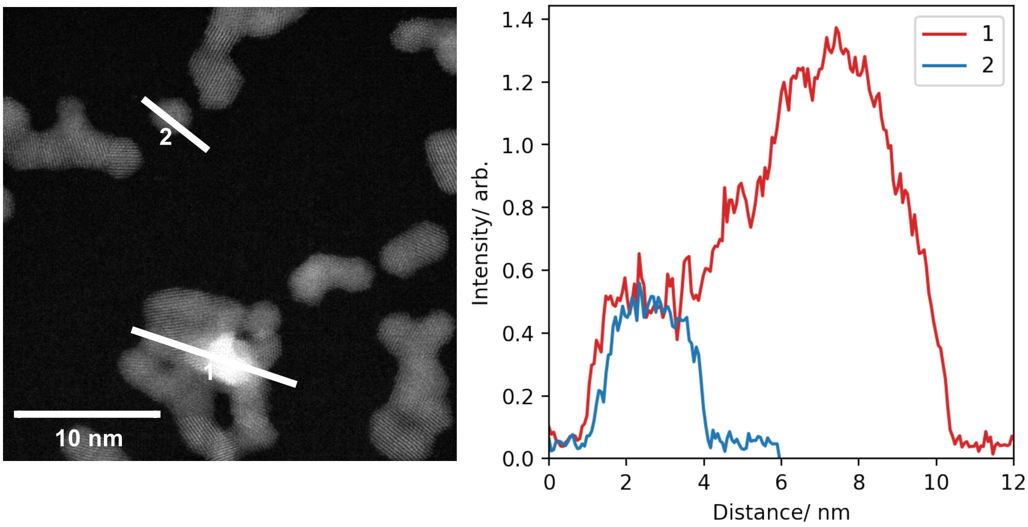

Figure 5.4.6: Intensity analysis of Pt_{923} sample after 2 CVs between 0 and 1.45 V vs RHE at 0.1 Vs^{-1}. (left) HAADF-STEM image and (right) corresponding line profiles.

High magnification HAADF-STEM imaging shown in Figure 5.4.6 and Figure 5.4.7 reveals that in many cases the nanoparticle structures formed by potential conditioning have sintered in the third dimension normal to the support. This is in contrast to the sintering observed at lower anodic potential limits which appeared to be isolated to two dimensions. This results in brighter features in the images due to the increased platinum thickness. In Figure 5.4.6 a line profile taken across a thicker region shows that the HAADF intensity is ~2.5 times more across this region compared to a singlet nanoparticle. The measured lattice spacings are consistent with low index platinum lattice spacings. The sintered nanoparticle geometries are still chain-like and the collision boundaries can be easily visualised in many cases.

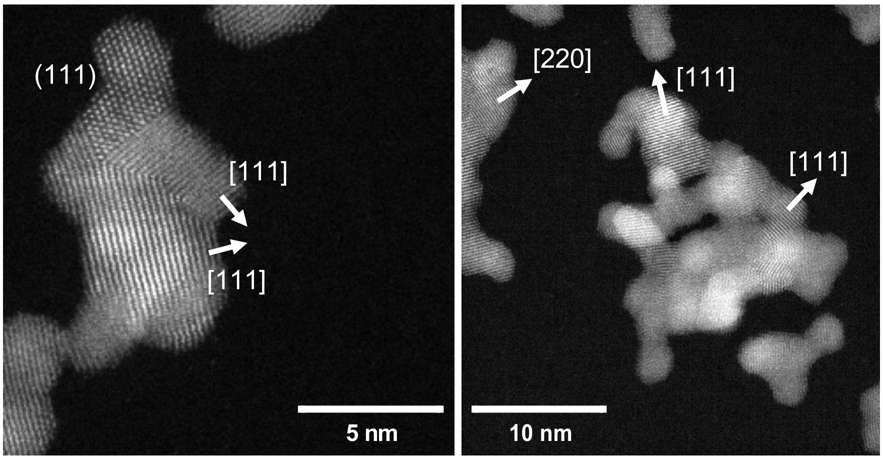

Figure 5.4.7: High magnification HAADF-STEM images of sintered nanoparticles conditioning after 2 CVs between 0 and 1.45 V vs RHE at 0.1 Vs^{-1}.

5.5 Beyond 1.45 V vs RHE

To test how the model Pt_{923} clusters behave under more extreme conditions, a sample was prepared and subjected to 125 CVs between 0 and 1.65 V vs RHE at 0.1 Vs^{-1}. The sample morphology after potential conditioning does not resemble the initial morphology at all, see Figure 5.5.1. The Pt_{923} clusters, initially well-defined, have formed numerous structures including large spherical nanoparticles, branch-like structures, and some nanoparticles which are smaller than the initial clusters as-deposited. There is no order in the nanoparticle size distribution post-conditioning demonstrating the breakdown point of the initially prepared well-defined cluster sample.

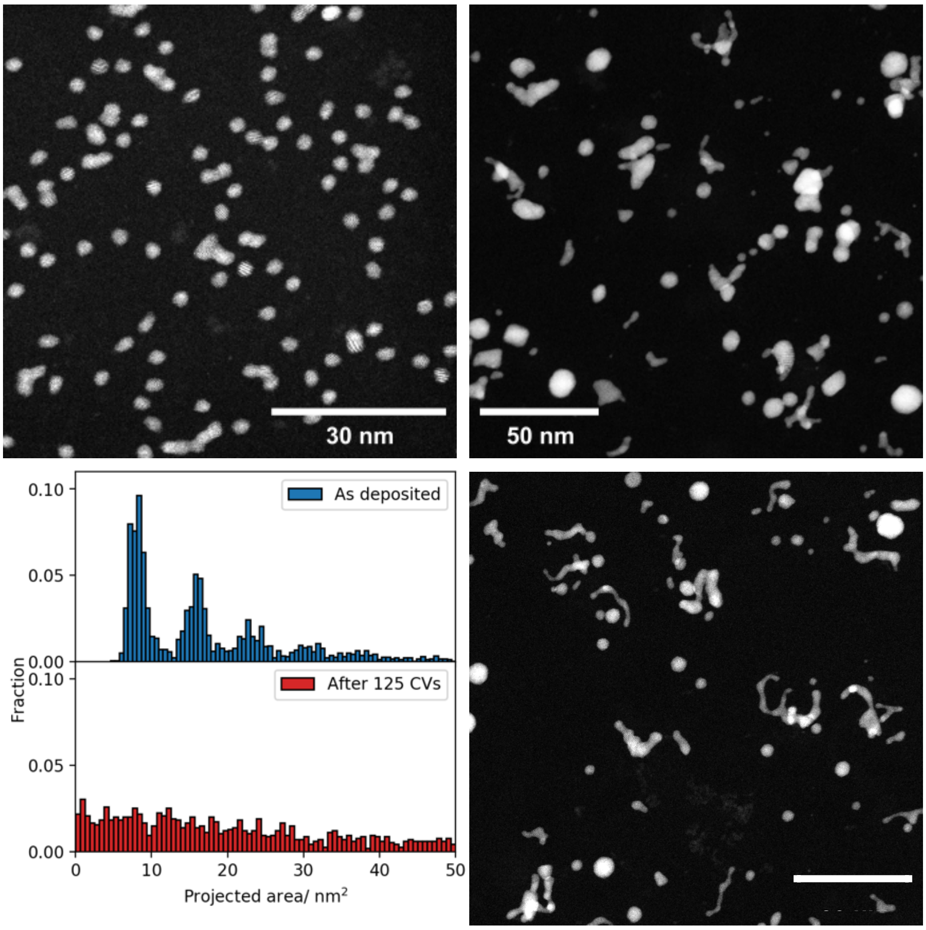

Figure 5.5.1: Pt_{923} after 125 CVs between 0 and 1.65 V vs RHE at 0.1 Vs^{-1}. (top left) HAADF-STEM image of Pt_{923} sample as-deposited, and (top and bottom right) post-conditioning. (bottom left) size distribution of Pt_{923} sample (top, blue) as-deposited and (bottom, red) post-conditioning.

High magnification imaging of the nanoparticle morphologies post-conditioning, shown in Figure 5.5.2, reveals an array of new structures previously unseen in Pt_{923}. Most of nanoparticles, including those with chain-like morphologies, had

FCC based structures. The observed nanoparticle also exhibit decahedral and icosahedral structures, both of which are twinned structures.

Previous studies[43] into the structures of mass-selected platinum clusters prepared through magnetron sputtering revealed predominantly FCC structures, such as cuboctahedrons. Icosahedral platinum clusters ~9 nm in edge length have been synthesised before[191], however it is believed that the icosahedral structure is only favourable in small clusters due to internal strain[13,191]. The structures of mass-selected gold clusters have previously been shown to change under reaction conditions[37]. The structures observed represent a change from FCC Pt_{923} clusters and may be formed from the coalescence of smaller nanoparticles[188] or possibly dissolution and redeposition due to potential cycling. The degradation of platinum at high anodic limits has been well documented[86,94,106,192].

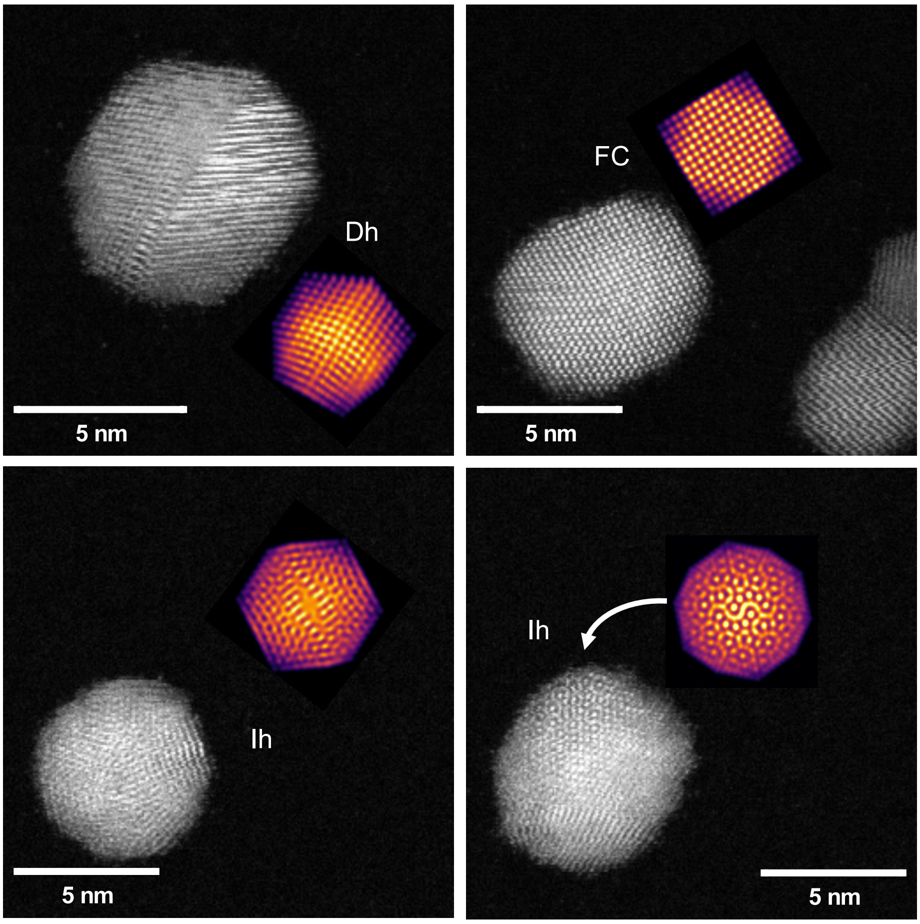

Figure 5.5.2: HAADF-STEM images of nanoparticles observed after Pt_{923} cluster sample was subjected to 125 CVs between 0 and 1.65 V vs RHE at 0.1 Vs^{-1}. The observed structures include (clockwise from top left): decahedral, FCC, twinned nanoparticle with icosahedral features, and icosahedron. The coloured insets are the matched simulated platinum cluster structures from a kinematically simulated atlas.

The increased anodic potentials used in this experiment have been shown to dissolve more platinum during potential cycling[190], and when combined with the large number of potential cycles it is likely that significant amounts of dissolution and redeposition have occurred during the experiment to produce the significant change in nanoparticle morphology observed. The presence of nanoparticles smaller than Pt_{923} after potential cycling are indicative of dissolution and redeposition as these would not be produced by Smoluchowski ripening. The evolution of different structures due to potential cycling will require more experiments to elucidate their observation, however this experiment clearly demonstrates an upper limit to the anodic potential and number of cycles that would allow for benign electrochemical activation.

5.6 Control Experiments

The potential cycling experiments have shown that cluster migration and coalescence is the primary form of ripening and that the degree of ripening is affected by the anodic potential limit. STEM imaging of the same areas after electrochemical conditioning provide a snapshot of the system as it is evolving due to energy input, however it does not afford information as to how cluster migration is affected at any individual potential.

5.6.1 Anodic sweep

As the cluster migration appears to be affected by anodic potential, a Pt_{923} sample was prepared and subjected to one linear sweep voltammetry (LSV) experiment between 0 and 1.45 V vs RHE at a sweep rate of 50 mVs^{-1}. The sample morphology as-deposited and after LSV is shown in Figure 5.6.1.

The clusters remain mostly isolated Pt_{923} singlets as demonstrated in Figure 5.6.1 and Figure 5.6.2. The LSV does not appear to have induced significant cluster migration, or in fact any sintering. The nearest neighbour distribution does appear to be more skewed towards smaller nearest neighbour distances, which is the behaviour consistent with cluster migration, however the deviation is small when compared to the potential cycling experiments.

This cluster density used in this experiment is consistent with that used in section 5.2.2 where Pt$_{923}$ was subjected to 25 CVs between 0 and 1.05 V vs RHE. In the latter case there was no significant sintering, due to the reduced potential, however the larger number of cycles did induce significant cluster migration. This experiment points towards successive oxidation and reduction as the driver for cluster migration.

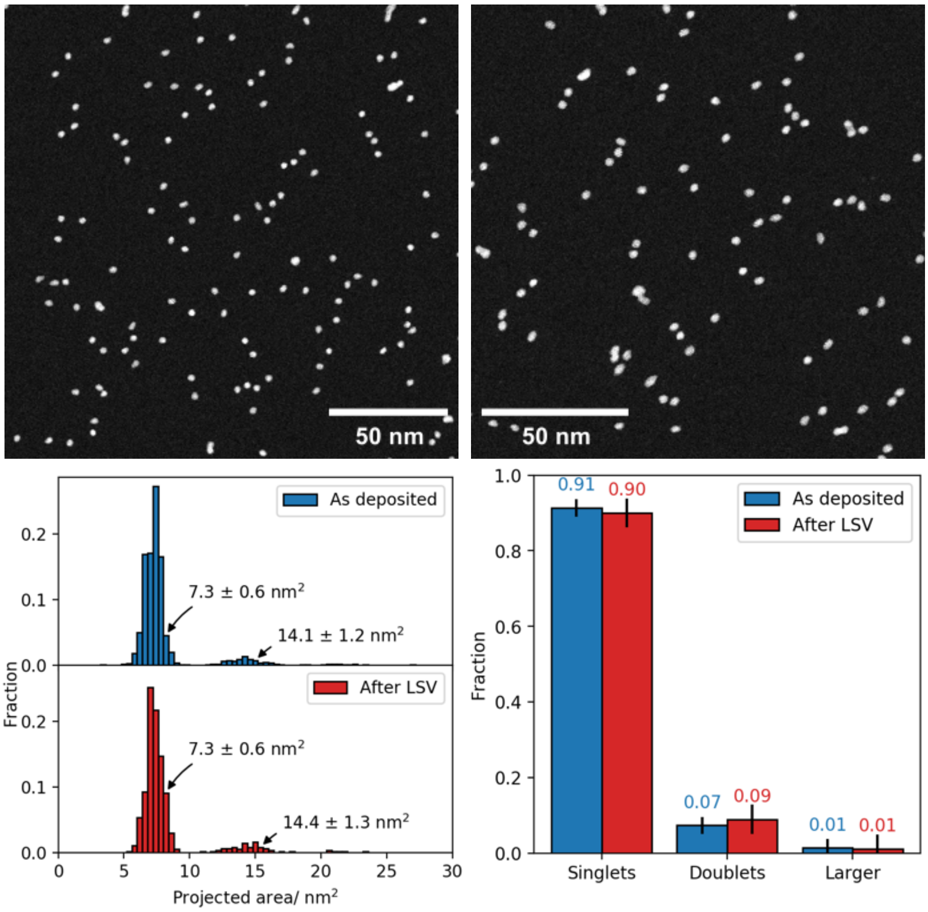

Figure 5.6.1: Pt$_{923}$ sample after LSV from 0 to 1.45 V vs RHE at 50 mVs^{-1}. (top row) HAADF-STEM images of Pt$_{923}$ sample (left) as-deposited, and (right) after LSV. Note the different image scales. (bottom row) (left) size distribution of Pt$_{923}$ as-deposited (blue) and after LSV (red), and (right) the population distribution in each case.

In this chapter all of the previous potential cycling experiments have been initiated in the anodic direction, meaning that on the final sweep the platinum is oxidised and then reduced before the experiment is terminated at 0 V vs RHE. In this case, however, the LSV experiment was terminated at 1.45 V vs RHE where the platinum is expected to be oxidised[189]. High magnification HAADF-STEM imaging was performed to observe the nanoparticle structures after LSV as shown in Figure 5.6.3. The observed nanoparticles have measured lattice spacings such as 0.22 and 0.19 nm which are with consistent Pt(111) and Pt(200). The expected lattice spacings for platinum oxide are smaller than that of pure platinum due to its reduced lattice constant of 0.31 nm[193]. The imaged nanoparticles do not appear to have an oxide shell and have cuboctahedral structures which is as expected for as-deposited Pt_{923}.

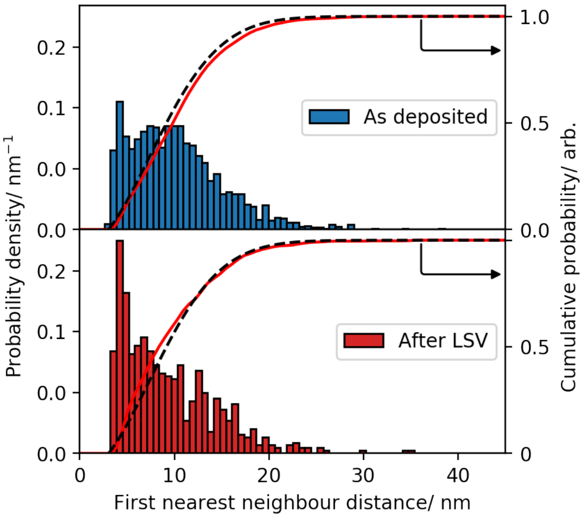

Figure 5.6.2: First nearest neighbour distribution of Pt_{923} (upper, blue) as-deposited at a density of 3000 per square micron and after LSV from 0 to 1.45 V vs RHE at 50 mVs^{-1} (lower, red). The cumulative distributions are plotted as the red curve in each case. The black dashed curve is the cumulative distribution expected for a random distribution of particles with number density 3000 per square micron, as measured in STEM.

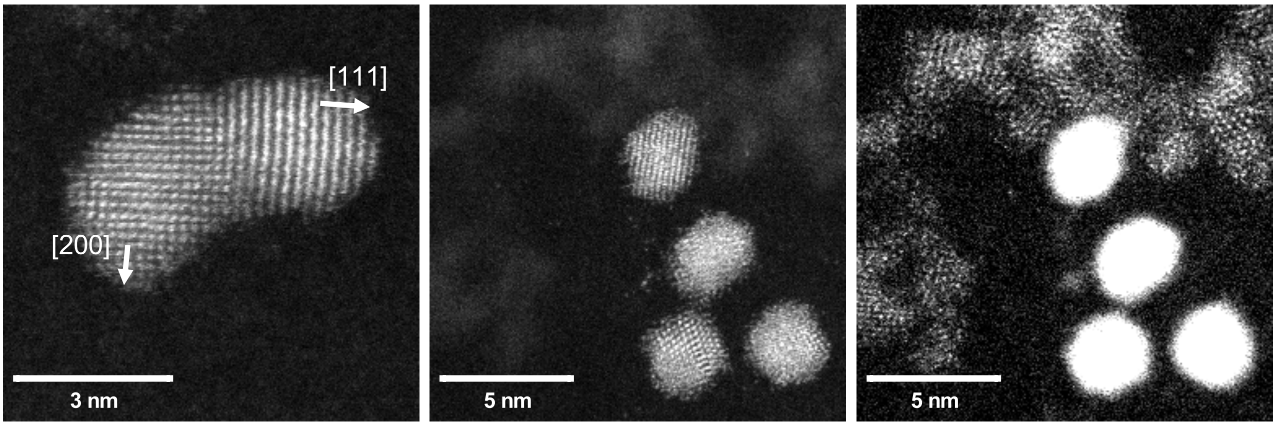

Figure 5.6.3: High magnification HAADF-STEM imaging of Pt_{923} sample after LSV from 0 to 1.45 V vs RHE at 50 mVs^{-1}. (left) platinum nanoparticle agglomerate with lattice spacings consistent with pure Pt, (center) group of platinum clusters, and (right) same image as center taken with different defocus and image contrast showing platinum atoms.

5.6.2 Potential hold

Two Pt_{923} samples were deposited with a density of 6000 ± 500 clusters per square micron and one was subjected to potential holding at a cathodic potential of 0 V vs RHE and the other was held at an anodic potential of 1.20 V vs RHE. In both cases a step potential was applied with a step width of ten seconds. In both cases no significant amounts of sintering occurred. The nearest neighbour distributions are shown in Figure 5.6.4. In both cases the nearest neighbour distribution post-hold is slightly skewed to smaller nearest neighbour distances, however the deviation is small compared to the as-deposited distribution and expected distribution and much smaller than the change observed after potential cycling indicating that successive oxidation and reduction is necessary for cluster migration.

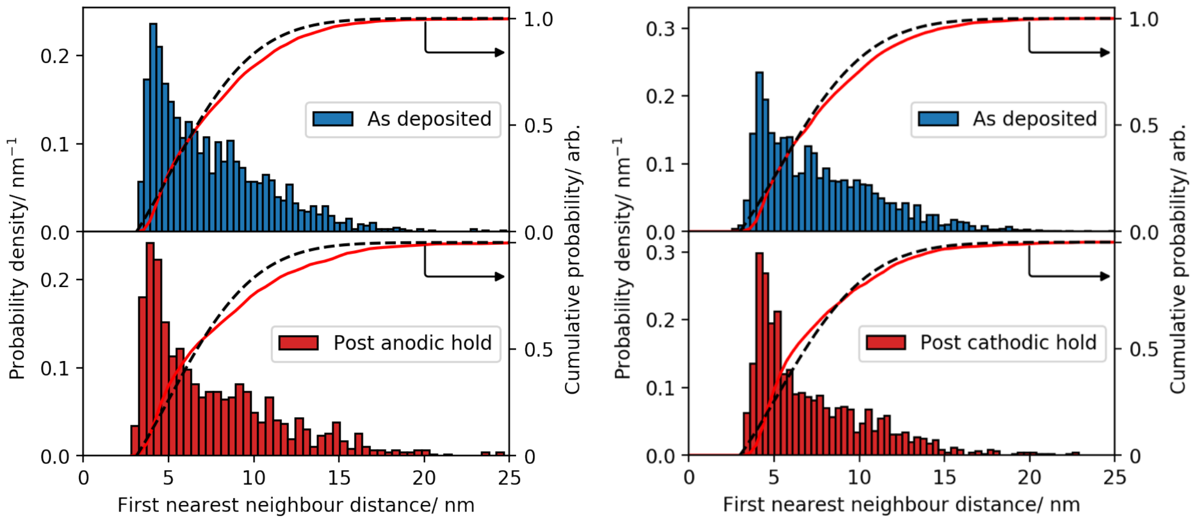

Figure 5.6.4: First nearest neighbour distribution of Pt_{923} (upper, blue) as-deposited at a density of 6000 per square micron and after potential holds (lower, red) at anodic (left) and cathodic (right) potentials. The cumulative distributions are plotted as the red curve in each case. The black dashed curve is the cumulative distribution expected for a random distribution of particles with number density 6000 per square micron, as measured in STEM.

5.6.3 Au_{923}

In an attempt to elucidate the effect of nanoparticle oxidation on the observed ripening, Au_{923} samples were produced and subjected to potential cycling. Gold is more resistant than platinum to oxidation, requiring an anodic potential larger than 1.20 V vs RHE. Both platinum[89] and gold[194] are known to be carbon oxidation catalysts, so by restricting the applied potential window to between 0 and 1.05 V vs RHE it is possible to isolate the effect of nanoparticle oxidation. Au$_{923}$ were produced using the magnetron sputtering gas aggregation cluster source with an Au target (Pi-KEM) and soft-landed at 1 eV onto an amorphous carbon TEM grid.

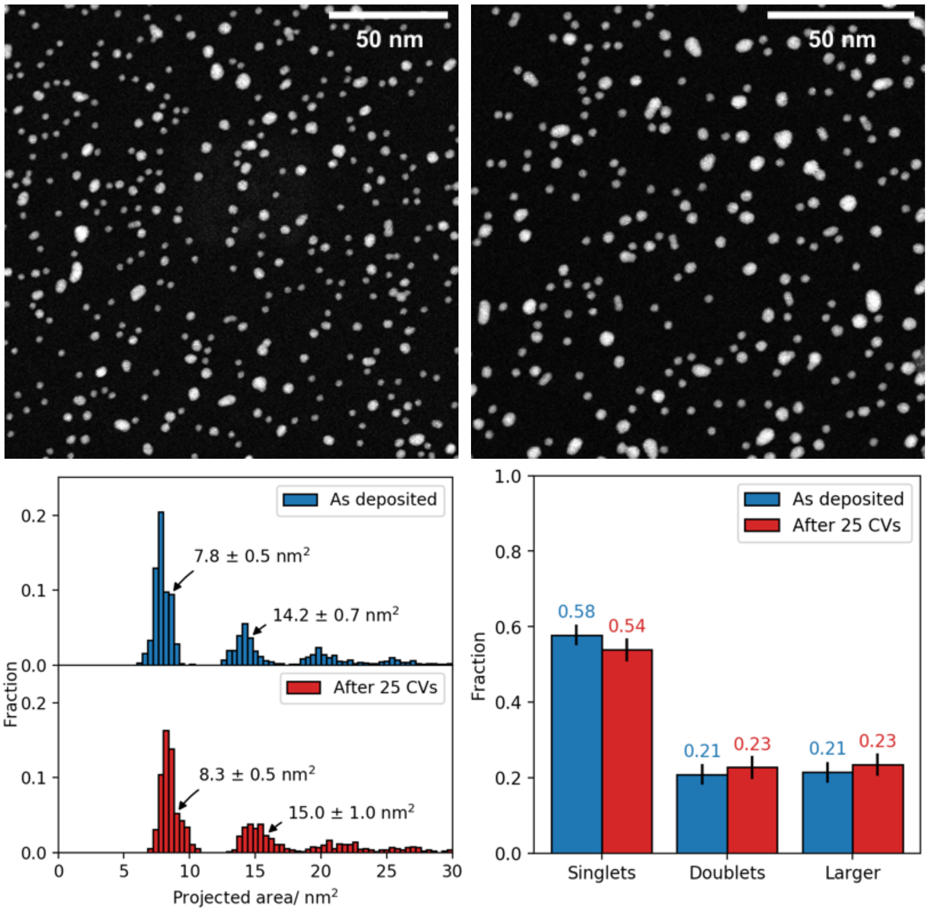

Figure 5.6.5: Au$_{923}$ sample after 25 CVs between 0 and 1.05 V vs RHE at 0.1 Vs^{-1}. (top row) HAADF-STEM images of Au$_{923}$ (left) as-deposited, and (right) after 25 CVs. Note the difference image scales. (bottom row) (left) size distribution of Au$_{923}$ as-deposited (blue) and post-conditioning (red), and (right) the population distribution in each case.

The sample morphology as-deposited can be seen in Figure 5.6.5. It is worth noting that Au$_{923}$ appears to have a different sintering mechanism compared to Pt$_{923}$. Whilst Pt$_{923}$ tends to form chain-like structures during coalescence, coalesced Au$_{923}$ clusters form more spherical nanoparticles. This is likely due to many factors including cluster structure, as Au$_{923}$ commonly have five-fold characteristics[44], the differing melting temperatures of the materials[195], and different surface energies.

The sample size distribution as-deposited and post-potential conditioning is shown in Figure 5.6.5. The size distribution is quantised as multiples of Au_{923} singlets, similar to that observed with Pt_{923}. The population distribution, however, shows that no significant sintering occurs due to the potential conditioning. Under the same potential conditions, and at a slightly smaller cluster density in section 5.2.1, the Pt_{923} sample had a 12 % reduction in singlets due to sintering. The nearest neighbour distribution shown in Figure 5.6.6 also shows no significant deviation from the initial distribution after potential cycling. A statistical analysis shows no change in number density or coverage, within one standard deviation, due to the potential conditioning. Gold clusters have been shown to sinter more readily than platinum[182], however a change in number density due to the potential conditioning was not observed.

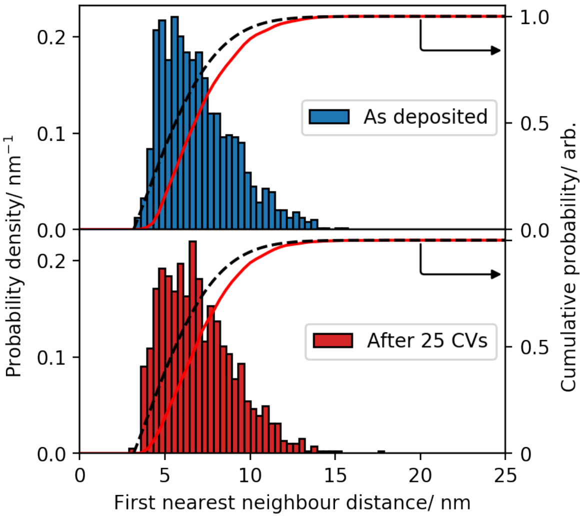

Figure 5.6.6: First nearest neighbour distribution of Au_{923} (upper, blue) as-deposited at a density of 8000 per square micron and after 25 CVs between 0 and 1.05 V vs RHE at 0.1 Vs^{-1} (lower, red). The cumulative distributions are plotted as the red curve in each case. The black dashed curve is the cumulative distribution expected for a random distribution of particles with number density 8000 per square micron, as measured in STEM.

5.7 Discussion

A relationship between the degree of nanoparticle ripening and the anodic limit of electrochemical potential conditioning in deaerated sulphuric acid has been established. Potential conditioning involving cyclic voltammetry has been widely used in the past to achieve a standard platinum surface that could be compared between laboratories[196]. As many studies now involve shaped nanoparticles[28,30,31,197], it is important to ensure that the nanoparticle structure studied is the same described and often imaged in TEM. These experiments show that the effect of potential conditioning on platinum nanoparticles on carbon supports, even to modest potentials such as 1.05 V vs RHE, is not benign and that this should be considered before any electrochemical activation.

Specifically, potential cycling induces a nanoparticle migration effect. Hartl et al.[93] have studied the effect of potential conditioning on physically deposited platinum clusters on amorphous carbon supports previously, albeit the clusters were not mass-selected as in this study. Cluster migration was observed when the clusters were subjected to potential conditioning between 0.06 and 1.06 V vs RHE in perchloric acid electrolyte. In the same study it was found that oxygenated and deaerated electrolyte led to cluster migration and sintering, however sintering was suppressed when the electrolyte was saturated with carbon monoxide, possibly due to repulsion between dipole moments of the adsorbed CO molecules on the platinum clusters. The authors also found that potential cycling in a limited potential window, up to 0.55 V vs RHE, did not induce cluster migration and this has been confirmed by other groups through accelerated stress testing[86].

Castanheira et al.[86,172] observed platinum migration and sintering on carbon supports using step potential cycling between 0.6 and 1.0 V vs RHE that simulated PEM fuel cell load cycling. The degree of sintering and support corrosion increased as the anodic limit was increased to 1.5 V vs RHE to simulated start-up/shut-down conditions in their experiment. Similar results were found by Zana et al.[94], who also showed that platinum migration and coalescence can be reduced even at high anodic potentials if platinum is not reduced during the cycle, ie. by cycling between 1.0 and 1.5 V vs RHE. The experiments described in this chapter confirm the results found by Hartl et al. in many cases, including that potential holds do not induce migration, but also build upon different aspects such as the effect of potential conditioning and the inherent suppression of Ostwald ripening by using mass-selected clusters[198].

The type of nanoparticle ripening observed due to potential conditioning is migration and sintering, also known as Smoluchowski ripening and sometimes best explained as ‘hit-and-stick’[84,93]. STEM imaging confirmed that the branch-like structures are formed from the collisions of two or more clusters, and often the collision leaves a characteristic grain boundary in the sintered nanoparticle[188,199]. Further image analysis, confirmed by both the projected area and integrated HAADF intensity distributions, confirms that the larger branch-like nanoparticles are made up of quantised units of Pt_{923} clusters and that nanoparticles made up of precisely six Pt_{923} clusters have been observed using integrated intensity analysis. Whilst the STEM imaging clearly points towards predominantly Smoluchowski ripening, Ostwald ripening must also be considered. As an atomistic process Ostwald ripening would be expected to shrink and grow clusters at different rates depending on their size. This mechanism would produce clusters smaller and larger than singlets at sizes that are not quantised[80]. This effect has not been observed after potential cycling up to an anodic limit of 1.45 V vs RHE. As the driving force for Ostwald ripening is the reduction of overall surface energy[199] by growing larger clusters at the expense of smaller ones, this effect is effectively suppressed by size-selection of the initially deposited clusters. Wettergren et al.[198] have studied the effect of nanoparticle ripening on unimodal and bimodal mass-selected Pt_{22} and Pt_{68} clusters. They found that both unimodal Pt_{22} and Pt_{68} samples had high sintering resistance at elevated temperatures over 21 hours, however Pt_{68} grew at the expense of Pt_{22} in the combined Pt_{22}+Pt_{68} sample under the same conditions, showing that Ostwald ripening can be suppressed by well-defined cluster distributions.

Cluster migration is induced at all anodic limits tested in this study: 1.05, 1.20, and 1.45 V vs RHE. Platinum cluster migration on carbon supports has been observed previously during potential cycling[31,86,93]. It is difficult to determine whether higher anodic limits induce more migration. Given that the sweep rate was 0.1 Vs^{-1} in all cases a higher anodic potential would mean that the clusters are at anodic potentials for longer times and therefore longer migration distances would be expected. LSV and anodic hold experiments at 1.20 V vs RHE showed that no significant migration occurred over 10 s which suggests that the observed migration is driven by repetitively oxidising and reducing the platinum and carbon support. It has been shown previously that the interaction between platinum and carbon is reduced when either the platinum[200] or carbon[201] is oxidised and the reduction of oxidised carbon supports has also been shown to induce cluster migration[202]. Carbon oxidation may also lead to support degradation[86,172] and subsequent nanoparticle detachment[86,94,172,203] which is thought to arise from the weakened platinum-carbon interaction[31]. At all anodic potential limits tested carbon oxidation is possible (E^0_{C/CO_2} = 0.207 V vs. NHE at 298 K) although it is well known to be kinetically slow[172,204]. The oxidation and reduction of functionalised carbon species such as quinones[205] may play a role in weakening the platinum-carbon interaction.

A classic mean free path model can be used to explain how the nanoparticle density and number of potential cycles affects the number of collision events between clusters. In the two-dimensional case, clusters may be modelled as disks with radius r and a collision will occur when the center of any two disks are within $2r$ of each other. In this case a cluster will sweep out an area $4rv\Delta t$ over time Δt where the individual cluster linear velocity is v. Therefore N diffusing clusters will cover an area $A = Nr\sqrt{8}\bar{v}\Delta t$ in the same time and so the collision probability is $P = \rho r\sqrt{8}\bar{v}\Delta t$ where $\rho = N/A_T$ is the number density of the system. As the number of cycles is directly proportional to time it can be assumed that more cycles will induce more collisions. If every collision results in sintering then the behaviour may be considered ‘hit-and-stick’ as described earlier. In many cases, especially at 1.05 V vs RHE anodic limit, clusters are observed to have grouped together as a result of potential cycling with an edge-edge spacing of less than 1 nm. The clusters have likely collided in this case and are interacting in some way but sintering is not energetically favourable. Mass-selected platinum cluster arrays have been observed before for cluster sizes 2-5 nm[182,206], which exhibit a characteristic edge-edge separation of ~1 nm. The study by Bardotti et al.[182] was mostly inconclusive as to the nature of the cluster-cluster gap, although the surface passivation of platinum due to trace species in vacuum, such as carbon monoxide, was considered due to platinum’s high reactivity. It is possible the support affects the electronic structure of the system to create a barrier to sintering[206]. As to whether sintering occurs as a result of collision is more complex than a simple hit-and-stick mechanism.

In contrast to the migration effect observed, the degree of sintering increases with the anodic potential limit. At the anodic potential limits applied in this experiment platinum undergoes different degrees of oxidation. It has been suggested that hydroxyl ions may adsorb onto Pt(111) surfaces above 0.55 V vs RHE[207] depending on the anion interaction. At higher potentials 2D platinum oxide species form on Pt(111) at 1.05 V vs RHE and 3D PtO_2 starts to form and grow above 1.30 V vs RHE[207]. These results have been confirmed on platinum nanoparticles as small as 1 nm[189] using in-situ x-ray photoelectron spectroscopy. The HER performance trends described in the previous chapter appear to roughly coincide with the onset of these platinum oxidation potentials: 1.05 V vs RHE is the upper potential limit before HER performance improvement and 1.30 V vs RHE is the start of the HER performance plateau. The experiments performed in this chapter shed more light on the HER performance data.

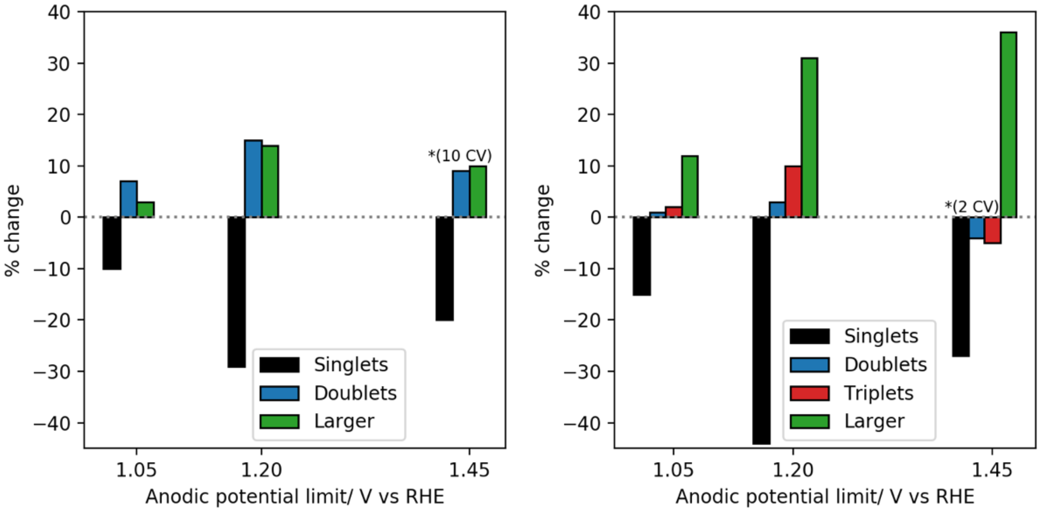

Figure 5.7.1: Comparison of the changes in particle size after potential conditioning (left) at intermediate cluster densities (6000-7000 per square micron) and (right) at high cluster densities (11500-14500 per square micron). 25 CVs were performed at anodic limits of 1.05 and 1.20 V vs RHE, whereas 10 and 2 CVs were performed at intermediate and high densities respectively for an anodic limit of 1.45 V vs RHE as labelled on the plots.

A comparison of the observed population changes for each anodic limit is shown in Figure 5.7.1. Considering the intermediate cluster density experiments, 6000-7000 per square micron, the data shows that the proportion of singlets decreases with increasing anodic limit. At 1.45 V vs RHE the sample was subjected to only 10 CVs compared to 25 in the other two cases, however the mean free path argument suggests that the number of sintering events would only increase with more potential cycles. Despite this the decrease in the singlet fraction is larger than that observed at 1.05 V vs RHE. In the high-density case it can be seen that potential cycling to an anodic limit of 1.45 V vs RHE induces significant sintering such that even the fraction of doublets and triplets decrease as a result of sintering into larger nanoparticles. This result was achieved with only two potential cycles, demonstrating that even a small number of potential cycles can have a large impact on the sample morphology depending on the potentials applied. It also shows how critical the nanoparticle density is to limiting coalescence. The higher degree of sintering is likely brought on by two effects. Firstly any contaminants adsorbed on the platinum surfaces are more likely to be oxidatively removed at higher potentials[31], and the presence of contaminants is thought to be at the core of the trend in HER data shown in the previous chapter. Surface contamination is a possible cause for the characteristic spacing observed between neighbouring platinum clusters[182]. Secondly, it is well known that oxidation and reduction cycles roughen platinum surfaces and above can lead to dissolution[162,189,208–210]. As platinum surfaces are reduced they will restructure and clusters in close proximity may sinter due to the movement of surface material possibly bridging the gap[129]. Alternatively, platinum dissolved in the electrolyte due to surface restructuring may be redeposited onto neighbouring clusters and effectively bridge the gap. The work by Zana et al.[94] confirms that platinum reduction is needed to induce coalescence. Full coalescence follows initial necking and subsequent neck growth[81]. At higher anodic potentials platinum will form a thicker oxide shell and subsequent reduction will involve the movement of more material, leading to increased chances of necking and coalescence between neighbouring clusters.

From this information the behaviour of the system can be broadly explained. Potential cycling induces some nanoparticle mobility per cycle as long as the platinum is both oxidised and reduced in the cycle[93,94]. The platinum-carbon interaction is weakened by the formation of oxidised platinum[200] and carbon[201] species allowing the clusters to diffuse more freely on the surface where they may collide and interact with another cluster. Any surface adsorbed species are removed due to high anodic potentials[31]. Platinum reduction in the cathodic sweep induces cluster surface roughening. For clusters in close proximity the movement of platinum material due to roughening may bridge the gap and initiate necking and subsequent sintering. This process is exacerbated for higher anodic limits to the reduced cluster-surface interaction and increased volume of material involved during platinum reduction.

The control experiments agree with this interpretation in a few ways. Firstly, anodic and cathodic potential hold experiments do not induce significant amounts of migration or sintering, this is in agreement with previous studies[93,94]. The observation that cycling is needed induce migration is thought to arise from the changing hydrophobicity of the carbon support due to intercalation of oxygen and subsequent cluster wetting[93]. The lack of observed migration by Au_{923} clusters under the same conditions as Pt_{923} adds to this interpretation as gold oxidises at higher potentials and therefore does not undergo the oxidation and reduction needed to induce migration.

In summary well-defined Pt923 clusters deposited onto amorphous carbon TEM grids are used as model catalysts and subjected to electrochemical conditioning or 'activation' in acidic electrolyte. HAADF-STEM imaging reveals that potential conditioning induces migration and subsequent coalescence. The amount of sintering is found to be dependent on the anodic potential limit of the conditioning cycles, where higher anodic potentials induce more sintering. Ostwald ripening is suppressed due to the well-defined cluster size, demonstrating the versatility of size-selection towards creating model nanoparticles.

6 The effect of plasma treatment on Pt_{923} clusters

In the field of electron microscopy the high energy electron beam has been known to produce contamination build-up leading to image artefacts, due to a charge and heating effect[135,136]. A technique called 'beam showering'[42,198,211] is often employed in-situ which can help to mitigate this problem. Beam showering involves subjecting a sample to the electron beam at low current density for prolonged times. This technique, however, is localised to a small area of beam exposure, typically no more than a square micron, and it is known that prolonged beam exposure produces a heating effect which can cause nanoparticle sintering and restructuring[212].

Plasma cleaning is a low-cost technique that is commonly used in surface science to functionalise surfaces[213–215] and remove organic contaminants. In contrast to beam showering the plasma exposure area can be on the order of tens of centimeters, and the choice of plasma gas can produce different types of surface functionalisation. Duan et al.[216] showed that just 10 seconds exposure to low intensity oxygen plasma can be enough to remove organic and fluorine-based surface contaminants and Gehl et al.[215] showed that other plasma gases, including hydrogen and nitrogen, can also achieve the same effect. Plasma etching is of particular importance in the field of microelectronics[214,217] to increase bonding strengths between materials and is commonly employed to remove capping ligands used during wet synthesis of nanoparticles[218,219].

Whilst plasma treatment may remove many surface contaminants, the physical effect on the surface and subjects of interest must be addressed. Studies on silver nanoparticles have shown that oxygen plasma treatment may induce Ostwald ripening[216,220] and coalescence[216,220–222]. Plasma treatment studies on platinum nanoparticles have shown that oxygen plasma treatment may induce sintering[223] and surface smoothing[224].

Gehl et al.[215] studied the effect of plasma treatment on well-ordered platinum-based nanoparticle arrays. They found that oxygen plasma mostly retains the array ordering, however this order is completely destroyed when hydrogen or nitrogen plasma is used. The nanoparticles were found to have oxidised during oxygen plasma treatment, however subsequent hydrogen or argon plasma treatment was found to reduce these formed oxides.

Williams et al.[225] studied the effect of oxygen and argon plasma treatments on platinum thin films. Platinum surfaces treated with argon plasmas showed no distinct difference from non-treated surfaces in terms of optical properties and hydrophilicity. The surface roughness, however, had increased as a result of the plasma treatment due to surface bombardment with argon ions. In contrast oxygen plasma treated platinum surfaces had increased hydrophilicity as measured through water contact angle, and a reduced surface roughness. XPS measurements revealed that the oxygen plasma treated surfaces contained platinum oxide species which were not present in untreated and argon-treated plasma surfaces. Interestingly the authors showed that a reduced platinum surface can be achieved after oxygen plasma treatment by subsequent treatment with argon plasma, demonstrating the versatility of surface functionalisation through plasma treatment.

Yajima[226] demonstrated the that platinum surfaces can be oxidised and reduced by oxygen and hydrogen plasmas respectively. In the study the authors used a helium plasma to reduce the oxidised platinum, albeit to less effect than hydrogen plasma, and this was put down to oxide etching as helium has no reducing power. Lee et al.[227] studied the effect of plasma treatment on different metals. They found that all plasma treatments acted to reduce the amount of surface carbon contamination, and that oxygen plasma treatment led to an increase in work function of the metals studied due to the formation of oxide species.

In a more detailed study Philips et al.[228] found that oxygen plasma etching proceeded by concomitant action by oxygen ions and electrons. The surface morphology of platinum films after extended oxygen plasma treatment resulted in the formation of small octahedral nanoparticles. The surface morphology after argon plasma treatment remained relatively featureless.

Tsoukalas et al.[220] studied the effect of plasma treatment on physically deposited silver nanoparticles. They found that the nanoparticle size increased with prolonged oxygen plasma treatment, and that samples with higher initial nanoparticle densities grew quicker. As the nanoparticle diameter increased the nanoparticle number density decreased, consistent with Ostwald ripening. The plasma gas composition also had an effect; by studying the surface morphology after plasma treatment with different oxygen-argon plasma gas mixtures the authors found that the nanoparticles grew more with increasing oxygen concentration. In the case of silver nanoparticles, the formation of silver oxide is thermodynamically favourable at room temperature, and so the formation of silver oxide species effectively weakens the Ag-Ag bond increasing the ripening rate.

Baümer et al.[215] studied the effect of different plasma gases on ligand-protected nanoparticle arrays. They found that hydrocarbon-based ligands could be removed by all tested plasma gases, but only oxygen plasma retained the mesoscopic order of the sample. The authors note, however, that whilst the removal of ligands through plasma treatment should reveal metallic nanoparticle surfaces, the metallic nature of the bare nanoparticles is affected by the plasma exposure and the substrate.

In this chapter the effect of plasma exposure on model Pt_{923} clusters will be explored. The effect of plasma treatment on ligand-protected nanoparticles and nanoparticle arrays have been studied as previously described, however the effect of plasma treatment on well-defined physically deposited nanomaterials is yet to be studied. These experiments have implications concerning the use of plasma as a cleaning mechanism for ligand-synthesised and well-defined, shaped nanoparticles. The effects of two common plasma gases, oxygen and argon, on bare clusters and its effect on the cluster-surface interaction will be studied.

6.1 Experimental

Pt_{923} clusters were synthesised using the cluster source, described in chapter 2. The clusters were soft-landed at 1 eV per atom onto amorphous carbon film TEM grids and were transferred through atmosphere between the cluster source, electron microscope, and plasma cleaner. After plasma exposure the samples were immediately reimaged and were exposed to atmosphere for no more than five minutes.

A Henniker HPT-100 plasma cleaner was used for plasma treatment in this study. Plasma power was typically 100 W with 10 sccm gas flow inlet unless stated otherwise. The chamber pressure under these conditions was ~0.6 mbar during treatment. Pure argon and oxygen were used as plasma gases (BOC).

6.2 Pt_{923}

6.2.1 Oxygen plasma

Figure 6.2.1 shows the effect of oxygen plasma treatment on Pt_{923} clusters. The sample morphology, size distribution, and nearest neighbour distribution of the as-deposited sample show high homogeneity where approximately 82 % of the deposited nanoparticles are Pt_{923} singlets. The nearest neighbour distribution resembles the expected distribution for randomly deposited particles.

The sample was then subjected to 30 seconds of oxygen plasma treatment and immediately reimaged. The clusters appear to have grouped and sintered, forming chain-like structures not dissimilar to those found during electrochemical conditioning performed in chapter 5. The Pt_{923} singlet peak projected area has decreased by approximately 8 % which is likely due to the sputtering effect caused by ion bombardment in the plasma. The nearest neighbour distribution has become bimodal which is indicative of cluster grouping as discussed in chapter 5. The nearest neighbour bimodality consists of a peak centered at ~5 nm originating from nanoparticles situated in groups and a broader peak centered at ~12 nm. The overall nearest neighbour distribution no longer resembles a truly random distribution due to the oxygen plasma-induced nanoparticle migration. The size distribution consists of predominantly singlets and doublets, albeit that the reduction in projected area of the singlet peak suggests that the singlet size is no longer consistent with the as-deposited size of 923 atoms. The fraction of larger nanoparticles has also increased, which can be put down to a migration and sintering induced by the oxygen plasma.

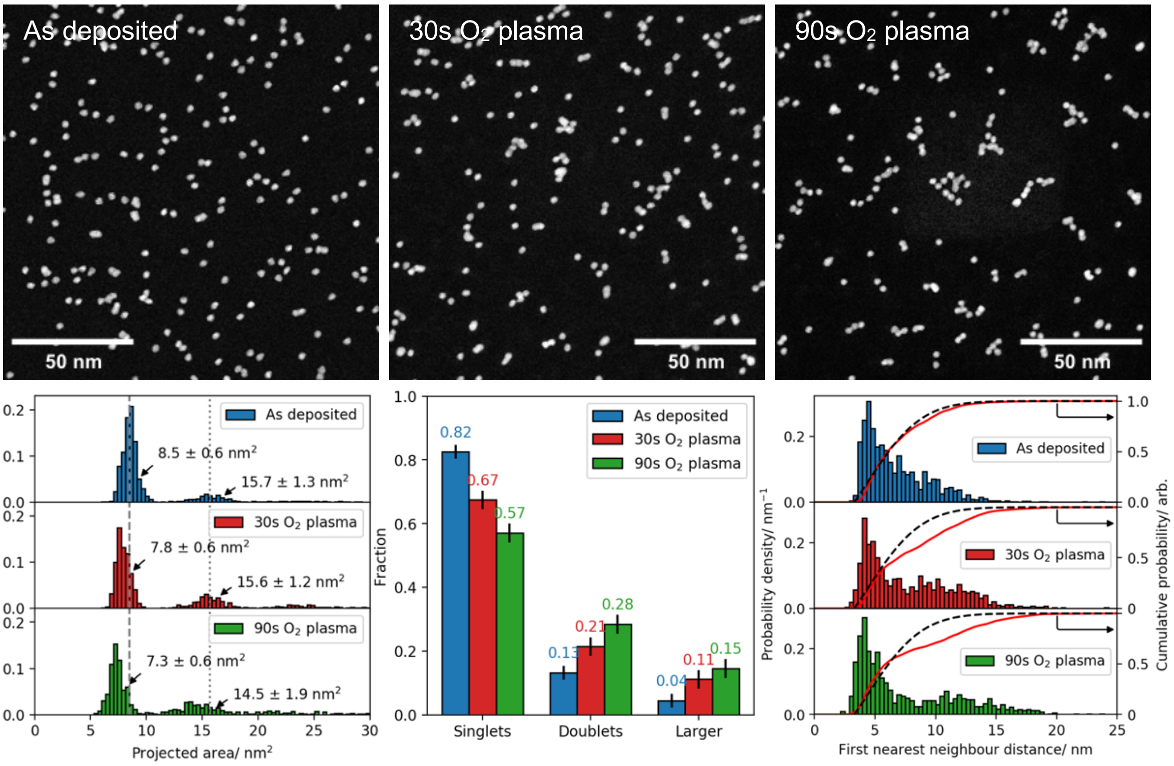

Figure 6.2.1: Pt_{923} sample exposed to oxygen plasma. (top row) HAADF-STEM images of Pt_{923} sample as-deposited (left) and after exposure to 30 s (center) and 90 s (right) oxygen plasma. (bottom row) size distribution of Pt_{923} sample (left) as-deposited (blue), and after exposure to oxygen plasma for 30 s (red) and 90 s (green). Grey dashed and dotted lines represent the average as-deposited size for Pt_{923} singlets and doublets respectively. (center) population distribution calculated from the sample size distribution. (right) nearest neighbour distributions. Red line is the nearest neighbour CDF and the black dashed line is the expected CDF for randomly deposited particles at a number density of 7200 per square micron.

After a further 60 s exposure to oxygen plasma, for 90 s total, the sample was reimaged. The increased exposure to oxygen plasma has exacerbated the aforementioned migration and sintering, and the fraction of observed singlet nanoparticles has been reduced to 57 %. The singlet size has reduced further by 9 % for a total reduction in projected area of 14 % from the as-deposited size. The size distribution shows that the size of the larger clusters remains quantised. Both the singlet and doublet size have decreased as a result of plasma exposure which suggests that this effect is as a result of ion bombardment and sputtering opposed to Ostwald ripening, which predicts the decrease in size of smaller particles (singlets) at the expense of growth of larger ones (doublets). The observed behaviour appears to consistent with Smoluchowski ripening combined with sputtering.

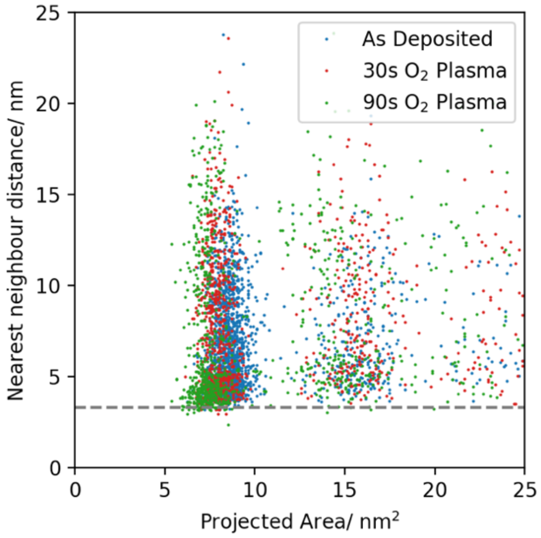

Figure 6.2.2: Scatter plot of nanoparticle size and nearest neighbour distance. Grey dashed line is the Pt_{923} singlet diameter.

The nearest neighbour distribution has become increasingly unimodal around 5 nm. In a hit-and-stick[93] type growth mechanism as two nanoparticles sinter the effective nearest neighbour of the agglomerated nanoparticle may be expected to increase. In order to see if this is the case the correlation between nanoparticle size and nearest neighbour distance is shown in Figure 6.2.2. The graph shows clustering around the singlet and doublet sizes in all cases, as expected, but there does not appear to be any direct correlation between nanoparticle size and nearest neighbour distance. The graph confirms that the minimum centre-center nearest neighbour distance is the Pt_{923} singlet diameter.

As the first nearest neighbour distance only takes into account one neighbour in any direction, it does not account for a possible 'capture region' on the surface. In the case where clusters agglomerate from random walks on the surface it may be expected that larger clusters are more immobile to due increased van der Waals interaction with the surface[79] and therefore act as material 'sinks'. In this case the larger agglomerated nanoparticles may be expected to have a larger capture region as they assimilate nearby colliding clusters. A Voronoi tessellation was computed to calculate each nanoparticles' capture region. This analysis has been shown to be suitable for similar studies on ordered nanoparticles structures[229]. The capture region was determined by the area of each Voronoi cell, and the results are shown in Figure 6.2.4. The correlation results obtained through both the nearest neighbour distance and Voronoi methods look markedly similar.

There does not appear to be any correlation between nanoparticle size and nearest neighbour distance or capture region, which may be expected if the cluster migration on the surface is random.

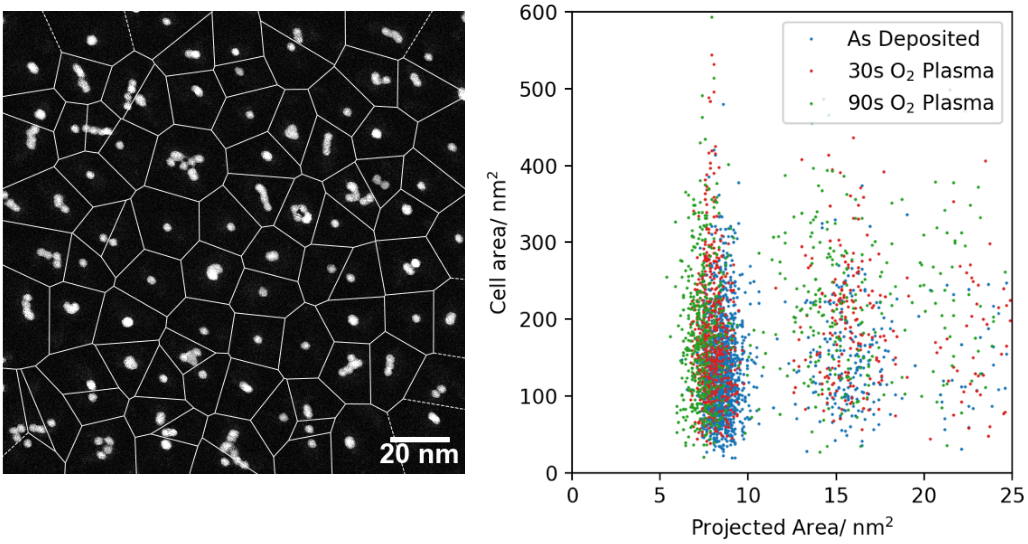

Figure 6.2.3: Voronoi tessellation analysis of Pt_{923} sample after oxygen plasma treatment. (left) visualisation of Voronoi tessellation on HAADF-STEM image of Pt_{923} after 90 s exposure to oxygen plasma. The white lines represent the Voronoi cell boundaries. (right) correlation between nanoparticle size and Voronoi cell area.

Segmentation analysis was performed on the images after 90 s of exposure to oxygen plasma to further elucidate the form of the nearest neighbour distribution. The first nearest neighbour distribution of the segmented nanoparticles is shown in Figure 6.2.4. The image was convoluted with a Laplacian of Gaussian filter to detect the nanoparticles. As the agglomerated nanoparticles are chain-like the convolution can segment the agglomerated nanoparticles in many cases, although not with perfect accuracy. This analysis underestimates the number of clusters for features with this geometry. The number density before segmentation was 4800 ± 900 per square micron, and this increases after segmentation to 7100 ± 1000 per square micron, which is comparable to the as-deposited number density of 7200 ± 400 per square micron. This is consistent with cluster migration as a ripening mode and implies that cluster detachment from the support is limited. The nearest neighbour distribution after segmentation shows that after exposure to oxygen plasma 75 % of the nanoparticles originally deposited are now situated less than 5 nm from another nanoparticle, this compares to 31 % as-deposited.

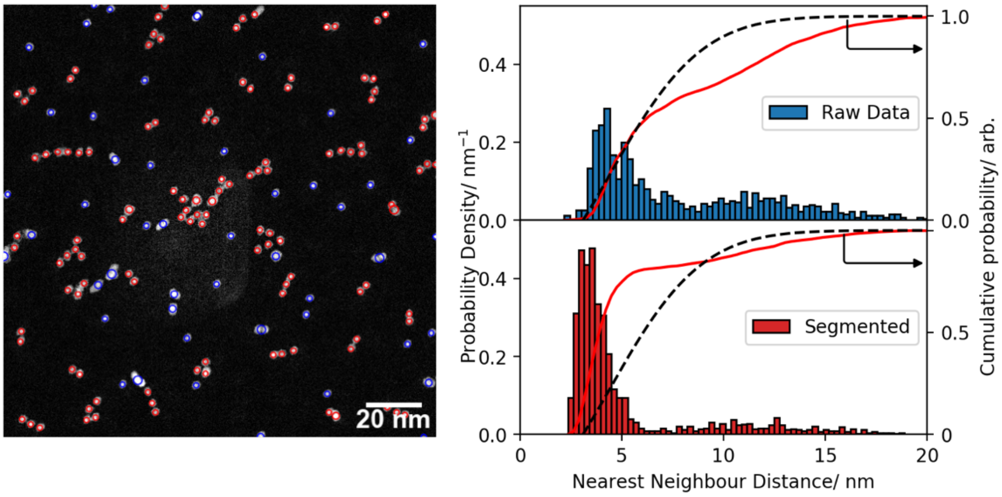

Figure 6.2.4: Segmentation analysis of Pt_{923} sample after oxygen plasma treatment. (left) HAADF-STEM image of Pt_{923} sample after exposure to oxygen plasma for 90 s. Circles indicate the positions of the particles found by convolution with a Laplacian of Gaussian kernel. The circle colour is red if the cluster has a nearest neighbour less than 5 nm away and blue otherwise. The radius of each circle indicates the kernel size that produced the detection. (right) distribution of sintered nanoparticles (blue), and distribution after image segmentation (red). The nearest neighbour CDF is plotted as a red curve in both cases. The black dashed curve represents the expected CDF for a randomly deposited sample at the as-deposited number density of 7200 per square micron.

The segmented nearest neighbour analysis for the sample as-deposited and after 30 s and 90 s oxygen plasma exposure is shown in Figure 6.2.5. The as-deposited distribution is very similar to the raw data in Figure 6.2.1 and in good agreement with the expected random distribution. This is to be expected as a majority of the nanoparticles as-deposited are singlets and therefore unaffected by the segmentation analysis. The as-deposited segmented distribution confirms the validity of the analysis. It can be seen in Figure 6.2.5 that longer oxygen plasma exposure times lead to an increasingly unimodal nearest neighbour distribution as an increasing fraction of the sample have migrated into groups or sintered. The modal nearest neighbour distance as-deposited is 4.6 nm, which decreases successively to 3.8 nm and then 3.6 nm after 30 s and 90 s oxygen plasma exposure due to increased sintering. The segmentation analysis further confirms the grouping and sintering effect as a result of oxygen plasma previously discussed.

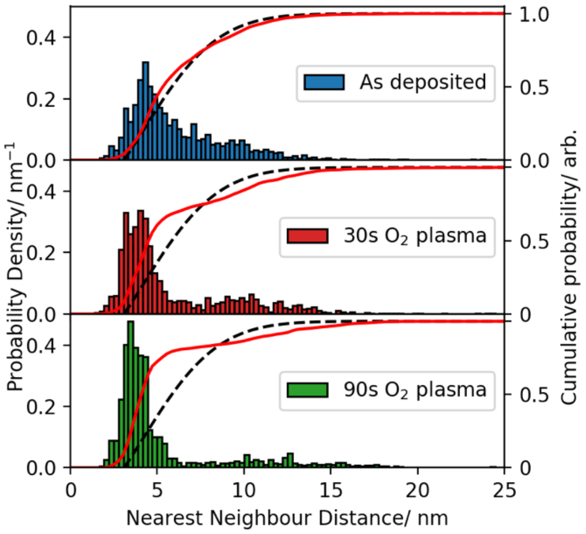

Figure 6.2.5: Segmented nearest neighbour analysis of Pt_{923} *sample as-deposited (blue) and after 30 s (red) and 90 s (green) exposure to oxygen plasma.*

High magnification STEM imaging was performed to check for signs of nanoparticle restructuring or oxidation. Figure 6.2.6 shows selected high magnification HAADF-STEM images. In all cases the most frequent lattice spacing was 0.22 nm, corresponding to Pt(111). In some cases a lattice spacing of 0.14 nm was observed, which corresponds to Pt{220}. There were no significant signs of nanoparticle restructuring due to oxygen plasma other than what could be attributed to restructuring due to sintering. The as-deposited clusters have predominantly FCC structures and this is unchanged after plasma exposure.

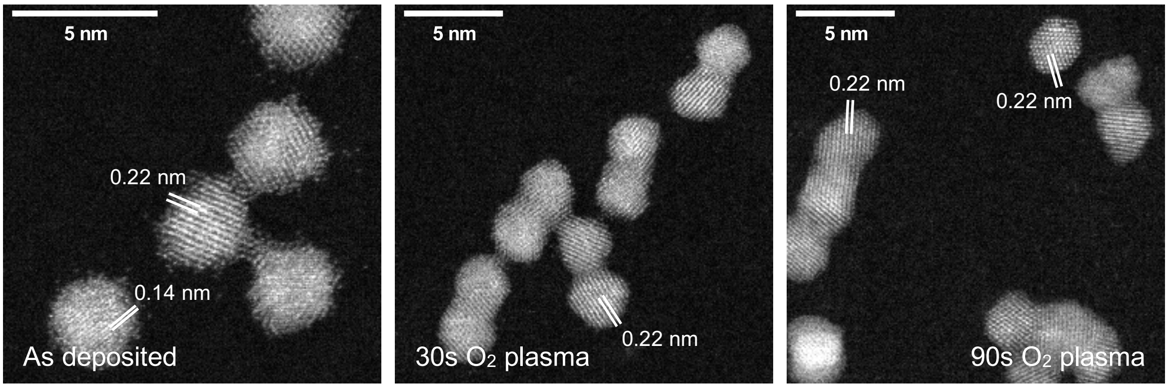

Figure 6.2.6: High magnification HAADF-STEM images of Pt_{923} *sample (left) as-deposited, and after exposure to oxygen plasma for 30 s (center) and 90 s (right).*

One subtle sign of platinum oxidation was observed across hundreds of nanoparticles. Figure 6.2.7 shows a high magnification HAADF-STEM image of a platinum nanoparticle and its corresponding FFT. The dominant frequencies in the FFT are from 0.22 nm lattice spacings which are attributable to Pt(111) and consistent with the observed truncated octahedral structure. Closer analysis of the FFT reveals 0.25 nm lattice spacings which are not consistent with FCC platinum. Banerjee et al.[230,231] have previously observed 0.25 nm lattice spacings in studies of platinum oxidation, which have are attributable to bcc Pt_3O_4(211)[232] as confirmed through x-ray diffraction. FFT filtering reveals that the 0.25 nm lattice spacings arise from the dull region of the nanoparticle. Platinum oxide would be expected to appear low intensity[42] with respect to pure platinum under HAADF conditions due to its reduced density and small scattering contribution from low atomic number oxygen.

For a majority of nanoparticles, no indication of platinum oxidation could be observed. EDX was also performed, however no oxygen signal could be recorded and the nanoparticles suffered severe electron beam damage due to prolonged exposure, sometimes completely disintegrating after 15 s beam exposure. It is possible that the reducing effect of the electron beam[233] could remove a thin oxide layer from the surface of the nanoparticles under imaging conditions[234]. It may also be possible that platinum oxide is not stable at these sizes. For example, gold has been shown to oxidise after during exposure to oxygen plasma[235], however magic-number Au_{55} has been shown to be exceptionally resistant to oxidation by oxygen plasma treatment[236].

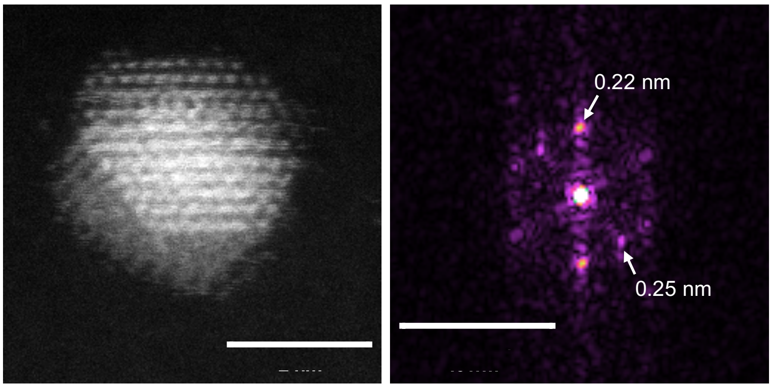

Figure 6.2.7: High magnification HAADF-STEM image of Pt nanoparticle after 90 s oxygen plasma exposure showing possible oxidation and corresponding FFT.

6.2.2 Argon plasma

To further elucidate the mechanism of cluster migration the experiment performed in section 6.2.1 was repeated with argon plasma. The sample morphology as-deposited and after exposure to argon plasma for 30 s and 90 s is shown in Figure 6.2.8. The sample size distribution and first nearest neighbour distributions show that the sample morphology is identical to the oxygen plasma treatment study presented in section 6.2.1.

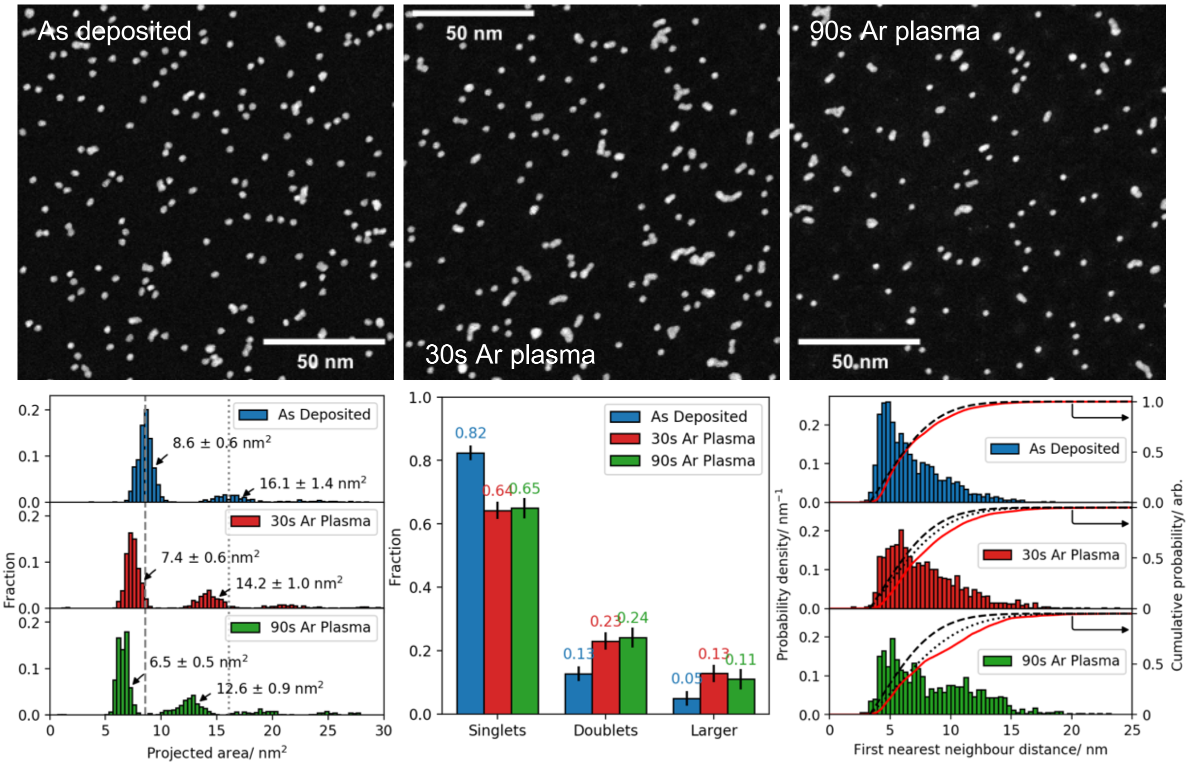

Figure 6.2.8: Pt_{923} sample exposed to argon plasma. (top) HAADF-STEM images of Pt_{923} sample as-deposited (left) and after exposure to 30 s (center) and 90 s (right) argon plasma. (bottom) size distribution of Pt_{923} sample (left) as-deposited (blue), and after exposure to argon plasma for 30 s (red) and 90 s (green). Grey dashed and dotted lines represent the average as-deposited size for Pt_{923} singlets and doublets respectively. (center) population distribution calculated from the sample size distribution. (right) nearest neighbour distributions. Red line is the nearest neighbour CDF and the black dashed line is the expected CDF for randomly deposited particles at a number density of 7200 per square micron. The black dotted lines are the expected nearest neighbour CDFs for randomly deposited particles at the measured number density in each case.

The sample was exposed to argon plasma for 30 s after initial imaging. The HAADF-STEM images appear to show an increase in agglomeration, and the population distribution shows that the number of singlet clusters have decreased from 82 to 64 % at the expense of larger clusters. These statistics are similar to those found after the same duration of oxygen plasma exposure. The Pt_{923} singlet and doublet peak remain well defined but have shifted to lower sizes which implies the ejection of material through sputtering. No small clusters of atoms are observed on the substrate, however, which may be expected if adatoms are ejected from the cluster surface. If Ostwald ripening was significant as a result of plasma exposure the doublet size may be expected to grow as the singlet size decreases. This is not observed and in fact all doublets observed after argon plasma exposure are smaller than the mean doublet size as-deposited. This leads to the assumption that material is lost during plasma exposure, possibly into the gas phase.

The nearest neighbour distribution does not appear to have changed its functional form as a result of argon plasma treatment, indicating that the clusters are still randomly arranged. The nearest neighbour CDF agrees well with the expected distribution for randomly arranged particles with a number density of 6000 nanoparticles per square micron, which is the measured number density from HAADF-STEM and is shown as the black dotted line in Figure 6.2.8. It should be noted that the deviation from the expected values likely arises due to the fact that the clusters are modelled as uniform hard disks with diameter d_{923} = 3.2 nm, however the population distribution shows that for over one third of observed nanoparticles this assumption is not accurate. This overall arrangement of clusters on the support differs from the morphology observed after oxygen plasma exposure since sintering has been induced but the overall cluster arrangement is still uniform. On the other hand, oxygen plasma exposure induces cluster migration and subsequent sintering.

The sample was then exposed to argon plasma for a further 60 s, for 90 s total, and reimaged. The effects observed after 30 s of argon plasma exposure appear to have compounded. The size distribution shows that the nanoparticles remain well defined as singlets and doublets, however the size of all nanoparticles has decreased further such that the singlet size is now 25 % smaller than as-deposited. Interestingly further exposure to argon plasma has not resulted in more sintering. The population distribution remains unchanged from those measured after just 30 s of exposure to argon plasma. The nearest neighbour distribution also shows that the sample morphology still resembles a random distribution; the black dotted curve in Figure 6.2.8 is calculated from the measured number density of 4900 nanoparticles per square micron.

These observations point to the conclusion that argon plasma exposure does not lead to cluster migration. This in turn can explain the observation that increased argon plasma exposure does not lead to increased sintering. The initial small amount of sintering observed can be explained by cluster proximity. The argon plasma sputters the clusters leading to an ejection of material from the cluster surface and reducing the overall nanoparticle size, which is observed. Some ejected atoms may be vaporised, leading to and overall loss of material, whilst some may be ejected from the clusters but remain bound to the substrate. It has been shown for small gold clusters that single atoms bridging the cluster-cluster gap mediate a jump-to-contact mechanism[129] leading to cluster coalescence. In this case any further plasma exposure would not lead to sintering as the initial exposure induced sintering between any clusters in close proximity and argon plasma exposure does not lead to cluster migration.

As plasma treatment is a low temperature process[237], and measured sample temperatures increased by only ~10 degrees over the sputtering time, a heating induced migration effect can be neglected[215]. The lack of cluster migration observed due to argon plasma exposure may be due to the creation of more defect sites in the amorphous carbon by the plasma. It has been reported that higher surface defect densities on graphite, induced be argon ion bombardment, leads to reduced cluster coalescence[238]. Theoretical calculations have showed that the adsorption energy for small gold clusters interacting with dangling bonds from a carbon vacancy may be larger than 2 eV and ten times higher than on pristine graphite[239]. Studies involving platinum clusters suggest that migration is reduced by cluster trapping on defects in carbon nanotubes[240].

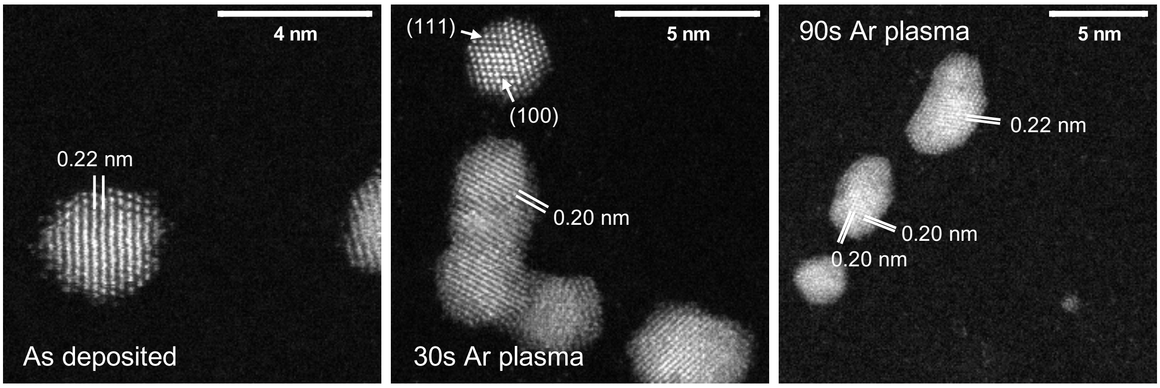

Figure 6.2.9: High magnification HAADF-STEM images of Pt_{923} sample (left) as deposited, and after exposure to argon plasma for 30 s (center) and 90 s (right).

High magnification HAADF-STEM imaging did not reveal any significant structural changes due to argon plasma exposure. Representative images are shown in Figure 6.2.9. Atomic spacings of 0.22 and 0.20 nm are attributed to Pt(111) and Pt{200} planes respectively. The singlet clusters shown in the as-deposited image and the image after exposure to 30 s argon plasma are both cuboctahedral in structure. The structures were identified by comparison with a structure atlas[42,58]. In the latter case the cluster is on-axis with (111) and (100) facets clearly visible.

6.3 Oxygen plasma followed by argon plasma

To further identify the migration mechanism observed one Pt_{923} sample was subjected to 60 s oxygen plasma and then subjected to a further 30 s of argon plasma. The sample morphology and statistics are shown in Figure 6.3.1. The initial exposure to oxygen plasma has led to migration and sintering in some cases, as evidenced by the population and nearest neighbour distribution, consistent with section 6.2.1.

The sample was then exposed to 30 s of argon plasma and reimaged. Approximately 10 % of the singlet clusters sintered following exposure to argon plasma. The nearest neighbour distribution however remains very similar in shape to the distribution after oxygen plasma exposure, which suggests that the clusters have not migrated further. Closer inspection of the STEM images shows that the arrangement of nanoparticles after oxygen and subsequent argon plasma exposure are similar, except for the increase in sintered nanoparticles. This behaviour is the same as observed for argon plasma exposure in section 6.2.2; argon plasma exposure does not appear to lead to migration, however exposure leads to sintering presumably through the ejection of adatoms which subsequently initiate bridging between nanoparticles in close proximity.

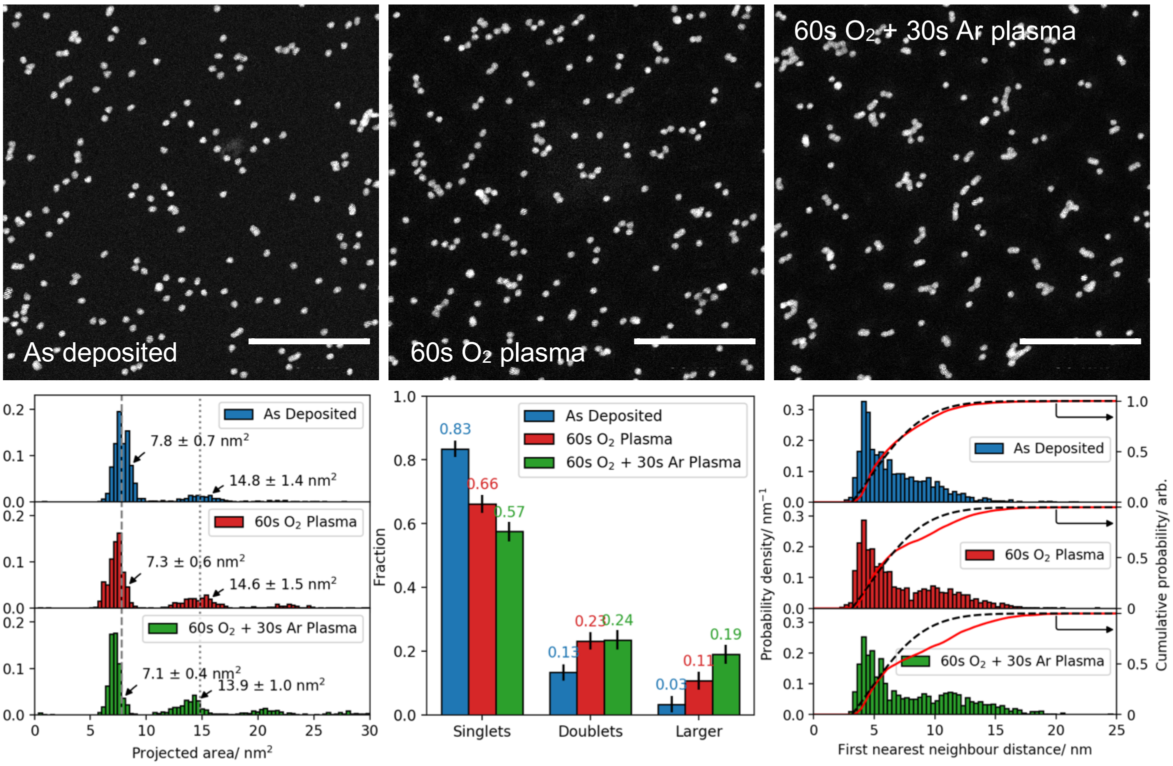

Figure 6.3.1: Pt$_{923}$ sample exposed to oxygen then argon plasma. (top) HAADF-STEM images of Pt$_{923}$ sample as-deposited (left) and after exposure to 60 s oxygen plasma (center) and a further 30 s argon plasma (right). (bottom) size distribution of Pt$_{923}$ sample (left) as deposited (blue), and after exposure to oxygen plasma for 60 s (red) and further exposure to 30 s argon plasma (green). Grey dashed and dotted lines represent the average as-deposited size for Pt$_{923}$ singlets and doublets respectively. (center) population distribution calculated from the sample size distribution. (right) nearest neighbour distributions. The red line is the nearest neighbour CDF and the black dashed line is the expected CDF for randomly deposited particles at a number density of 6800 per square micron.

6.4 Au$_{923}$

To test whether migration and sintering behaviours are unique to platinum clusters, Au$_{923}$ clusters were synthesised and exposed to both oxygen and argon plasmas. Platinum is a well-known carbon oxidation catalyst[89], and gold has also shown ability to oxidise carbon but is markedly worse than platinum[241]. It should be noted however that a few studies have shown that gold nanoparticles are active for carbon monoxide oxidation[11,19]. Au$_{923}$ clusters were produced using the cluster source described in chapter 2 and deposited at 1 eV per atom onto amorphous carbon film TEM grids.

6.4.1 Oxygen plasma

The sample morphology and statistics of the as-deposited Au_{923} sample are shown in Figure 6.4.1, which show that the majority of clusters are well-defined Au_{923} singlets. The nearest neighbour distribution confirms that the clusters are initially randomly arranged. Interestingly the functional form of the nearest neighbour CDF is that of a random distribution, however there is an offset between the measured nearest neighbour distribution and the expected distribution. The measured nearest neighbour distribution is better fit if the cluster size is ~0.5 nm larger, which is approximately the minimum cluster-cluster gap before coalescence proceeds which has been observed for gold clusters and islands[129]. The structure of coalesced gold clusters is different to that of platinum clusters. Sintered platinum clusters form branch-like structures and the sintering boundary can be determined by visual inspection. Despite the energy input during electrochemical cycling, plasma exposure, or under a high energy electron beam, the platinum clusters observed in this thesis do not fully coalesce to form spherical nanoparticles which may be expected due to a reduction in surface energy[199]. The sintering mechanism precedes by neck formation and growth[79], and platinum clusters do not appear to grow in the direction normal to the support. In contrast, coalesced gold clusters sinter to form larger spherical nanoparticles which is may due to the larger surface diffusivity of gold compared to platinum[242]. This is demonstrated in the as-deposited size distributions of Pt_{923} and Au_{923}. Pt_{923} doublets are on average 90 % larger than the singlets in terms of projected area, compared to 70 % for Au_{923} doublets. From a geometric standpoint, a spherical cluster formed from two identically sized smaller clusters would have a projected area that is 60 % larger than each of its constituents. This is in good agreement with the observed sizes.

The sample was then subjected to 30 s of oxygen plasma exposure and reimaged. The sample morphology shows the formation of larger clusters, with a 10 % reduction in observed Au_{923} singlets. The sample size distribution remains well defined, consisting of singlet and doublets clusters, however the singlet size has decreased by ~10 %, which possibly due to the sputtering effect of the plasma as observed previously. The nearest neighbour distribution exhibits a small amount of bimodality due to migration and sintering.

The sample was then exposed to oxygen plasma for a further 60 s, for 90 s total, and reimaged. The size distribution shows that the singlet size has further decreased such that it is now 15 % smaller than originally deposited. The total fraction of singlets has not decreased after this round of plasma exposure; this contrasts with the behaviour observed for Pt$_{923}$ (see section 6.2.1) where increasing oxygen plasma exposure leads to increased sintering. The nearest neighbour distribution shows increased bimodality which is similar to Pt$_{923}$ exposed to oxygen plasma in section 6.2.1.

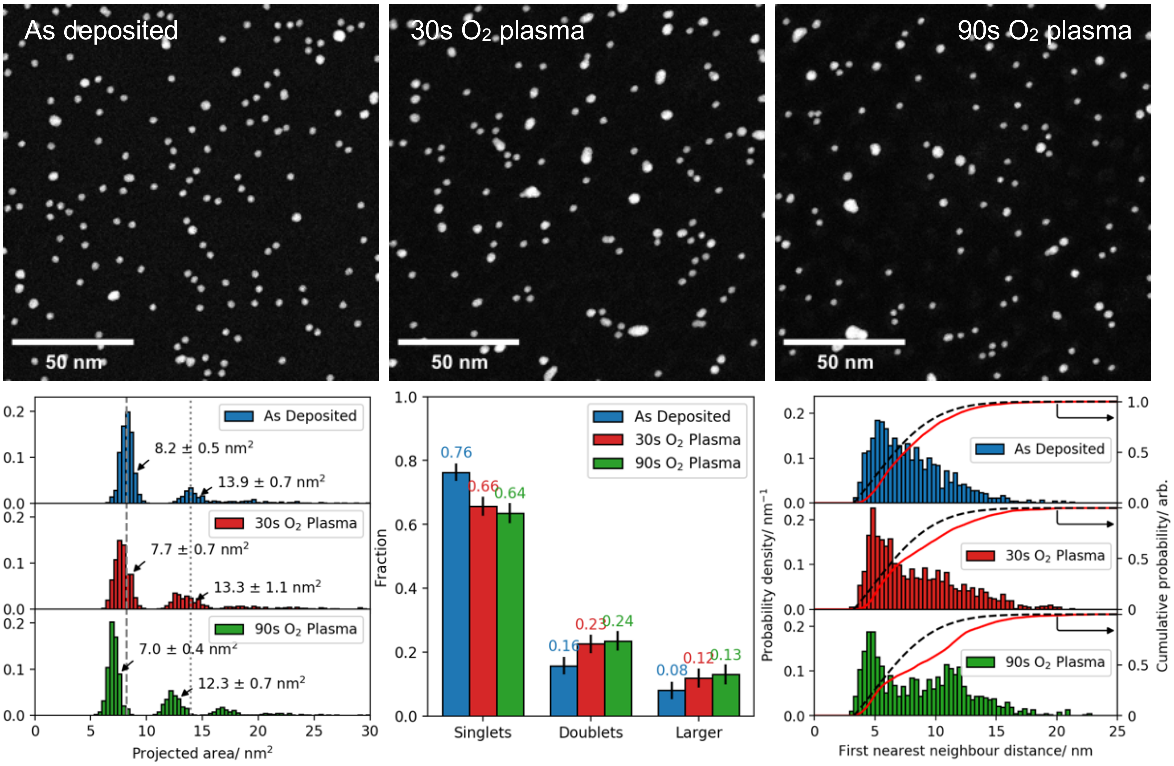

Figure 6.4.1: Au$_{923}$ sample exposed to oxygen plasma. (top) HAADF-STEM images of Au$_{923}$ sample as-deposited (left) and after exposure to 30 s (center) and 90 s (right) oxygen plasma. (bottom) size distribution of Au$_{923}$ sample (left) as-deposited (blue), and after exposure to oxygen plasma for 30 s (red) and 90 s oxygen plasma (green). Grey dashed and dotted lines represent the average as-deposited size for Au$_{923}$ singlets and doublets respectively. (center) population distribution calculated from the sample size distribution. (right) nearest neighbour distributions. Red line is the nearest neighbour CDF and the black dashed line is the expected CDF for randomly deposited particles at a number density of 6000 per square micron.

The measured change in sample coverage as a result of plasma exposure is in agreement with the expected coverage due to nanoparticles at the measured radius and number density, ie. $C_{obs} \approx \rho_i \pi \bar{r}_i^2$, which indicates minimal nanoparticle detachment.

High magnification imaging, shown in Figure 6.4.2, reveals that Au_{923} have cuboctahedral (Oh), and decahedral (Dh) structures, which are structures that have been observed previously[14,42]. No clear oxide shell was observed during imaging and EDX measurements did not yield any conclusive results due to low signal and beam damage issues. The structures observed after oxygen plasma exposure were also octahedral and decahedral in nature, which suggests that no significant structure change occurs due to exposure to oxygen plasma.

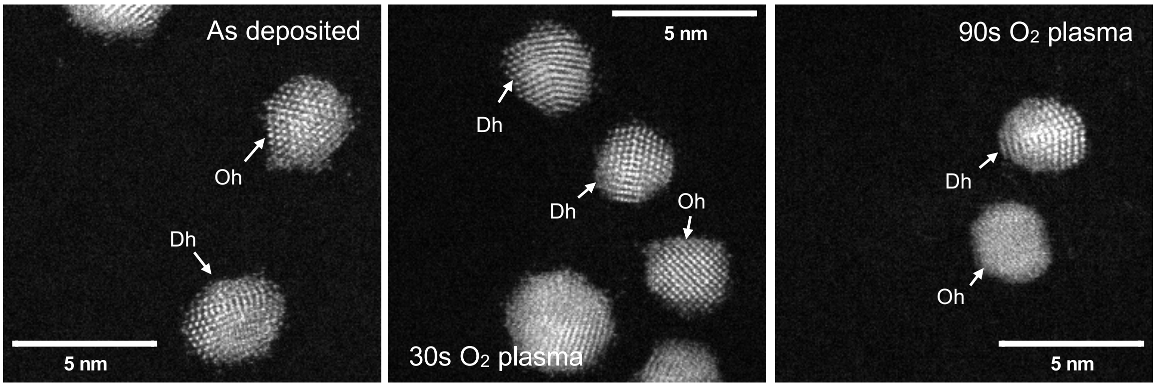

Figure 6.4.2: High magnification HAADF-STEM images of Au_{923} sample (left) as deposited, and after exposure to oxygen plasma for 30 s (center) and 90 s (right).

6.4.2 Argon plasma

A similar experiment was performed exposing Au_{923} to argon plasma. The as-deposited sample morphology and statistics are shown in Figure 6.4.3. The size and nearest neighbour distributions show well-defined gold clusters arranged randomly on the surface.

The sample was then exposed to argon plasma for 30 s. The size distribution and sample morphology show that the majority of nanoparticles are still singlets and doublets, albeit the size of each nanoparticle has reduced due to sputtering. The fraction of singlets has reduced from 75 % as-deposited to 68 % after argon plasma exposure, at the expense of larger nanoparticles. The nearest neighbour distribution does not exhibit bimodality suggesting that the clusters have not migrated, which is the same behaviour as observed for Pt_{923} in section 6.2.2.

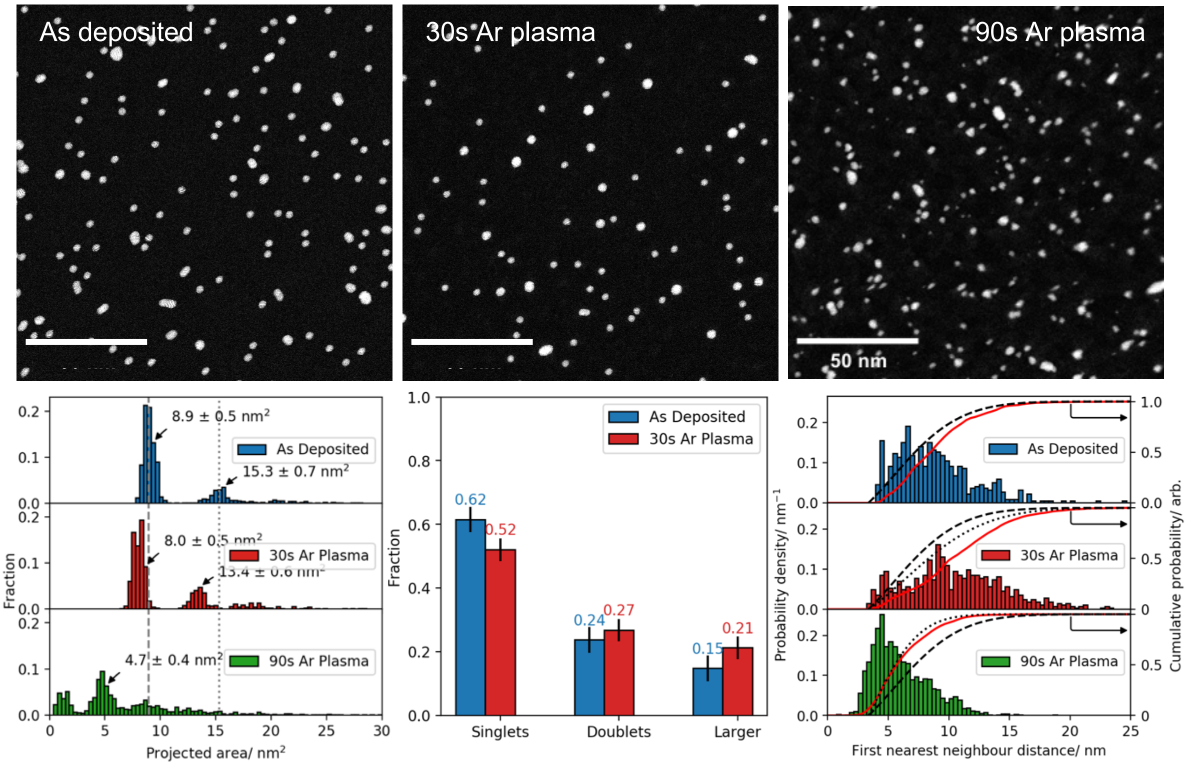

Figure 6.4.3: Au$_{923}$ sample exposed to argon plasma. (top) HAADF-STEM images of Au$_{923}$ sample as-deposited (left) and after exposure to 30 s (center) and 90 s (right) argon plasma. (bottom) size distribution of Au$_{923}$ sample (left) as-deposited (blue), and after exposure to argon plasma for 30 s (red) and 90 s oxygen plasma (green). Grey dashed and dotted lines represent the average as-deposited size for Au$_{923}$ singlets and doublets respectively. (center) population distribution calculated from the sample size distribution, note that the distribution after 90 s plasma exposure is not shown as it cannot be determined accurately. (right) nearest neighbour distributions. Red line is the nearest neighbour CDF and the black dashed line is the expected CDF for randomly deposited particles at a number density of 5000 per square micron.

The sample was then exposed to argon plasma for a further 60 s, for 90 s total, and reimaged. The HAADF-STEM images and corresponding size distribution in Figure 6.4.3 show that the sample morphology no longer resembles a mass-selected sample and the observed clusters range in size from a few atoms to approximately the Au$_{923}$ doublet size. The nearest neighbour distribution however agrees well with a random distribution at the measured number density of 9000 per square micron. The wavy pattern observed in the HAADF-STEM is due to clusters coming into and out of focus during imaging. This is likely due to thinning of the amorphous carbon layering the TEM grid by the argon plasma. The carbon layer may have reduced conductivity due to thinning and local charging effects by the electron beam attract and repel the grid producing *z*-oscillations and the resulting focal shift.

Selected high magnification HAADF-STEM images are shown in Figure 6.4.4. Despite the reduction in cluster size due to successive argon plasma exposure the clusters have decahedral and FCC geometries which are consistent with as-deposited Au_{923} structures[44].

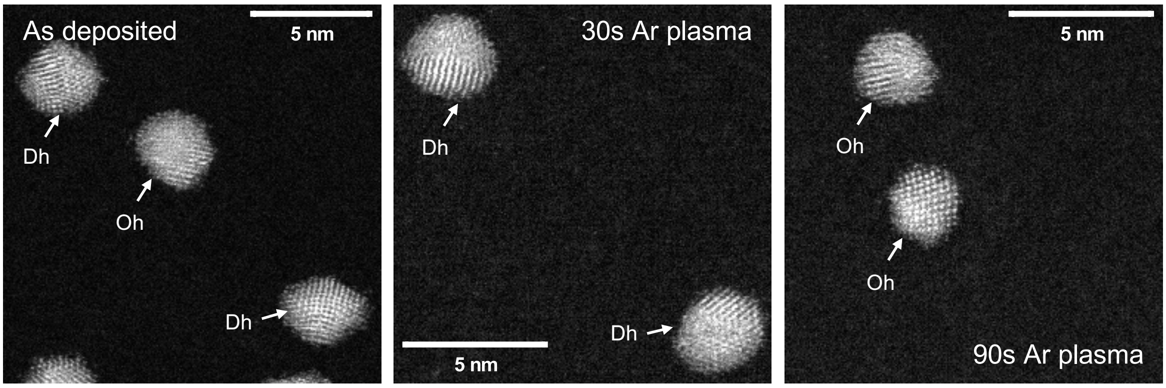

Figure 6.4.4: High magnification HAADF-STEM images of Au_{923} sample (left) as-deposited, and after exposure to argon plasma for 30 s (center) and 90 s (right).

6.5 Discussion

The results presented in this chapter have two main conclusions. Firstly, the effect of plasma treatment on mass-selected catalytically relevant noble metal clusters have been quantified, confirming the invasive nature of the procedure. The well-defined model clusters used here exhibited a decrease in size due to exposure to both oxygen and argon plasmas due to a sputtering effect. Exposure to oxygen plasma almost certainly leads to nanoparticle oxidation, however observation of this effect was limited by transport through atmosphere between the plasma cleaner and electron microscope. For both gold and platinum clusters argon plasma exposure produced increased amounts of sputtering compared to oxygen plasma which is in agreement with the effect of argon plasma on extended platinum surfaces[225]. Secondly, for metal nanoparticles on carbon supports it appears that oxidation is necessary for nanoparticle migration.

It has been reported by Chu et al.[243] that platinum nanoparticles on alumina supports show increased rates of migration and coalescence when heated in a wet hydrogen atmosphere. The rate of coalescence was not observed under a pure hydrogen or oxygen atmosphere and the authors attribute the observed migration to repetitive platinum oxidation and reduction leading to a weakening of the platinum support interaction due to the formation of water at the interface on reduction.

Regarding gold clusters, it has been shown that exposing gold surfaces to oxygen plasma will form Au_2O_3[235,244], however that this oxide is also unstable and will reduce under ambient conditions[244]. Sintering and oxidation of ligand-protected gold nanoparticles has also been observed after exposure to oxygen plasma[245]. XPS studies on carbon supports exposed to oxygen plasma reveal oxidised carbon surface species[213] and previous reports have suggested that such species induce cluster migration by weakening of the cluster-surface interaction[93].

The observed results are very similar to the study described in chapter 5. In both cases energy input induces platinum and carbon oxidation which leads to cluster migration and subsequent sintering. Electrochemical studies have suggested that migration is mediated by repetitive oxidation and reduction, weakening the cluster-support interaction. The oxygen plasma experiments described in this chapter do not have such fine-grained temporal information and any reduction on exposure to air from vacuum is yet to be explored. It may be possible that migration proceeds during the reduction of oxidised species created by the plasma, this has been suggested in electrochemical environments[94]. Previous in-situ environmental TEM studies have shown that even small amounts of water vapour introduced to an oxygen atmosphere can supress oxidation and initiate reduction[246]. The relatively high base pressures used in these experiments ~0.6 mbar allow for the possibility of ambient water vapour to mediate nanoparticle reduction.

The results in chapter 5 showed that an anodic potential limit of 1.05 V vs RHE caused migration of Pt_{923} clusters but not Au_{923}. Within this potential window platinum was oxidised by the adsorption of hydroxyl and subsequently reduced, however the anodic potentials were not sufficient to oxidise gold. The weakening of the cluster-substrate interaction by successive oxidation and reduction manifested in the migration of Pt_{923} clusters, however this was not observed for Au_{923} due to the lack of oxidation. By comparison, both Pt_{923} and Au_{923} clusters are oxidised by oxygen plasma and successively reduced by exposure to atmosphere which resulted in migration. Combining all this information suggests that nanoparticle oxidation and reduction is required to initiate migration.

In contrast, exposing the clusters to argon plasma did not lead to migration. This adds to the oxidation-induced cluster migration argument as argon plasma does not have any oxidising power. It is possible that cluster migration may have been inhibited by the formation of defect sites in the amorphous carbon by sputtering[247], however the amorphous carbon support is already highly defective. Oxygen plasma also etches carbon[248], however the etching proceeds by chemical processes in addition to physical sputtering. The lack of migration observed after argon plasma treatment rules out migration due to cluster charge transfer or neutralisation effect[249,250].

In conclusion the effect of oxygen and argon plasma treatment on well-defined mass-selected bare platinum and gold clusters has been studied. The results show that the use of plasma treatment for contamination removal may be effective but the treatment is not benign on the nanoparticles. Both oxygen and argon plasma gradually sputter away the nanoparticle surfaces for an overall loss of material. Nanoparticles in close proximity have been shown to sinter as a consequence of plasma treatment. Finally, oxygen plasma treatment induces migration of both nanoparticle materials on amorphous carbon supports which is due to an oxidation effect rather than charge transfer or neutralisation by the plasma.

7 Conclusions and outlook

The aim of this work was to characterise physically deposited mass-selected platinum clusters. In the first experimental chapter mass-selected clusters were soft-landed onto amorphous carbon films and imaged with HAADF-STEM. Pt_{55} clusters did not exhibit crystalline structures and Pt_{147} were identified as having icosahedral-like features. Larger clusters, with 309, 561, 923, and 1415 atoms, had FCC structures as the degree of crystallinity increased with size. As platinum is an FCC metal these results suggest that platinum clusters have bulk-like structures from sizes of a couple hundred atoms. The STEM electron beam was shown to initiate cluster sintering at high magnifications which is likely due to a heating effect. The validity and accuracy of various image thresholding algorithms was discussed as they pertain to quantify nanoparticle sizes which is an important parameter used when studying nanoparticle size effects. Further analysis of the integrated HAADF intensity of mass-selected clusters showed that they may be used as mass calibration balances to quantify the size of unknown nanoparticles. The integrated HAADF intensity was shown to be independent of imaging magnification.

In the second experimental chapter mass-selected clusters were characterised electrochemically through cyclic voltammetry. The initial electrochemical characterisation of mass-selected platinum clusters on HOPG showed that the CV response was dependent on the potential conditioning history of the sample which was possibly due to a contamination removal effect. Repeated characterisation and performance testing on glassy carbon supports by collaborators confirmed this trend. The hydrogen evolution performance of the clusters improved with increasing potential limit, in agreement with the CV response, and approximately in line with the onset of platinum oxidation.

The effect of electrochemical conditioning on Pt_{923} clusters on amorphous carbon supports was studied with STEM in the third chapter. Ex-situ imaging revealed that clusters migrated due to potential cycling and the degree of sintering was shown to increase with sample density and the anodic limit of potential conditioning. Cluster migration and sintering proceeded by Smoluchowski ripening rather than atomistic processes and no significant amounts of material were lost as a result. Control experiments on Au_{923} showed that migration was not induced because the experimental potentials were not sufficient for oxidation. Potential hold and linear sweep voltammetry experiments confirm that both nanoparticle oxidation and reduction are necessary to induce migration.

In the final chapter the effect of plasma treatment on well-defined catalytically relevant nanoparticles was studied. Plasma treatment is commonly used in electron microscopy and post-synthesis to remove contamination; the results of this chapter, however, show that the effect of plasma treatment on the nanoparticles must be carefully considered. Both oxygen and argon plasmas resulted in sputtering of gold and platinum nanoparticles whereas only oxygen plasma treatment induced nanoparticle migration.

Nanoparticle migration on carbon supports was shown to proceed by nanoparticle oxidation under electrochemical and plasma treatment conditions. In the former case oxidation and reduction are driven by electrochemical surface processes, and in the latter oxidation is driven by reaction with oxygen ions and radicals in the plasma and subsequent reduction with water vapour. Future experiments may consider whether similar behaviour is observed at different cluster sizes. The question remains as to the origin of the surface processes driving nanoparticle migration. This question is well-suited to be studied by in-situ electrochemical TEM[108,110] which would be able to observe migration in real time and resolve the electrochemical potential required to drive migration. These experiments would be able to answer the questions raised in this thesis conclusively and bring the dream of ‘catalysts by design’ one step closer to reality.

8 References

1. BP. *BP Statistical Review of World Energy*. (2019).
2. Dunn, B., Kamath, H. & Tarascon, J.-M. Electrical Energy Storage for the Grid: A Battery of Choices. *Science (80-.).* **334**, 928–935 (2011).
3. Denholm, P., O'Connell, M., Brinkman, G. & Jorgenson, J. Overgeneration from Solar Energy in California: A Field Guide to the Duck Chart. *NREL* 46 (2015).
4. Fichtner, M. Nanoscale Materials For Hydrogen and Energy Storage. in *Frontiers of Nanoscience* **1**, 270–297 (Elsevier Ltd, 2009).
5. - International Energy Agency, I. *Global EV Outlook 2017. IEA Pub* (OECD, 2017). doi:10.1787/9789264278882-en
6. Nykvist, B. & Nilsson, M. Rapidly falling costs of battery packs for electric vehicles. *Nat. Clim. Chang.* **5**, 329–332 (2015).
7. Yoshida, T. & Kojima, K. Toyota MIRAI Fuel Cell Vehicle and Progress Toward a Future Hydrogen Society. *Interface Mag.* **24**, 45–49 (2015).
8. IEA. *The Future of Hydrogen*. (2019). doi:10.1016/S1464-2859(12)70027-5
9. Armaroli, N. & Balzani, V. The Hydrogen Issue. *ChemSusChem* **4**, 21–36 (2011).
10. Alivisatos, A. P. Semiconductor Clusters, Nanocrystals, and Quantum Dots. *Science (80-.).* **271**, 933–937 (1996).
11. Haruta, M., Kobayashi, T., Sano, H. & Yamada, N. Novel Gold Catalysts for the Oxidation of Carbon Monoxide at a Temperature far Below 0 °C. *Chem. Lett.* **16**, 405–408 (1987).
12. Heer, W. de. The physics of simple metal clusters: experimental aspects and simple models. *Rev. Mod. Phys.* **65**, 611–676 (1993).
13. Martin, T. P. Shells of Atoms. *Phys. Rep.* **273**, 199–241 (1996).
14. Wells, D. M., Rossi, G., Ferrando, R. & Palmer, R. E. Metastability of the atomic structures of size-selected gold nanoparticles. *Nanoscale* 7, 6498–6503 (2015).
15. de Heer, W. a., Knight, W. D., Chou, M. Y. & Cohen, M. L. Electronic Shell Structure and Metal Clusters. *Solid State Phys.* **40**, 93–181 (1987).
16. Blackmore, C. E., Rees, N. V & Palmer, R. E. Modular construction of size-selected multiple-core Pt–TiO 2 nanoclusters for electro-catalysis. *Phys. Chem. Chem. Phys.* **17**, 28005–28009 (2015).
17. Courtney, C. M. *et al.* Photoexcited quantum dots for killing multidrug-resistant bacteria. *Nat. Mater.* (2016). doi:10.1038/nmat4542
18. Xia, Y., Yang, H. & Campbell, C. T. Nanoparticles for catalysis. *Acc. Chem. Res.* **46**, 1671–1672 (2013).
19. Haruta, M. When gold is not noble: Catalysis by nanoparticles. *Chem. Rec.* **3**, 75–87 (2003).
20. Valden, M., Lai, X. & Goodman, D. W. W. Onset of Catalytic Activity of Gold Clusters on Titania with the Appearance of Nonmetallic Properties. *Science (80-.).* **281**, 1647–1650 (1998).
21. Bell, A. The Impact of Nanoscience on Heterogeneous Catalysis. *Science (80-.).* **1083671**, 299 (2003).

22. Linic, S., Christopher, P. & Ingram, D. B. Plasmonic-metal nanostructures for efficient conversion of solar to chemical energy. *Nat. Mater.* **10**, 911–21 (2011).

23. Naitabdi, A., Ono, L. K. & Roldan Cuenya, B. Local investigation of the electronic properties of size-selected Au nanoparticles by scanning tunneling spectroscopy. *Appl. Phys. Lett.* **89**, 2004–2007 (2006).

24. Kruis, F. E., Fissan, H. & Peled, A. Synthesis of nanoparticles in the gas phase for electronic, optical and magnetic applications - A review. *Journal of Aerosol Science* **29**, 511–535 (1998).

25. Chen, C.-C. *et al.* Three-dimensional imaging of dislocations in a nanoparticle at atomic resolution. *Nature* **496**, 74–77 (2013).

26. Shan, H. *et al.* Nanoscale kinetics of asymmetrical corrosion in core-shell nanoparticles. *Nat. Commun.* **9**, 1–9 (2018).

27. Nagao, H., Ichiji, M. & Hirasawa, I. Synthesis of Platinum Nanoparticles by Reductive Crystallization Using Polyethyleneimine. *Chem. Eng. Technol.* **40**, 1242–1246 (2017).

28. Chiu, C.-Y. *et al.* Platinum nanocrystals selectively shaped using facet-specific peptide sequences. *Nat. Chem.* **3**, 393–399 (2011).

29. Arán-Ais, R. M., Vidal-Iglesias, F. J., Solla-Gullón, J., Herrero, E. & Feliu, J. M. Electrochemical Characterization of Clean Shape-Controlled Pt Nanoparticles Prepared in Presence of Oleylamine/Oleic Acid. *Electroanalysis* **27**, 945–956 (2015).

30. Strasser, P., Gliech, M., Kuehl, S. & Moeller, T. Electrochemical processes on solid shaped nanoparticles with defined facets. *Chem. Soc. Rev.* **47**, 715–735 (2018).

31. Arán-Ais, R. M. *et al.* Identical Location Transmission Electron Microscopy Imaging of Site-Selective Pt Nanocatalysts: Electrochemical Activation and Surface Disordering. *J. Am. Chem. Soc.* **137**, 14992–14998 (2015).

32. Dietz, T. G., Duncan, M. A., Powers, D. E. & Smalley, R. E. Laser production of supersonic metal cluster beams. *J. Chem. Phys.* **74**, 6511–6512 (1981).

33. Liu, L. & Corma, A. Metal Catalysts for Heterogeneous Catalysis: From Single Atoms to Nanoclusters and Nanoparticles. *Chem. Rev.* **118**, 4981–5079 (2018).

34. Knight, W. D. *et al.* Electronic shell structure and abundances of sodium clusters. *Phys. Rev. Lett.* **52**, 2141–2143 (1984).

35. Mackay, A. L. A dense non-crystallographic packing of equal spheres. *Acta Crystallogr.* **15**, 916–918 (1962).

36. Hu, K.-J. *et al.* The effects of 1-pentyne hydrogenation on the atomic structures of size-selected Au N and Pd N (N = 923 and 2057) nanoclusters. *Phys. Chem. Chem. Phys.* **16**, 26631–26637 (2014).

37. Hu, K. J. *et al.* Atomic Resolution Observation of a Size-Dependent Change in the Ripening Modes of Mass-Selected Au Nanoclusters Involved in CO Oxidation. *J. Am. Chem. Soc.* **137**, 15161–15168 (2015).

38. Marks, L. D. Surface structure and energetics of multiply twinned particles. *Philos. Mag. A* **49**, 81–93 (1984).

39. Billinge, S. J. L. & Levin, I. The Problem with Determining Atomic Structure at the Nanoscale. *Science (80-.).* **316**, 561–565 (2007).

40. Navarro, J. R. G. *et al.* Synthesis, electron tomography and single-particle optical response

of twisted gold nano-bipyramids. *Nanotechnology* **23**, (2012).

41. Li, Z. Y. *et al.* Three-dimensional atomic-scale structure of size-selected gold nanoclusters. *Nature* **451**, 46–48 (2008).
42. Dawn Michelle Foster. Production and characterisation by scanning transmission electron microscopy of size-selected noble metal nanoclusters. (University of Birmingham, 2017).
43. Blackmore, C. E., Garden, A. L. & Palmer, R. E. Study and identification of Platinum nano-cluster structure. 1–9
44. Plant, S. R., Cao, L. & Palmer, R. E. Atomic Structure Control of Size-Selected Gold Nanoclusters during Formation. *J. Am. Chem. Soc.* **136**, 7559–7562 (2014).
45. Kerpal, C. *et al.* Structures of Platinum Oxide Clusters in the Gas Phase. *J. Phys. Chem. A* **117**, 1233–1239 (2013).
46. Bromann, K. *et al.* Controlled Deposition of Size-Selected Silver Nanoclusters. *Science (80-.).* **274**, 956–958 (1996).
47. Carroll, S. J. *et al.* Pinning of size-selected Ag clusters on graphite surfaces. *J. Chem. Phys.* **113**, 7723–7727 (2000).
48. Di Vece, M., Palomba, S. & Palmer, R. E. Pinning of size-selected gold and nickel nanoclusters on graphite. *Phys. Rev. B* **72**, 073407 (2005).
49. Palmer, R. E., Pratontep, S. & Boyen, H.-G. Nanostructured surfaces from size-selected clusters. *Nat. Mater.* **2**, 443–448 (2003).
50. Claeyssens, F., Pratontep, S., Xirouchaki, C. & Palmer, R. E. Immobilization of large size-selected silver clusters on graphite. *Nanotechnology* **17**, 805–807 (2006).
51. Wisniak, J. The History of Catalysis. From the Beginning to Nobel Prizes. *Educ. Química* **21**, 60–69 (2018).
52. Zhang, L. *et al.* Platinum-based nanocages with subnanometer-thick walls and well-defined, controllable facets. *Science* **349**, 412–416 (2015).
53. Strasser, P. Catalysts by Platonic design. *Science* **349**, 379–80 (2015).
54. Imaoka, T. *et al.* Platinum clusters with precise numbers of atoms for preparative-scale catalysis. *Nat. Commun.* **8**, 688 (2017).
55. Curry, S. W. Platinum Catalysts in Petroleum Refining. *Platin. Met. Rev.* **1**, 38–43 (1957).
56. Harding, D. J., Kerpal, C., Rayner, D. M. & Fielicke, A. Communication: The structures of small cationic gas-phase platinum clusters. *J. Chem. Phys.* **136**, (2012).
57. Baletto, F., Ferrando, R., Fortunelli, A., Montalenti, F. & Mottet, C. Crossover among structural motifs in transition and noble-metal clusters. *J. Chem. Phys.* **116**, 3856–3863 (2002).
58. Blackmore, C. E. Experimental and Theoretical Studies of the Atomic Structure of Platinum-based Nanoclusters. (University of Birmingham, 2016). doi:10.1016/0956-7151(90)90008-5
59. Eftekhari, A. Electrocatalysts for hydrogen evolution reaction. *Int. J. Hydrogen Energy* **42**, 11053–11077 (2017).
60. Jiao, Y., Zheng, Y., Jaroniec, M. & Qiao, S. Z. Design of electrocatalysts for oxygen- and hydrogen-involving energy conversion reactions. *Chemical Society Reviews* **44**, 2060–2086 (2015).
61. Roy A. Periana,* Douglas J. Taube, Scott Gamble, Henry Taube, Takashi Satoh, H. F.

Platinum Catalysts for the High-Yield Oxidation of Methane to a Methanol Derivative. *Science (80-.).* **280**, 560–564 (1998).

62. Heiz, U., Sanchez, A., Abbet, S. & Schneider, W.-D. Catalytic Oxidation of Carbon Monoxide on Monodispersed Platinum Clusters: Each Atom Counts. *J. Am. Chem. Soc.* **121**, 3214–3217 (1999).
63. Strasser, P. & Kühl, S. Dealloyed Pt-based core-shell oxygen reduction electrocatalysts. *Nano Energy* **29**, 166–177 (2016).
64. Beermann, V. *et al.* Rh-Doped Pt-Ni Octahedral Nanoparticles: Understanding the Correlation between Elemental Distribution, Oxygen Reduction Reaction, and Shape Stability. *Nano Lett.* **16**, 1719–1725 (2016).
65. Chong, L. *et al.* Ultralow-loading platinum-cobalt fuel cell catalysts derived from imidazolate frameworks. *Science (80-.).* **362**, 1276–1281 (2018).
66. Li, M. *et al.* Single-atom tailoring of platinum nanocatalysts for high-performance multifunctional electrocatalysis. *Nat. Catal.* **2**, 495–503 (2019).
67. Banham, D. & Ye, S. Current status and future development of catalyst materials and catalyst layers for proton exchange membrane fuel cells: An industrial perspective. *ACS Energy Letters* **2**, 629–638 (2017).
68. Fisher, A. C. *Electrode Dynamics.* (Oxford University Press, 1996).
69. Li, Y. *et al.* MoS 2 Nanoparticles Grown on Graphene: An Advanced Catalyst for the Hydrogen Evolution Reaction. *J. Am. Chem. Soc.* **133**, 7296–7299 (2011).
70. Zeng, M. & Li, Y. Recent advances in heterogeneous electrocatalysts for the hydrogen evolution reaction. *J. Mater. Chem. A* **3**, 14942–14962 (2015).
71. Ahmad, H., Kamarudin, S. K., Minggu, L. J. & Kassim, M. Hydrogen from photo-catalytic water splitting process: A review. *Renew. Sustain. Energy Rev.* **43**, 599–610 (2015).
72. Wang, Z. *et al.* An ultrafine platinum–cobalt alloy decorated cobalt nanowire array with superb activity toward alkaline hydrogen evolution. *Nanoscale* **10**, 12302–12307 (2018).
73. *IUPAC Compendium of Chemical Terminology.* (IUPAC, 2009). doi:10.1351/goldbook
74. US Office of energy efficiency & renewable energy. 3.4 Fuel Cells. *Fuel Cell Technol. Off. Multi-Year Res. Dev. Demonstr. Plan* **2015**, 3.4.1-3.4.58 (2017).
75. Yu, C. *et al.* Growth Trajectories and Coarsening Mechanisms of Metal Nanoparticle Electrocatalysts. *ChemCatChem* **4**, 766–770 (2012).
76. Wynblatt, P. & Gjostein, N. A. Particle growth in model supported metal catalysts—I. Theory. *Acta Metall.* **24**, 1165–1174 (1976).
77. Chen, L.-Q. Chemical potential and Gibbs free energy. *MRS Bull.* **44**, 520–523 (2019).
78. Hansen, T. W., DeLaRiva, A. T., Challa, S. R. & Datye, A. K. Sintering of Catalytic Nanoparticles: Particle Migration or Ostwald Ripening? *Acc. Chem. Res.* **46**, 1720–1730 (2013).
79. Wynblatt, P. & Gjostein, N. A. Supported metal crystallites. *Prog. Solid State Chem.* **9**, 21–58 (1975).
80. Adibi, P. T. Z. In situ Studies of Platinum Catalyst Sintering. (Chalmers University of Technology, 2016).
81. Kolosov, A. Y. *et al.* Estimation of the Dihedral Angle Between Metal Nanoparticles During Their Coalescence. *J. Nano- Electron. Phys.* **9**, 05042-1-05042–4 (2017).

82. Fukamori, Y. *et al.* Fundamental Insight into the Substrate-Dependent Ripening of Monodisperse Clusters. *ChemCatChem* **5**, 3330–3341 (2013).
83. Witten, T. A. & Sander, L. M. Diffusion-limited aggregation. *Phys. Rev. B* **27**, 5686–5697 (1983).
84. Witten, T. A. & Sander, L. M. Diffusion-limited aggregation, a kinetic critical phenomenon. *Phys. Rev. Lett.* **47**, 1400–1403 (1981).
85. Celardo, G. L. *et al.* Evidence of diffusive fractal aggregation of TiO2 nanoparticles by femtosecond laser ablation at ambient conditions. *Mater. Res. Express* **4**, 015013 (2017).
86. Dubau, L., Castanheira, L., Berthomé, G. & Maillard, F. An identical-location transmission electron microscopy study on the degradation of Pt/C nanoparticles under oxidizing, reducing and neutral atmosphere. *Electrochim. Acta* **110**, 273–281 (2013).
87. Wakisaka, M., Asizawa, S., Uchida, H. & Watanabe, M. In situ STM observation of morphological changes of the Pt(111) electrode surface during potential cycling in 10 mM HF solution. *Phys. Chem. Chem. Phys.* **12**, 4184 (2010).
88. Imai, H. *et al.* In Situ and Real-Time Monitoring of Oxide Growth in a Few Monolayers at Surfaces of Platinum Nanoparticles in Aqueous Media In Situ and Real-Time Monitoring of Oxide Growth in a Few Monolayers at Surfaces of Platinum Nanoparticles in Aqueous. 6293–6300 (2009). doi:10.1021/ja810036h
89. Oi Uchisawa, J., Obuchi, A., Zhao, Z. & Kushiyama, S. Carbon oxidation with platinum supported catalysts. *Appl. Catal. B Environ.* **18**, L183–L187 (1998).
90. Lafforgue, C., Maillard, F., Martin, V., Dubau, L. & Chatenet, M. Degradation of Carbon-Supported Platinum-Group-Metal Electrocatalysts in Alkaline Media Studied by in Situ Fourier Transform Infrared Spectroscopy and Identical-Location Transmission Electron Microscopy. *ACS Catal.* 5613–5622 (2019). doi:10.1021/acscatal.9b00439
91. Sode, A., Musgrove, A. & Bizzotto, D. Stability of PtZn nanoparticles supported on carbon in acidic electrochemical environments. *J. Phys. Chem. C* **114**, 546–553 (2010).
92. Elgrishi, N. *et al.* A Practical Beginner's Guide to Cyclic Voltammetry. *J. Chem. Educ.* **95**, 197–206 (2018).
93. Hartl, K. *et al.* Electrochemically induced nanocluster migration. *Electrochim. Acta* **56**, 810–816 (2010).
94. Zana, A. *et al.* Probing Degradation by IL-TEM: The Influence of Stress Test Conditions on the Degradation Mechanism. *J. Electrochem. Soc.* **160**, F608–F615 (2013).
95. Kuzume, A., Herrero, E. & Feliu, J. M. Oxygen reduction on stepped platinum surfaces in acidic media. *J. Electroanal. Chem.* **599**, 333–343 (2007).
96. Granqvist, C. G. & Buhrman, R. A. Size Distributions for Supported Metal Catalysts. *J. Catal.* **42**, 477–479 (1976).
97. Virkar, A. V. & Zhou, Y. Mechanism of Catalyst Degradation in Proton Exchange Membrane Fuel Cells. *J. Electrochem. Soc.* **154**, B540 (2007).
98. Binnig, G., Rohrer, H., Gerber, C. & Weibel, E. 7 × 7 Reconstruction on Si(111) Resolved in Real Space. *Phys. Rev. Lett.* **50**, 120–123 (1983).
99. Williams, D. B. & Carter, C. B. *Transmission Electron Microscopy- A Textbook for Materials Science. Micron* (2008).
100. Otten, M. T. High-Angle annular dark-field imaging on a tem/stem system. *J. Electron*

Microsc. Tech. **17**, 221–230 (1991).

101. Wang, Z. W. *et al.* Quantitative Z-contrast imaging in the scanning transmission electron microscope with size-selected clusters. *Phys. Rev. B* **84**, 073408 (2011).
102. Jones, L. Quantitative ADF STEM: acquisition, analysis and interpretation. *IOP Conf. Ser. Mater. Sci. Eng.* **109**, 012008 (2016).
103. Wang, Z. L. New developments in transmission electron microscopy for nanotechnology. *Adv. Mater.* **15**, 1497–1514 (2003).
104. Biroju, R. K. *et al.* Hydrogen Evolution Reaction Activity of Graphene–MoS 2 van der Waals Heterostructures. *ACS Energy Lett.* **2**, 1355–1361 (2017).
105. Winey, M., Meehl, J. B., O'Toole, E. T. & Giddings, T. H. Conventional transmission electron microscopy. *Mol. Biol. Cell* **25**, 319–323 (2014).
106. Zadick, A., Dubau, L., Zalineeva, A., Coutanceau, C. & Chatenet, M. When cubic nanoparticles get spherical: An Identical Location Transmission Electron Microscopy case study with Pd in alkaline media. *Electrochem. commun.* **48**, 1–4 (2014).
107. Simonsen, S. B. *et al.* Direct observations of oxygen-induced platinum nanoparticle ripening studied by in situ TEM. *J. Am. Chem. Soc.* **132**, 7968–7975 (2010).
108. Park, J. H. *et al.* In situ EC-TEM Studies of Metal Thin Film Corrosion in Liquid Solutions at Elevated Temperatures. *Microsc. Microanal.* **24**, 254–255 (2018).
109. Li, D. *et al.* Direction-Specific Interactions Control Crystal Growth by Oriented Attachment. *Science (80-.).* **336**, 1014–1018 (2012).
110. Hodnik, N., Dehm, G. & Mayrhofer, K. J. J. Importance and Challenges of Electrochemical in Situ Liquid Cell Electron Microscopy for Energy Conversion Research. *Acc. Chem. Res.* **49**, 2015–2022 (2016).
111. Pratontep, S., Carroll, S. J., Xirouchaki, C., Streun, M. & Palmer, R. E. Size-selected cluster beam source based on radio frequency magnetron plasma sputtering and gas condensation. *Rev. Sci. Instrum.* **76**, (2005).
112. Pearmain, D., Park, S. J., Abdela, A., Palmer, R. E. & Li, Z. Y. The size-dependent morphology of Pd nanoclusters formed by gas condensation. *Nanoscale* **7**, 19647–19652 (2015).
113. Escalera-López, D. *et al.* Enhancement of the Hydrogen Evolution Reaction from Ni-MoS 2 Hybrid Nanoclusters. *ACS Catal.* **6**, 6008–6017 (2016).
114. Swann, S. Magnetron sputtering. *Phys. Technol.* **19**, 67–75 (1988).
115. von Issendorff, B., Palmer, R. E. & von Issendorff, B. A new high transmission infinite range mass selector for cluster and nanoparticle beams. *Rev. Sci. Instrum.* **70**, 4497–4501 (1999).
116. Gholhaki, S. *et al.* Exposure of mass-selected bimetallic Pt–Ti nanoalloys to oxygen explored using scanning transmission electron microscopy and density functional theory. *RSC Adv.* **8**, 27276–27282 (2018).
117. Van Der Walt, S. *et al.* Scikit-image: Image processing in python. *PeerJ* **2014**, (2014).
118. Oliphant, T. E. Python for scientific computing. *Comput. Sci. Eng.* **9**, 10–20 (2007).
119. Hunter, J. D. Matplotlib: A 2D graphics environment. *Comput. Sci. Eng.* **9**, 99–104 (2007).
120. Nečas, D. & Klapetek, P. Gwyddion: An open-source software for SPM data analysis.

Central European Journal of Physics **10**, 181–188 (2012).

121. Otsu, N. A Threshold Selection Method from Gray-Level Histograms. *IEEE Trans. Syst. Man. Cybern.* **9**, 62–66 (1979).

122. Glasbey, C. A. An Analysis of Histogram-Based Thresholding Algorithms. *CVGIP Graph. Model. Image Process.* **55**, 532–537 (1993).

123. Xu, X., Xu, S., Jin, L. & Song, E. Characteristic analysis of Otsu threshold and its applications. *Pattern Recognit. Lett.* **32**, 956–961 (2011).

124. Yang, X., Shen, X., Long, J. & Chen, H. An Improved Median-based Otsu Image Thresholding Algorithm. *AASRI Procedia* **3**, 468–473 (2012).

125. Coudray, N., Buessler, J.-L. & Urban, J.-P. Robust threshold estimation for images with unimodal histograms. *Pattern Recognit. Lett.* **31**, 1010–1019 (2010).

126. Ng, H.-F., Jargalsaikhan, D., Tsai, H.-C. & Lin, C.-Y. An improved method for image thresholding based on the valley-emphasis method. in *2013 Asia-Pacific Signal and Information Processing Association Annual Summit and Conference* **0**, 1–4 (IEEE, 2013).

127. Rosin, P. L. Unimodal thresholding. *Pattern Recognit.* **34**, 2083–2096 (2001).

128. Canny, J. A Computational Approach to Edge Detection. *IEEE Trans. Pattern Anal. Mach. Intell.* **PAMI-8**, 679–698 (1986).

129. Neng, W., Shuang-ying, L., Jun, X. & Martini, M. A 'jump-to-coalescence' mechanism during nanoparticle growth revealed by in situ aberration-corrected transmission electron microscopy observations. *Nanotechnology* **27**, 205605 (2016).

130. Wang, Z. W. *et al.* Counting the atoms in supported, monolayer-protected gold clusters. *J. Am. Chem. Soc.* **132**, 2854–2855 (2010).

131. Ustarroz, J. *et al.* Mobility and Poisoning of Mass-Selected Platinum Nanoclusters during the Oxygen Reduction Reaction. *ACS Catal.* **8**, 6775–6790 (2018).

132. Nesselberger, M. *et al.* The effect of particle proximity on the oxygen reduction rate of size-selected platinum clusters. *Nat. Mater.* **12**, 919–924 (2013).

133. Torquato, S., Lu, B. & Rubinstein, J. Nearest-neighbour distribution function for systems on interacting particles. *J. Phys. A. Math. Gen.* **23**, L103–L107 (1990).

134. Torquato, S., Lu, B. & Rubinstein, J. Nearest-neighbor distribution functions in many-body systems. *Phys. Rev. A* **41**, 2059–2075 (1990).

135. Ennos, A. E. The origin of specimen contamination in the electron microscope. *Br. J. Appl. Phys.* **4**, 101–106 (1953).

136. Horiuchi, S. *et al.* Contamination-Free Transmission Electron Microscopy for High-Resolution Carbon Elemental Mapping of Polymers. *ACS Nano* **3**, 1297–1304 (2009).

137. Young, N. P. *et al.* Weighing supported nanoparticles: Size-selected clusters as mass standards in nanometrology. *Phys. Rev. Lett.* **101**, 28–31 (2008).

138. Wang, Z. W. & Palmer, R. E. Intensity calibration and atomic imaging of size-selected Au and Pd clusters in aberration-corrected HAADF-STEM. *J. Phys. Conf. Ser.* **371**, 012010 (2012).

139. Tripković, V., Cerri, I., Bligaard, T. & Rossmeisl, J. The Influence of Particle Shape and Size on the Activity of Platinum Nanoparticles for Oxygen Reduction Reaction: A Density Functional Theory Study. *Catal. Letters* **144**, 380–388 (2014).

140. Vidal-Iglesias, F. J. *et al.* Shape-dependent electrocatalysis: ammonia oxidation on platinum nanoparticles with preferential (100) surfaces. *Electrochem. commun.* **6**, 1080–1084 (2004).

141. Koper, M. T. M. Structure sensitivity and nanoscale effects in electrocatalysis. *Nanoscale* **3**, 2054 (2011).

142. Hjorth Larsen, A. *et al.* The atomic simulation environment—a Python library for working with atoms. *J. Phys. Condens. Matter* **29**, 273002 (2017).

143. Koch, C. Determination of Core Structure Periodicity and Point Defect Density Along Dislocations. (Arizona State University, 2002).

144. He, D. S., Li, Z. Y. & Yuan, J. Kinematic HAADF-STEM image simulation of small nanoparticles. *Micron* **74**, 47–53 (2015).

145. Curley, B. C. *et al.* Combining Theory and Experiment to Characterize the Atomic Structures of Surface-Deposited Au 309 Clusters. *J. Phys. Chem. C* **111**, 17846–17851 (2007).

146. Wang, Z. W. & Palmer, R. E. Determination of the ground-state atomic structures of size-selected Au nanoclusters by electron-beam-induced transformation. *Phys. Rev. Lett.* **108**, 1–5 (2012).

147. Foster, D. M., Ferrando, R. & Palmer, R. E. Experimental determination of the energy difference between competing isomers of deposited, size-selected gold nanoclusters. *Nat. Commun.* **9**, 1323 (2018).

148. Liu, J., Foster, D., Li, Z. Y., Wilkinson, N. & Yuan, J. Coalescence dynamics of size-selected gold clusters studied by time-resolved transmission electron microscopy. *J. Phys. Conf. Ser.* **902**, 012008 (2017).

149. Zheng, H., Mirsaidov, U. M., Wang, L.-W. & Matsudaira, P. Electron Beam Manipulation of Nanoparticles. *Nano Lett.* **12**, 5644–5648 (2012).

150. Asoro, M. A., Kovar, D., Shao-Horn, Y., Allard, L. F. & Ferreira, P. J. Coalescence and sintering of Pt nanoparticles: in situ observation by aberration-corrected HAADF STEM. *Nanotechnology* **21**, 025701 (2010).

151. Lange, A. P. *et al.* Dislocation mediated alignment during metal nanoparticle coalescence. *Acta Mater.* **120**, 364–378 (2016).

152. Arblaster, J. W. Crystallographic properties of Platinum. *Platin. Met. Rev.* **41**, 12–21 (1997).

153. Xia, Y., Harrison, P., Ornelas, I. M., Wang, H. L. & Li, Z. Y. *Effects of defocus and magnification on HAADF intensity of nanoclusters in STEM images.* (2019).

154. Imaoka, T. *et al.* Magic number Pt13 and misshapen Pt12 clusters: Which one is the better catalyst? *J. Am. Chem. Soc.* **135**, 13089–13095 (2013).

155. Tyo, E. C. & Vajda, S. Catalysis by clusters with precise numbers of atoms. *Nat. Nanotechnol.* **10**, 577–588 (2015).

156. Li, M. *et al.* Ultrafine jagged platinum nanowires enable ultrahigh mass activity for the oxygen reduction reaction. *Science (80-.).* **354**, 1414–1419 (2016).

157. Huang, X. *et al.* High-performance transition metal-doped Pt3Ni octahedra for oxygen reduction reaction. *Science* **348**, 1230–4 (2015).

158. Zhang, J., Sasaki, K., Sutter, E. & Adzic, R. R. Stabilization of Platinum Oxygen-Reduction

Electrocatalysts Using Gold Clusters. *Science (80-.).* **315**, 220–222 (2007).

159. Nair, R. R. *et al.* It's still all about graphene. *Nature Materials* **10**, 1 (2011).
160. Seifalian, A. A new era of cancer treatment: carbon nanotubes as drug delivery tools. *Int. J. Nanomedicine* 2963 (2011). doi:10.2147/IJN.S16923
161. Climent, V. & Feliu, J. M. Thirty years of platinum single crystal electrochemistry. *J. Solid State Electrochem.* **15**, 1297–1315 (2011).
162. Drnec, J., Harrington, D. A. & Magnussen, O. M. Electrooxidation of Pt(111) in acid solution. *Curr. Opin. Electrochem.* **4**, 69–75 (2017).
163. Jerkiewicz, G., Vatankhah, G., Lessard, J., Soriaga, M. P. & Park, Y.-S. Surface-oxide growth at platinum electrodes in aqueous H2SO4. *Electrochim. Acta* **49**, 1451–1459 (2004).
164. Chen, D. *et al.* Determining the Active Surface Area for Various Platinum Electrodes. *Electrocatalysis* **2**, 207–219 (2011).
165. Arenz, M. *et al.* The effect of the particle size on the kinetics of CO electrooxidation on high surface area Pt catalysts. *J. Am. Chem. Soc.* **127**, 6819–6829 (2005).
166. Urchaga, P., Baranton, S., Coutanceau, C. & Jerkiewicz, G. Electro-oxidation of CO chem on Pt nanosurfaces: Solution of the peak multiplicity puzzle. *Langmuir* **28**, 3658–3663 (2012).
167. Affrossman, S. & Cvetanović, R. J. DISPLACEMENT OF C 4 -HYDROCARBON MOLECULES ADSORBED ON PLATINUM. *Can. J. Chem.* **42**, 1206–1211 (1964).
168. Vidaković, T., Christov, M. & Sundmacher, K. The use of CO stripping for in situ fuel cell catalyst characterization. *Electrochim. Acta* **52**, 5606–5613 (2007).
169. KRISHNAN, K. S. & GANGULI, N. Large Anisotropy of the Electrical Conductivity of Graphite. *Nature* **144**, 667–667 (1939).
170. Supplies, S. GLASSY CARBON PRODUCT INFORMATION. (2019).
171. Tsunoyama, H. *et al.* Size-Effect on Electrochemical Hydrogen Evolution Reaction by Single-Size Platinum Nanocluster Catalysts Immobilized on Strontium Titanate. *Top. Catal.* **61**, 126–135 (2018).
172. Castanheira, L. *et al.* Carbon Corrosion in Proton-Exchange Membrane Fuel Cells: Effect of the Carbon Structure, the Degradation Protocol, and the Gas Atmosphere. *ACS Catal.* **5**, 2184–2194 (2015).
173. Li, F. & Lannin, J. S. Radial distribution function of amorphous carbon. *Phys. Rev. Lett.* **65**, 1905–1908 (1990).
174. Benck, J. D., Pinaud, B. A., Gorlin, Y. & Jaramillo, T. F. Substrate Selection for Fundamental Studies of Electrocatalysts and Photoelectrodes: Inert Potential Windows in Acidic, Neutral, and Basic Electrolyte. *PLoS One* **9**, e107942 (2014).
175. Yi, Y. *et al.* Electrochemical corrosion of a glassy carbon electrode. *Catal. Today* **295**, 32–40 (2017).
176. Cherevko, S., Topalov, A. A., Zeradjanin, A. R., Katsounaros, I. & Mayrhofer, K. J. J. Gold dissolution: towards understanding of noble metal corrosion. *RSC Adv.* **3**, 16516 (2013).
177. Jiang, W., Tang, F. & Gan, L. Electrochemical stability of Au-TEM grid with carbon supporting film in acid and alkaline electrolytes for identical-location TEM study. *J. Electroanal. Chem.* **826**, 46–51 (2018).

178. Haberland, H., Insepov, Z. & Moseler, M. Molecular-dynamics simulation of thin-film growth by energetic cluster impact. *Phys. Rev. B* **51**, 11061–11067 (1995).

179. Rattunde, O. *et al.* Surface smoothing by energetic cluster impact. *J. Appl. Phys.* **90**, 3226–3231 (2001).

180. Ziff, R. M., McGrady, E. D. & Meakin, P. On the validity of Smoluchowski's equation for cluster–cluster aggregation kinetics. *J. Chem. Phys.* **82**, 5269–5274 (1985).

181. Thompson, H. R. Distribution of Distance to Nth Neighbour in a Population of Randomly Distributed Individuals. *Ecology* **37**, 391–394 (1956).

182. Bardotti, L., Tournus, F., Mélinon, P., Pellarin, M. & Broyer, M. Mass-selected clusters deposited on graphite: Spontaneous organization controlled by cluster surface reaction. *Phys. Rev. B* **83**, 035425 (2011).

183. Zhu, C. *et al.* In-situ liquid cell transmission electron microscopy investigation on oriented attachment of gold nanoparticles. *Nat. Commun.* **9**, 421 (2018).

184. Zheng, H. *et al.* Observation of Single Colloidal Platinum Nanocrystal Growth Trajectories. *Science (80-.).* **324**, 1309–1312 (2009).

185. Liao, H.-G., Cui, L., Whitelam, S. & Zheng, H. Real-Time Imaging of Pt3Fe Nanorod Growth in Solution. *Science (80-.).* **336**, 1011–1014 (2012).

186. Martinez, G. T. *et al.* Quantitative STEM normalisation: The importance of the electron flux. *Ultramicroscopy* **159**, 46–58 (2015).

187. Lee, J., Yang, J., Kwon, S. G. & Hyeon, T. Nonclassical nucleation and growth of inorganic nanoparticles. *Nat. Rev. Mater.* **1**, 16034 (2016).

188. Grammatikopoulos, P., Sowwan, M. & Kioseoglou, J. Computational Modeling of Nanoparticle Coalescence. *Adv. Theory Simulations* **1900013**, 1900013 (2019).

189. Mom, R. *et al.* The Oxidation of Platinum under Wet Conditions Observed by Electrochemical X-ray Photoelectron Spectroscopy. *J. Am. Chem. Soc.* **141**, 6537–6544 (2019).

190. Topalov, A. a. *et al.* Towards a comprehensive understanding of platinum dissolution in acidic media. *Chem. Sci.* **5**, 631–638 (2014).

191. Zhou, W., Wu, J. & Yang, H. Highly uniform platinum icosahedra made by hot injection-assisted GRAILS method. *Nano Lett.* **13**, 2870–2874 (2013).

192. Meier, J. C. *et al.* Degradation mechanisms of Pt/C fuel cell catalysts under simulated start-stop conditions. *ACS Catal.* **2**, 832–843 (2012).

193. Ellinger, C., Stierle, A., Robinson, I. K., Nefedov, A. & Dosch, H. Atmospheric pressure oxidation of Pt(111). *J. Phys. Condens. Matter* **20**, 184013 (2008).

194. Wei, Y. *et al.* Highly Active Catalysts of Gold Nanoparticles Supported on Three-Dimensionally Ordered Macroporous LaFeO 3 for Soot Oxidation. *Angew. Chemie Int. Ed.* **50**, 2326–2329 (2011).

195. Aliofkhazraei, M. *Handbook of Nanoparticles. Handbook of Nanoparticles* (Springer International Publishing, 2016). doi:10.1007/978-3-319-15338-4

196. Chen, Q.-S., Solla-Gullón, J., Sun, S.-G. & Feliu, J. M. The potential of zero total charge of Pt nanoparticles and polycrystalline electrodes with different surface structure: The role of anion adsorption in fundamental electrocatalysis. *Electrochim. Acta* **55**, 7982–7994 (2010).

197. Vidal-iglesias, F. J., Arán-Ais, R. M., Solla-Gullón, J., Herrero, E. & Feliu, J. M. Electrochemical Characterization of Shape-Controlled Pt Nanoparticles in Different Supporting Electrolytes. *ACS Catal.* **2**, 901–910 (2012).

198. Wettergren, K. *et al.* High sintering resistance of size-selected platinum cluster catalysts by suppressed ostwald ripening. *Nano Lett.* **14**, 5803–5809 (2014).

199. José-Yacamán, M. *et al.* Surface diffusion and coalescence of mobile metal nanoparticles. *J. Phys. Chem. B* **109**, 9703–9711 (2005).

200. Bittencourt, C. *et al.* Platinum–carbon nanotube interaction. *Chem. Phys. Lett.* **462**, 260–264 (2008).

201. Yu, X. & Ye, S. Recent advances in activity and durability enhancement of Pt/C catalytic cathode in PEMFC. *J. Power Sources* **172**, 133–144 (2007).

202. Zhao, Z., Dubau, L. & Maillard, F. Evidences of the migration of Pt crystallites on high surface area carbon supports in the presence of reducing molecules. *J. Power Sources* **217**, 449–458 (2012).

203. Cho, E., Yitamben, E. N., Iski, E. V., Guisinger, N. P. & Kuech, T. F. Atomic-scale investigation of highly stable Pt clusters synthesized on a graphene support for catalytic applications. *J. Phys. Chem. C* **116**, 26066–26071 (2012).

204. Maillard, F., Bonnefont, A. & Micoud, F. An EC-FTIR study on the catalytic role of Pt in carbon corrosion. *Electrochem. commun.* **13**, 1109–1111 (2011).

205. Maillard, F. *et al.* Influence of particle agglomeration on the catalytic activity of carbon-supported Pt nanoparticles in CO monolayer oxidation. *Phys. Chem. Chem. Phys.* **7**, 385–393 (2005).

206. Tainoff, D. *et al.* Self-Organization of Size-Selected Bare Platinum Nanoclusters: Toward Ultra-dense Catalytic Systems. *J. Phys. Chem. C* **112**, 6842–6849 (2008).

207. Huang, Y.-F., Kooyman, P. J. & Koper, M. T. M. Intermediate stages of electrochemical oxidation of single-crystalline platinum revealed by in situ Raman spectroscopy. *Nat. Commun.* **7**, 12440 (2016).

208. Sugawara, Y., Okayasu, T., Yadav, A. P., Nishikata, A. & Tsuru, T. Dissolution Mechanism of Platinum in Sulfuric Acid Solution. *J. Electrochem. Soc.* **159**, F779–F786 (2012).

209. Ruge, M. *et al.* Structural Reorganization of Pt(111) Electrodes by Electrochemical Oxidation and Reduction. *J. Am. Chem. Soc.* **139**, 4532–4539 (2017).

210. Jacobse, L., Huang, Y. F., Koper, M. T. M. & Rost, M. J. Correlation of surface site formation to nanoisland growth in the electrochemical roughening of Pt(111). *Nat. Mater.* **17**, 277–282 (2018).

211. Jian, N. Scanning Transmission Electron Microscopy of Atomic Structure of Nanoparticle. (University of Birmingham, 2016).

212. Vasileiadis, T. *et al.* Ultrafast Heat Flow in Heterostructures of Au Nanoclusters on Thin-Films: Atomic-Disorder Induced by Hot Electrons. *ACS Nano* **12**, 7710–7720 (2018).

213. Massoni, N., Beaumont-Martinent, A. & Laurent, J. Y. Effect of an oxygen plasma treatment on the specific surface of platinum electrodeposits for fuel cells. *J. Power Sources* **166**, 68–73 (2007).

214. Hsueh, Y.-C., Wang, C.-C., Liu, C., Kei, C.-C. & Perng, T.-P. Deposition of platinum on oxygen plasma treated carbon nanotubes by atomic layer deposition. *Nanotechnology* **23**,

405603 (2012).

215. Gehl, B. *et al.* Structural and chemical effects of plasma treatment on close-packed colloidal nanoparticle layers. *Adv. Funct. Mater.* **18**, 2398–2410 (2008).

216. Duan, Y., Rani, S., Newberg, J. T. & Teplyakov, A. V. Investigation of the influence of oxygen plasma on supported silver nanoparticles. *J. Vac. Sci. Technol. A Vacuum, Surfaces, Film.* **36**, 01B101 (2018).

217. Blackstock, J. J., Stewart, D. R. & Li, Z. Plasma-produced ultra-thin platinum-oxide films for nanoelectronics: Physical characterization. *Appl. Phys. A Mater. Sci. Process.* **80**, 1343–1353 (2005).

218. Kielbassa, S. *et al.* On the Morphology and Stability of Au Nanoparticles on TiO 2 (110) Prepared from Micelle-Stabilized Precursors. *Langmuir* **22**, 7873–7880 (2006).

219. Gun, J. *et al.* Oxygen plasma-treated gold nanoparticle-based field-effect devices as transducer structures for bio-chemical sensing. *Microchim. Acta* **164**, 395–404 (2009).

220. Tang, J., Photopoulos, P., Tserepi, A. & Tsoukalas, D. Two-dimensional nanoparticle self-assembly using plasma-induced Ostwald ripening. *Nanotechnology* **22**, 235306 (2011).

221. Ma, S. *et al.* Low temperature plasma sintering of silver nanoparticles. *Appl. Surf. Sci.* **293**, 207–215 (2014).

222. Liu, W. *et al.* Recent Progress in Rapid Sintering of Nanosilver for Electronics Applications. *Micromachines* **9**, 346 (2018).

223. Bandak, J. *et al.* Interconnected electrocatalytic Pt-metal networks by plasma treatment of nanoparticle-peptide fibril assemblies. *RSC Adv.* **9**, 5558–5569 (2019).

224. Yang, H., Zhang, J., Sun, K., Zou, S. & Fang, J. Enhancing by Weakening: Electrooxidation of Methanol on Pt3Co and Pt Nanocubes. *Angew. Chemie Int. Ed.* **49**, 6848–6851 (2010).

225. Li, Z., Beck, P., Ohlberg, D. A. ., Stewart, D. R. & Williams, R. S. Surface properties of platinum thin films as a function of plasma treatment conditions. *Surf. Sci.* **529**, 410–418 (2003).

226. Yajima, T. Electrochemical characteristics of platinum surface treated by RF plasma. *Surf. Coatings Technol.* **112**, 80–84 (1999).

227. Kim, S. Y. *et al.* Effect of N2, Ar, and O2 plasma treatments on surface properties of metals. *J. Appl. Phys.* **103**, 076101 (2008).

228. Chou, C. H. & Phillips, J. Platinum metal etching in a microwave oxygen plasma. *J. Appl. Phys.* **68**, 2415–2423 (1990).

229. Krejci, A. J., Garcia, A. M., Pham, V. H., Sun, S. & Dickerson, J. H. Comparing highly ordered monolayers of nanoparticles fabricated using electrophoretic deposition: Cobalt ferrite nanoparticles versus iron oxide nanoparticles. *J. Electrochem. Soc.* **162**, D3036–D3039 (2015).

230. Banerjee, R. *et al.* Ambient Oxidation of Ultrasmall Platinum Nanoparticles on Microporous Carbon Catalyst Supports. *ACS Appl. Nano Mater.* **1**, 5876–5884 (2018).

231. Banerjee, R., Liu, Q., Tengco, J. M. M. & Regalbuto, J. R. Detection of Ambient Oxidation of Ultrasmall Supported Platinum Nanoparticles with Benchtop Powder X-Ray Diffraction. *Catal. Letters* **147**, 1754–1764 (2017).

232. Galloni, E. E. & Roffo, A. E. The Crystalline Structure of Pt 3 O 4. *J. Chem. Phys.* **9**, 875–877 (1941).

233. Su, D. S. *et al.* Electron beam induced reduction of V2O5 studied by analytical electron microscopy. *Catal. Letters* **75**, 81–86 (2001).

234. Campos, A. *et al.* Plasmonic quantum size effects in silver nanoparticles are dominated by interfaces and local environments. *Nat. Phys.* **15**, 275–280 (2019).

235. Yamamoto, M. *et al.* Comparison of Argon and Oxygen Plasma Treatments for Ambient Room-Temperature Wafer-Scale Au–Au Bonding Using Ultrathin Au Films. *Micromachines* **10**, 119 (2019).

236. Boyen, H. G. *et al.* Oxidation-resistant gold-55 clusters. *Science (80-.).* **297**, 1533–1536 (2002).

237. Plasma, H. Plasma Cleaning for UHV Applications. (2019).

238. Yang, D.-Q. & Sacher, E. Ar+-induced surface defects on HOPG and their effect on the nucleation, coalescence and growth of evaporated copper. *Surf. Sci.* **516**, 43–55 (2002).

239. Akola, J. & Häkkinen, H. Density functional study of gold atoms and clusters on a graphite (0001) surface with defects. *Phys. Rev. B* **74**, 165404 (2006).

240. Bao, X. *et al.* Carbon vacancy defect-activated Pt cluster for hydrogen generation. *J. Mater. Chem. A* **7**, 15364–15370 (2019).

241. Gibbs, T. K., McCallum, C. & Pletcher, D. The oxidation of carbon monoxide at platinum and gold metallized membrane electrodes. *Electrochim. Acta* **22**, 525–530 (1977).

242. Alonso, C. *et al.* The Evaluation of Surface Diffusion Coefficients of Gold and Platinum Atoms at Electrochemical Interfaces from Combined STM-SEM Imaging and Electrochemical Techniques. *J. Electrochem. Soc.* **137**, 2161–2166 (1990).

243. CHU, Y. On the sintering of platinum on alumina model catalyst. *J. Catal.* **55**, 281–298 (1978).

244. Tsai, H. *et al.* Instability of gold oxide Au2O3. *Surf. Sci.* **537**, L447–L450 (2003).

245. Ono, L. K. & Cuenya, B. R. Formation and thermal stability of Au2O3 on gold nanoparticles: Size and support effects. *J. Phys. Chem. C* **112**, 4676–4686 (2008).

246. Yoshida, H., Omote, H. & Takeda, S. Oxidation and reduction processes of platinum nanoparticles observed at the atomic scale by environmental transmission electron microscopy. *Nanoscale* **6**, 13113–13118 (2014).

247. Zou, Y., Walton, A. S., Kinloch, I. A. & Dryfe, R. A. W. Investigation of the Differential Capacitance of Highly Ordered Pyrolytic Graphite as a Model Material of Graphene. *Langmuir* **32**, 11448–11455 (2016).

248. Holland, L. & Ojha, S. The chemical sputtering of graphite in an oxygen plasma. *Vacuum* **26**, 53–60 (1976).

249. Wörz, A. S., Heiz, U., Cinquini, F. & Pacchioni, G. Charging of Au atoms on TiO2 thin films from CO vibrational spectroscopy and DFT calculations. *J. Phys. Chem. B* **109**, 18418–18426 (2005).

250. Sen, D., Thapa, R. & Chattopadhyay, K. K. Small Pd cluster adsorbed double vacancy defect graphene sheet for hydrogen storage: A first-principles study. *Int. J. Hydrogen Energy* **38**, 3041–3049 (2013).